Performance of Selected Adsorbents for CO_2 Capture: Equilibrium and Column Dynamics Study

Thesis

Submitted in partial fulfillment of the
requirements for the degree of

DOCTOR OF PHILOSOPHY

by

Satyannarayana Edubilli

Department of Chemical Engineering

Indian Institute of Technology Guwahati

Guwahati 781039, INDIA

January, 2020

Department of Chemical Engineering
Indian Institute of Technology Guwahati
Guwahati 781039 (INDIA)

CERTIFICATE

It is certified that the work contained in the thesis entitled **"Performance of Selected Adsorbents for CO_2 Capture: Equilibrium and Column Dynamics Study"**, by **Satyannarayana Edubilli** has been carried out under my supervision and that this work has not been submitted elsewhere for a degree.

_____

(Dr. Sasidhar Gumma)
Professor
Department of Chemical Engineering
Indian Institute of Technology Guwahati
Guwahati 781039 (India)

Dedicated To

To My Parents

&

Beloved Sister 'Sunitha'

ACKNOWLEDGEMENTS

It is my great pleasure to thank each and every one who helped directly or indirectly to complete my research work and made this thesis possible. I owe my deepest gratitude to all of them.

I would first like to acknowledge my supervisor **Prof. Sasidhar Gumma** for his valuable guidance throughout the research work. I thank him for his encouragement, patience towards research and support, which enabled me to develop a better understanding of the subject leading to the present thesis. My sincere thanks also goes to **Prof. Prabirkumar Saha** for his administrative supervisor support (January'2017- July'2018). I would also like to acknowledge my sincere gratitude to my doctoral committee members, Prof. Bishnupada Mandal, Prof. Amit Kumar and Prof. Mohammad Qureshi, for their advice and suggestions throughout my research work.

My sincere thanks go to the faculty members of Department of Chemical Engineering, IIT Guwahati, for their continuous suggestions and inspirations. I also like to express my thanks to the staff members for making a homely atmosphere.

I would like to thank the Central Instruments Facility and Analytical Lab Facility, Department of Chemical Engineering of IIT Guwahati for providing the facilities to carry out BET, TGA, FTIR, FESEM and XRD analysis.

Coming to Lab mates, it was a wonderful journey of knowledge and idea sharing while working with **Dr. Prashant Mishra**, special thanks goes to him. I must grateful to other lab mates Dr. Debjyoti Sahu, Mr. Abhik Bhattacharjee, Mr. Ramesh Tellagorla, Mr. Prudhviraj Medikonda,

and Mr. Pradip Das. I am also thankful to other lab mates such as Mr. Vyas, Mr. Rajsekhar, Mr. Mudit, Mr. Manik, Mr. Sagar and Ms. Mousumi for maintaining a nice lab environment.

I cannot forget to thank my friends here at IITG: Dr. Srinivasarao Manne, Dr. Pradeep Sadhu, Dr. Sunil, Dr. Kiran, Dr. Kishore, Dr. Santosh, Dr. Ganesh, Dr. Murali, Dr. Anil, Dr. Chinna, Dr. Rajsekhar, Mr. Supriyo, Dr. Kundu, Mr. Srinu Nagireddi, Mr. Durga Prasad Kelli, Dr. Naik, Dr. Unnava, Dr. Mallikarjunredy, Mr. Sunku, Mr. Sashi, Dr. Narasimha, Mr. Bharath, Dr. Santosh, Mr. Hanumanth, Mr. Rambabu, Mr. Prasad, Mr. Harish, Mr. Pradeep, Mr. Ramu for the lovely support in making my stay at IIT Guwahati memorable. I also thankful to all the members of **weekend cricket group** and **badminton group** at IITG.

This journey would not have been possible without the support of my friends outside IITG, Mr. Rambabu, Mr. Nookaraju, Mr. Giri, Mr. Jaipal, Mr. Anil, Mr. Praveen, Mr. Mohan, Mr. Ramesh, Mr. Tentu, Ms. Ramya, Ms. Goli, Ms. Prasanna, and Ms. Krishnaveni, thank you for your thoughts, well-wishes/prayers, phone calls, e-mails, texts, visits and being there whenever I needed a friend.

Finally, deep heartedly, I thank my parents and my sister for their encouragement, blessings and motivation at each and every step.

Date:

Place: _____

(Satyannarayana Edubilli)

ABSTRACT

In the last two decades, metal organic frameworks (MOFs) have emerged as promising materials for gas separation and storage. Majority of the literature on MOF materials for gas separation is limited to equilibrium measurements due to the complexity associated in dynamic measurements such as the column break through studies and development of process cycles. Other reasons contributing to this trend include, the challenges involved in scale up of the synthesis procedure (to produce sufficient MOF material for the column studies) and that in pelletization of the synthesized MOF powders.

In this work, the metal organic frameworks UiO-66, MIL-101(Cr), Cu-BTC and MIL-53(Al) are systematically investigated for CO_2/N_2 separation. In the first part of work, the chosen MOFs are synthesized in 10 g level. Then the synthesized MOF powders are shaped into pellets using poly vinyl alcohol (PVA) as the binder. The effect of shaping on structural and functional characteristics of MOF are examined through the BET surface area analysis, FESEM, FTIR, TGA and XRD analysis.

The pure component isotherms of CO_2, N_2 are measured on MOF powders and pellets. About 14-20% decrease in CO_2 adsorption capacity is observed after pelletization. Although, a reduction in specific loadings is observed, the change in volumetric capacity is lower, due to the increase in bulk density after pelletization.

A single column PVSA experimental set up is developed and experimentally validated using zeolite 13X adsorbent. The breakthrough experiments conducted using synthetic dry flue gas (15% CO_2, balance N_2) as feed in a column containing about 8 to 12g of the MOF pellets (at 1.3

bar and 300 K) reveal preferential adsorption of CO_2 over N_2 and the CO_2 separation. The process performance of MOF pellets is evaluated in three different PVSA cycles using the single column. The inclusion of purge and rinse step result in an increase of N_2 product purity and CO_2 product purity respectively. The best performance achieved with the employed 5-step (pressurization, adsorption, CO_2 rinse, blowdown and N_2 purge along with evacuation) PVSA cycle on the four chosen MOFs is CO_2 purity (35%-68%), CO_2 recovery (54%-61%) and CO_2 productivity (0.075-0.269 $kgCO_2/(kg_{ads} \cdot h)$. The findings from PVSA suggest that these MOF materials are promising for CO_2/N_2 separation at low CO_2 concentrations, however a multi-bed PVSA may be needed to meet the process performance parameters for industrial requirement (CO_2 purity >95%, CO_2 recover >95%).

CONTENTS

PAGE NO:

LIST OF TABLES

LIST OF FIGURES

Nomenclature

b	Second virial coefficients for adsorption, mol^{-1} kg
$b^{(0)}$ and $b^{(1)}$	Temperature independent parameters of second virial coefficients, mol^{-1} kg and mol^{-1} kg K, respecively
c	Third virial coefficients for adsorption, mol^{-2} kg^2
$c^{(0)}$ and $c^{(1)}$	Temperature independent parameters of third virial coefficients, mol^{-2} kg^2 and mol^{-2} kg^2 K, respecively
C_i	Concentration at the column outlet
C_0	Concentration at the column outlet
B^{gas}	Gas phase second virial coefficient, m^3 $Kmol^{-1}$
Δh_{ads}	Enthalpy of adsorption, kJ mol^{-1}
$\Delta h_{ads,0}$	Enthalpy of adsorption at zero coverage, kJ mol^{-1}
M_0	True adsorbent weight including bucket weight in vacuo, g
M_{eq}	Adsorbent plus bucket weight at equilibrium, g
N	Excess amount adsorbed, mol kg^{-1}
N^{max}	Saturation capacity, mol kg^{-1}
N_1^{max} and N_2^{max}	Saturation capacities of sites 1 and 2, respectively, in DSL model, mol kg^{-1}
P	Pressure, bar
P/P^0	Relative pressure
R	Universal gas constant, J mol^{-1} K^{-1}
T	Temperature, K
V	Volume, m^3
V_{bucket}, V_s	Buoyancy volume of bucket and impenetrable solid volume, respectively, cm^3

$V_{buoyancy}$	Buoyancy volume of the sample, cm^3
PVA@MOF	Shaped MOF pellets
F_{PRES}	Feed Pressurization Flow rate
F_{FEED}	Feed Flow rate
F_{PUR}	N_2 Purge Flowrate
F_{RIN}	CO_2 Rinse Flow rate
BT	Breakthrough time
t_{FEED}	Feed step time during a process cycle
t_{PUR}	Purge step time during a process cycle

ABBREVIATIONS

BDC	Benzene 1,4-dicarboxylic acid
BTC	Benzene 1,3,5-tricarboxylic acid
MOFs	Metal organic framework
MIL	Materials Institute Lavoisier
HKUST	Hong Kong University of Science and technology
UiO-66	Universitetet i Oslo
PVA	Polyvinyl alcohol
lp	Large pore
np	Narrow pore
VSA	Vacuum swing adsorption

PSA	Pressure swing adsorption
PVSA	Pressure vacuum swing adsorption
BET	Brunauer-Emmett-Teller
TGA	Thermo gravimetric analysis
FTIR	Infrared
XRD	X-ray diffraction
FESEM	Field Emission Scanning Electron Microscopy

CHAPTER 1

INTRODUCTION

Over the last few decades, metal organic framework materials have been extensively studied and emerged as promising materials for CO_2 capture. Although MOFs has shown good CO_2 equilibrium adsorption capacities, these materials still present stiff challenges in terms of scale up synthesis and process development. This chapter presents a discussion on CO_2 emissions, CO_2 capture technologies, adsorption processes and adsorbent materials. The research objectives of the present work are presented.

1.1 Climate change and CO_2 emissions

With the growing global population, more and more countries started industrialization to meet the energy needs. The major part of the world's energy demand is supplied by burning of the fossil fuels. The fossil energy resources are abundant in nature but upon combustion, they produce large quantities of carbon. Due to this in the last five decades, the concentration of CO_2 present in the atmosphere is increased from 310 ppm to over 380 ppm [1]. According to Intergovernmental Panel on Climate Change (IPCC) report, CO_2 concentration in atmosphere at the end of year 2100 may raise up to 570 ppm [2]. So, recently there is a growing concern worldwide regarding global warming which is mainly induced by the emission of carbon dioxide into the atmosphere.

Even though efforts are now underway to replace coal based resources by use of nuclear power and use of natural gas but it is very hard to replace all the coal based power plants due to the concerns of economic and non-availability of energy sources. Hence, development of energy efficient and economically viable technologies for capture and sequestration of CO_2 from coal-fired power plants is necessary to address the problem of global warming and climatic change.

1.2 CO_2 capture technologies

The three major approaches to reduce the CO_2 emissions from power plants are (Figure 1.1),

Pre-Combustion: Pre-combustion capture involves de-carbonation by gasification of the primary fuel, coal or biomass. The fuel is first burnt in the presence of oxygen or air to produce syn gas. The CO produced further converted to CO_2 by Water-Gas-Shift reaction to yield H_2. The concentration of CO_2 in mixture can range from 15-50%. This high CO_2 Concentration offers some potential advantage over the post combustion method, which removes dilute CO_2 (~3-15% CO_2 in N_2 from flue gas at low pressures) to separate the CO_2. On the other hand, the total capital cost of base gasification process are often more expensive than the coal fired power plants.

Oxy-fuel Combustion: Oxy-fuel combustion is the process of combusting fuel in the stream of a nearly pure oxygen environment instead of air. The resulted gaseous combustion reaction product comprised mainly of CO_2 (up to 89 vol %) and water. In this method, a simple CO_2 separation and purification is sufficient due to high CO_2 concentration in the flue gas. On the other hand, the challenge lies in obtaining the large quantities of pure oxygen which results in increase of capital cost and energy consumption.

Post-Combustion: The flue gas from combustion of fossil fuels in presence of air contains CO_2, H_2O, N_2, O_2, SOx and NOx etc. The SOx and NOx are removed by sending the flue gas to desulphurization unit. Then the CO_2 can be separated from this flue gas by employing a suitable

separation process. The major challenges in CO_2 removal are low CO_2 concentration (typically 3-15%) and high temperatures of flue gas streams compared to the other two capture options. Despite these challenges, the post combustion capture offers flexibility and can be retrofitted to the existing coal fired power plant without requiring substantial change in basic combustion technology.

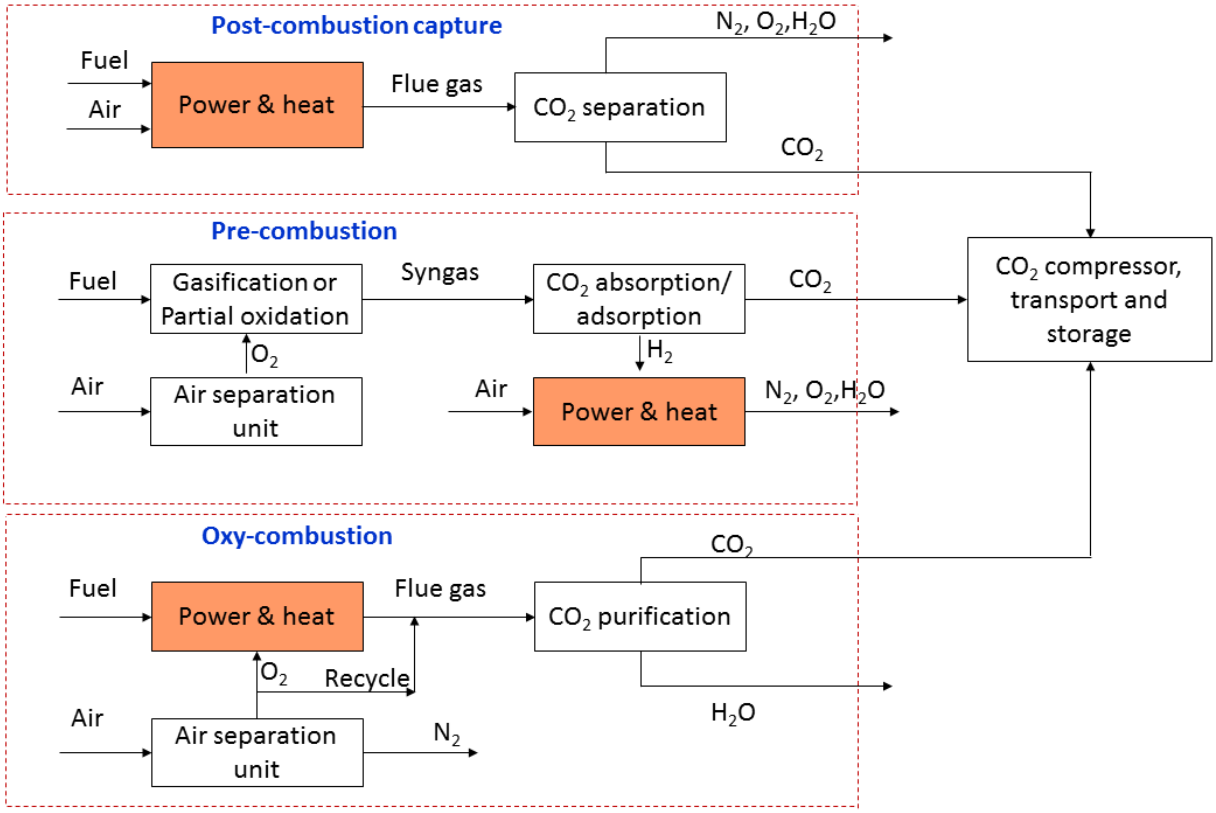

Figure 1.1: Schematics of CO_2 capture technologies for power plants [2].

There are several technologies available for post combustion CO_2 capture namely conventional (Absorption) and new emerging technologies (Cryogenic distillation, Membranes and Adsorption) Generally, a solvent is used to absorb the CO_2 present in the gas stream by forming an exothermic chemical reaction at room temperature (Absorption). Then the CO_2 absorbed is recovered by reversing the reaction at an elevated temperatures (stripping or regeneration). Monoethanolamine (MEA) is the most widely used solvent for CO_2 capture in natural gas industry for the past 60 years. However, the absorption process has some disadvantages like requirement of large volumes

of solvent, low CO_2 capture loadings, highly energy intensive and assisted with problems like corrosion in the presence of Oxygen, solvent degradation may occur in the presence of SOx, NOx in coal fired flue gas streams. Therefore, the development of new amine solvents and alternative methodologies are currently being explored. In cryogenic separation, the flue gas is first compressed to a high pressure and then sent to a heat exchanger for cooling. Then the liquefied CO_2 is collected from the column bottom and the gaseous N_2 can be collected at the top of the column. Cryogenic separation is also highly energy intensive.

Membrane separation is another alternative technology currently being investigated for the gaseous separation. The development of membranes with higher selectivity is still under research phase. On the other hand, like absorption process, membrane process also has some drawbacks like low CO_2 selectivity and fouling. Besides various process technology options available for CO_2 capture from flue gas, adsorption processes using novel solid sorbents capable of reversibly capturing CO_2 is deemed as a promising technology. In general, adsorption process serves as a potential technology in terms of its flexibility, simplicity of its design, greater capacity, and reduced energy requirement for regeneration and ease of operation. However, a suitable adsorbent is necessary to achieve this objective.

1.3 Adsorption process and porous adsorbents

1.3.1 Adsorption

Adsorption is a surface phenomenon by which molecules, known as adsorbates, are concentrated near a solid surface in excess of the bulk concentration [3]. The solid on which adsorption occurs is called adsorbent. The adsorption process can be broadly divided into two categories based on the nature of surface forces: physisorption and chemisorption. In physisorption, the interaction

between the adsorbent and adsorbates are of a physical nature involving van der Waals forces. Where as in case of chemisorption, the interactions are of a chemical nature involving the reaction or dissociation of the fluid molecule. In chemisorption, there is necessarily contact between the adsorbate molecule and adsorbent surface, therefore it is confined to a single layer or mono layer. On the other hand, in physisorption, at sufficiently high pressures adsorption is assumed to be occur in multiple layers.

1.3.2 Cyclic adsorption processes

Adsorption processes are broadly classified as pressure swing (PSA) and temperature swing (TSA) adsorption processes. In a PSA process, the adsorption takes place at high pressures and desorption occurs at atmospheric pressures, whereas in TSA process, desorption is facilitated by heating. If the cycle switches between adsorption at atmospheric level and desorption at vacuum then it is called vacuum swing adsorption (VSA) process. Pressure vacuum swing adsorption (PVSA) cycles have adsorption step at pressures above atmospheric and desorption under vacuum. The salient feature of a PSA process lies in the fact that pressure can be changed much more rapidly, thus making it possible to operate a PSA process on a faster cycle, thereby increasing the throughput per unit of adsorbent bed volume. On the other hand, in case of a TSA process, long cycle times are required for the adsorption bed to cool down, which could affect the throughput of the process. However, TSA is preferred to PSA in the case of strongly adsorbed species, for which a variation of pressure is not sufficient to regenerate the adsorbent.

1.3.3 Conventional adsorbent materials

For the success of any adsorption based process, the important component is the adsorbent. The suitable adsorbent for any application should have the following characteristics like high adsorption capacity, high selectivity, mild conditions for regeneration, stability during the

adsorption-desorption cycles, tolerance to the presence of moisture and impurities in the feed gas and should be low in cost.

There are many adsorbent materials reported in literature for adsorptive separation but only a few have survived the technological progress. Some well-known adsorbent materials are silica gel, activated alumina, activated carbon, carbon molecular sieves and zeolites. Each of these adsorbents has certain specific features towards adsorptive separation/purification.

Activated carbon: Activated carbons are composed of carbon-containing biological materials such as coal (e.g. bituminous coal, lignite), industrial by-products (e.g. scraps of polymeric materials, petroleum, coke pitch), and wood or other biomass materials (e.g. cocoanut shells, saw dust) [4]. Therefore, activated carbons have a huge advantage over other adsorbents in terms of the low cost of raw materials. The production of activated carbon is consist of two steps: thermal decomposition of carbonaceous material followed by activation with steam or carbon dioxide at elevated temperature (700-1100 ^{o}C) [5]. Activated carbons have some limitations such as, limited CO_2 removal at high pressure and low temperature [6], low adsorption capacity and selectivity at low partial pressures of CO_2 [7].

Silica gel: Partial dehydrated form of polymeric colloidal silicic is known as silica gel ($SiO_2.nH_2O$) [8]. The presence of hydroxyl group in the structure yields polarity and it exhibits selectivity for polar adsorbates such as water, alcohol, amine etc. over non-polar adsorbates. It is known to show good selectivity for phenols and aromatic hydrocarbons and it is used in the arosorb process to separate aromatic hydrocarbons from paraffin's [8]. Silica gel has been widely used as a desiccant due to its very high capacity for moisture. Moreover, the regeneration temperatures are quite low (around 150 °C) in comparison with zeolites which should be regenerated at very high temperatures (~350 °C) to completely remove the adsorbed moisture [9].

Activated Alumina: Activated alumina is a porous high area form of aluminium oxide, prepared either directly from bauxite ($Al_2O_3.3H_2O$) or from monohydrate by dehydration or recrystallization at elevated temperature. The surface is more polar than that of silica gel and has both acidic and basic character [8]. At elevated temperatures the capacity of activated alumina is higher than that of silica gel and it was used as desiccant for drying warm air or gas streams. However, for this application it has been largely replaced by molecular sieve adsorbent which exhibit both higher capacity and lower vapor pressure.

Zeolites: The zeolites are made of tetrahedral frameworks of silica and alumina. The presence of the alumina atom in the convectional zeolites based on silicate frameworks lead to a negative charge on the framework, with exchangeable cations within the pore structure (usually Na or other alkali or alkaline earth metals). This unique structure of zeolite enables the alkali cations to generate strong electrostatic interactions with acidic molecules such as CO_2 [10, 6]. Therefore, varying the Si/Al ratio and nature of the extra-framework cations can play a significant role in controlling the CO_2 adsorptive properties. Some zeolites (Zeolite 13X) have shown very promising CO_2 adsorption capacities [11] and selectivity's at lower pressures, but they have limited high pressure capacity compared to activated carbons due to low pore volume. In addition, due to strong affinity for CO_2 at low pressure, the regeneration energy requirement of Zeolite 13X is also high.

1.3.4 Novel adsorbents

The above discussed conventional adsorbents were commercialized successfully and have been used for various industrial applications. However, as the need grows for more efficient and economic gas separation processes, the worldwide synthetic community focused their research towards development of novel adsorbent materials.

In the late eighties and nineties of the last century R. Robson and co-workers [12, 13] extensively studied on the targeted synthesis of porous three dimensional structures. They utilized organic linkers of distinct geometrics together with metal ions and yielded supermolecular structures exhibiting a specific structure type, for example diamond [14-15], rutile [16-17] or PtS-like [18-19] networks, which feature the same topology as the respective inorganic materials, but with largely extended cell parameters. Interestingly, their results shown that the polymeric structures can be controlled by the choice of solvent, counterion of the metal precursor and reaction temperature giving rise to a rich host guest chemistry [13]. However, due to the regularly charged character of these coordination polymers and weak coordination bonds between the ligands and single metal nodes, the structural collapse was observed after removal of guest molecules.

In 1997, S. Kitagawa and co-workers was first reported the reversible adsorption of small gas molecules (CH_4, N_2, O_2) in the microporous metal organic framework (MOF) $[Co_2(bipy)_3(NO_3)_4]_n$. These MOF materials has permanent porosity and do not collapse upon the removal of guest molecules from pores [20]. The major breakthrough was achieved two years later by the group of O. M. Yaghi [21] with the synthesis of highly porous MOF-5 ($[Zn_4O(bdc)_3]_n$). This opened the window for synthesis of large number of metal organic frameworks.

1.4 Background of the present research work

In the past two decades, Metal Organic Framework (MOF) materials emerged as new and promising materials for separation/storage of gases like CH_4, H_2 and CO_2, due to their high surface area and tunable pore size. MOFs are 3-dimensional porous crystalline structures composed of metal ions interconnected with organic linkers. The structure and properties of the materials can be designed and systematically tuned by proper choice of metal atom and organic linkers. This

ability to rationally design and modify the crystal structures is the key to achieve high adsorption loadings and selectivity for CO_2. Several research groups in the world are working to synthesize MOFs with exceptionally high surface areas and higher CO_2 loadings. The CO_2 and N_2 adsorption measurements on the reported MOFs indicating their importance in flue gas separation [22].

Majority of the literature on MOF materials for gas separation is limited to equilibrium measurements due to the complexity associated in dynamic measurements such as the column break through studies and development of process cycles. Other reasons contributing to this trend include, the challenges involved in scale up of the synthesis procedure (to produce sufficient MOF materials for the column studies) and that in pellatization of the synthesized MOF powders (necessary to minimize the pressure drop in column).

In the present work, we have chosen four well studied metal organic frameworks and their CO_2/N_2 separation performance was evaluated experimentally through the following formulated objectives.

1.5 Research Objectives

This doctoral project aims at studying the CO_2/N_2 separation performance of selected metal organic frameworks (MOFs) UiO-66, Cr-BDC (or, MIL-101)), Cu-BTC (or, HKUST-1), and flexible MOF (MIL-53(Al)). It covers the following topics,

(I) Scale up synthesis of the above chosen MOF materials and their characterization.

(II) Effect of pellatization on textural, structural and adsorption characteristics of MOFs.

(III) Measurement of pure component equilibrium adsorption isotherms of CO_2 and N_2 on above mentioned MOFs in powder and pellet forms.

(IV) Thermodynamic modelling of the measured equilibrium isotherms.

(V) Development of a Pressure Vacuum Swing Adsorption (PVSA) system for breakthrough and process cyclic experiments.

(VI) Investigation of CO_2/N_2 separation performance of MOF pellets through PVSA process.

The arrangement of this thesis is done as follows.

Chapter 1 discusses the details of CO_2 emissions, CO_2 capture technologies and the definition of adsorption along with an overview on various types of adsorbents, their importance and limitations. It also includes background and objectives of the present research work. **Chapter 2** gives a detailed report on design and synthesis of metal organic frameworks. The structures of chosen UiO-66, MIL-101(Cr), Cu-BTC and MIL-53(Al) MOF materials are described. CO_2, N_2 equilibrium adsorption uptakes, breakthrough and process cycle studies on MOFs as well as on some conventional adsorbents has also been presented. **Chapter 3** includes relevant theory related to adsorption and isotherm modeling. The pressure swing adsorption process performance indicators are also explained. **Chapter 4** provides the details and protocol for various experiments performed in this work. The MOF synthesis procedures followed are included. Physical properties and purities of gases considered for this work are provided. **Chapter 5** discusses the development of experimental set up for binary breakthrough and process cycle experiments. **Chapters 6, 7, 8, 9** contains the results of the scale up synthesis, pellet preparation, pure component isotherms, binary mixture breakthrough and process cycle experiments on the chosen MOFs UiO-66, MIL-101(Cr), Cu-BTC and MIL-53(Al) respectively. **Chapters 10** outlines conclusions and future scope.

CHAPTER 2

LITERATURE REVIEW

2.1 Metal Organic Frameworks

The origin of the term “metal-organic framework” is attributed to Omar Yaghi [23, 24], a pioneer in MOF development. Metal-organic frameworks (MOFs), also known as metal-organic networks, or coordination polymers, represent a class of porous materials [23-31] containing metal ions linked by organic bridging ligands. The structures resulting from metal-ligand linkages can be discrete zero-dimensional (0D) molecular complexes or infinite one/two/three-dimensional (1D/2D/3D) architectures. A variety of MOFs can be designed systematically by changing the organic linker, metal node, reaction conditions. The synthesis of new MOF materials has grown at an enormous rate with in the past two decades (Figure 2.1).

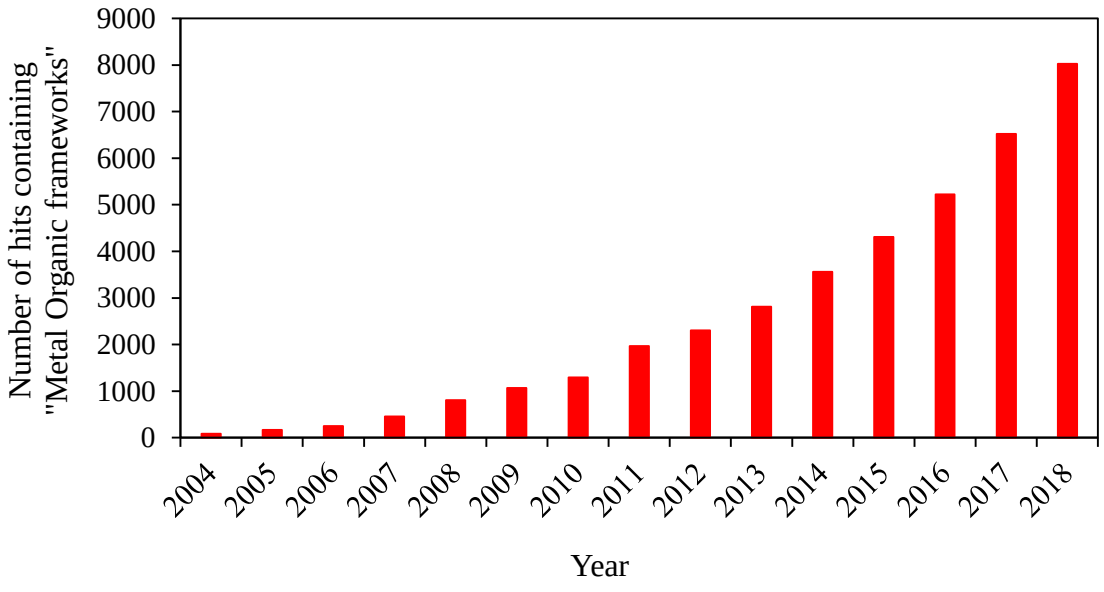

Figure 2.1: Number of citations containing the key word “Metal Organic frameworks” in the past 15 years (source: SciFinder Scholar, accessed on 25/12/2019).

2.1.1 Synthesis of MOFs

MOF synthesis can be a bottom up approach, which is the process of making a complex product from basic building blocks. There are many materials synthesis methods which have been used for MOF synthesis, including solvothermal synthesis (conventional approach), microwave synthesis [32], sonication synthesis [33], mechanochemical synthesis [34], and solid state synthesis [32]. Among these, solvothermal method is the most widely used due to resultant formation of stable MOF structures. In solvothermal synthesis, the metal precursors and organic ligands are typically combined in polar solvents such as water, alcohols, acetone, acetonitrile or dialkyl formamides and heated in sealed vessels such as Teflon-lined stainless steel bombs or glass vials, generating autogenous pressure. The metal ion source is typically a salt with nitrate/chloride as the counterion. Altering the cation in the metal source can lead to significantly different MOF structures [35]. Modulators can also be added to affect particle growth and or alter the MOF structure. Typically, modulators are weak acids which can coordinate with the metal ions in the solution, stabilizing or inhibiting transient structures, thus allowing a degree of control over the nucleation and growth [36]. The coordination of the metal node and organic linkers strongly depends on the temperature of the reaction. For example, seven different cobalt succinates solids were obtained using the same starting mixture and by only varying the reaction temperature [37]. Choice of synthesis temperature is typically determined by trial-and-error, as there are many unknown factors influencing the synthesis mechanism. Some of the representative examples of organic ligands used in metal-organic frameworks are shown in Table 2.1.

Table 2.1: Some commonly used organic linkers in MOF synthesis.

Organic Linker		**MOF**	**Surface Area (m^2 g^{-1})**	**Ref.**
Name	**Structure**			
benzene 1,4-dicarboxylic acid (BDC)	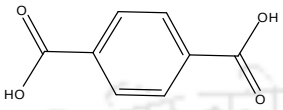	UiO-66	1400	[38]
		MIL-53	1140	[39]
		MIL-101	2674	[40]
2-amino, benzene 1,4-dicarboxylic acid	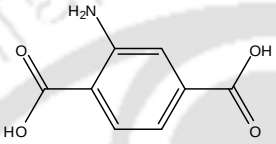	NH_2-MIL-53	960	[41]
		IRMOF-3	2160	[42]
benzene 1,3,5-tricarboxylic acid (BTC)	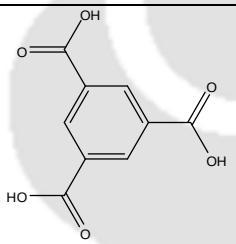	Cu-BTC or HKUST	1482	[43]
		MIL-100	1810	[44]
2,5-dihydroxy, benzene 1,4-dicarboxylic acid	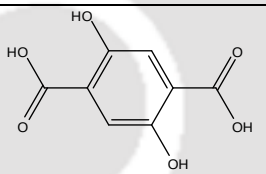	MOF-74 or M/DOBDC (M = Mg, Zn etc.)	885 – 1800	[45,46]
benzene 1,4-dicarboxylic acid and 1,4-diaza bicycle [2,2,2] octane	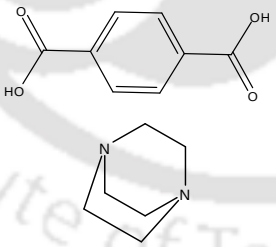	$M_2(BDC)_2DABCO$ or M/DABCO	1400 – 1925	[47,48]

2.1.2 Classification of MOFs

Following a suggestion made by Kitagawa in 1998 [49], MOFs were classified in three categories, 1st, 2nd, 3rd generation (Figure 2.2). The 1st generation MOFs collapse upon removal of guest molecules yielding an amorphous structure with no porosity. The 2nd generation MOFs are rigid and remain unchanged upon adsorption and desorption of guest molecules. Usually, these 2nd generation MOFs present a normal type-I shape adsorption isotherm. Due to their permanent porosity, large specific surface areas and pore volumes, 2nd generation MOFs have been extensively studied for their adsorption based applications such as gas storage [50-53], gas separations [54-56], catalysis [57-58] and drug delivery [59-60]. Cu-BTC, MIL-101(Cr) and UiO-66 (Zr) are some of the most studied 2nd generation MOFs for CO_2 capture. The 3rd generation MOFs (flexible/dynamic MOFs) represents a very unique class of materials. These materials undergo a structural transition (also known as breathing phenomena) when the guest molecules are inserted or removed, and are affected by external stimuli, such as pressure, temperature and adsorbent history [49, 61]. These flexible MOFs exhibits stepwise adsorption upon adsorption of CO_2 or some other molecules.

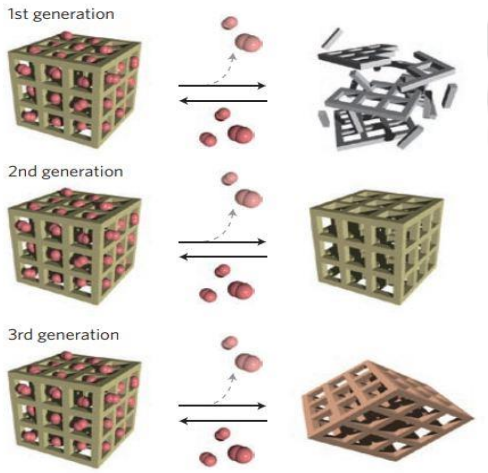

Figure 2.2: The three generations of co-ordination polymers according to S. Kitagawa [49]

2.2 Structural features of the chosen MOFs in the present study

2.2.1 Cu-BTC or HKUST-1

Cu-BTC [$Cu_3(BTC)_2$, BTC = 1,3,5-benzenetricarboxylate] also known as HKUST-1 is a 2nd generation MOF. It was first reported by Chui et al. [62] in 1999. In this framework, two octahedrally co-ordinated Cu atoms are connected to eight oxygen atoms of tetracarboxylate units to form a dimeric Cu paddle wheel. Each BTC ligand holds three dimeric Cu paddle wheels to form a microporous open framework with face-centered cubic symmetry. One unit cell dimension of Cu-BTC can be represented as a = b = c = 26.343 Å. The large cavities are connected through square-shaped windows with a diameter of ca. 9 Å. This structure is shown in Figure 2.3.

As-synthesized Cu-BTC MOF contains bound solvent molecules on the axial sites of each Cu^{2+} metal center. These solvent molecules can be removed in vacuo at elevated temperatures to create open binding sites for guest molecules. Cu-BTC is the most widely studied MOF material till date.

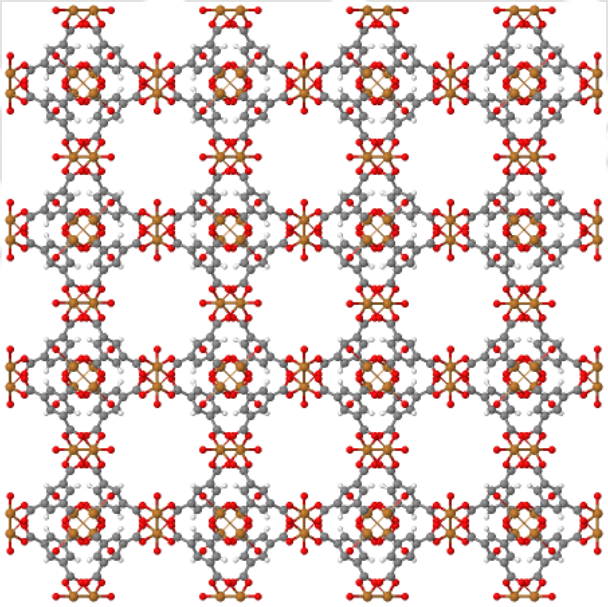

Figure 2.3: Crystal Structure for Cu-BTC MOF: Copper-Orange, Oxygen-Red, Carbon-Grey [63]

2.2.2 Cr-BDC or MIL-101(Cr)

Cr-BDC [BDC = 1,4-benzenedicarboxylate] framework or MIL-101 (MIL stands for Material of Institute Lavoisier) has a complex structure. It was first synthesized and reported by Férey et al. [64]. The synthesized product showed a very high surface area (BET, 4100 $m^2 g^{-1}$) and pore volume (1.41 cc $g^{-1)}$. They reported that MIL-101 to be very stable for months under ambient conditions and has high thermal stability (up to 473 K). Its structure can remain stable in the presence of different organic solvents. These properties caught the attention of researches working in the field of adsorptive separation.

Cr-BDC is synthesized from the linkage of terephthalic acid (H_2BDC) anions and inorganic trimer as represented in Figure 2.4. The as-synthesized Cr-BDC contains removable water molecules and therefore coordinated unsaturated metal sites (cus) are available once the MOF is activated. Unit cell dimensions can be represented as a = b= c = 88.869 Å, volume is 702 $Å^3$. Removal of guests results into an accessible pore diameters of size ~29 Å and 34 Å.

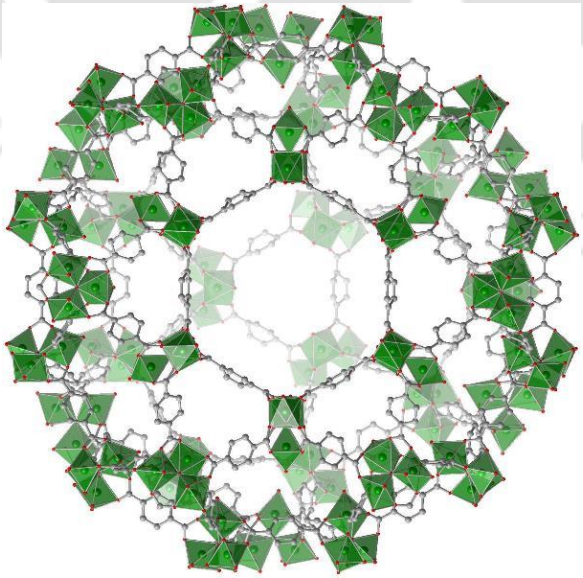

Figure 2.4: Crystal Structure for Cr-BDC MOF: Chromium-Green, Oxygen-Red, Carbon-Grey [65].

2.2.3 UiO-66 (Zr)

UiO-66 (UiO stands for University of Oslo) is a Zr-based MOF, in which rigid $Zr_6O_4(OH)_4$ octahedral groups are connected by the BDC linkers. It was first reported by Cavka et. al [66]. The Zr-O bonds formed between the cluster and carboxylate ligands is believed to be the source of increased stability of Zr-based MOFs. Specifically, the combination of strong Zr−O bonds and the ability of the inner Zr_6-cluster to rearrange reversibly upon removal or addition of μ_3-OH groups without any changes in the connecting carboxylates are thought to contribute to the greater stability of UiO-66. These properties made UiO-66, an attractive material for a wide variety of applications, including gas adsorption and separations, drug delivery, toxic chemical sensing and removal, and catalysis. Various functionalized derivatives of UiO-66 have also been synthesized: UiO-66-X (X = NH_2, OH, NO_2, etc.). The crystal structure is shown in Figure 2.5. Unit cell dimensions can be represented as a = b= c = 20.7465 Å with a pore size of 6 Å.

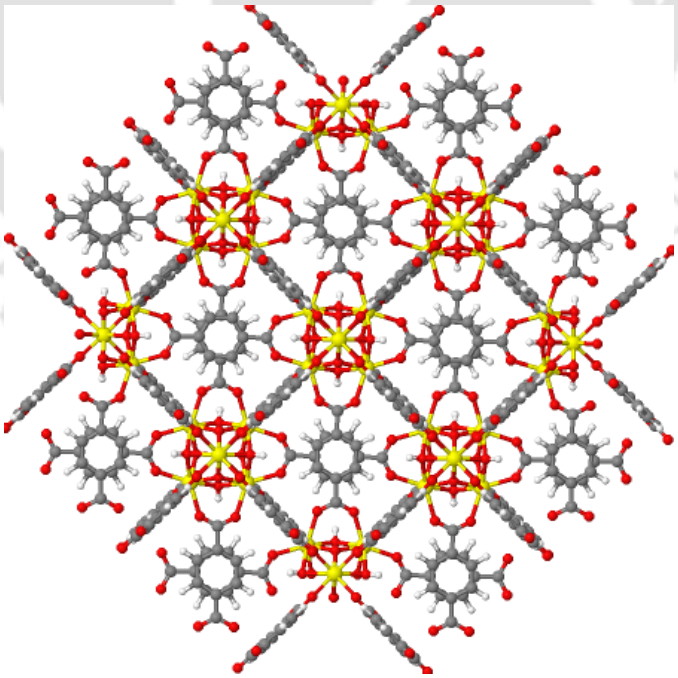

Figure 2.5: Crystal Structure for UiO-66 MOF: Zirconium-Yellow, Oxygen-Red, Carbon-Grey [67]

2.2.4 MIL-53(Al)

MIL-53(Al) is a 3rd generation MOF (flexible/dynamic framework). It was first synthesized by the group of Ferry in 2002 [68]. MIL-53(Al) is comprised of $AlO_4(OH)_2$ corner-sharing octahedral chains connected by terephthalate groups to form a three dimensional structure with 8.5 Å pores. This material has attracted the attention of researchers due to its structural flexibility and the breathing or shrinking of pores [69] during adsorption between two distinct phases called the large-pore phase (lp) and the narrow pore phase (np), which have a remarkable difference in cell volume of up to 35% (from 1412 $Å^3$ to 947 $Å^3$) [68]. At higher temperature and in the absence of guest molecules, the lp phase is the most stable form. However, in the course of gas adsorption (such as CO_2), the lp phase transforms into the np phase at low pressures, and the reverse transformation occurs at higher pressure. This phenomena is illustrated in Figure 2.6.

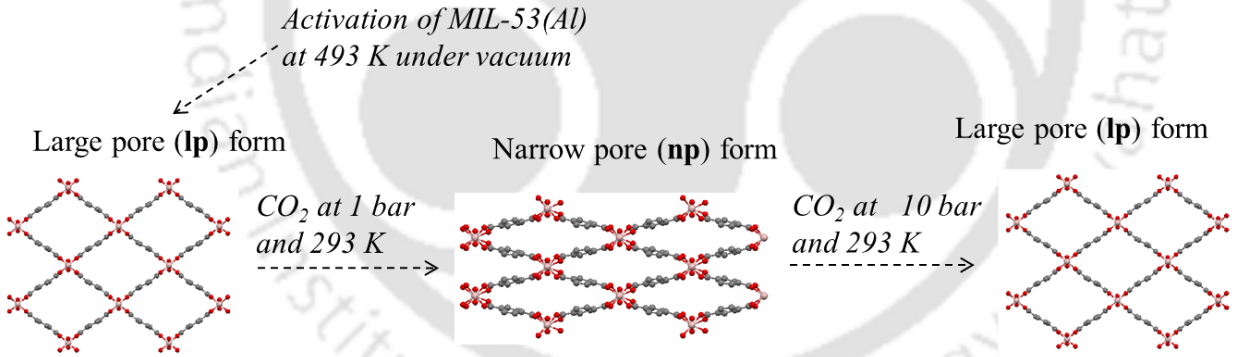

Figure 2.6: Structural transformation in MIL-53(Al) [39]

Other factors affect the structural transition in MOFs are temperature [69] and mechanical pressure [70].

2.3 Literature review on CO_2 adsorptive separation in MOFs

The screening of new adsorbent materials for CO_2 capture depends on many factors such as adsorption capacity, selectivity, regenarability and performance under dynamic process conditions. However, majority of the MOF literature is limited to the equilibrium CO_2 adsorption capacity measurements. Literature on the dynamic breakthrough experiments and process cycle evaluation is rather limited. Table 2.2 represents the low pressure (<1.2 bar) CO_2 adsorption capacities on several metal organic frameworks. Most of these MOFs exhibit good uptake capacities at pressures at and above 1 bar. Since CO_2 loadings at 0.15 bar (i.e. ~ CO_2 pressure in flue gas) are more relevant. CO_2 uptake on various MOFs at pressure relevant to flue gas conditions is listed in Table 2.3. As, N_2 is the other major component in flue gas, N_2 uptake capacities at 1 bar on various MOFs are listed in Table 2.4. For the sake of comparison, CO_2, N_2 adsorption data on some conventional adsorbents is also included.

The reported equilibrium adsorption uptakes of CO_2 and N_2 in Tables 2.2-2.4 clearly indicate that MOF materials have higher CO_2 loadings compared to the conventional adsorbent materials. Moreover, significant difference was also observed between the CO_2 and N_2 capacities at the flue gas conditions. However, breakthrough performance of adsorbent columns is an important characteristic required to evaluate the potential of adsorbents for PSA applications. There have been a few dynamic breakthrough and process cycle evaluation studies of MOF adsorbents for CO_2 separation.

Bastin et al. [100] first reported the experimental separation and removal of CO_2 from its binary CO_2/N_2 and CO_2/CH_4 and ternary $CO_2/CH_4/N_2$ mixtures in a microporous MOF (MOF-508b) using breakthrough experiments.

Liu et al. [101] studied the dry CO_2/N_2 (15:85) mixture breakthrough experiments at 25 ^oC on Ni/DOBDC MOF and reported a CO_2/N_2 selectivity of 45. With introduction of 3 wt% RH water, the CO_2/N_2 selectivity decreased to 22.

Asadi et al. [102] studied the breakthrough curves of CO_2/CH_4 (4.3/83, balance He) mixture on Cu-BTC tablets (purchased from BASF). The adsorption capacity on the pellet form shows 20% reduction due to the shaping. They filled the adsorbent column with 55.8 g of Cu-BTC tablets. At a total feed flow rate of 13.6 SCCM and 308 K and 1.1 bar, the weakly adsorbed component CH_4 was first observed at the bed outlet after 50 s and the strongly adsorbed component CO_2 was detected after 250 s.

Sunil et al. [103] investigated the CO_2/CH_4 separation performance of amino-MIL-53(Al) MOF and compared with zeolite 13X. Amino-MIL-53(Al) pellets were prepared by pressing the powder at a pressure of ca~400 bar in a hydraulic press. Around 715 mg of amino-MIL-53(Al) and 972

mg of 13X zeolite were used for the breakthrough experiments. CO_2/CH_4 (40/60) binary adsorption breakthrough experiments at 1 bar, 303 K and a total flow of 20 Nml/min revealed that Zeolie 13X has high breakthrough time (~10 min) compared to amino-MIL-53(Al) (~2.9 min). However, the desorption experiments (i.e. 20 Nml/min of He purge) revealed that the complete CO_2 desorption was achieved in amino-MIL-53(Al) and in case of zeolite 13X, it was only 69%.

Remy et al. [104] investigated the potential of well-known MOF Mg/DOBDC (Mg-MOF-74) at low pressures through dynamic column experiments. The CO_2/CH_4 (50/50) mixture breakthrough curves on a column packed with Mg-MOF-74 pellets (~ 50 mg) at 308 K and 1 bar indicated a higher CO_2 capacity and separation efficiency for the MOF with respect to the benchmark 13X zeolite. The MOF regained 81% of its original capacity when purged with helium at 308 K for 10 min and fully regenerated at 353 K, which indicates the complete desorption of CO_2 on this material. They also found that, the performance of Mg-MOF-74 severely deteriorated upon long-term exposure to water and oxygen (which are relevant impurities in CO_2 separation from flue gas).

Kizzie et al. [105] studied CO_2/N_2 breakthrough curves using various relative humidities (RHs) with the M/DOBDC (M=Zn, Ni, Co, Mg) series. They found that the Ni and Co based adsorbents retained 60 and 85% of their original CO_2 capacity after hydration in 70% RH, storage for two weeks, then thermally regenerated at 150 ^oC in argon. The analogous Mg and Zn adsorbents showed more severe reduction of CO_2 capacity after the same treatment.

Kim et al [106] carried out the scale up synthesis of UiO-66 in a 100 L pilot scale batch reactor. The obtained powder in the scale up synthesis was comparable to the standard UiO-66. In this study, UiO-66 pellets were prepared by extrusion using polyvinyl alcohol (PVA) as a binder. They

have measured the CO_2/N_2 (40/60) breakthrough curves at 1 bar and 20 bar. The shape of breakthrough was sharper for pellets compared to powder. However, the breakthrough time for pellets is lower compared to the powder due to the densification process. The UiO-66 pellets were grounded and sieved into different particle size groups. The study on effect of pellet size revealed that with increase in particle size, adsorption capacity decreased.

Dasgupta et al. [107] evaluated Ni/DOBDC (CPO-27-Ni) MOF for flue gas separation. They have formulated CPO-27-Ni/alginate spheres and performed CO_2/N_2 breakthrough experiments in dry and wet feed conditions. With the inclusion of 4 mol % water in the feed, the loss in CO_2 breakthrough time of about 15% was observed.

Finsy et al. [108] studied the CO_2/CH_4 separation performance of MIL-53(Al). They produced MOF pellets using poly vinyl alcohol (PVA) as binder and the reduction in adsorption capacity observed after shaping was about 32%. They have investigated the flexibility in MIL-53(Al) under dynamic conditions by performing CO_2/CH_4 (50/50) breakthrough experiments over a pressure range of 1 to 8 bar. Up to 5 bar, the materials has shown an average separation factor of about 7 and above 5 bar pressure, the average separation factor decreased to about 4 due to the structural transition.

Even though the available column dynamic studies on MOFs are limited, they have clearly shown that MOF materials can be useful in adsorptive separation of flue gas, bio gas etc. The next step in exploring these materials for practical applications is their process performance evaluation. However, to the best of our knowledge only few process studies were reported in literature. Table 2.5 shows the process performance of Cu-BTC and UiO-66 MOFs for CO_2/N_2 separation. For the sake of comparison the process performance of conventional adsorbents is also included.

Table 2.2: CO_2 adsorption capacities of various adsorbents at 1 bar pressure

Adsorbent	**BET Surface area (m^2 g^{-1})**	**Temperature (K)**	**Pressure (bar)**	**Capacity (mol kg^{-1})**	**Reference**
Cu-BTC	1663	295	1.0	5.80	[71]
MIL-101 (Cr)	2674	295	1.0	2.80	[40]
MIL-53(Al)	1300	298	1.0	2.41	[72]
MOF-2	345	298	1.0	0.60	[73]
MOF-5(IRMOF-1)	2833	298	1.0	1.0	[73]
IRMOF-3	2160	298	1.0	1.1	[73]
IRMOF-6	2516	298	1.0	1.05	[73]
IRMOF-11	2096	298	1.0	1.5	[73]
MOF-177	4508	298	1.0	0.8	[73]
MOF-505 (NOTT-100)	1547	298	1.0	3.2	[73]
Mg/DOBDC	1800	293	1.0	8.0	[74]
Ni/DOBDC	1218	298	1.0	6.9	[75]
Co/DOBDC	1080	296	1.0	6.7	[76]
MOF-74 (Zn/DOBDC)	816	298	1.0	4.6	[73]

Table 2.2 contd.

Adsorbent	**BET Surface area (m^2 g^{-1})**	**Temperature (K)**	**Pressure (bar)**	**Capacity (mol kg^{-1})**	**Reference**
MIL-47 (V)	600	298	1.0	1.84	[25]
Zn/DABCO	1725	298	1.0	2.00	[77]
Ni/DABCO	1705	298	1.0	2.00	[77]
Cu-BTC (4 wt% H_2O)	-	298	1.0	6.13	[78]
Cu-BTC (8 wt% H_2O)	-	298	1.0	3.95	[78]
Cu-BTTri	1750	313	1.0	1.90	[79]
$Cu_3(TATB)_2$ or (PCN-6)	3811	298	1.0	3.61	[80]
bio-MOF-11	1040	298	1.0	3.45	[81]
SNU-50	2300	298	1.0	3.11	[82]
$Zn(almeIm)_2$ or ZIF-93	864	298	1.0	1.52	[83]
NH_2-MIL-53(Al)	960	298	1.0	2.72	[72]
Zeolite 13X	616	298	1.0	4.7	[84]
Zeolite 5A	-	303	1.2	3.07	[85]
Activated carbon (Norit R1)	1450	298	1.0	2.5	[86]
Silicalite	440	304	0.79	1.31	[87]

Table 2.3: Representative literature of CO_2 Uptake in Selected MOFs at pressure relevant to flue gas conditions

Adsorbent	**Temperature (K)**	**CO_2 uptake at 0.15 bar (mol kg^{-1})**	**Reference**
Cu-BTC	293	2.64	[88]
MIL-53(Al)	298	0.386	[72]
Mg-DOBDC	303	4.68	[89]
Ni-DOBDC	298	3.84	[75]
Co-DOBDC	298	3.23	[25]
Zn-DOBDC	296	1.73	[76]
MIL-47	298	0.25	[25]
Ni-DABCO	298	0.27	[72]
IRMOF-1 or MOF-5	298	0.11	[25]
MOF-177	298	0.14	[90]
IRMOF-3	298	0.14	[20]
ZIF-8	298	0.14	[25]
SNU-50	298	0.66	[70]
Cu-BTTri	298	0.66	[91]
ZIF-78	298	0.75	[92]
Cr-BDC	298	0.18	[40]
UiO-66	298	0.16	[42]
ZIF-100	298	0.23	[93]

Table 2.4: Representative literature for N_2 adsorption

Adsorbent	Temperature (K)	Pressure (bar)	N_2 uptake (mol kg^{-1})	Reference
Cu-BTC	295	1.00	0.31	[71]
MIL-53(Al)	303	1.00	0.20	[95]
Mg-DOBDC	294	1.02	0.85	[96]
Ni-DOBDC	294	1.03	0.74	[96]
Co-DOBDC	294	1.04	0.72	[96]
Cu-DABCO	294	1.33	0.14	[96]
Ni-DABCO	294	1.32	0.37	[96]
Zn-DABCO	294	1.00	0.18	[96]
MOF-177	298	1.00	0.20	[90]
MOF-253	298	1.00	0.13	[95]
Cu-BTTri	298	1.00	0.17	[92]
ZIF-78	298	1.00	0.13	[93]
Zeolite 13X	298	2.00	0.80	[84]
Zeolite 5 A	298	1.10	0.39	[98]
Silicalite	298	1.20	0.27	[99]

Table 2.5: Representative process literature on flue gas separation

Adsorbent	No. of beds	Cycle Sequences	y_{CO2}	Adsorption Temperature (°C)	Adsorption/ Desorption pressure (bar)	CO_2 Purity (%)	CO_2 Recovery (%)	Reference
Cu-BTC pellets	1	FP,FD,RIN,BD,PUR	0.15	35	2.0/0.15	60-72	62-64	[109]
UiO-66/ Alginate beads	1	FP,FD,RIN,BD,PUR	0.15	55	2.0/0.15	61.0	65.00	[110]
Zeolite 13X	1	FP,FD,BD,PUR	0.15	50	1.3/0.1	33.30	86.50	[111]
Zeolite 13X	1	FP,FD,RIN,BD,PUR	0.15	35	2.0/0.15	65-76	53-61	[109]
Activated Carbon	1	FP,FD,BD,PUR	0.15	100	1.3/0.15	49.70	66.80	[112]
Zeolite 5A	1	FP,FD,DP,BD,PUR	0.15	30	1.5/0.1	53.90	91.00	[113]*
Zeolite 5A	2	FP,FD,BD,PUR	0.15	25	1.5/0.1	50.67	95.04	[113]*
Zeolite 5A	2	FP,FD,RIN,BD,PUR	0.15	25	1.5/0.1	69.15	98.92	[113]*
Zeolite 5A	2	FP,FD,RIN,PE,BD, PUR,PE	0.13	22	1.2/0.1	56.93	87.96	[113]*
K^+-Zeolite 13X	2	FP,FD,RIN,BD,PUR	0.15	25	2.0/0.03	92.00	80.00	[114]

*denotes simulation studies; FP: Feed Pressurization, FD: Feed, BD: Blow down, RIN: Rinse, PUR: Purge

CHAPTER 3

THEORY

In this chapter, theory related to adsorption isotherms, classification and thermodynamic modelling are discussed. Various adsorption isotherm models used in the present work are presented. The pressure swing adsorption (PSA) process performance indicators are explained.

3.1 Adsorption isotherm

When a gas (adsorbate) is comes into contact with a solid surface, an equilibrium distribution of adsorbate molecule takes place between the solid surface and gas phase. The amount of gas adsorbed on the solid surface is a function of two variables (pressure and temperature)

$$N = f\{P, T\} \tag{3.1}$$

Where, N is the amount adsorbed, P is the pressure and T is the temperature.

The relation between the equilibrium amount adsorbed and the total pressure of the fluid phase at a particular temperature is called an adsorption isotherm [115]. It can be expressed as

$$[N]_T = f\{P\} \tag{3.2}$$

Figure 3.1 shows adsorption isotherms. In Figure 3.1, we can also note that how adsorption/ desorption is facilitated with change in temperature or pressure. Adsorption is always an exothermic process while desorption is always endothermic. Adsorption favors at low temperatures, while desorption at high temperature.

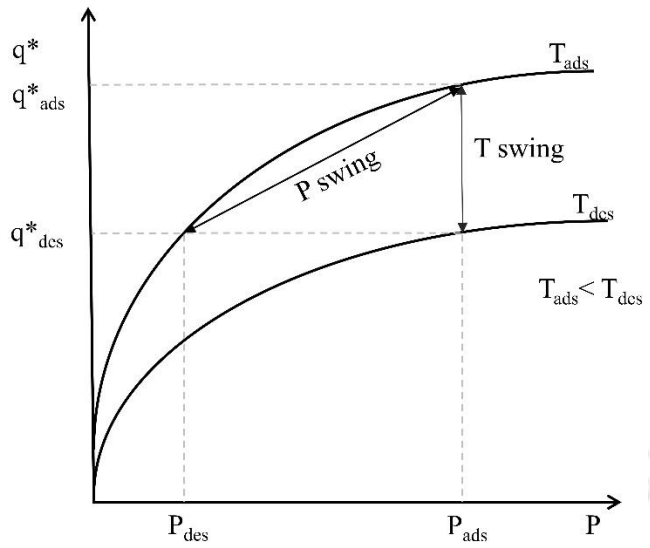

Figure 3.1: Adsorption isotherms and change in equilibrium solid loading with pressure and temperature

At very low adsorbate concentrations, the adsorption isotherm attains linear form, called Henry's law and Henry's constant is defined as the slope of the isotherm at the limit of zero pressure.

In general mathematical form, Henry's constant can be written as

$$\beta = \left(\frac{N}{P} \right)_{P \to 0} \qquad 3.3$$

The IUPAC classification of adsorption isotherms is shown in figure 3.2. Type I represent the adsorption characteristics of microporous adsorbent and are common in gas-solid adsorption systems. The adsorption occurs by filling of micro pores and limited to a few molecular layers. The type II isotherms are observed in case of nonporous or macroporous adsorbent. These isotherms often have an inflection point, which indicates the stage where the monolayer coverage is complete and multilayer adsorption begins to occur. This type of behavior is pretty common in the case of physical adsorption.

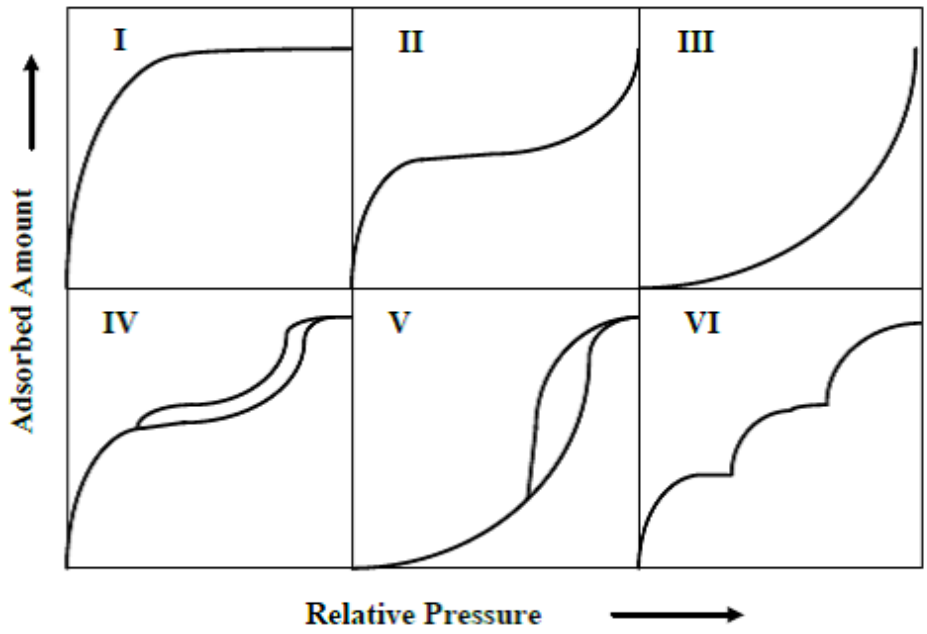

Figure 3.2: The IUPAC classification of adsorption isotherms [116]

Non-porous or macroporous adsorbents show types II, III and VI isotherms whereas mesoporous adsorbents exhibit types IV and V isotherms. Shape of isotherms itself indicate that there is stronger gas-solid interactions for type II and IV and weaker one for type III and V. Shape of type VI suggests the multilayer formation either on a plane surface or on the walls of pores which are much larger than the molecular diameter of the adsorbate molecule.

3.2 Pure gas adsorption isotherm models

In this section, the various adsorption isotherm models used in the present work are presented.

3.2.1 Langmuir model

At higher pressures, beyond the Henry's law region, the isotherm typically becomes nonlinear. For microporous adsorbent, the isotherm is generally of type I form where the isotherm is approaches

a saturation limit at high partial pressures. The simplest model capable of representing such behavior is Langmuir model with some assumptions that adsorption occurs at a fixed number of distinct sites, each site can hold only one molecule, there is no interaction between the molecules adsorbed on solid surface and all sites are energetically equivalent. Based on these assumptions Langmuir equation can be represented by

$$N = \frac{N^{max} \beta P}{1 + \beta P} \tag{3.4}$$

Where, P is the pressure (bar), N^{max} (mol kg^{-1}) is the maximum loading corresponding to monolayer coverage and β (mol kg^{-1} bar^{-1}) is Henry constant. Saturation capacity is considered to be independent of temperature; and the temperature dependency for Henry's constant is expressed by

$$\beta = \beta_o \exp^{\beta_1/T} \tag{3.5}$$

Where, T is temperature in K. The two parameters β_0 and β_1 are related to entropy and enthalpy of adsorption at zero loading, respectively.

3.2.2 Dual Site Langmuir (DSL) Isotherm

The Dual Site Langmuir (DSL) model is a four parameter model, assumes the existence of two distinct category of sorption sites of different energetic. Each site follows a Langmuir adsorption behavior. A DSL model is represented by

$$N = \frac{N_1^{max} \beta_1 P}{1 + \beta_1 P} + \frac{N_2^{max} \beta_2 P}{1 + \beta_2 P} \tag{3.6}$$

Where, P is the pressure (bar), N_1^{max} and N_2^{max} (mol kg^{-1}) are the saturation capacities of sites 1 and 2. β_1 and β_2 are the affinity parameters for sites 1 and 2, respectively. The temperature dependency of affinity parameters is given by

$$\beta_1 = \beta_1^{(0)} \exp^{\beta_1^{(1)}/T} \quad ; \qquad \beta_2 = \beta_2^{(0)} \exp^{\beta_2^{(1)}/T} \tag{3.7}$$

The Henry's constant in DSL model is given by

$$\beta = N_1^{max} \beta_1 + N_2^{max} \beta_2 \tag{3.8}$$

3.2.3 Virial Isotherm Model

The Virial equation is mathematically very versatile and can able to accommodate heterogeneity in adsorption. If we consider the adsorbed layer to obey the general form of Virial equation, the resulting isotherm equation can be written as

$$\ln(P/N) = k + bN + cN^2 \tag{3.9}$$

Where, P is the pressure and k is related to the Henry's Law constant and b, c are second and third virial coefficients respectively. The temperature dependency of these virial cofficents is

$$b = b_0 + \frac{b_1}{T} \; ; \qquad c = c_0 + \frac{c_1}{T} \tag{3.10}$$

Henry's constant β is given by

$$\beta = e^{-k} \tag{3.11}$$

3.3 Enthalpy of adsorption

Enthalpy of adsorption is an important factor for adsorption processes as the amount of heat required to drive adsorption and desorption during industrial scale cycles can be significant. Enthalpy of adsorption indirectly gives the measure of adsorbate-adsorbent interaction strength. The enthalpy of adsorption is usually obtained from experiments or model parameters using the following equation [117]

$$\Delta h_{ads} = -R \left. \frac{\partial(\ln P)}{\partial(1/T)} \right|_N \qquad 3.12$$

Where Δh_{ads} is enthalpy of adsorption (kJ mol^{-1}), P is adsorption pressure, T is temperature (K), N is amount adsorbed (mol kg^{-1}) and R is gas constant (J mol^{-1} K^{-1}).

This equation can be fit to a plot of lnP vs 1/T at various constant loadings, and the slope is directly related to Heat of Adsorption at that loading. Isotherms measured at three separate temperatures are required, in order to determine a statistically relevant linear fit. The enthalpy of adsorption of various models used in the present work are represented by

Langmuir Model: $\Delta h_{ads} = \beta_1 R$ 3.13

DSL Model: $\Delta h_{ads} = R \left(\frac{b_1 N_1^{max} b(1+cP)^2 + c_1 N_2^{max} c(1+bP)^2}{N_1^{max} b(1+cP)^2 + N_2^{max} c(1+bP)^2} \right)$ 3.14

Virial Model: $\Delta h_{ads} = -R\,(\beta_1 + b_1 N + c_1 N^2)$ 3.15

3.4 PSA performance indicators

The last few decades have seen a considerable increase in the applications of adsorptive gas separation technologies, such as pressure swing adsorption (PSA). The key separation principle used in a PSA operation is based on adsorption phenomena. PSA processes involve selectively adsorbing certain components of a gas mixture on a micro/mesoporous solid adsorbent at a relatively high pressure, via gas-solid contact in a packed column, in order to produce a gas stream enriched in less strongly adsorbed components of the feed gas. The adsorbed components are then desorbed from the solid by lowering their gas-phase partial pressures inside the column to enable adsorbent re-usability. Desorbed gases, as a result, are enriched in the more strongly adsorbed components of the feed gas. No external heat is generally used for desorption. The selectivity in a PSA process comes from differences in either adsorption equilibrium or adsorption kinetics between the components to be separated. While a PSA process carries out adsorption at superambient pressure and desorption at near-ambient pressure level, a vacuum swing adsorption (VSA) process undergoes adsorption at near-ambient pressure, while desorption is achieved under vacuum. The process performance of any adsorbent material was evaluated using the process performance indicators defined in equations 3.16 to 3.18.

$$\text{Product purity} = \frac{\text{Amount of component in the product stream}}{\text{Total amount of product stream}} \qquad 3.16$$

$$\text{Product recovery} = \frac{\text{Amount of component in the product stream}}{\text{Amount of component in the feed stream}} \qquad 3.17$$

$$\text{Adsorbent productivity} = \frac{\text{Amount of product component produced per cycle}}{(\text{Amount of adsorbent used})(\text{PSA cycletime})} \qquad 3.18$$

CHAPTER 4

EXPERIMENTAL

This chapter presents the details and protocols for various experiments performed in this work. The synthesis procedures followed for the synthesis of different MOFs are included. Physical properties and purities of gases considered for this work are provided.

4.1 Synthesis

The various routes available for MOF material synthesis are solvo thermal, sonochemistry, mechano chemistry, electrochemistry, and microwave assisted synthesis. Among these, solvothermal reactions using untoxic solvents are ecofriendly compared to the others routes. The synthesis of MOFs are not only targeted to achieve well designed pore structures with high surface areas and also they have to be scalable at low cost to yield higher purities with good yield.

Figure 4.1: Reactors used in small scale and scale up synthesis of MOFs

The small scale synthesis (~1 g product) of the selected materials was carried under solvothermal conditions. Four number of 16ml Teflon lined stainless steel autoclave bombs were used. To scale up the synthesis at 10 g level, a 500 ml Teflon lined stainless steel autoclave bomb of dimensions 114.92 mm ID, 124.73 mm OD, 5 mm thickness and 194 mm in height was designed, the photographs of autoclaves used for small scale and large scale synthesis can be seen in figure 4.1. For the scale up synthesis, initial design contains a Teflon O-ring to seal the lid and lower part of the reactor. However, a leakage was found during the 3-day synthesis of MIL-53(Al) at 220 ^{o}C due to the softening of Teflon O-ring at this temperature. To avoid this leakage, the reactor design was modified: a one inch screw was drilled through the reactor lid, this screw pushes the Teflon lid on the lines shown to achieve good seal. Instead of Teflon O-ring, six numbers of 6mm stainless steel screws were used to seal the lid and lower part of the reactor. Different parts of the designed reactor and the modifications made can be seen in the Figure 4.2.

Initial design using Teflon O-ring

Leakage found due to the melting of used Teflon O-ring at 220 ^{0}C

Teflon liner with lid placed inside the reactor

Teflon O-ring removed, six nos of 6 mm screws and 1-inch screw through SS lid are used to seal the reactor

Figure 4.2: Initial design, modifications made and final design of autoclave reactor for scale up synthesis

4.1.1 Synthesis of UiO-66

Zirconium (IV) chloride ($ZrCl_4$, Merck), 1, 4-benzene dicarboxylic acid (BDC, Merck), N,N-dimethylformamide (DMF, Merck), Hydrochloric acid (HCl, Merck) and Ethanol (Merck) were used as obtained from the vendors without further purification. UiO-66 was synthesized following the procedure reported by Katz et. al. [119]. 30 g $ZrCl_4$, 1200 ml DMF and 240 ml concentrated HCl were mixed and sonicated for 20 minutes until fully dissolved. 29.52 g organic linker BDC and 2400 ml DMF were then added and the mixture was sonicated for an additional 20 minutes to ensure complete dissolution. The resulting solution was transferred into polypropylene vials and placed in a hot air oven at 80 ^oC for overnight; the vials were cooled to room temperature naturally. The mother liquor was decanted and the resulting product was washed with DMF (2x4000 ml) and then with Ethanol (2x4000 ml). Then the product was filtered and dried under vacuum at 90 ^oC for 12h. The final obtained product of 24.03 g which was 81% of yield corresponds to the organic linker used was stored in a polypropylene bottle.

4.1.2 Synthesis of Cu-BTC

Cu-BTC was synthesized according to the procedure suggested by Liu et al. [120]. 10 g of 1,3,5-benzenetricarboxylic acid was dissolved in 300 ml of a 1:1 mixture of Ethanol/N,N-dimethylformamide. In another conical flask 20.77 g of copper (II) nitrate trihydrate was dissolved in 150 ml of deionized water. The two solution mixtures were then mixed and stirred for about 15 min. The resultant solution mixture was placed in a 500 ml polypropylene vial and kept at 360 K for 10 h. Then the plastic vial with product was allowed to reach room temperature normally. The resultant Blue crystals were isolated by filtration and extracted for 48 hours with methanol using a soxhlet extractor to remove the solvated DMF. Then the product was dried at 100 ^oC in a hot air

oven. The final obtained product of 9 g which was 90% of yield correspond to the organic linker was stored in methanol.

4.1.3 Synthesis of MIL-101(Cr)

Small scale synthesis (general procedure): MIL-101(Cr) was synthesized according to the procedure given by Férey et al. [64]. 4 g of Chromium nitrate nonahydrate was dissolved in 48 ml of deionized water. To this solution mixture, 1.64 g of 1, 4-benzenedicarboxylic acid (BDC) was added; 0.5 ml of Hydrofluoric acid was added drop wise under stirring for about 15 min. Then the resulting solution mixture was transferred into a Teflon lined stainless steel autoclave and kept at 493 K for 8 hours. The autoclave reactor was allowed to reach room temperature normally. A fine green colored powder is obtained as major product. The significant amount of unreacted BDC was found along with product in the form of needle shaped colorless crystals. To remove this, the contents were transferred into a conical flask and under stirring N,N dimethylformamide was added incrementally to dissolve the unreacted BDC. The product was filtered and dried at 423 K overnight. An additional ethanol rinse step is performed to remove the unreacted BDC, in this step for about 200 mg of product 15 ml of ethanol is added and placed in polypropylene vial at 373 K for 20 h. The product is filtered, washed with ethanol and finally dried at 423 K overnight. The weight of the final product obtained was 0.81 g which was 50% of yield corresponds to the linker used.

HF free synthesis: The high yield, fluoride free and large scale MIL-101 synthesis reported by Zhao et. al. [121] was adopted. 32 g of Chromium nitrate nonahydrate was dissolved in 400 ml of deionized water. To this solution mixture, 13.55 g of 1, 4-benzenedicarboxylic acid (BDC) was added; 5.2 ml of Conc. HNO_3 was added drop wise under stirring for about 15 min. Then the

resulting solution mixture was transferred into a Teflon-lined stainless steel autoclave and kept at 473 K for 15 hours. The autoclave reactor was allowed to reach room temperature normally. The mother liquor was decanted by centrifuging at 4700 rpm for 30 minutes. Then the resulted product washed with DMF (2 x 750 mL) and Ethanol (2 x 750 mL). Then the product dried in air at room temperature for 2 days to yield MIL-101(Cr) crystals. The final obtained product with a yield of 65% corresponds to organic linker stored in a polypropylene bottle.

4.1.4 Synthesis of MIL-53(Al)

The material, MIL-53(Al) was synthesized under hydrothermal conditions following the procedure given by Loiseau et al. [29]. Starting materials are 10.13 g of aluminium nitrate nonahydrate, 2.24 g of 1, 4-benzenedicarboxylic acid (BDC) and 38.8 ml of deionized water. Resultant solution mixture was placed in a Teflon lined stainless steel autoclave at 493 K for 72 hours. The product was cooled to room temperature, filtered and washed with deionized water. For removal of excess BDC, typically 1 g of MIL-53 was dispersed in 25 ml of DMF and introduced in Teflon lined steel autoclave for 15 hr at 423 K. The product was cooled, filtered and calcined overnight at 553 K. 1.1 g of final product (yield: 50%) was obtained and stored in a polypropylene bottle.

4.2 Pelletization of synthesized MOF materials for column studies

The use of adsorbent materials in the form of powders to perform breakthrough studies results in large pressure drops inside the column, hence these materials has to be shaped into small beads or pellets which possesses good thermal and mechanical strengths. The common pelletization method reported in literature is by use of the binders. In this method, the shaping of powders is done by preparation of powder-binder paste for extrusion or drying. In addition to binders, direct application of pressure on to powder was also the commonly used method.

4.2.1 Use of clay binders

Generally, commercial zeolite pellets contain about 25% of clay as binding agent. Initially attempts were made to make MOF pellets using bentonite clay binder. 5 wt%, 10 wt%, 15 wt% and 20 wt% of bentonite in MOF mixtures are prepared and to each mixture 2 to 3 ml of water added. The slurry type mixtures are made like pellets by using a syringe and kept at room temperature for one day. To check the thermal stability, they are heated to 100 ^{0}C slowly and observed no strength for the prepared pellets. However, the problem with these clay binders is that they have to be calcined at higher temperatures to make the adsorbent surface available for adsorbates. Due to the lower thermal stability of MOFs compared to practical adsorbents made this method unsuccessful for the pellet making of selected MOFs.

4.2.2 Direct application of pressure

The synthesized powders are pressed using a pellet making press at different pressures by applying force in the range of 1 to 10 tons. We found that the formed pellets do not enough strength for column studies. However, by direct application of pressure the physical properties of MOFs like specific surface area and pore volume decrease drastically, and hence this method was unsuccessful.

4.2.3 Use of Quicklime, Cement and white Portland cement as binders

Quicklime, cement and white portland cement were used as binders to harden the MOF pellets. Initially, MOF was heated at 473 K and different amounts of binder (10, 20, 30, 40 wt %) were added with sufficient quantity of water; the prepared pellets were stronger and have thermal strength upto 170 ^{0}C. However, then BET surface area analysis on the prepared MOF-binder pellets indicated a drastic decrease in surface area. Surface area of MIL-53 (Al) material decreased

from 1200 m^2 g^{-1} to 90 m^2 g^{-1} for MIL53-cement pellets and to 48 m^2 g^{-1} for MIL53-quiklime pellets.

4.2.4 Use of Molecular gastronomy method

In 2014, Spjelkavik al et.al [122] prepared shaped CPO-27-Ni metal organic framework spheres using molecular gastronomy technique. The CPO-27-Ni particles dispersed in either chitosan or alginate and then they are added drop wise to $BaCl_2$ or $CaCl_2$ solutions. In this work, we tried to make MOF beads following the above procedure. MIL-53(Al) was mixed with alginate binder and $CaCl_2$ was used as gelling agent. The experimental conditions used to make MOF beads and the textural properties of obtained beads are given in Table 4.1. As shown in the table 4.1, parameters such as the mass ratio of adsorbent to alginate, wt % of gelling solution and gelling time were varied to optimize the bead preparation.

Table 4.1: Experimental conditions used to make beads by molecular gastronomy method

Mass of MOF (g)	Mass of sodium alginate (g)	Mass of water (g)	$Cacl_2$ in gelling solution (wt %)	Gelling time (min)	BET Surface area (m^2g^{-1})	Pore volume (cc/g)	Remarks
--	--	--	--	--	1070	0.49	Pure MIL-53(Al)
2.4	0.100	10	0.4	30	807	--	No strength at 130 ^oC
2.4	0.100	10	0.6	30	801	0.447	No strength at 130 ^oC
2.4	0.100	10	1.2	30	619	0.348	No strength at 130 ^oC
2.0	0.300	10	0.4	30	771	0.435	No strength at 140 ^oC

Compared to the pure MOF powder, the BET surface area of the MOF pellets decreased by about 25-42%. On the other hand, the thermal treatment of formulated pellets indicate that the pellets are stable up to about 130 ^{o}C.

4.2.5 Use of Polymer binders

Following the procedure reported by Finsy et al. [108], an attempt was made to make MOF pellets using PVA/H_2O mixture as binder. A 15 wt% PVA/H_2O mixture was prepared by adding 17.65 g of poly vinyl alcohol (PVA, Merck) to 100 ml of deionized water. Then the solution mixture was heated at 90 ^{O}C in a two necked round bottom flask with a thermometer and a reflux condenser unit. A clear gelatinous mixture was obtained after complete dissolution of PVA in water. The ratio of MOF to binder was varied to optimize the binder content. The resulting MOF pellets were thermally treated up to 180 ^{o}C and then subjected to physical characterization. Detailed discussion on the results from this text is given in Sections 6.2, 7.2 ,8.2 and 9.3.

4.3 Material Characterization Methods

4.3.1 Surface Area Analysis

The BET surface area of all the samples was estimated using the N_2 adsorption isotherms at 77K. These were measured in a Autosorb iQ (Make: Quantachrome Instruments, USA) adsorption apparatus and the software used to analyze the data is ASiQwin from Quantachrome Instruments. Prior to the measurement, samples were degassed at 423 K under vacuum for 4 hours. The specific surface area was evaluated in the relative pressure range (P/P_0) of 0.05-0.30 using the BET model.

BET Method: In 1938, Stephen Brunauer, Paul Hugh Emmett, and Edward Teller (BET) developed a mathematical model to measure the two important attributes of porous materials i.e. surface area and pore volume. The BET method had five major assumptions

a) Each adsorption site has equivalent energy (i.e. homogeneous) and can adsorb one molecule of adsorbate to form monolayer
b) No lateral interaction between the molecules
c) Upper most layer will approximate a liquid phase and is in equilibrium with the vapor phase
d) The energy of desorption for each molecule in the first layer at solid surface is equivalent to the heat of adsorption, while for all additional layers, it is the heat of condensation i.e. $E_2=E_3=E_4=\ldots=E_n=E_L$.
e) At saturation pressure (i.e. P/P_0 approaches unity), the number of layers becomes infinity.

The resultant BET equation is

$$\frac{1}{v[(p_0/p)-1]}=\frac{c-1}{v_m c}\left(\frac{p}{p_0}\right)+\frac{1}{v_m c} \qquad (4.1)$$

Where p and p_0 are equilibrium and saturation pressure of adsorbate at the temperature of adsorption, v is the volume of gas adsorbed, v_m is the monolayer adsorbed quantity, R is the ideal gas constant and c is the BET constant,

$$c=\exp\left(\frac{E_1-E_L}{RT}\right) \qquad (4.2)$$

Where E_1 is heat of adsorption for the first layer, and E_L is that for second and higher layers and is equal to heat of liquefaction.

The experimental data plotted between $\frac{1}{v[(p_0/p)-1]}$ vs $\frac{p}{p_0}$ yields a straight line with y- intercept I= $\frac{1}{v_m c}$ and slope A= $\frac{c-1}{v_m c}$. The obtained slope and intercept are used to calculate the monolayer adsorbed gas quantity v_m and BET constant c. The following equations can be used

$$v_m = \frac{1}{A+I} \; ; \qquad c = 1 + \frac{A}{I} \tag{4.3}$$

The total surface area and specific surface area are given by

$$S_{total} = \frac{v_m N_{av} s}{V} \; ; \qquad S_{BET} = \frac{S_{total}}{a} \tag{4.4}$$

Where N_{av} is Avogadro's number, s is coverage w.r.t. a single adsorbing molecule, V is the molar volume of adsorbate gas and 'a' is the mass of the absorbent. Typically, isotherms using N_2 at 77 K are used to estimate the BET surface area.

4.3.2 Thermo gravimetric analysis

Thermogravimetric analysis (TGA) is a method of thermal analysis in which changes in physical and chemical properties of materials are measured as a function of temperature (with constant heating rate), or as a function of time (with constant temperature and/or constant mass loss). The instrument contains a high temperature furnace and a precise mass balance. A purge gas stream is passed over the sample and the system temperature is incrementally raised while the change in mass of the material is recorded. The TGA plot (weight loss as a function of temperature) reveals information about the activation and decomposition temperatures of the material.

In the present work, a Mettler TOLEDO analyzer (model no. TGA/SDTA851e) and NETZSCH analyzer (model no. STA449 F3 Jupiter) are used for TGA analysis of MOF powder and pellets. About 10 mg of the sample placed in TGA and temperature was ramped from 25 ^oC to 800 ^oC at

a constant rate of about 10°C/min under an inert atmosphere (N_2 flow of about 40 cm^3 min^{-1}). In this work, TGA is also used to determine the quantity of polymer binder present in the formulated MOF pellets.

4.3.3. Powder X-Ray Diffraction

Powder X-ray diffraction (PXRD) is a powerful tool for determining the crystal structure of a material. All atoms in crystalline materials are considered as sets of parallel crystallographic planes which are characterized by Miller indices (h k l). Diffraction maxima occur when a certain set of crystallographic planes fulfill conditions for constructive interference provided by the Bragg's law [124]

$$2d \sin\theta = n\lambda \qquad (4.5)$$

Where λ is the radiation wavelength, d is the distance between two successive crystal planes, θ is the angle between incident beam and the crystallographic plane, and n is an integer value. X-ray tube, the detector, and the sample are located on the focusing circle. The X-ray tube is fixed, and the detector moves along the goniometer circle with an angular speed which is two times that of the sample (the rotational axes of the sample and of the detector coincide). During the XRD analysis the detector is always at 2θ angle and the sample surface is always at θ angle with respect to the incident beam. The detector scans around the sample in the specified 2θ intervals and records the angle and the intensity of diffracted radiation.

Powder X-ray diffraction (PXRD) patterns of all samples prepared in this work were measured on a Bruker D8 advance instrument operating at 40 kV and 40 mA using a Cu-Kα radiation source.

4.3.4 Field Emission Scanning Electron Microscopy (FESEM)

The FESEM technique images a sample surface by raster scanning over it with a high energy beam of electrons instead of light. Within the high vacuum column these so-called primary electrons are focused and deflected by electronic lenses to produce a narrow scan beam that bombards the object. As a result, secondary electrons are emitted from each spot on the object. The angle and velocity of these secondary electrons relates to the surface structure of the object. A detector catches the secondary electrons and produces an electronic signal. This signal is amplified and transformed to a video scan-image that can be seen on a monitor or to a digital image that can be saved and processed further. The function of the electron gun is to provide a large and stable current in a small beam, the morphologies of MOF materials and MOF pellets synthesized in this work were characterized by a FESEM (Make: Zeiss, Model: Sigma) instrument. The sample dispersed in 2-propanol was dropped on an aluminum foil, dried under vacuum overnight and then sputtered with gold, prior to mounting in the instrument.

4.3.5 Fourier Transform Infrared Spectroscopy (FTIR)

FTIR is an important analytical method to determine the bonding mechanisms in solids and on surfaces. Molecular vibrations can be related directly to the symmetry of molecules, and so it is often possible to determine precisely how a molecule bonds on surfaces or as a component in a solid phase from its infrared spectrum. In this work, The FT-IR spectra of pure MOF powder, polymer binder PVA and MOF pellets were compared. The interferometer consists of a beam splitter, a fixed mirror, and a mirror that translates back and forth, very precisely. The beam splitter is made of a special material that transmits half of the radiation striking it and reflects the other half. Radiation from the source strikes the beam splitter and separates into

two beams. One beam is transmitted through the beam splitter to the fixed mirror and the second is reflected off the beam splitter to the moving mirror. The fixed and moving mirrors reflect the radiation back to the beam splitter. Again, half of this reflected radiation is transmitted and half is reflected at the beam splitter, resulting in one beam passing to the detector and the second back to the source. A FT-IR Perkin Elmer instrument was employed to record the FTIR spectra of materials in the wave number range of 4000-500 cm^{-1}.

4.3.6 Drop Test

To measure the ability of dried pellets to remain intact during handling and column studies, drop tests were conducted as described by Kawatra et. al. [124]. 30 number of pellets were dried at 100 ^{o}C for 3 hours and dropped repeatedly from a height of 0.5m onto a stainless steel plate. The number of broken pellets was recorded.

4.3.7 Compression test

The strength of formulated MOF pellets was measured using UTM compression test using a 5 kN Electromechanical Universal Testing Machine (Make: Zwick Roell; Model: Z005TN). Compression test was performed at a speed of 0.05 mm/min.

4.4 Pure component equilibrium adsorption measurement

The pure component equilibrium adsorption isotherms can be measured by various methods, the two most important are gravimetric and volumetric. Operation of these methods depend on a few common as well as specific corrections and assumptions. The pure component equilibrium adsorption isotherms of CO_2, N_2 on Zeolite 13 X pellets, Cu-BTC powder, Cu-BTC pellets, MIL-53(Al) powder and MIL-53(Al) pellets in this work were measured by gravimetric method using

a Rubotherm Magnetic Suspension balance. The equilibrium isotherms on MIL-101(Cr) powder, MIL-101(Cr) pellets, UiO-66 powder and UiO-66 pellets are measured by volumetric method using a Quantachrome iSorb high pressure equipment. Except for MIL-53(Al), the choice of measurement equipment is purely based on the availability of that equipment. Whereas, in case of MIL-53(Al), to investigate the flexibility or breathing phenomena of this material, the manually operated Rubotherm Magnetic Suspension balance is chosen over the fully automated Quantachrome iSorb high pressure equipment.

4.4.1 Experimental systems used for equilibrium adsorption measurements

4.4.1.1 Gravimetric system

The experimental set up used for gravimetrically measure the adsorption isotherm consists of a Rubotherm Magnetic Suspension balance. The schematic of the complete experimental set up is shown in Figure 4.3.

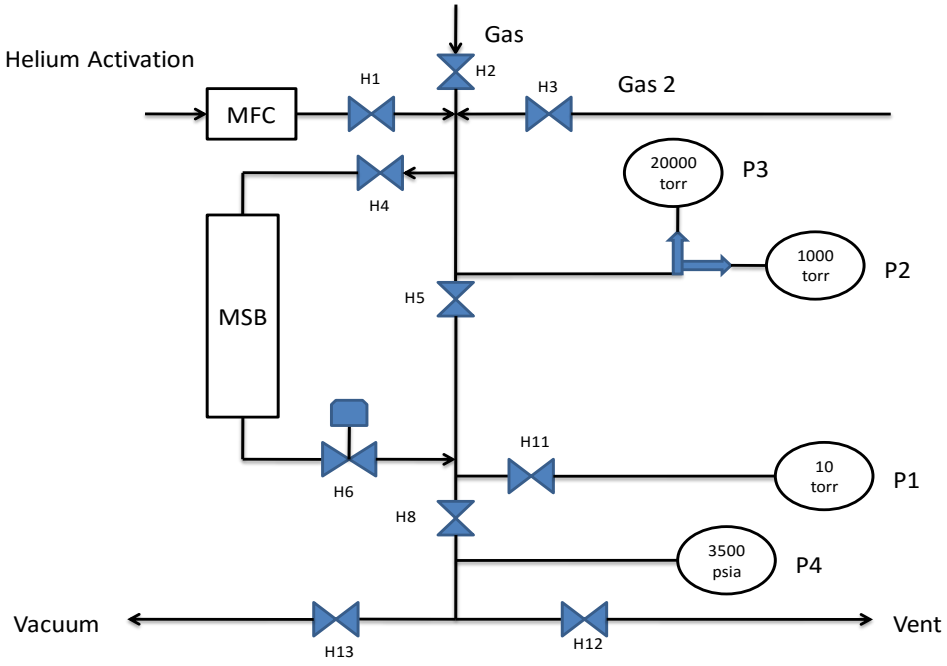

Figure 4.3: Schematic of gravimetric experimental set up used in the work

Nomenclature: MSB # Magnetic Suspension Balance, H1-H13 # Pneumatic Valves, P1-P4# Pressure Transducer, MFC # Mass Flow Controller

The experimental setup can be broadly divided into three major sections.

Feed: The feed section consists of inlet connected to a compressed helium/adsorbate supply. During activation/regeneration a controlled flow of an inert gas is flown over the adsorbent using the mass flow controller, MFC.

Balance and pressure chamber: A three-position magnetic suspension balance supplied by M/S Rubotherm Corporation, Germany is the main accessory of the equipment.

The balance can be divided into two parts:

1. The lower pressure chamber containing the sample and
2. The section containing all the electronic components of the assembly

In the pressure chamber, the sample is placed in a bucket, suspended from a permanent magnet. The upper section contains an electro-magnet suspended from the load cell of a microbalance. Current supplied to the outside electro-magnet positions the permanent magnet in the pressure chamber so that only the magnet or both the magnet and the bucket are lifted. The force on the load cell of the microbalance is directly proportional to the mass on the permanent magnet in the lower chamber. The assembly thus provides a way to rezero the balance (by tarring after lifting only the permanent magnet) before measuring the actual mass of the sample at any point during the experiment. Hence, zero-drift is compensated at all times.

A thermocouple placed close to the adsorbent in the pressure chamber measures the temperature inside the system while adsorption taking place also.

Vacuum / vent section: The vent valve is used to decrease the pressure in the system to atmospheric. The vacuum valve is connected to a vacuum pump, to reach sub-atmospheric pressure in the balance.

4.4.1.1.1 Experimental Procedure

The experiments were conducted following the procedure outlined below.

a) First the adsorbent was thoroughly activated at high temperature (see Table 4.3) for 6 hours. During this process helium flows over the sample at 30 cc min^{-1} under vacuum and the sample is cooled down to experimental temperature.

b) The balance assembly was maintained at a constant temperature by circulating the water from water bath through the jacket surrounding the assembly.

c) After desired temperature was established in the system, the gas of interest was introduced to the desired experimental pressure and sufficient time was allowed for equilibrium.

d) The weight of the solid and sinker were recorded along with the pressure, temperature of the balance and ambient temperature.

e) The pressure in the system was increased in a controlled fashion, obtaining equilibrium measurements at intermediate pressures.

f) The above two steps are repeated up to the desired pressure.

g) After that for desorbing the adsorbate from the solid, the system was evacuated and regenerated with heating and/or helium purging which can be used for the other measurement.

4.4.1.1.2 Calculations

4.3.1.1.2.1 Calculation of buoyancy volume

Once activation was complete, the pressure chamber of the balance was completely evacuated and then cooled down to the experimental temperature. The signal of the microbalance M_{t0} is a result of evacuated weight of the sample and that of the bucket.

$$M_{t0} = M_{bucket,0} + M_{sample,0} \quad (4.6)$$

At equilibrium, the excess amount adsorbed, M_{ex} is related to the microbalance reading M_t and the buoyancy force acting on the bucket and sample by the relationship

$$M_{ex} = M_t - M_{t0} + V_{buoyancy}\,\rho^{gas} \quad (4.7)$$

$V_{buoyancy}$ is the buoyancy volume and ρ^{gas} is density of the bulk gas at equilibrium temperature and pressure. In order to calculate excess amount adsorbed from microbalance signal it is necessary to have knowledge of the buoyancy volume, which is sum of the bucket volume and impenetrable solid volume V_s.

$$V_{buoyancy} = V_{bucket} + V_s \quad (4.8)$$

Buoyancy volume is usually obtained by helium run on the adsorbent at different pressures. These experiments are performed usually around room temperature. If excess amount adsorbed for helium is zero (non-adsorbing) ie., $M_{ex}=0$ then Eq. (4.7) reduces to

$$M_t = -V_{buoyancy}\,\rho^{gas} + M_{t0} \quad (4.9)$$

The above equation can be written as follows

$$MP1 - ZP = -V_{buoyancy}\,\rho^{gas} + M_{t0} \quad (4.10)$$

The graph is plotted density of helium at different pressures against change in microbalance signal. Buoyancy volume is thus obtained from slope of the plot of the change in microbalance signal against helium density.

4.4.1.1.2.2 Calculation of excess amount adsorbed

An adsorption isotherm measurement involves obtaining the micro balance signal at several bulk gas pressures keeping temperature constant. As explained above the excess amount adsorbed for a gas is given by

$$M_{ex} = M_t - M_{t0} + V_{buoyancy}\,\rho^{gas} \quad (4.11)$$

$V_{buoyancy}$ is obtained from helium measurements. The bulk gas density is calculated from second Virial coefficient.

$$B_{gas} = A + \frac{B}{T} + \frac{C}{T^3} + \frac{D}{T^8} + \frac{E}{T^9} \tag{4.12}$$

$$\rho_{gas} = \frac{-1 + \sqrt{1 + 4\frac{B_{gas} \times P}{R \times T}}}{2B_{gas}} \tag{4.13}$$

Finally, the amount adsorbed in mol/kg, was calculated using

$$N = \frac{(M_t - M_{t,0} + V_{buoyancy}.\rho^{gas})}{M_{t,0}.M_W} \tag{4.14}$$

4.4.1.2 Volumetric system

The volumetric set up used for isotherm measurement was Quantachrome iSorb hp1 (Make: Quantachrome instruments, USA). The schematic of the volumetric set up is shown in Figure 4.4. The main components are

a) Manifold of accurately known volume

b) Vacuum system with valve to manifold

c) Source of adsorptive gas with valve to manifold

d) Source of He gas with valve to manifold

e) Analysis cell (sample tube) of precisely known free or void-space

f) Accurate pressure transducers and temperature sensors

4.4.1.2.1 Experimental protocol

The adsorbent sample is activated at high temperature (See Table 4.3) under vacuum for 6 hrs. The activated weight of the sample is recorded. Once the sample cell with activated adsorbent connected to the system, full evacuation of manifold and sample cell are done. Then, the void volume of the analysis cell is calibrated using the He gas. The manifold is charged to a pressure $P_{m,}$ preparing the instrument to dispense a dose of adsorptive onto the sample. Finally, the adsorption amount is calculated by subtracting the number of remaining moles of adsorbate at the adsorption equilibrium from the number of introduced moles of adsorbate by using the ideal gas equation.

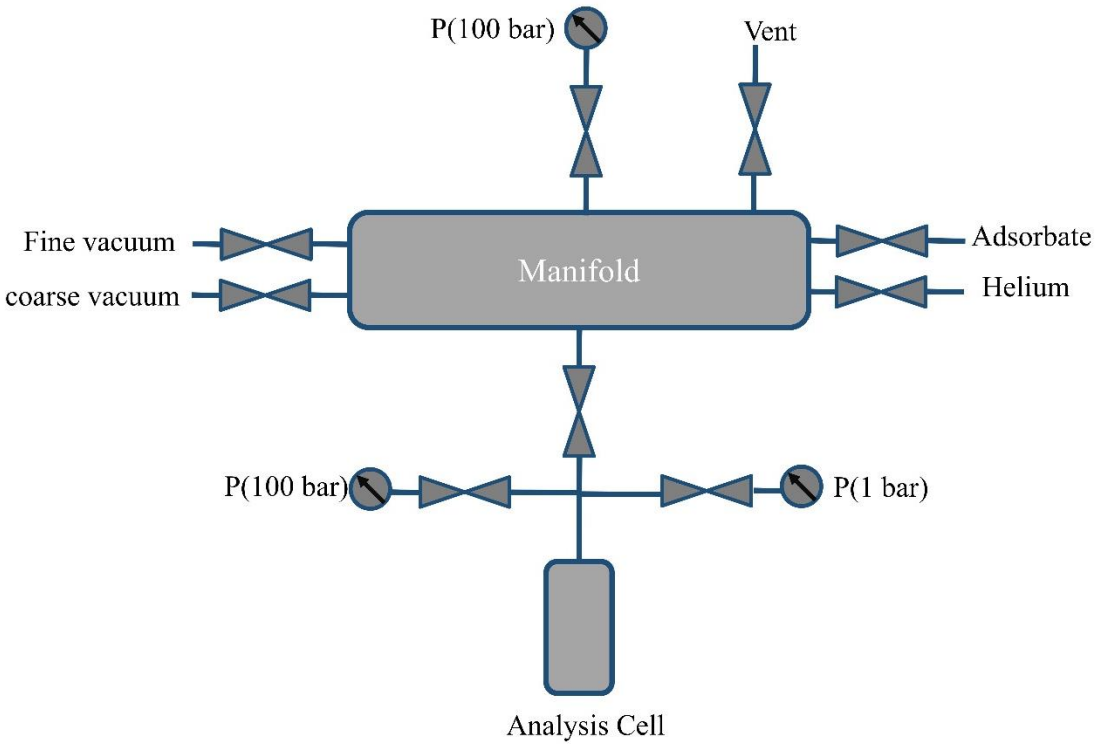

Figure 4.4: Schematic of volumetric adsorption apparatus

4.5 Breakthrough and process cycle experiments

The apparatus used to perform breakthrough and process cycle experiments was constructed in-house. The development and experimental validation of the in-house constructed apparatus is given in the **chapter 5**. The formulated MOF pellets of about 10 g were packed inside the adsorbent column. Thereafter, activation of the sample was done by heating at 150 ^{o}C (< 200 ^{o}C, to avoid the decomposition of PVA used in the prepared pellets) under N_2 purge flow of 60 cm^3 min^{-1} for 6 hrs. The binary gas mixture about 15% CO_2 and balance N_2 was prepared in laboratory and used as feed in the breakthrough and PVSA experiments. For all the materials studied, the experimental temperature was 300 K and column pressure was fixed using a back pressure regulator. At the beginning of each breakthrough experiment, column was initially pressurized with helium and then the flow was switched to the feed gas (pure/binary mixture). The composition at the outlet of the bed outlet was analyzed periodically using GC, until the column outlet gas composition reaches the feed gas composition.

A three step PVSA cycle consists of pressurization with feed to 1.3 bar, adsorption at 1.3 bar, and counter-current blow down to 0.1 bar was initially considered. This elementary PVSA cycle, was further modified to include a countercurrent nitrogen purge step and/or a co-current heavy reflux step (CO_2 rinse). The effect of various steps on the process performance was studied. While the step times for adsorption, purge and rinse were configured based on the CO_2 breakthrough time. The step times for pressurization and blow down were fixed for all the experiments performed.

4.6 Purity of gases

The minimum percentage purity of different gases used during experiments was more than 99.9%. Table 4.2 gives a detail of percentage purity of all the gases along with their suppliers.

Table 4.2: Details of gases used in this study

Gas	Minimum Percentage Purity (Approximately)	Supplier
Helium	99.995	Assam Air Products
Carbon dioxide	99.99	Jainex Gases Company
Nitrogen	99.99	Jainex Gases Company
Hydrogen	99.99	Assam Air Products
Argon	99.995	Jainex Gases Company

4.7 Experimental conditions of equilibrium adsorption isotherms

Adsorption equilibrium isotherms of pure CO_2 and pure N_2 on the synthesized MOF materials and their pellets were measured by gravimetric/volumetric methods for a wide range of pressures and temperatures. The details are given in Table 4.3.

Table 4.3: Experimental conditions for various equilibrium adsorption measurements

Adsorbent	Adsorbate	$T_{Equlibrium}$ (K)	$T_{Activation}$ (K)	Pressure range (bar)	Method
Zeolite 13X pellets	CO_2	298, 318, 358	510	0-20	gravimetric
	N_2	298, 318, 358	510	0-20	
Cu-BTC powder	CO_2	300, 318, 338	420	0-20	gravimetric
	N_2	300, 318, 338	420	0-20	
Cu-BTC pellets	CO_2	300	420	0-2	gravimetric
	N_2	300,318,338	420	0-20	
MIL-53(Al) powder	CO_2	300,314,358	493	0-12	gravimetric
	N_2	300	493	0-12	
MIL-53(Al) pellets	CO_2	300	413	0-12	gravimetric
	N_2	300	413	0-12	
MIL-101(Cr) powder	CO_2	298, 318, 348	473	0-20	volumetric
	N_2	298, 318, 348	473	0-50	
MIL-101(Cr) pellets	CO_2	298	423	0-20	volumetric
	N_2	298	423	0-50	
UiO-66 powder	CO_2	298, 318, 348	473	0-10	volumetric
	N_2	298, 318, 348	473	0-50	
UiO-66 pellets	CO_2	298	423	0-10	volumetric
	N_2	298	423	0-50	

CHAPTER 5

Development of a 1-Bed Pressure Vacuum Swing Adsorption (PVSA) apparatus: Experimental validation with Zeolite-13X adsorbent

In this chapter, the development of experimental set up for binary breakthrough and process cycles experiments is discussed elaborately. To validate the designed system, the experimental demonstration of CO_2 capture from a dry synthetic flue gas containing 15 % CO_2 and 85% N_2 on benchmark adsorbent Zeolite 13X was studied. Binary breakthrough experiments were first carried out followed by the 4-step PVSA process experiments. At steady sate, the process performance indicators i.e. CO_2 purity and CO_2 recovery were evaluated. The obtained experimental values were compared with those in the literature.

5.1 Description of the designed experimental set up

A simplified schematic of in-house built single column unit is shown in Figure 5.1. The complete schematic can be seen in Figure 5.2.

The overall experimental set up consists the following major sections

a. **Feed Section:** The feed section consists of one mass flow meter (MFM1) (make: MKS instruments, Model: M100B Mass-flo®) connected to pure gas or gas mixture. The gas/gas mixture of our interest will be fed into to the column through Pneumatic Valve (PV).

b. **Column section:** The main part of the PVSA section is the adsorbent column. The adsorbent column was made of stainless steel with dimension of 10 mm I.D and a packing height of 300 mm. The adsorption pressure was controlled using a back pressure regulator (Make: Porter, Model: 9000). Pneumatic valves (Make: Swagelok) connected to an oil-free air compressor (Make: High Speed appliances, Model: HS-WP-1, Range 0-100 Psi) was used to direct gas flows to and from the column.

c. **Pressure manifold:** The pressure in various sections of the unit i.e. column top, column bottom, product section, blowdown section was measured via a pressure transducer mounted in the manifold (Make: MKS Instruments, Model: 690ARCTRB, Range: 0-25000 torr).

d. **Vacuum/Vent manifold:** Various sections in the unit are connected to vacuum/vent manifold that providing venting the relevant section to atmospheric pressure and subsequent evacuation upto pressure of 0.15 bar. A vacuum pump (Make: Tarson, Model: Rockyvac 410) is used for this purpose.

e. **Product and blowdown tanks:** These are two stainless steel tanks of volume ~2250 CC (N_2 product tank) and 125 CC (blowdown tank), used to collect column outlet content during the respective steps. They are also connected to pressure and vacuum manifolds.

f. **Purge section:** This section consists of one mass flow meter (MFM2) (make: MKS instruments, Model: M100B Mass-flo®) connected to pure N_2 cylinder.

g. **Data Acquisition Section:** During the experiments, process parameters like feed flow rate, product flowrate, purge and rinse flow rates changes very fast (can be seen in figure 5.3). The numerical integration of these flows were necessary for making mass balances to obtain the process performance characteristics (purity, recovery). So, a computer with a

data acquisition board (Make: National Instruments, Model: NI-USB-6229) along with homemade MATLAB code as acquisition software was used to accurately record readings of mass flow controller (MFC), mass flow meters (MFM1, MFM2) and pressure Transducer. The data acquisition rate was kept at 50 MHz. The obtained data from different electronics consists of noise, so a data smoothing function was used to minimize the noise. The data is collected as a voltage signal and converted to flowrates and pressure using the homemade MATLAB code. The recorded data acquisition plots during a three step (pressurization, adsorption, and blow down) cycle experiment can be seen in Figure 5.3.

h. Analysis section: This section is used to analyse the composition of different streams during breakthrough and process experiments. It includes a Gas Chromatography (GC) and a computer with a data acquisition system. The acquisition software used is Galaxy Chromatography data system version 1.8.504.2 provided by Varian technologies Ltd. The Gas Chromatography system is a Varian 450-GC with a TCD detector. Helium gas is used as reference gas.

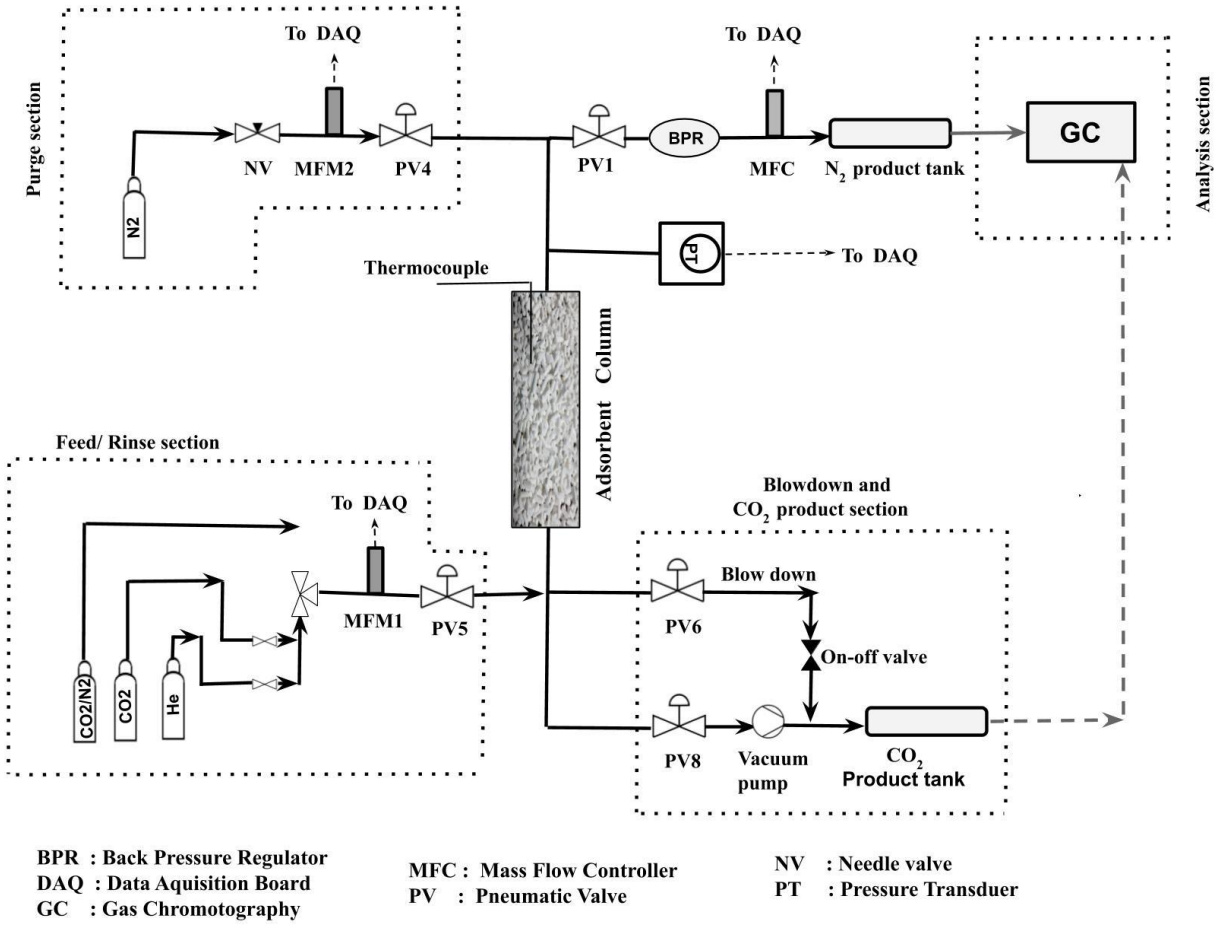

Figure 5.1: A simplified schematic of single column breakthrough and PVSA unit

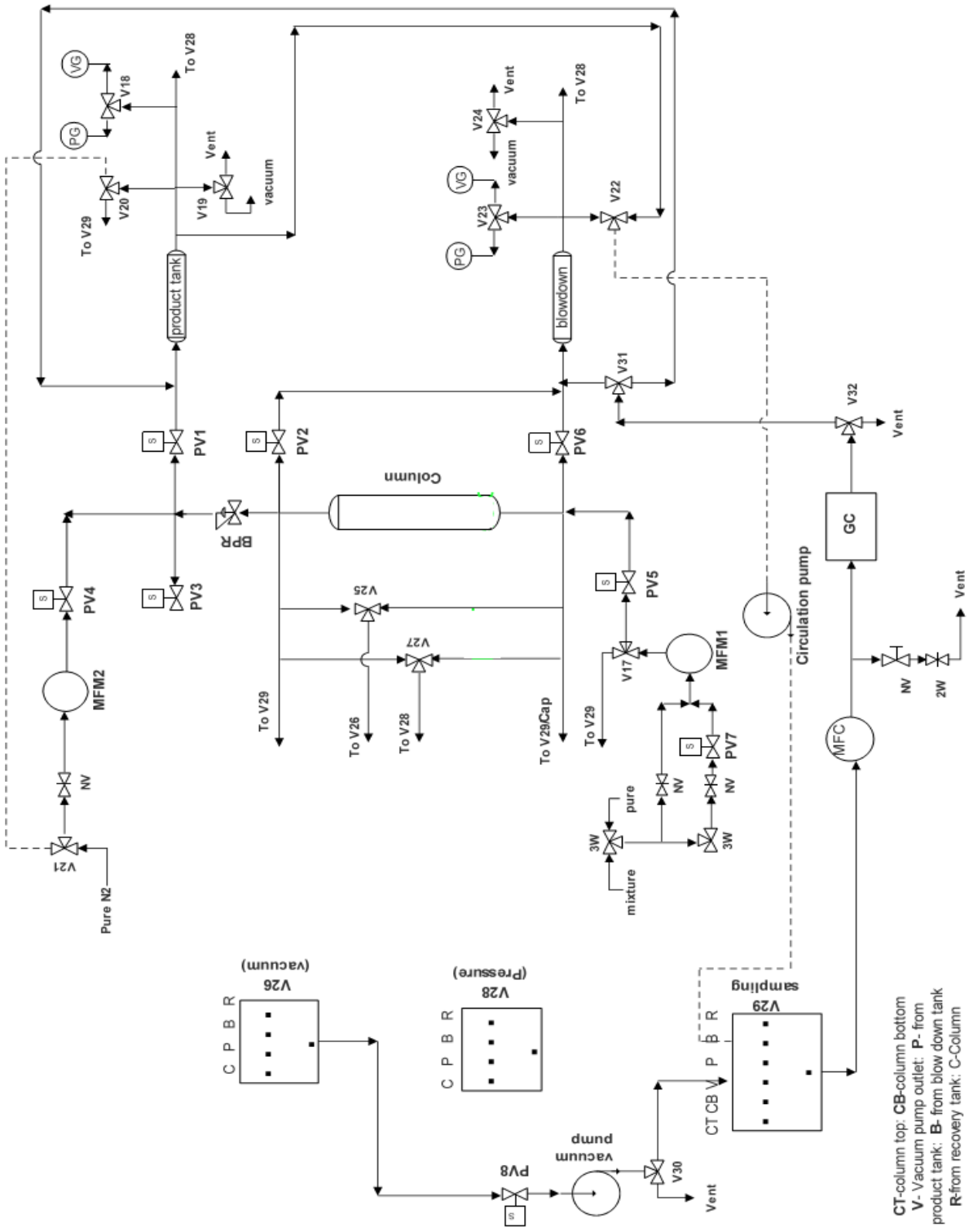

Figure 5.2: Complete schematic diagram of in house built experimental set up

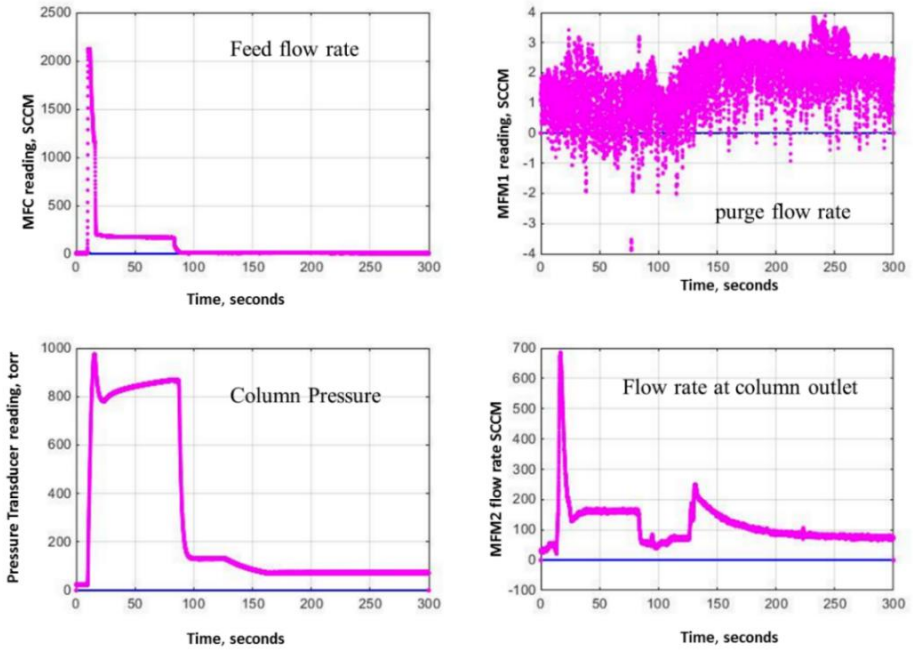

Figure 5.3: Data acquisition plots during a three-step PVSA cycle experiment

5.2 Calibration of mass flow meters and mass flow controller used in the designed system

The list of mass flow meters (MFM) and mass flow controller (MFC) used along with their specification and operating ranges are given in Table 5.1. Calibration of these meters and controller was carried using soap bubble flow meter. The calibration plots can be seen in Figures 5.4.

Table 5.1: List of MFMs and MFC used along with their specifications

Unit	Make	Model	Serial No	Range	Display Unit
MFM1	MKS	M100B Mass flo	21452761	0-2000 sccm	MKS-PR 4000B
MFM2	MKS	M100B Mass flo	21452760	0-2000 sccm	MKS-PR 4000B
MFC	Bronkhorst	F232M	M9205256A	0-10 lpm	Connected to DAQ

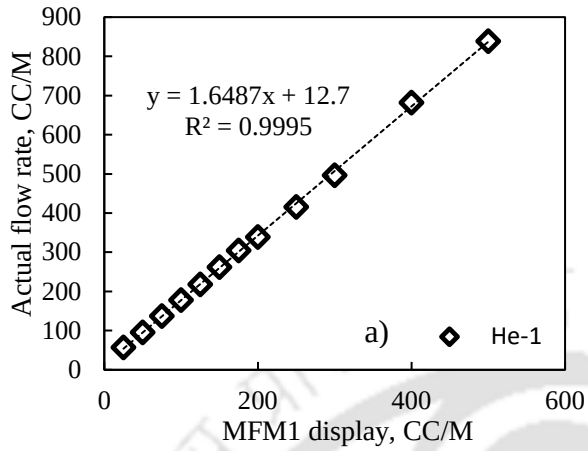

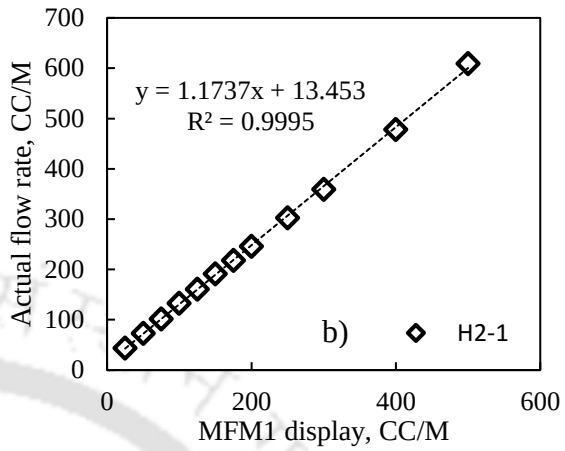

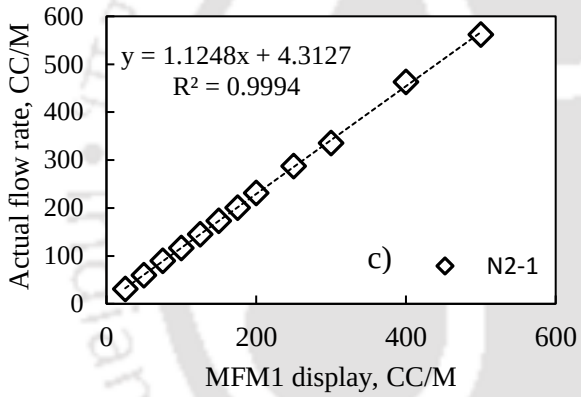

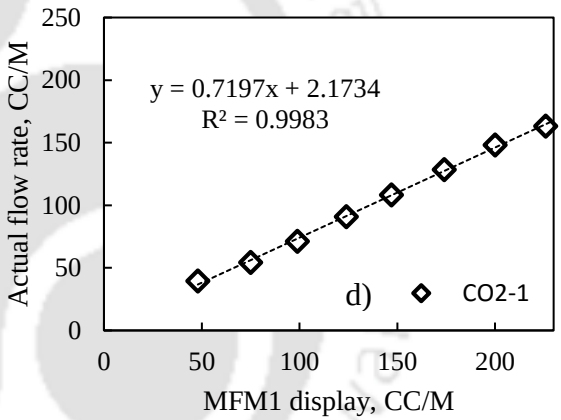

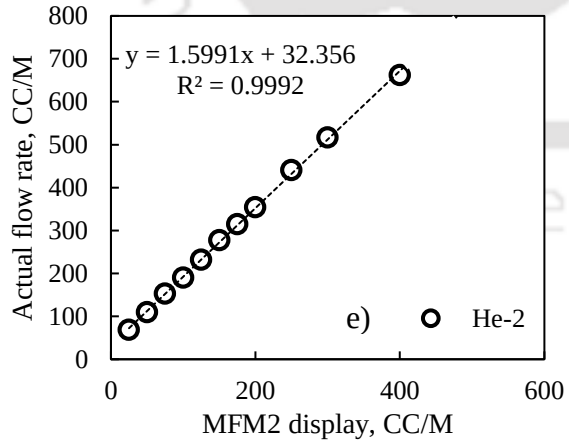

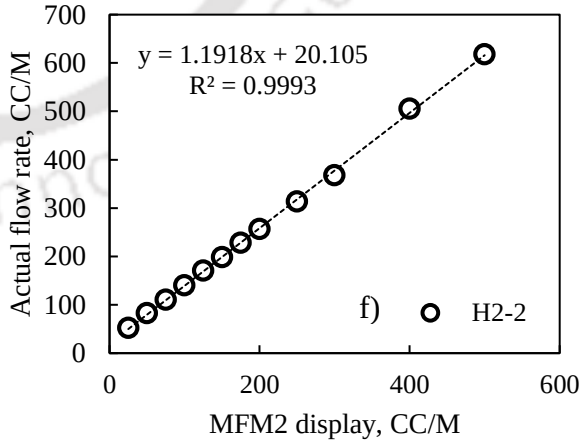

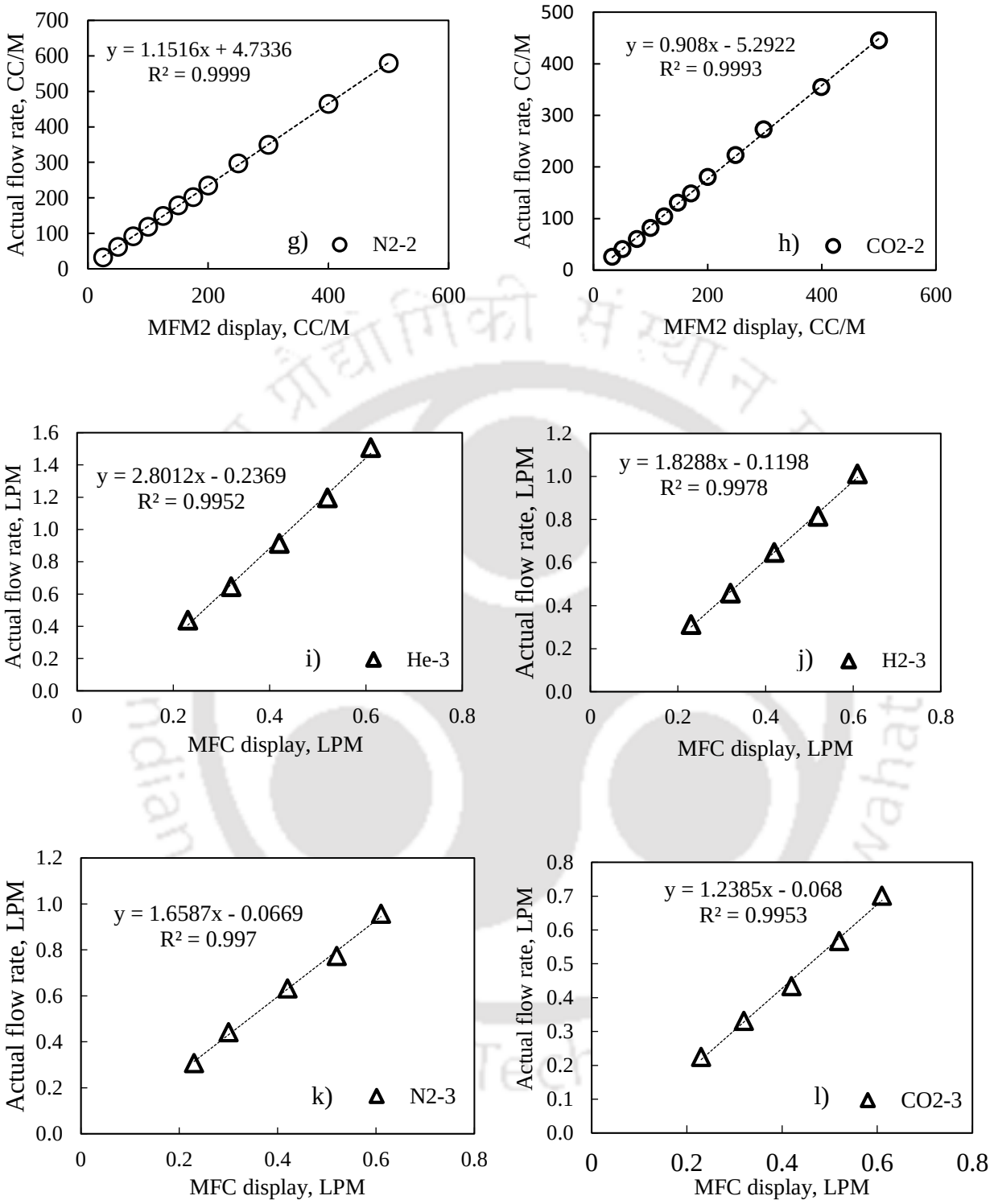

Figure 5.4 (a-l): Calibration plots of mass flow meters (1, 2) and mass flow controller (3) used in designed system for He, H_2, N_2 and CO_2 gasses.

5.3 Gas correction factor calculations for the used mass flow controller and meters

Generally, mass flow meter/controllers were calibrated with a specific gas (standard gasses: N_2, CH_4). The MFM/MFC provides a direct reading only for that specific gas. The same meter/controller can be used to read the flow rate of other gas/gas mixture by using Gas Correction Factor (GCF). A Gas Correction Factor (GCF) is used to indicate the ratio of flow rates of different gases that will produce the same output voltage from a mass flow controller/meter. The GCF is a function of specific heat, density, and the molecular structure of the gases.

The mass flow controller (Make: Bronkhorst high tech, model F-232M) purchased and used in the designed system was originally calibrated at manufacturer place using CH_4 as calibration gas between 0-10 NLPM.

The gas correction factor for gas 'X' flowing through this controller can be written as

$$GCF_X = \frac{d_{CH_4}.c_{CH_4}}{s_{CH_4}} \frac{s_X}{dx.c_X} \qquad 5.1$$

Where d_X = Standard density of gas X, in g/l; [d_{He} = 0.1786; d_{H2} = 0.0899; d_{CO2} = 1.964; d_{N2} = 1.250, and d_{CH4} = 0.715], C_X = Specific heat of gas X, in cal/g °C; [C_{He} =1.241; C_{H2} =3.419; C_{CO2} =0.2016; C_{N2} =0.2485 and C_{CH4} = 0.5328] and S_X = Molecular structure correction factor (1.030 for monatomic gasses, 1.000 for diatomic gases, 0.941 for triatomic gases and 0.880 for polyatomic gases) [1].

The substitution of these values in equation 5.1 yielded,

GCF_{CO2} =1.0288, GCF_{N2} = 1.393, GCF_{He} = 2.0117 and GCF_{H2} = 1.4084

The flow of other pure gasses through this mass flow controller can be calculated as

$$y_{CO_2} = y_{CH_4}.GCF_{CO_2}\ ;\quad y_{N_2} = y_{CH_4}.GCF_{N_2}\ ;\quad y_{H_2} = y_{CH_4}.GCF_{H_2}\ ;\quad y_{He} = y_{CH_4}.GCF_{He} \qquad 5.2$$

We have already calibrated the mass flow controller and meters under normal conditions using soap bubble meter. The obtained calibration curves are in the form of

$$y = m*x + C \qquad \text{(where y is actual display and x is display on controller/meter)} \qquad 5.3$$

For He gas flow through mass flow controller,

$$y_{He} = m_{He} * x + C \qquad 5.4$$

From equations 3.2 and 3.4,

$$y_{CH_4} = \frac{m_{He} * x + C}{GCF_{He}} \qquad 5.5$$

Similarly, for other gases

$$y_{CH_4} = \frac{m_{CO_2} * x + C}{GCF_{CO_2}};\qquad y_{CH_4} = \frac{m_{N_2} * x + C}{GCF_{N_2}};\qquad y_{CH_4} = \frac{m_{H_2} * x + C}{GCF_{H_2}} \qquad 5.6$$

by substituting the slope and intercept values from the calibration curves

$$y_{CH_4} = 1.3925*x - 0.1178 \qquad \text{(for He)} \qquad 5.7$$

$$y_{CH_4} = 1.2038*x - 0.0661 \qquad \text{(for } CO_2\text{)} \qquad 5.8$$

$$y_{CH_4} = 1.1907*x - 0.0480 \qquad \text{(for } N_2\text{)} \qquad 5.9$$

$$y_{CH_4} = 1.2985*x - 0.0851 \qquad \text{(for } H_2\text{)} \qquad 5.10$$

Where ‘x’ is the display on the mass flow controller.

For gaseous mixtures the gas correction factor is calculated by the following equation

$$GCF_{mix} = \frac{d_{CH4} * c_{CH4}}{s_{CH4}} * \frac{z_1 * s_1 + (1 - z_1) * s_2}{z_1 * d_1 * c_1 + (1 - z_1) * d_2 * c_2} \quad 5.11$$

Where Z_1 is the mole fraction of gas 1, Z_2 is the mole fraction of gas 2, d_X = Standard density of gas x, in g/l; C_X = Specific Heat of gas x, in cal/g° C and S_X = Molecular structure correction factor.

The mass flow meters (MFM1 & MFM2) were originally calibrated at manufactures factory using N_2 as calibration gas between 0 to 2000 CC/M. Similar to mass flow controller, the other pure gas flow and gas mixture flowing through MFMs were calculated.

5.4 GC Calibration

The GC calibration was performed using different compositions of CO_2 in N_2 and. The pure component CO_2, N_2 areas were used to back calculate the composition of an unknown mixture. The area obtained for a component in a mixture divided by its pure component area will gives the percentage composition of that component. The obtained calibration curves for CO_2, N_2 can be seen in Figures 5.5 a-b.

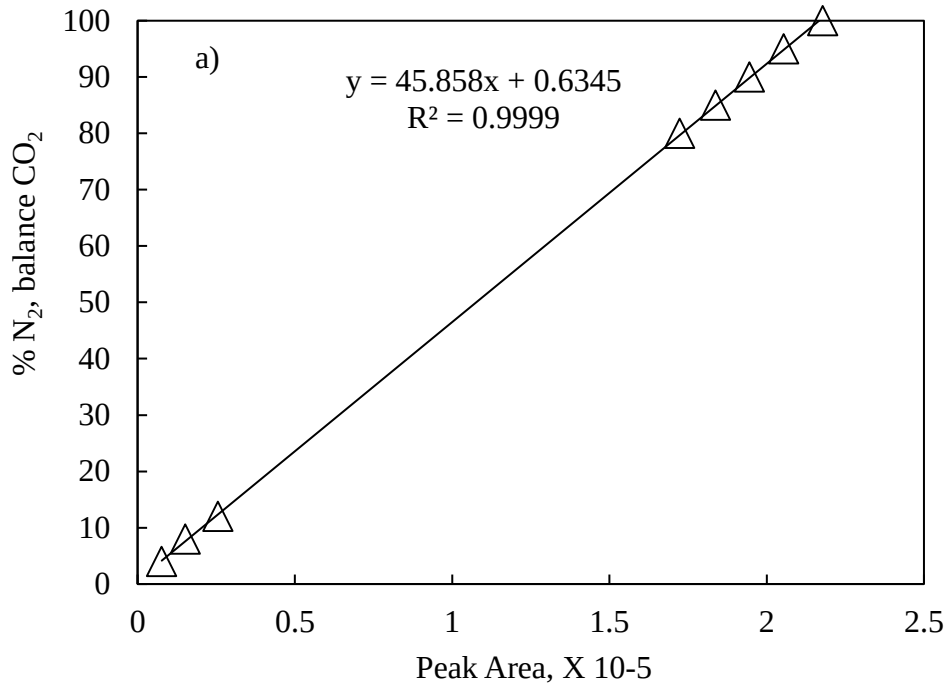

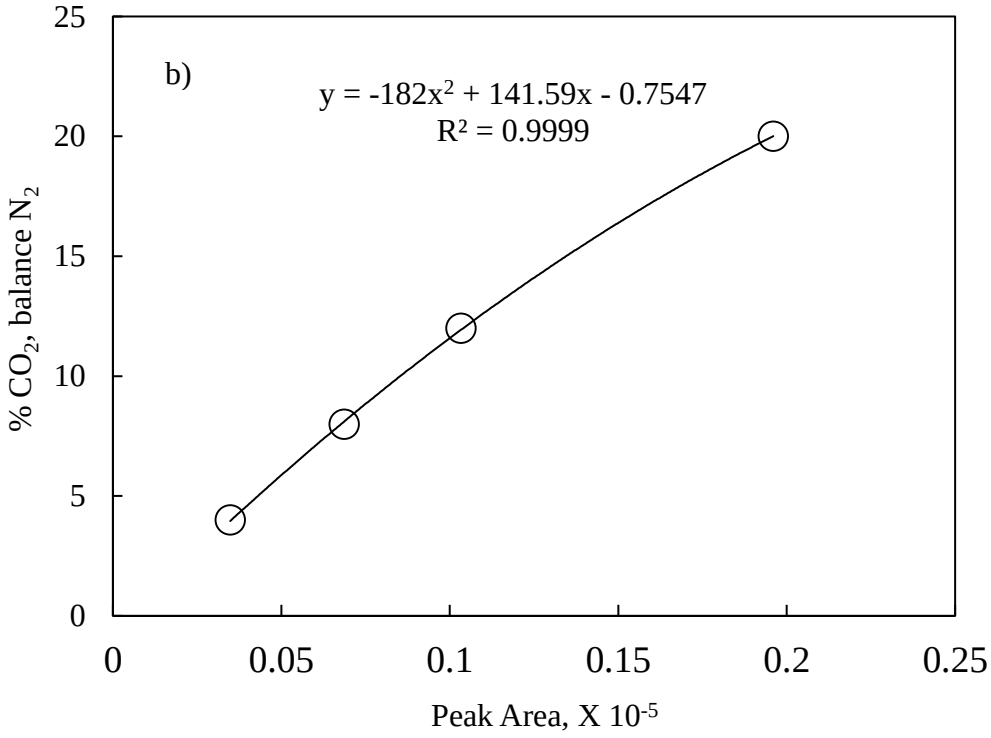

Figures 5.5(a-b): Gas Chromatography calibration curves for CO_2 and N_2

5.5 Breakthrough experiments on benchmark adsorbent: Zeolite 13X

In order to validate the designed experimental set up, binary breakthrough experiments were measured on benchmark adsorbent zeolite 13X. The adsorbent column was packed with 20 g of zeolite 13X pellets. Properties of the fixed bed column and experimental conditions for breakthrough experiments were given in Table 5.2.

To remove the moisture and other gas species present, an initial activation of adsorbent column was carried at 473 K under N_2 purge flow for 4 hours. The column was subsequently cooled to ambient temperature. Adsorption breakthrough experiments were carried out by first saturating the column with He gas at 1 bar and then introducing a feed containing 16% CO_2 and 84% N_2.

Table 5.2: Properties of the fixed bed column and experimental conditions for breakthrough experiments on Zeolite 13X

Mass of Zeolite 13X pellets	20 g
Mass of Zeolite 13X pellets(Activated weight)	19.52 g
Feed Concentration	16 % CO_2, 84% N_2
Temperature	300 K
Feed flow rate	1 LPM
Pressure	1.3 bar
Column length	300 mm
Column internal diameter	10 mm
Column initial condition	Filled with 1 bar He

During the breakthrough experiments, the column outlet stream was analysed periodically using the gas chromatography system. The gas chromatography system is a Varian GC-450 with a TCD detector and a fused silica capillary column with a 30 m x 0.53 mm ID was used for the separation of gas mixtures. The GC operating conditions for breakthrough measurements are injector's temperature: 120 ^{o}C, column oven temperature: 90 ^{0}C and column pneumatics mode is pressure. At these operating conditions, the observed GC retention times of CO_2 and N_2 are 1.39, 3.90 minutes respectively. A GC method was created in such a way that gas sampling valve of GC will inject sample at every one minute. The successive peaks obtained were identified by their retention times

Figure 5.6 Represents the breakthrough curves for a total feed flow rate of 1 LPM consists of 16% CO_2, balance N_2 at 1.3 bar and 300 K. As the mass transfer zone moves through the bed, the initially adsorbed N_2 was displaced by the strongly adsorbed CO_2: at this stage the outlet concentration of N_2 exceeds the inlet concentration of N_2 which is resulted as shoot up in N_2 concentration during N_2 breakthrough. The weakly adsorbed component N_2 was first observed at the column outlet at 3 minutes, whereas the strongly adsorbed component CO_2 was detected after 5 minutes. These breakthrough times were matching with the reported literature by Dantas et. al [111]. To check the repeatability of the experiment, the breakthrough experiments are repeated (Run1 and Run2). The breakthrough experimental curves obtained were sharp in nature: indicating the faster mass transfer rate inside the adsorbent bed.

The Figure 5.7 shows the results obtained for varied switch times of He to CO_2/N_2. After each breakthrough experiment, column was desorbed to 33 torr and on this adsorbent sample breakthrough experiments were performed.

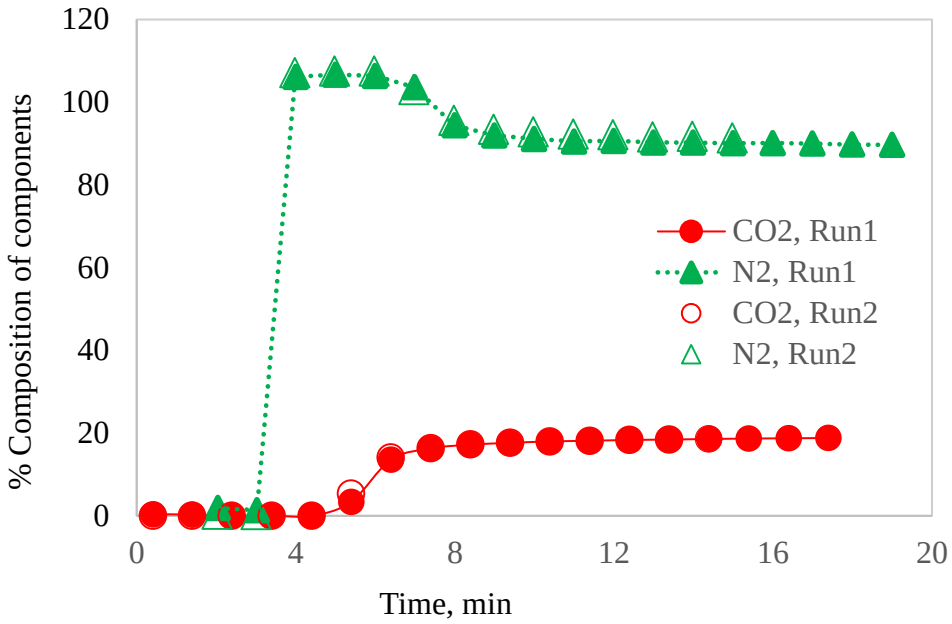

Figure 5.6: Breakthrough curves for a total feed flow rate of 1 LPM consists of 16% CO_2, balance N_2 at 1.3 bar and 300 K on Zeolite 13X

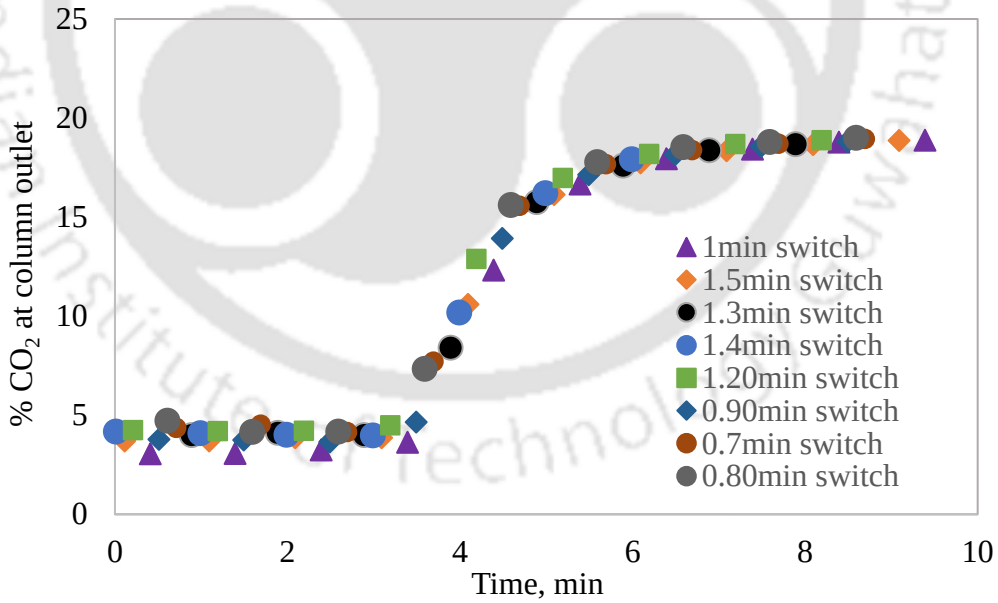

Figure 5.7: CO_2 Breakthrough curves on zeolite 13X, Feed: 16% CO_2 balance N_2, Feed flow rate: 1 LPM, Column pressure: 1.3 bar. He to CO_2/N_2 switch times are varied to obtain more points on breakthrough curve.

5.6 Process cycle experiments on Zeolite 13X

After performing the breakthrough experiments, the next step was to explore the PSA/PVSA cycle. Dantas et al. [111] reported a detailed experimental study of a basic 4-step PVSA process compromising of pressurization, adsorption, blowdown and evacuation steps. The 4-step cycle shown in Figure 5.8 comprises of the following steps

Pressurization: In this step, the column, which was under vacuum initially was pressurized to 1.3 bar, by introducing the feed at a predetermined flow rate from the feed end. During this step, the column outlet is closed using the pneumatic valve PV1 shown in Figure 5.1.

Adsorption/Feed: The column was continuously fed at the same flow rate, but with column outlet valve (PV1) is open now. The highly adsorbing component CO_2 is preferentially adsorbs while the low adsorbing component N_2 is withdrawn from the product end.

Counter-current blowdown: In this step, the feed end (valve PV5) was closed and the column was counter-currently depressurized to 0.1 bar through the valve PV6/PV8.

Purge along with evacuation: The column is then evacuated at 0.1 bar under N_2 purge flow (valves PV8 and PV4 are open).

The same 4-Step PVSA cycle was studied in the present work. It compromises of co-current pressurization with feed (16% CO_2, balance N_2); adsorption with feed at constant pressure of 1.3 bar and 1 LPM; and counter current blowdown by decreasing pressure approximately to 0.1 bar. The cycle experiments were performed on the same column used for breakthrough experiments (Table 5.2).

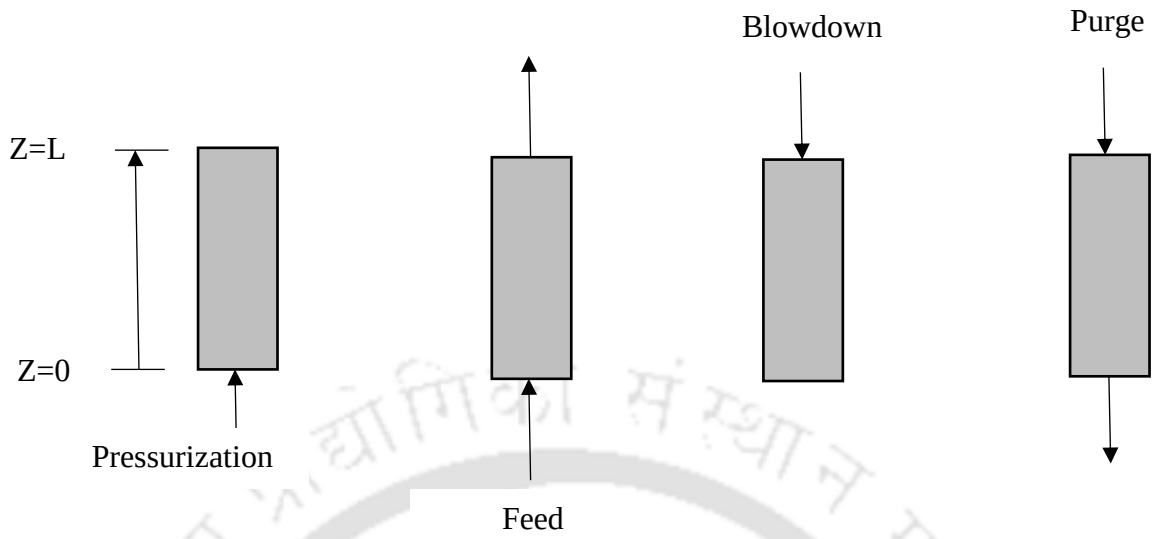

Figure 5.8: A schematic diagram of basic four-step PSA cycle

5.6.1 Protocol for cycle experiments

1. Initial activation of adsorbent at 473 K under N_2 purge flow of 45 cc/min for four hours. After completion of the activation, column was allowed to reach experimental temperature.
2. Pressurization with feed mixture (16% CO_2, balance N_2) for 10 seconds.
3. Adsorption with feed mixture (16% CO_2, balance N_2) for 60 seconds. During the adsorption step, the column outlet stream composition was analysed using GC.
4. Counter current blowdown of column pressure to approximately 0.1 bar.

At the end of adsorption step, column was at 1.3 bar pressure (P_{High}). A blowdown sampling loop was used to achieve the desorption pressure of 0.1 bar (P_{Low}). Prior to each cycle run, blowdown tank loop was fully vacuumed and once the adsorption step ends, the gas mixture in column (at P_{High}) was allowed to expand into this loop. With this expansion, column pressure was reached to a medium pressure ($P_{medium1}$) and the collected gas mixture composition in blowdown loop was

analyzed by sending it to GC. This procedure was repeated until the column pressure reaches to 0.1 bar. In order to calculate the number of moles of each component collected in blow down step, we must know the volume of blow down loop. Hence, blow down loop volume was measured by following method.

5.6.2 Blowdown tank loop volume calibration

The schematic of designed blowdown loop was shown in Figure 5.9. It consists of a 125 cc stainless steel tank, a mass flow controller, a GC sampling valve and one gas circulating pump.

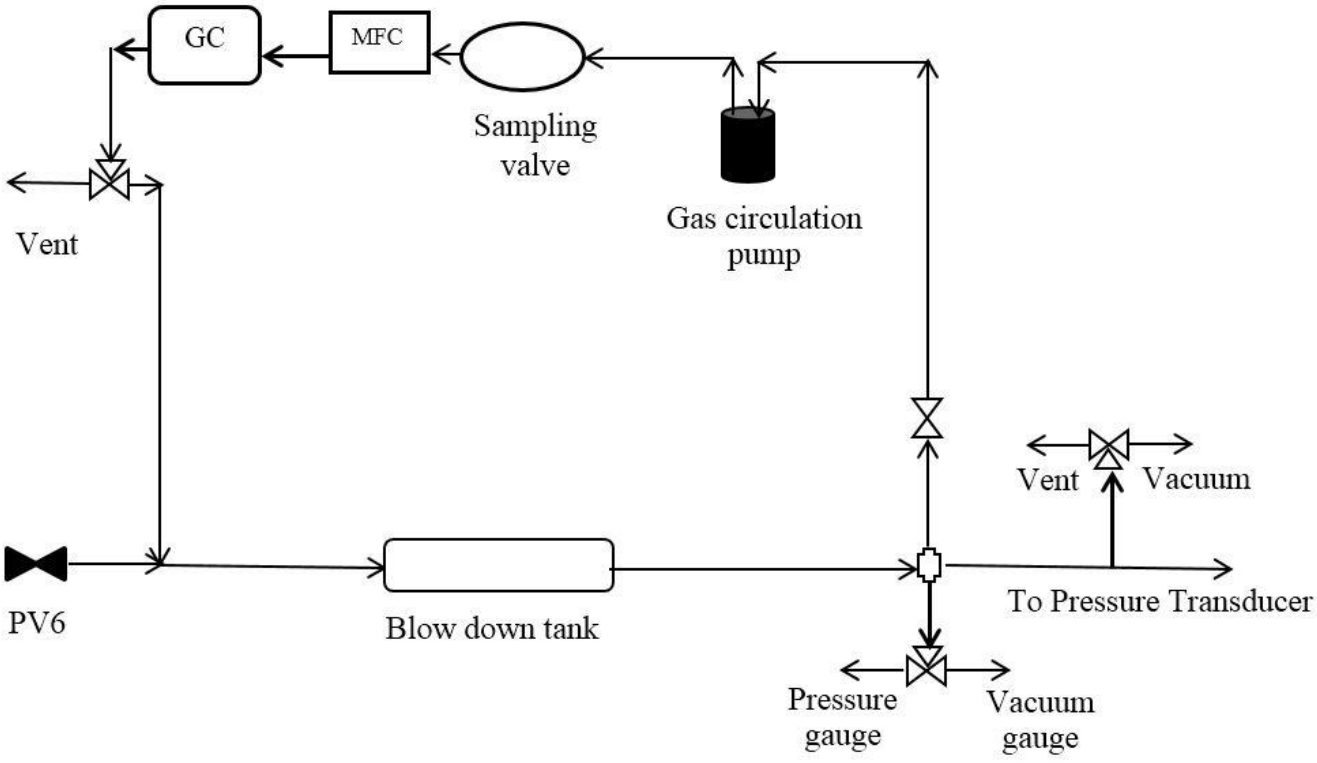

Figure 5.9. Schematic of blowdown tank loop

Blowdown tank loop volume ($V_{Blowdown\ loop}$) calibration experiments were performed using wet gas flow meter (GFM) and results were shown in Figure 5.10. Initially the blow down tank loop was filled with N_2 at a high pressure P_1 and then it was reduced to a pressure P_2. During this pressure reduction, the volume displaced in wet gas flow meter ($V_{displaced\ in\ GFM}$) was recorded at ambient temperature (To) and ambient pressure (Po). Assuming idea behavior of gas, we can write

$$\frac{P_1 V}{RT_1} - \frac{P_2 V}{RT_2} = n_{gas} = P_o V_{displaced\ in\ GFM} \quad 5.12$$

$$V_{blowdown\ loop} = \frac{P_o V_{displaced\ in\ GFM}}{(P_1 - P_2)} \quad 5.13$$

Table 5.3: Blowdown tank loop volume calculations

$P_{blowdown\ (initial)}$, torr	$P_{blowdown\ (final)}$, torr	$V_{gas\ displaced\ in\ GFM}$, CC	P1-P2, torr	$V_{blowdownloop}$, CC
9338	754	3015	8584	264.83
7945	751	2640	7194	276.81
7027	754	2265	6273	272.25
6040	754	1900	5286	271.02
5050	752	1585	4298	278.19
4040	753	1195	3287	274.20

The average volume of blowdown tank loop = 272.88 cc.

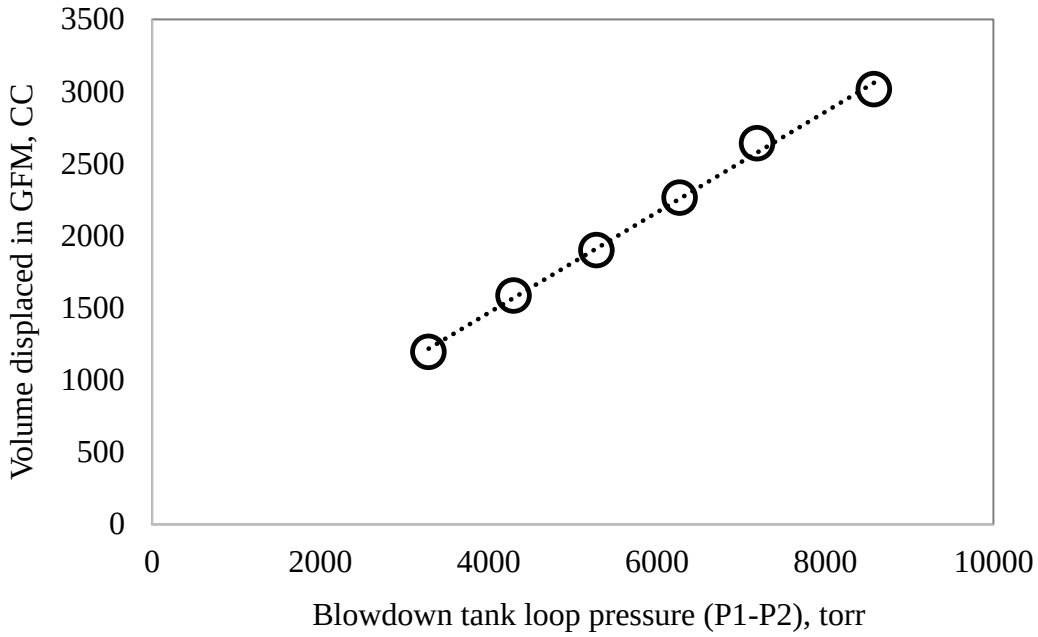

Figure 5.10: Blowdown tank loop volume calibration curve using wet gas flow meter

The volume of blowdown loop and pressure in each blowdown step are known now. By using this data we can calculate the number of moles of gas present in each blowdown step ($n_{blowdown,i}$). $n_{blowdown,i}$ will be used in the calculation of CO_2 purity and CO_2 recovery.

5.6.3 PVSA separation performance

The performance of the PVSA experiments was evaluated according to four basic parameters: purity and recovery of product (CO_2), purity of the stream to be purified (N_2) and productivity of the PVSA. They are defined by

$$N_2 \text{ purity} = \frac{moles\ of\ N2\ collected\ at\ column\ outlet\ during\ adsorption\ step}{moles\ of (CO2+N2) collected\ at\ column\ outlet\ during\ adsorption\ step} \qquad 5.14$$

CO_2 purity $= \dfrac{moles\ of\ CO2\ recovered\ in\ blowdown\ step}{moles\ of (CO2+N2) recovered\ in\ blow\ down\ step}$ 5.15

$$= \frac{\Sigma_i\ y_{CO2,i}\ n_{blowdown,i}}{\Sigma_i\ n_{blowdown,i}}$$

CO_2 recovery $= \dfrac{moles\ of\ CO2\ recovered\ in\ blowdown\ step}{moles\ of\ CO2\ fed\ during\ (pressurization+feed) steps}$ 5.16

$$= \frac{\Sigma_i\ y_{CO2,i}\ n_{blowdown,i}}{\int_{pres} y_{CO2,feed}\ F_1\ dt + \int_{ads} y_{CO2,feed}\ F_1\ dt}$$

Productivity $= \dfrac{moles\ of\ CO2\ recovered\ in\ blowdown\ step}{cycle\ time * weight\ of\ adsorbent}$ 5.17

$$= \frac{\Sigma_i\ y_{CO2,i}\ n_{blowdown,i}}{tcycle * wads}$$

Where, 'n' is moles of gas, F is flow rate, y_i is the mole fraction of component 'i', t_{cycle} is the cycle time and w_{ads} is the weight if the adsorbent.

Table 5.4 shows the evaluated PVSA process performance of Zeolite 13X. The approach to cyclic steady state was shown in terms of CO_2 product purity (%) and CO_2 product recovery (%) in Figure 5.11. In a typical experiment, the cyclic steady state (CSS) was achieved in about 20 cycles at which the difference between the CO_2 purity/recovery in consecutive cycles is less than 0.5%.

Table 5.4: PVSA performance of zeolite 13X

Cycle No	CO_2 Purity, %	N_2 Purity, %	CO_2 recovery, %
5	48.92	100.00	54.88
10	51.71	88.84	64.33
15	51.77	86.96	63.80
20(CCS)	51.44	84.86	63.46

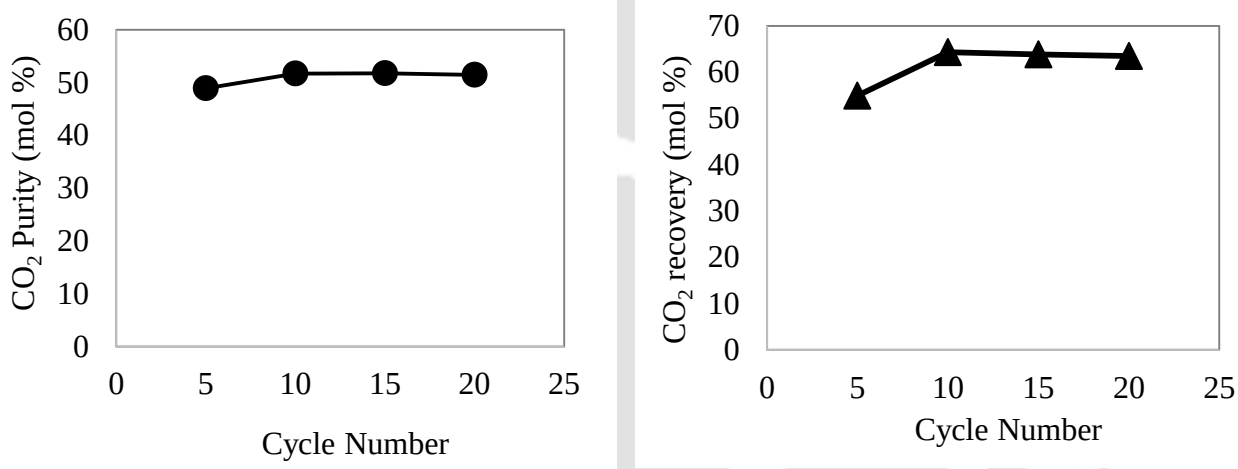

Figure 5.11: Approach to cyclic steady state

The performance of the studied four-step PVSA process was: CO_2 purity: 51.4%, CO_2 recovery: 63.5%. These obtained purity and recovery values were comparable to the experimentally studied Zeolite 13X performance by Dantas et al. [111]: CO_2 purity: 36.8%, CO_2 recovery: 90.0% and Zeolite 13X performance (P_{ads} = 2 bar, T_{ads}=35 ^oC) by Dasgupta et al [109]: CO_2 purity: 60%, CO_2 recovery 60 %. This valids our designed system.

CHAPTER 6

CO_2/N_2 SEPARATION PERFORMANCE ANALYSIS OF HIGHLY STABLE Zr-BASED MOF UiO-66

In the chapter, we report the evaluation of UiO-66 MOF for CO_2/N_2 separation. About 20 g of the material is first synthesized in powder form; pellets were made subsequently using polyvinyl alcohol as the binder. The effect of binder content on physical structure and equilibrium adsorption capacity of the material is discussed. Finally, the results of breakthrough measurements and process cycle experiments performed using these pellets in a packed column are presented.

6.1 Scale up synthesis

UiO-66 was successfully synthesized in 20 g level following the procedure reported by Katz et. al. [119] as described in section 4.1.1. The following two sections present the results of UiO-66 pellet preparation and characterization.

6.2 Pellet preparation

The procedure reported for preparation of MIL-53/PVA pellets by Finsy et. al. [108] was adopted. A 15 wt% PVA/H_2O mixture was prepared by adding 17.65 g of poly vinyl alcohol (PVA, Merck) to 100 ml of deionized water. Then the solution mixture was heated at 90 ^{O}C in a two necked round

bottom flask with a thermometer and a reflux condenser unit. A clear gelatinous mixture was obtained after complete dissolution of PVA in water. The mixture of MOF and PVA was prepared using sufficient amount (about 0.5 to 1 g) of water. The resulting MOF/PVA mixture was shaped into 1-2 mm diameter of MOF/PVA cylindrical pellets using a 6 ml syringe. The ratio of adsorbent to binder was varied. The obtained pellets were heated at 0.5 ^{o}C/min to reach 180 ^{o}C and kept at this temperature for 6 hours. The experimental conditions of the formulated pellets are given in Table 6.1. The photographs and scanning electron microscopy images of the synthesized powder and 41PVA@UiO-66 pellets are shown in Figure 6.1.

Table 6.1: Experimental conditions used and properties of formulated UiO-66 MOF pellets

Sample	Mass of MOF (g)	Mass of 15wt% PVA/water (g)	Mass of water (g)	BET Surface area (m^2g^{-1})	Pore volume (cc/g)	Bulk density (g/cc)
UiO-66	--	--	--	1378	0.80	0.25
33PVA@UiO-66	1.0	0.50	0.5-1.0	1274	0.76	0.32
41PVA@UiO-66	1.0	0.70	0.5-1.0	1195	0.69	0.34
50PVA@UiO-66	1.0	1.0	0.5-1.0	987	0.61	0.35

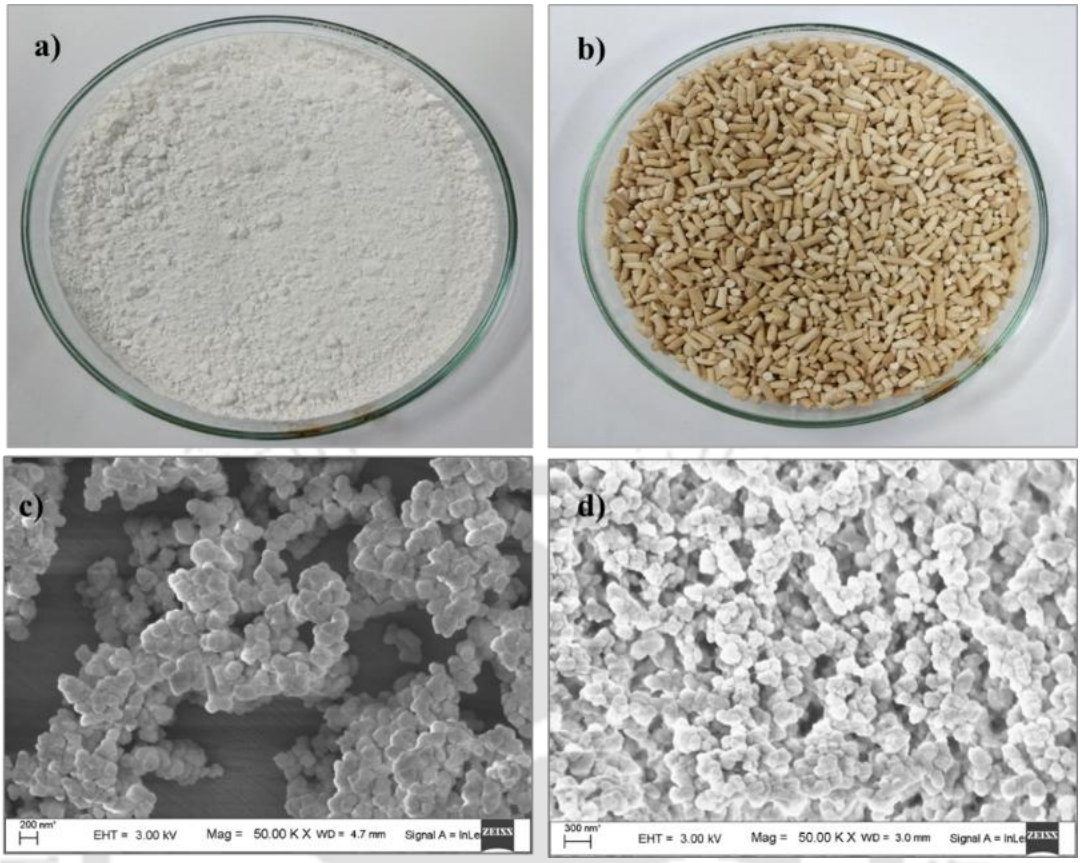

Figure 6.1: Images (a) UiO-66 powder, (b) 41PVA@UiO-66 pellets

FESEM images (c) UiO-66 powder, (d) 41PVA@UiO-66 pellets.

6.3 Characterization

6.3.1 Surface Area and Pore Volume Analysis

The experimental conditions and properties of the formulated PVA@UiO-66 pellets are given in Table 6.1. The N_2 physisorption isotherms (Figure 6.2) of powder and shaped pellets at 77 K are of type I isotherm, indicating the presence of microporous structure. The calculated BET specific surface area of UiO-66 was 1378 m^2/g and is comparable to the reported value of 1367 m^2/g by

Ren et. al. [125], and slightly higher than the values reported by Cmarik et. al. [126], Cao et. al. [127] and Xian et. al. [128].

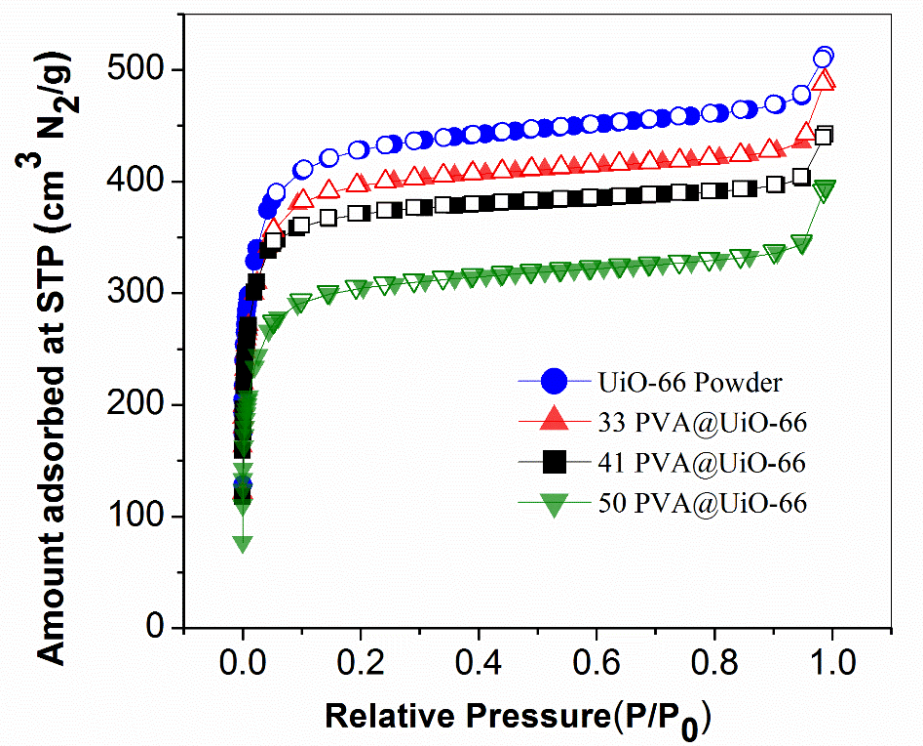

Figure 6.2: N_2 adsorption (filled symbols) - desorption isotherms (open symbols) of UiO-66 and 41PVA@UiO-66 samples

As indicated earlier, the pellets were prepared with different binder contents. They are denoted as 33PVA@UiO-66, 41PVA@UiO-66 and 50PVA@UiO-66 corresponding to the initial mass percent of PVA/H_2O (Table 6.1). Addition of nonporous polymer binder results decreases the specific surface area and porosity of the sample as expected; in addition to the mass of the binder, partial degradation of the porous structure also contributes to the loss in the specific surface area. A decrease in BET surface area of about 14 % was observed for 41PVA@UiO-66 compared to that of the powder UiO-66.

6.3.2 Mechanical strength of shaped PVA@UiO-66 pellets

(a) Drop Test

To measure the ability of the dried pellets to remain intact during the handling, drop tests were conducted as described by Kawatra et. Al. [124]. 30 number of pellets were dried at 100 ^{o}C for 3 hours and dropped repeatedly from a height of 0.5m onto a stainless steel plate. The number of broken pellets was recorded.

Figure 6.3a shows the results of drop test. All pellets withstand up to 150 drops. However, 33PVA@UiO-66 pellets began to break beyond 150 drops and at 200 drops about 20% of pellets were broken; on the other hand, 41PVA@UiO-66 and 50PVA@UiO-66 pellets have 0% breakage even at 200 drops, indicating good mechanical strength.

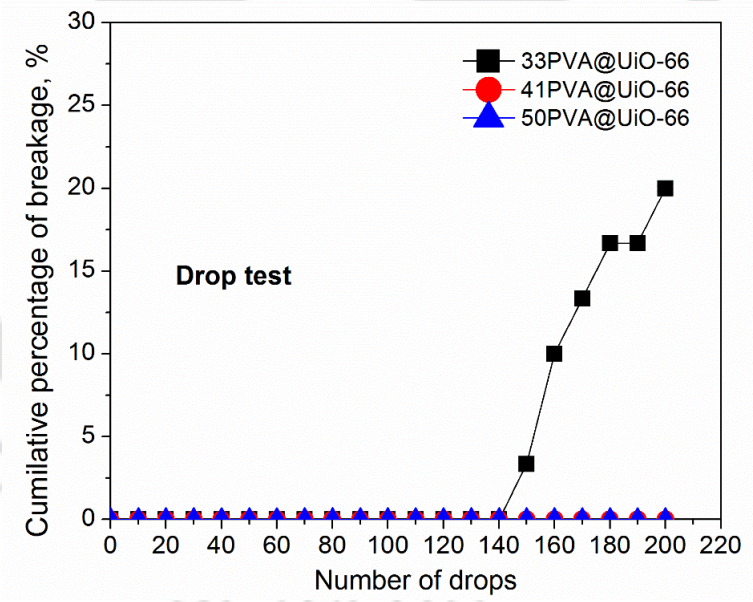

Figure 6.3a: Drop test results for shaped PVA@UiO-66 pellets

(b) Compression Test

The crush strength of 41PVA@UiO-66 pellets was measured using 5 kN Electromechanical Universal Testing Machine (UTM). Compression test was performed at a speed of 0.05 mm/min.

The results show a failure load (Fmax) of 18 N (see Fig 6.3b). Asadi et al. [129] reported a crush strength of Cu-BTC tablets as 16 N (purchased from BASF). Thus, the crush strength of our pellets was comparable to the commercial Cu-BTC MOF tablets provided by the BASF.

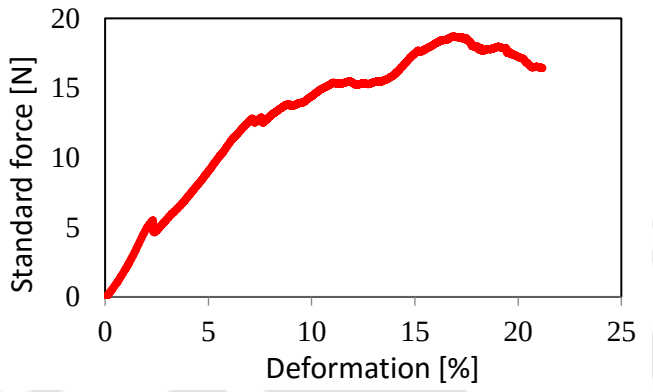

Figure 6.3b: UTM compressive test result of shaped 41PVA@UiO-66 pellets

Based on the textual characterization, drop test and crush strength results, 41PVA@UiO-66 pellets were chosen for further material characterization and experiments. From here onwards the term pellet refers to 41PVA@UiO-66 pellet.

6.3.3 Thermogravimetric Analysis

The thermogravimetry (TG) and differential thermogravimetry (DTG) curves of UiO-66 powder and 41PVA@UiO-66 pellet are shown in Figure 6.4. Two weight loss steps were observed for the powder sample. The initial weight loss below 120 ^{o}C is due to the removal of moisture; the second weight loss step that starts at about 450 ^{o}C corresponds to the decomposition of the sample and collapse of the crystal structure. In addition to these two weight loss steps, the TG curve of pellet sample exhibits an additional weight loss step between 200 ^{o}C to 350 ^{o}C, corresponding to the degradation of PVA. Thus, the TG results suggest that the prepared 41PVA@UiO-66 pellets are stable up to 200 ^{o}C and the calculated binder content in the pellets is about 9.3 wt%.

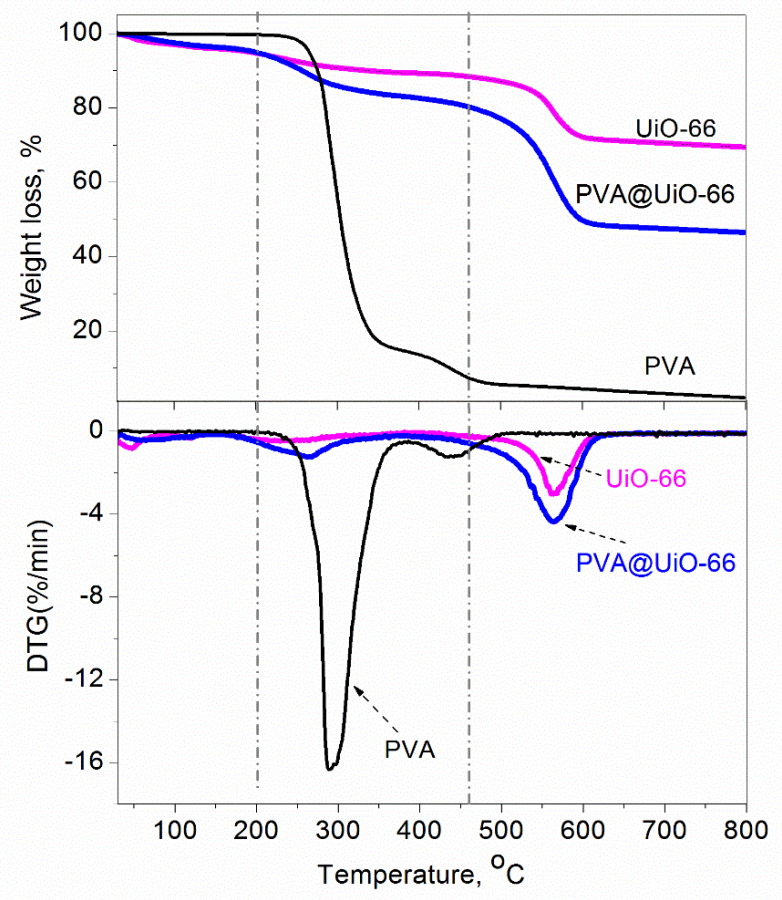

Figure 6.4: Thermogravimetry (TG) and differential thermogravimetry (DTG) curves of UiO-66 and 41PVA@UiO-66 samples.

6.3.4 FTIR-Analysis

The samples were further subjected to FTIR analysis and the corresponding spectra are given in Figure 6.5. The broad bond centered at 3400 cm^{-1} can be assigned to hydrogen bonded adsorbed water [130]. The two peaks at 2940 cm^{-1} and 2850 cm^{-1} are the characteristic bonds of asymmetric and symmetric C-H stretching in PVA, respectively [131]. The peaks at 1570 cm^{-1} and 1350 cm^{-1} correspond to the stretching vibrational bonds of C=O and C=C in the MOF structure, respectively [132]. The vibration peak at 750 cm^{-1} is attributed to the Zr-O stretching in the MOF because of the coordination of an oxygen atom with Zr.

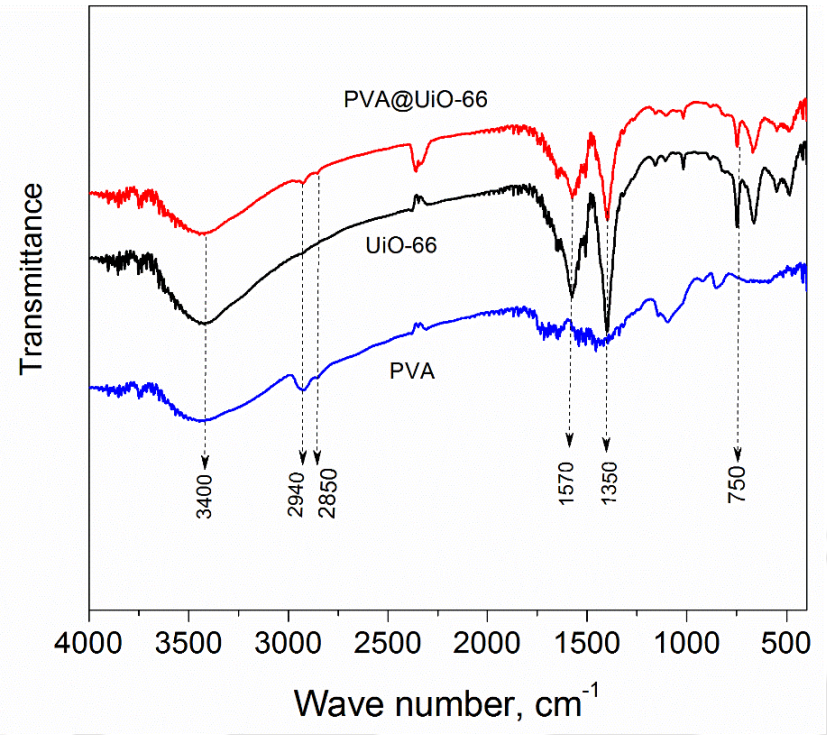

Figure 6.5: FTIR spectra of PVA, UiO-66 and 41PVA@UiO-66 samples

6.3.5 X-ray Diffraction (XRD) Analysis

The XRD patterns of powder and pellet samples are shown in Figure 6.6. The X-ray diffraction pattern of synthesized UiO-66 powder is in good agreement with the published literature data [127]. The observed identical patterns, indicating the crystal structure of the UiO-66 remains intact after pelletization.

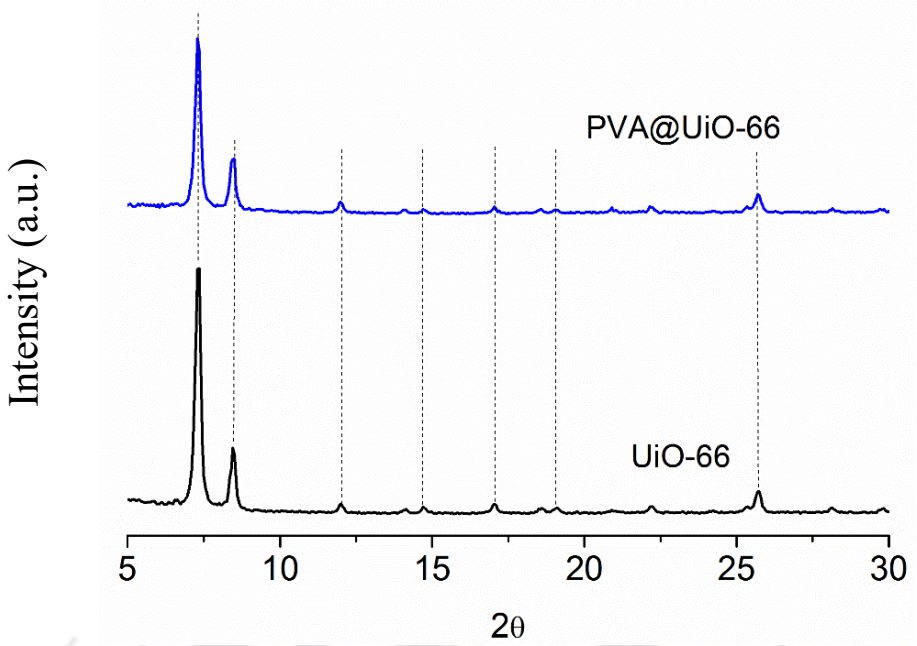

Figure 6.6: XRD patterns of UiO-66 and 41PVA@UiO-66 sample

6.4 Single component equilibrium adsorption isotherms

Pure component adsorption isotherms were measured using the volumetric set up described in section 4.4.1.2. Figures. 6.7 (a)-(b) presents the equilibrium adsorption isotherms of CO_2 and N_2 on UiO-66 powder at 298 K, 318 K and 348 K, and are well described by the Dual Site Langmuir and Langmuir isotherm models respectively. The model fit parameters were obtained by non-linear regression fits of the experimental isotherm data using Sigmaplot Software and given in Table 6.2. The loading for CO_2 at 298 K and 1 bar on UiO-66 powder, measured in this work is 1.3 mmol/g, which is higher than that on MOF-2 (0.6 mmol/g), MOF-177(0.8 mmol/g), MOF-5 (1.0 mmol/g), IRMOF-6 (1.05 mmol/g) and IRMOF-3 (1.1 mmol/g) [133]. However, the CO_2 loadings are lower when compared to Mg/DOBDC (8 mmol/g) [134], Cu-BTC (5.8 mmol/g) [135], Zeolite 13X (4.7 mmol/g) [136], MIL-53(Al) (2.3 mmol/g) [137] and Zn/DABCO (2.0 mmol/g) [138].

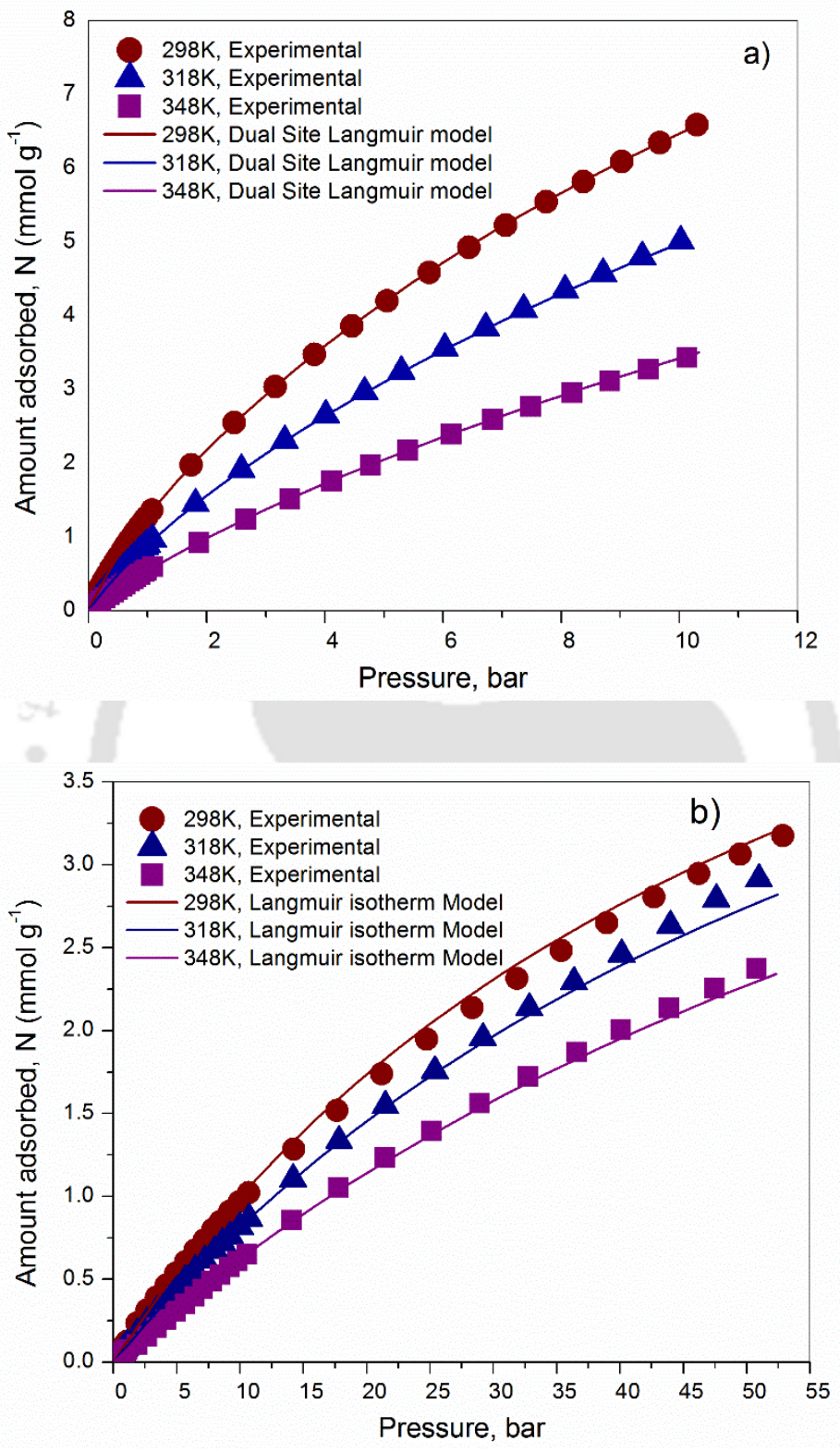

Figure 6.7: Isotherms on UiO-66 powder **(a)** CO_2 and **(b)** N_2. Lines are fits using model

Table 6.2: Isotherm Model Parameters at 298 K (DSL for CO_2 and Langmuir for N_2) on UiO-66 powder

Parameter	Adsorbates	
	CO_2	**N_2**
N_1^{max}, mmol g^{-1}	0.91	6.72
N_2^{max}, mmol g^{-1}	16.0	--
b_0, bar^{-1}	2.88E-04	4.23E-04
b_1, K	2437	1109
c_0, bar^{-1}	6.28E-05	--
c_1, K	2016	--

The enthalpy of adsorption for CO_2 and N_2 is calculated using model fit parameters and is given in Figure 6.8. The calculated enthalpy of adsorption at zero coverage on UiO-66 is -18.6 kJ/mol. This value is lower than that on MOFs like MIL-100 (-62 kJ/mol) [139], Ni/DOBDC (-36 kJ/mol) [140], MIL-101 (-32 kJ/mol) [139], Cu-BTC (-23 kJ/mol) [135] and zeolites like 13X (-49 kJ/mol) [136]. The value of enthalpy of adsorption of N_2 on UiO-66 at zero loading is - 9 kJ/mol which is comparable to the IRMOF-1(-8.3 kJ/mol) [141], IRMOF-3(-9 kJ/mol) [133], Zn/DABCO (-11 kJ/mol) [138] and MOF-177(-10 kJ/mol) [142] and lower than that on MIL-53(Al) (-15.9 kJ/mol) [137], and on silicalite (-16.7 kJ/mol) [143].

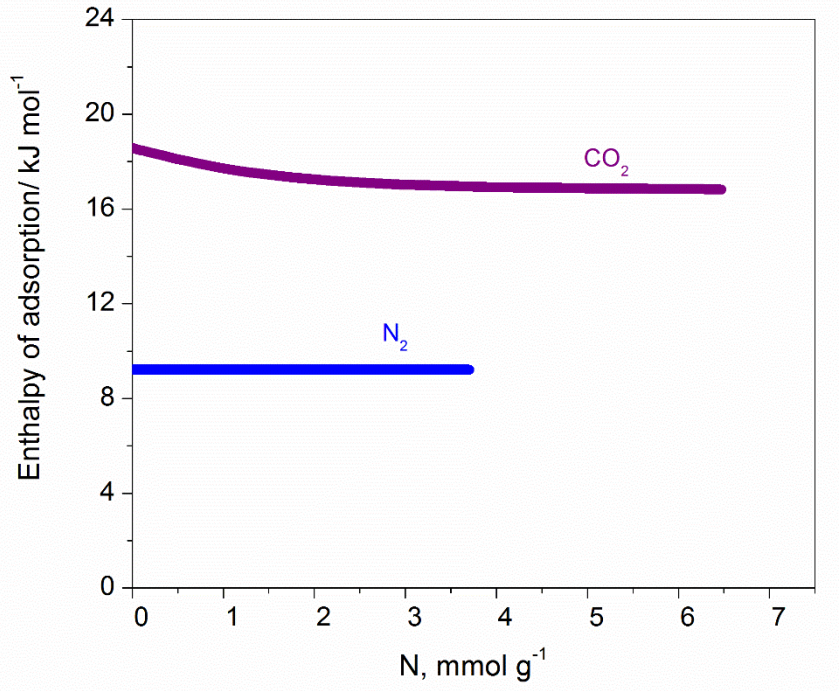

Figure 6.8: Variation of enthalpy of adsorption with loading

To investigate the effect of the pelletization on the adsorption properties, CO_2 and N_2 adsorption isotherms were measured on 41PVA@UiO-66 pellets at 298 K. Figure 6.9a compares the adsorption isotherms of powder and pellets in terms of amount adsorbed per gram of adsorbent (gravimetric loading). The volumetric loading capacity in amount adsorbed per unit volume of the solid is shown in Figure 6.9b. For both the probe gases, about 14-18% lower loadings were observed on the pellets compared to that on the powder, which was in accordance with the difference in specific surface areas of the two samples. In contrast, slightly higher loadings were noticed for pellets in terms of amount adsorbed per unit volume, which may be attributed due to the increase in bulk density of adsorbent sample upon pelletization (Table 6.1).

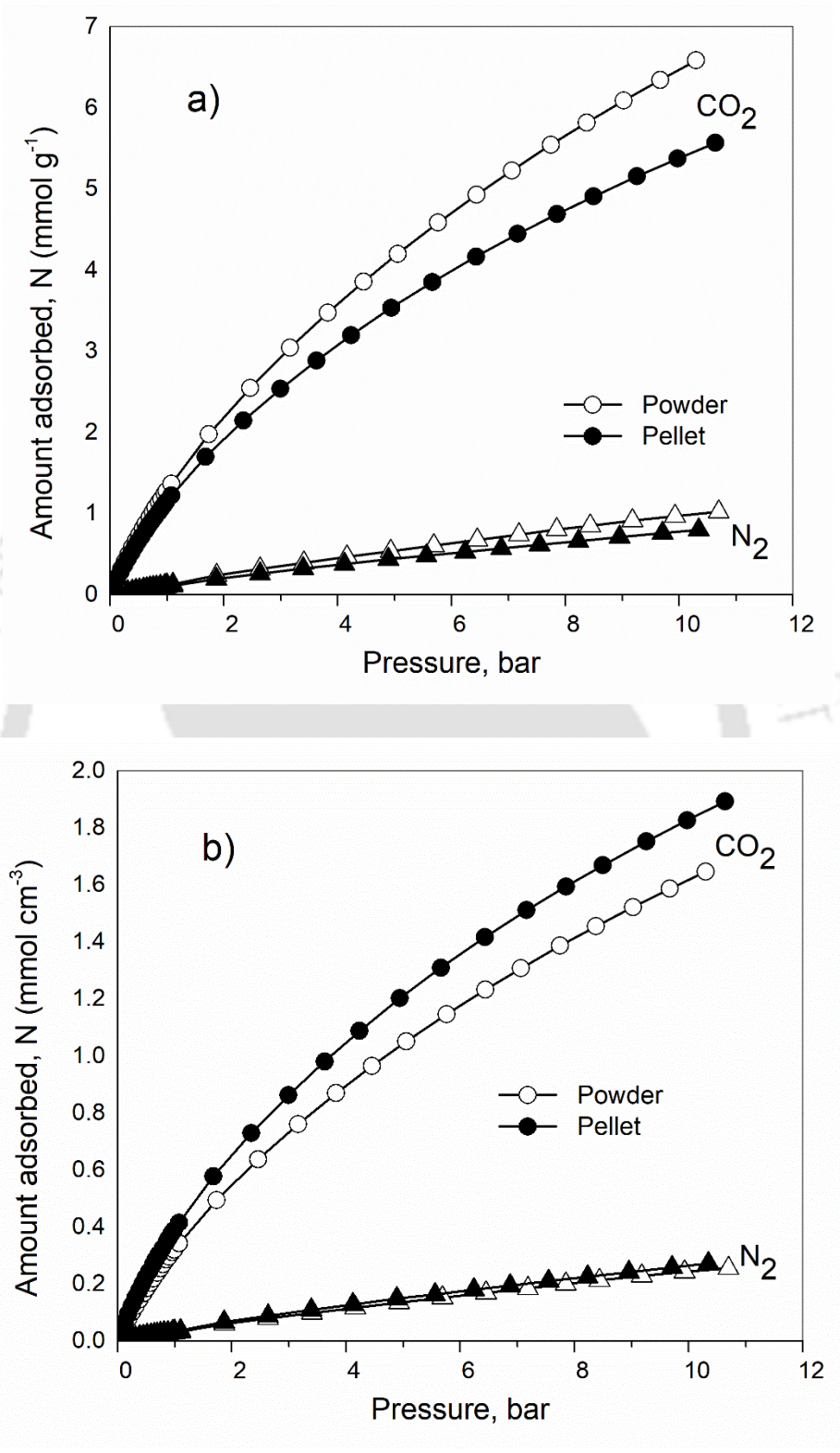

Figure 6.9: Adsorption isotherms at 298 K on powder and pellets a) amount adsorbed per gram b) amount adsorbed per cm^3

6.5 CO_2/N_2 separation: Binary breakthrough experiments

The operating conditions used in breakthrough experiments are tabulated in Table 6.3. Figure 6.10 represents the binary breakthrough curves for a total feed flow rate of 100 SCCM. Nitrogen, the low adsorbing component is first detected at the bed outlet after 60 seconds and CO_2, more strongly adsorbed component, is not detected until 306 seconds. The clear difference in breakthrough times, corroborates the ability of UiO-66 pellets to separate CO_2/N_2 mixtures.

Table 6.3: Properties of the fixed bed column and experimental conditions for breakthrough studies

Mass of adsorbent pellets (un activated), g	10.80
Mass of adsorbent pellets (activated), g	9.23
Feed Concentration, vol %	~15 % CO_2 balance N_2
Temperature, K	300
Feed flow rate, SCCM	50 – 200
Adsorption/Desorption Pressure, bar	1.3/0.1
Length of the column, mm	300
Internal Diameter of the column, mm	10

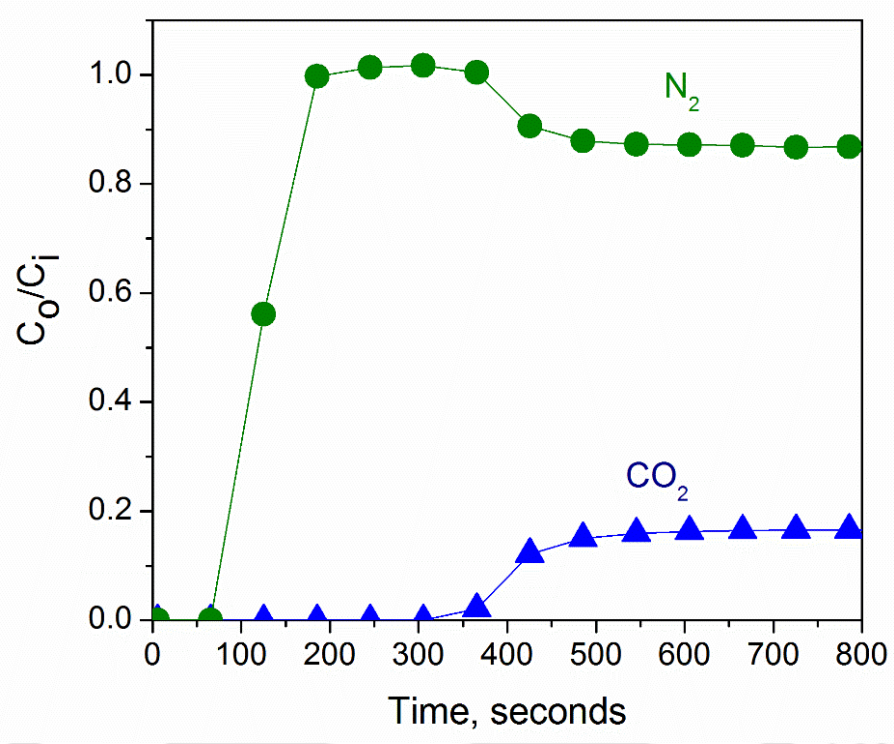

Figure 6.10: Binary mixture (CO_2/N_2: 15/85) breakthrough curves on PVA@UiO-66 pellets at 100 SCCM feed flow rate and 300 K.

Figure 6.11a shows the breakthrough curves of CO_2 in feed at different feed flow rates. As can be seen, the breakthrough times decrease with increase in the feed flow rate; the sharp nature of breakthrough curves suggests high mass transfer rates inside the adsorbent bed. Figure 6.11b is generated using the cumulative flow of the gas as abscissa (instead of the time). The overlap of the curves at different flow rates suggests that there are no significant mass transfer resistances with in the flow rate ranges under consideration. The measured breakthrough curves at different column pressures are given in Figure 6.12. As expected, breakthrough time increased with increase in column pressure. The CO_2 loading obtained from these binary breakthrough experiments at 1.3 bar (P_{CO2} = 0.2 bar) and 300 K is about 0.26 mmol/g, slightly lower than the corresponding pure component CO_2 equilibrium possibly due to slight co-adsorption of N_2.

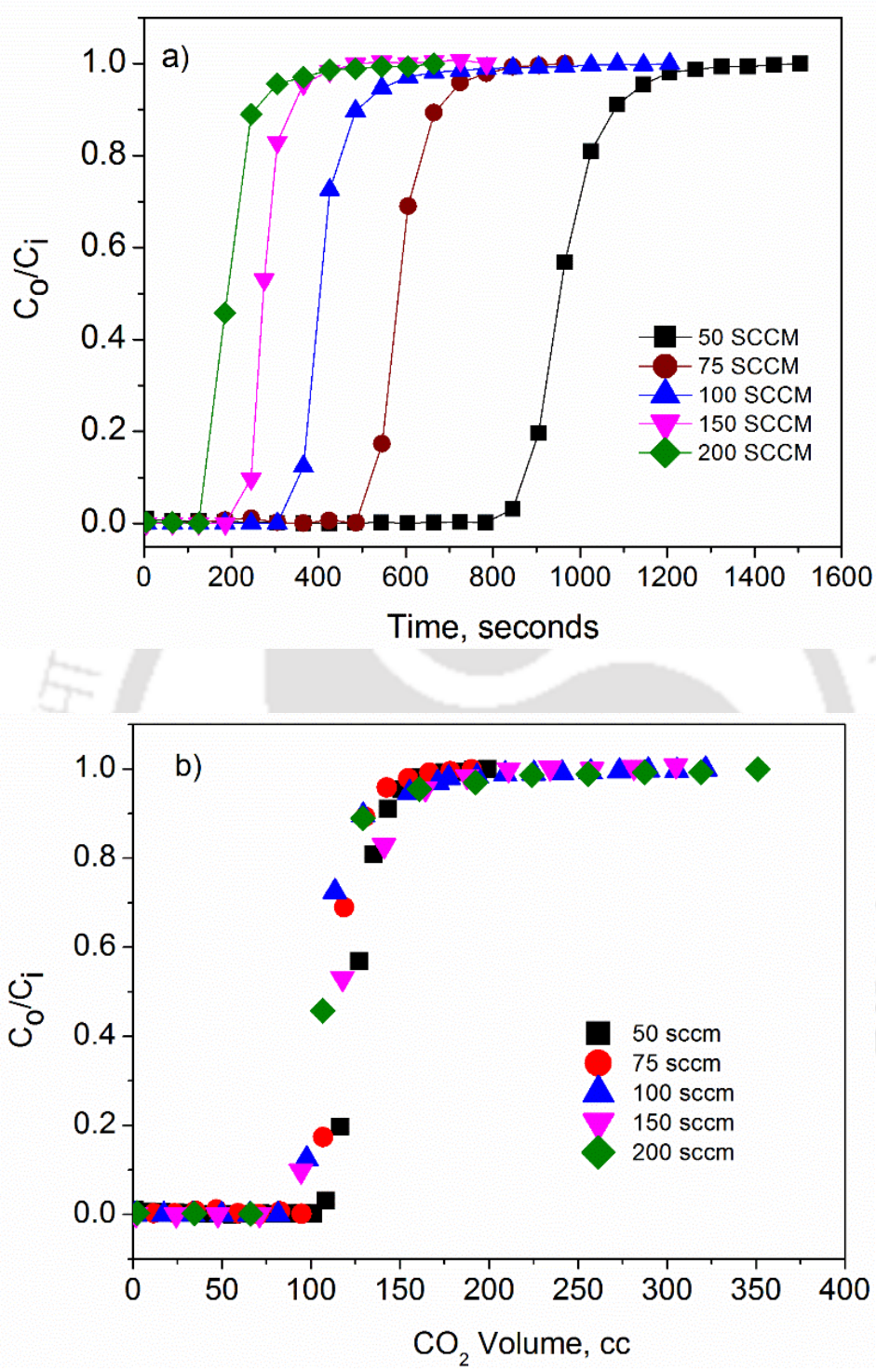

Figure 6.11: CO_2 breakthrough curves from binary mixture (CO_2/N_2:15/85) at different flow rates on PVA@ UiO-66 pellets at 300 K and 1.3 bar: Symbols are experimental data; lines are drawn as guide to eye.

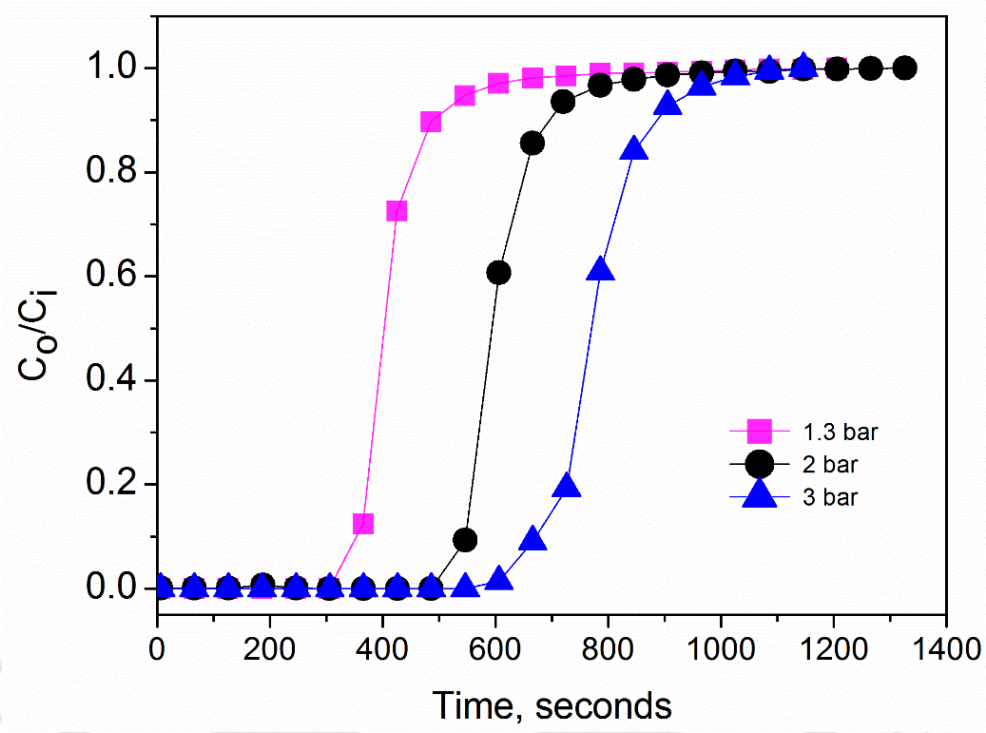

Figure 6.12: CO_2 breakthrough curves from binary mixture (CO_2/N_2:15/85) at different feed pressures on PVA@ UiO-66 pellets at 300 K and 100 SCCM: Symbols are experimental data; lines are drawn as guide to eye.

6.6 Single column PVSA experiments

The adsorbent process performance characteristics such as N_2 purity, CO_2 purity and CO_2 recovery are measured at cyclic steady state (CCS) condition. Various process cycle configurations were evaluated. Initially, a three step cycle with pressurization, feed, blow down was studied. Thereafter, N_2 purge step and heavy reflux steps (CO_2 rinse step) were also employed, to see their effect on the process performance. The sequence of cycle steps is shown schematically in Figure 6.13. All the cycle experiments are carried out at 300 K with 15% CO_2 in N_2 as feed mixture at a fixed feed flowrate of 100 SCCM. The feed pressurization and blowdown times were fixed at 80s and 10s respectively. Other process cycle step times viz. adsorption, rinse and purge were chosen based on the CO_2 breakthrough time (Table 6.4).

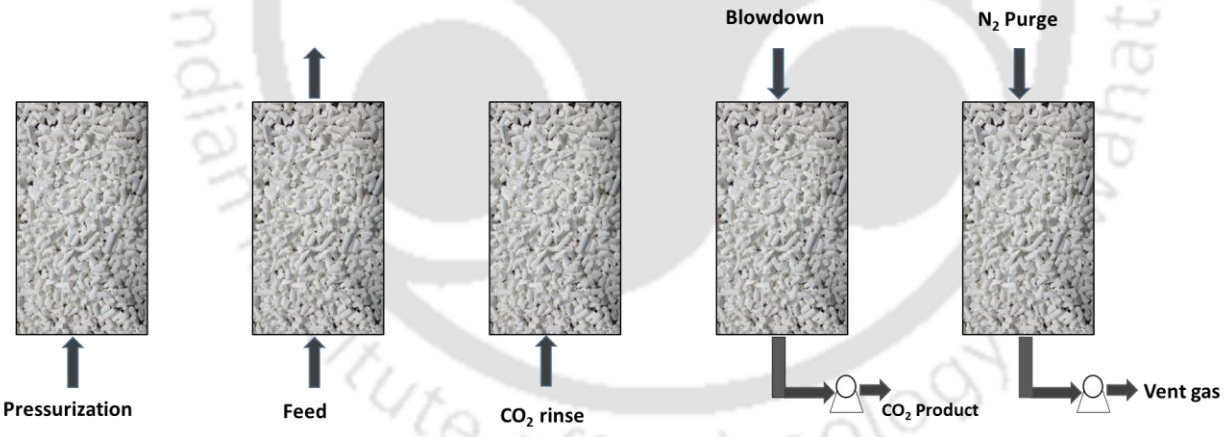

Figure 6.13: A Schematic diagram of PVSA cycle steps

Table 6.4: Duration of various steps used in the PVSA cycle

Step	Duration
Pressurization	80 seconds
Adsorption	40%, 60%, 80% of breakthrough time
Co-current rinse with heavy (CO_2) component	10%, 16%, 23% of breakthrough time
Blow down	10 seconds
Evacuation + purge with light (N_2) component	10%, 20%, 40% of breakthrough time

Feed composition: 15% CO_2, 85% N_2, Adsorption pressure: 1.3 bar, CO_2 Breakthrough time: 306s, Desorption pressure: 0.15 bar, Temperature: 300 K, Pressurization/feed/purge flow rate: 100 SCCM, CO_2 rinse flow rate: 50 SCCM.

In a typical experiment, the cyclic steady state (CSS) was achieved in about 20 cycles, ensured by a difference of less than 0.5% between the CO_2 purity/recovery obtained in consecutive cycles.

Figure 6.14 shows the effect of adsorption time on process performance of a three step PVSA cycle consists of feed pressurization to 1.3 bar, adsorption at 1.3 bar and blowdown to 0.1 bar. The feed flowrate was fixed at 100 SCCM and only the adsorption time was varied. With increase in adsorption time, the CO_2 product purity increased from 28.5% to 33.7% while the CO_2 product recovery and CO_2 productivity were decreased from 66.4% to 54.8% and 0.131 $kgCO_2/(kg_{ads}\cdot h)$ to 0.106 $kgCO_2/(kg_{ads}\cdot h)$ respectively. At an extended adsorption time (before breakthrough), more amount of CO_2 enters into the adsorbent bed to form a CO_2 saturated zone in larger proportion followed by a small N_2 rich zone. Thus, this results in increase of CO_2 product purity that was

obtained in the subsequent blowdown step. The decrease in CO_2 recovery observed is caused by the leakage of CO_2 into the column outlet stream during adsorption step at longer production step durations. All further process cycle experiments were carried out with adsorption step duration equal to 60 % of the break through time.

The best performance of the studied three-step (viz. pressurization, feed and blowdown) Skarstrom-type PVSA process was: CO_2 purity: 31.7%, CO_2 recovery: 59.4%, productivity: 0.117 $kgCO_2/(kg_{ads} \cdot h)$.

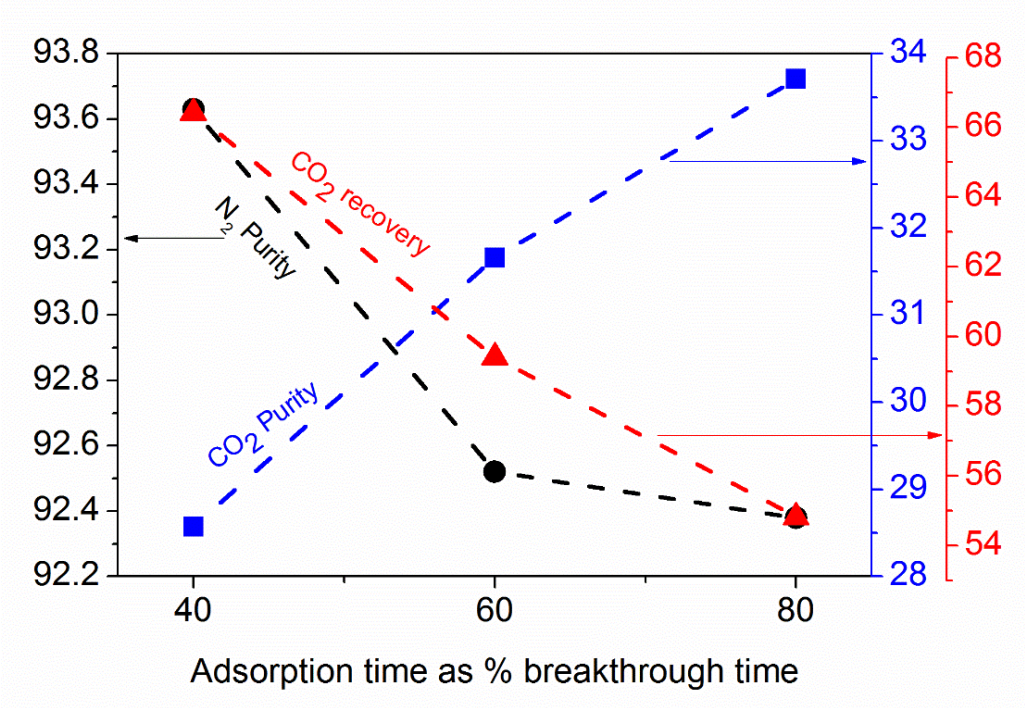

Figure 6.14: Effect of adsorption time on PVSA performance of PVA@UiO-66 pellets at 300 K. (CO_2 BT: 306 s; F_{PRES}= F_{FEED}=100 SCCM). Lines are drawn as guide to eye.

The effect of N_2 purge step time is shown in Figure 6.15. With the addition of a purge step, N_2 product purity increases from ~92.5% to ~99.9 % with a small reduction in CO_2 product purity and recovery. Purging the column before the next production steps removes any CO_2 left behind in the column thereby increasing the N_2 purity. The achieved 4-step PVSA process performance

was: CO_2 purity: 29.9%, CO_2 recovery: 56.0%, productivity: 0.077 $kgCO_2/(kg_{ads}\cdot h)$. The purity and productivity values were comparable to the experimentally studied Zeolite 13X performance by Dantas et al. [111]: CO_2 purity: 36.8%, CO_2 recovery: 90.0%, productivity: 0.0739 $kgCO_2/(kg_{ads}\cdot h)$ and simulated PVSA process performance of Zeolite 5A by Liu et al. [144]: CO_2 purity: 53.1%, CO_2 recovery: 91.0%, productivity: 0.0528 $kgCO_2/(kg_{ads}\cdot h)$.

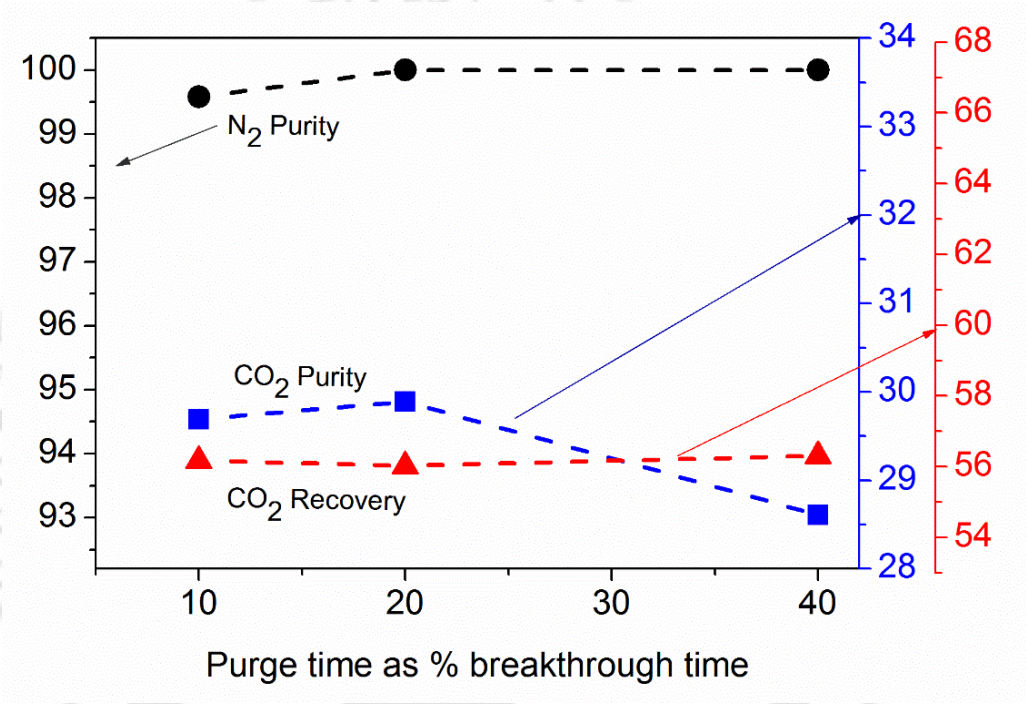

Figure 6.15: Effect of N_2 purge time on PVSA performance of PVA@UiO-66 pellets at 300 K. (CO_2 BT: 306 s; t_{FEED} = 183 s, $F_{PRES} = F_{FEED} = F_{PUR}$ =100 SCCM). Lines are drawn as guide to eye.

Figure 6.16 shows the effect of the addition of CO_2 rinse step. Due to the displacement of void fluid by pure CO_2 during the rinse step, a significant increase in CO_2 product purity (29.9% to 54.2%) is achieved.

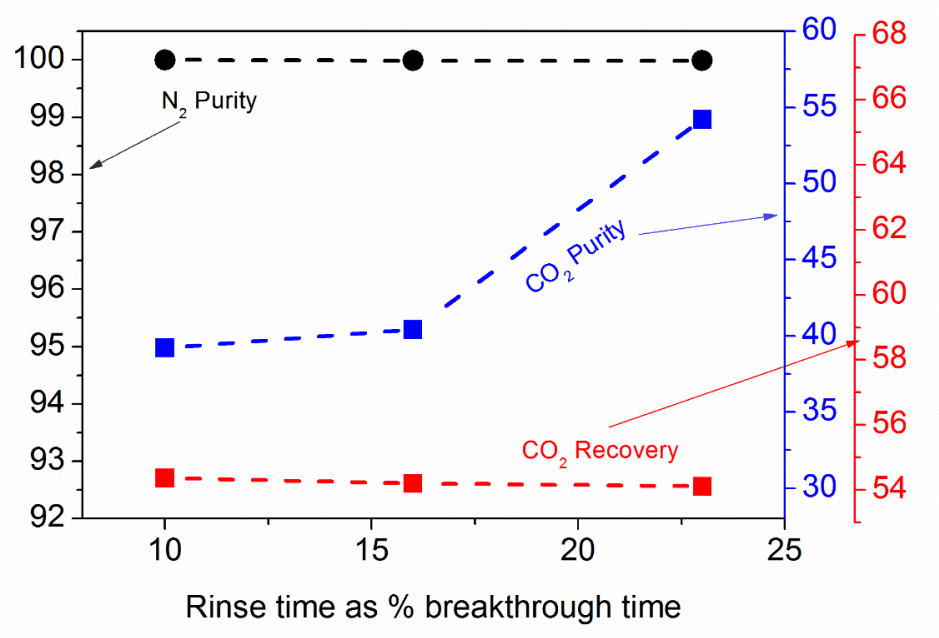

Figure 6.16: Effect of CO_2 rinse time on PVSA performance of PVA@UiO-66 pellets at 300 K. (CO_2 BT: 306 s; t_{FEED} = 183 s, t_{PUR}= 60 s, $F_{PRES} = F_{FEED} = F_{PUR}$ = 100 SCCM, F_{RIN} = 50 SCCM). Lines are drawn as guide to eye.

The evaluated overall process performance of 5-step (pressurization, feed, rinse, blowdown and purge) PVSA cycle at 300 K and 1.3 bar was: CO_2 purity: 54.2%: CO_2 recovery: 54.1%: productivity: 0.075 $kgCO_2/(kg_{ads}\cdot h)$. To the best of our knowledge, a few literature is available on PVSA performance of metal organic frameworks for CO_2/N_2 separation. Andersen et al. [110] claim a CO_2 purity of 61% and a CO_2 recovery of 65% on UiO-66/alginate beads at 328 K and 2 bar pressure. Dasgupta et al. [9] obtained a CO_2 purity ranging between 60% to 70% and a CO_2 recovery ranging between 62% to 64% using Cu-BTC metal organic framework at 308 K and 2 bar pressure. The results obtained with single column PVSA look promising. More detailed research is needed with multiple beds as well as the improvement and optimization of the process cycles.

CHAPTER 7

CO_2/N_2 SEPARATION PERFORMANCE ANALYSIS OF OPEN METAL SITE MOF MIL-101(Cr)

In this chapter, the open metal site MOF MIL-101(Cr) or Cr-BDC was investigated for CO_2/N_2 separation. A fluoride free scale up synthesis was adopted and about 20 g of the material is first synthesized in powder form; pellets were made subsequently using polyvinyl alcohol as the binder. The effect of binder on physical structure and equilibrium adsorption capacity of the material are discussed. The binary breakthrough experiments and process cycle studies are performed on the formulated pellets.

7.1 Scale up synthesis

MIL-101(Cr) (or Cr-BDC) was synthesized in 1 g level according to the procedure given by Férey et al. [64] as described in section 4.1.3. The obtained product showed a BET surface area of 2722 m^2 g^{-1} which was comparable to the reported literature values [145, 146]. To perform process experiments, we need a minimum of 10 g adsorbent pellets to fill the column. Hence, the scale up synthesis of adsorbent materials attempted using a designed 500 ml capacity Teflon lined stainless steel autoclave reactor (section 4.1). In scale up synthesis, following the Férey et al. [64]. procedure, the product yielded showed a BET surface area of 1200 m^2 g^{1}, which was very less when compared to the small scale synthesized product value of 2722 m^2 g^{-1}. The quantity of

hydrofluoric acid used as promotor during the large scale synthesis may be effecting the MOF synthesis. Hence, a fluoride free and large scale synthesis of Cr-BDC reported by Zhou et. al. [121] was adopted. The synthesis was carried out using 16 ml and 500 ml autoclave reactors (see table 7.1). The obtained products showed BET surface areas of 3100 $m^2 g^{-1}$ and 2690 $m^2 g^{-1}$ respectively with higher product yields compared to the standard HF synthesis. The repeatability check of the large scale HF free synthesis was also attempted in four batches and products obtained showed BET surface areas close to 2700 $m^2 g^{-1}$. This scale up HF free synthesized MIL-101(Cr)sample was used in the present work.

Table 7.1 BET Surface area of synthesized materials using 16 ml and 500 ml capacity autoclave reactor

Reactor capacity(ml)/solvent	Surface Area ($m^2 g^{-1}$)	Yield (%)
16/HF	2722	50
500/HF	1200	50
16/HNO_3	3100	68
500/HNO_3	2690	65

7.2 Pellet preparation

PVA@MIL-101 pellets were prepared according to the procedure suggested by Fisny et al. [108] using PVA as binder. MOF powder, 15 wt% PVA/H_2O and sufficient amount of water were mixed and shaped into 1-2 mm diameter of MOF/PVA cylindrical pellets using a 6 ml syringe. The obtained pellets were heated at 0.5 ^oC/min to reach 180 ^oC and kept at this temperature for 6 hours. The ratio of MOF powder to binder was varied to optimize the pellet preparation. The photographs and scanning electron microscopy images of the synthesized powder and 41PVA@MIL-101 are

shown in Figure 7.1. Table 7.2 shows the experimental conditions used for the pellet preparation. The final pellets are denoted as 33PVA@MIL-101, 41PVA@MIL-101 and 50PVA@MIL-101 corresponding to the initial weight percent of PVA/H_2O (Table 7.2).

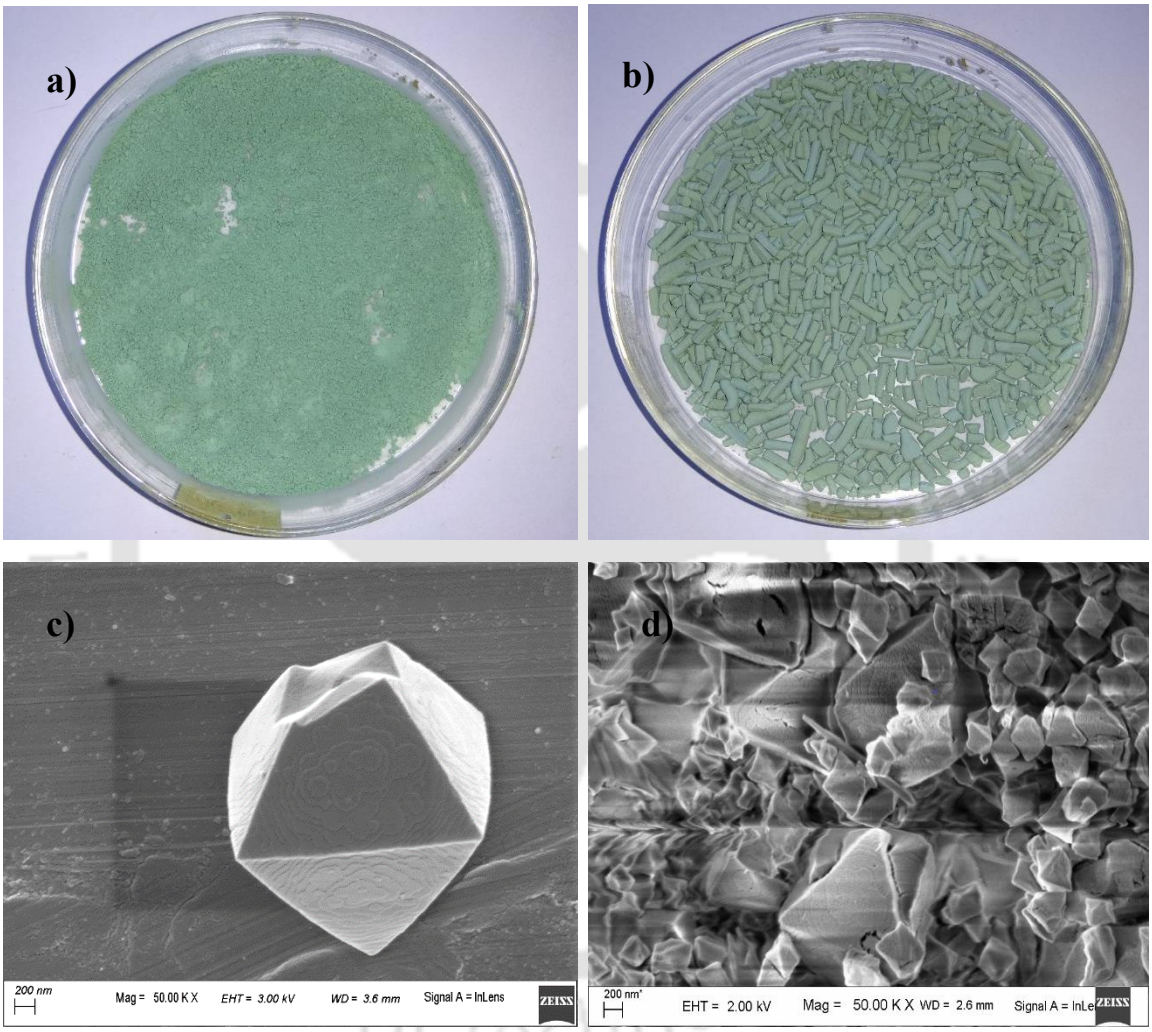

Figure. 7.1: Images (a) MIL-101(Cr) powder, (b) 41PVA@ MIL-101(Cr) pellets FESEM images (c) MIL-101(Cr) powder, (d) 41PVA@ MIL-101(Cr) pellets.

.

Table 7.2: Experimental conditions and properties of the formulated MIL-101 pellets.

Sample	Mass of MOF (g)	Mass of 15wt% PVA/water (g)	water (g)	BET Surface area (m^2g^{-1})	Pore volume (cc/g)	Bulk density (g/cc)
MIL-101	--	--	--	2690	1.62	0.25
33PVA@MIL-101	1.0	0.50	0.5-1	2228	1.59	---
41PVA@MIL-101	1.0	0.70	0.5-1	2050	1.49	0.31
50PVA@MIL-101	1.0	1.0	0.5-1	1622	1.22	---

7.3 Characterization

7.3.1 Surface Area and Pore Volume Analysis

The experimental conditions and properties of the formulated PVA@MIL-101 pellets are given in Table 7.2. The N_2 physisorption isotherms (Figure. 7.2) of powder and shaped pellets at 77 K are of type I isotherm, indicating the structures with micro pores. The calculated BET specific surface area of MIL-101 is 2690 m^2/g and is comparable to the reported value of 2549 m^2/g by Ye et al. [145] and slightly higher than the value reported by munusamy et al. [146]. Compared to the powder sample, a 17-39% decrease in BET surface area of prepared pellets was observed. The textual characterization results illustrate that with increase in binder content, a significant decrease in BET surface area and pore volume occurs, which was corresponding to the amount of binder used and the partial structural degradation that may occurred during the pelletization process.

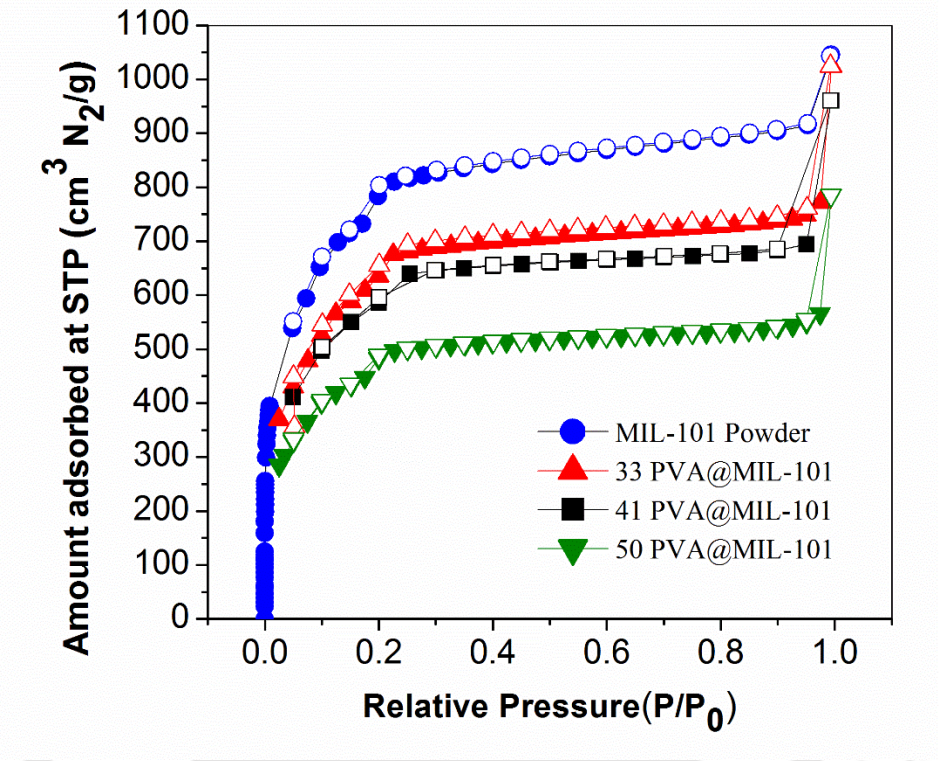

Figure 7.2: N_2 physisorption isotherms of MIL-101 powder and PVA@MIL-101 pellets at 77 K: Adsorption (filled symbols), Desorption (open symbols).

7.3.2 Drop test

The mechanical stability of prepared MOF pellets was tested by performing drop test. following the procedure by Kawatra et. al. [124], 30 number of dried pellets were dropped repeatedly on to a stainless steel plate from a height of 0.5 m. The number of broken pellets were recorded. Figure 7.3 shows the results of drop test. 33PVA@MIL-101 pellets were stable up to 80 drops and beyond that they started to break and at 130 drops about 23% pellets were broken. 41PVA@MIL-101 and 50PVA@MIL-101 pellets shown 0% breakage up to 130 drops.

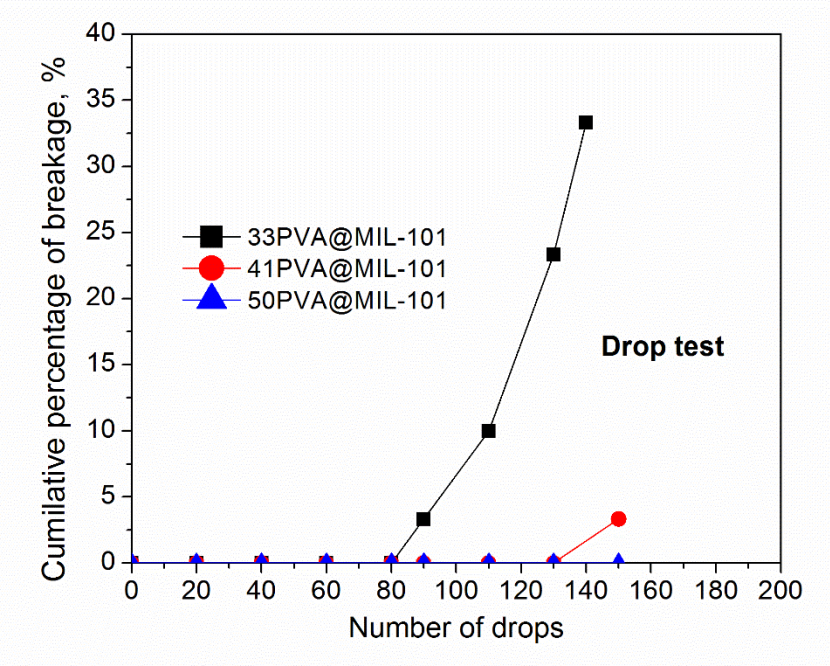

Figure 7.3: Drop test results for shaped 41PVA@MIL-101 pellets.

Based on the drop test results and surface area analysis 41PVA@MIL-101 pellets were used for further studies and from here onwards, the term pellet refers to 41PVA@MIL-101 sample.

7.3.3 Thermogravimetric Analysis

Figure 7.4 shows the obtained TG and DTG curves of powder, pellet and pure PVA samples. The initial weight loss at around 100 ^{o}C is due to moisture removal from the materials. The TG curve of pellet sample has an additional weight loss around 200 ^{o}C, which was correspond to the decomposition of PVA in the pellet. At temperatures higher than 350 ^{o}C, powder and pellet samples degraded due to the decomposition of organic linker. From the TG curves, the calculated binder content in pellets was about 5%. The TG curve suggests that MIL-101(Cr) powder was stable up to 350 ^{o}C and MIL-101 pellets were stable up to 200 ^{o}C.

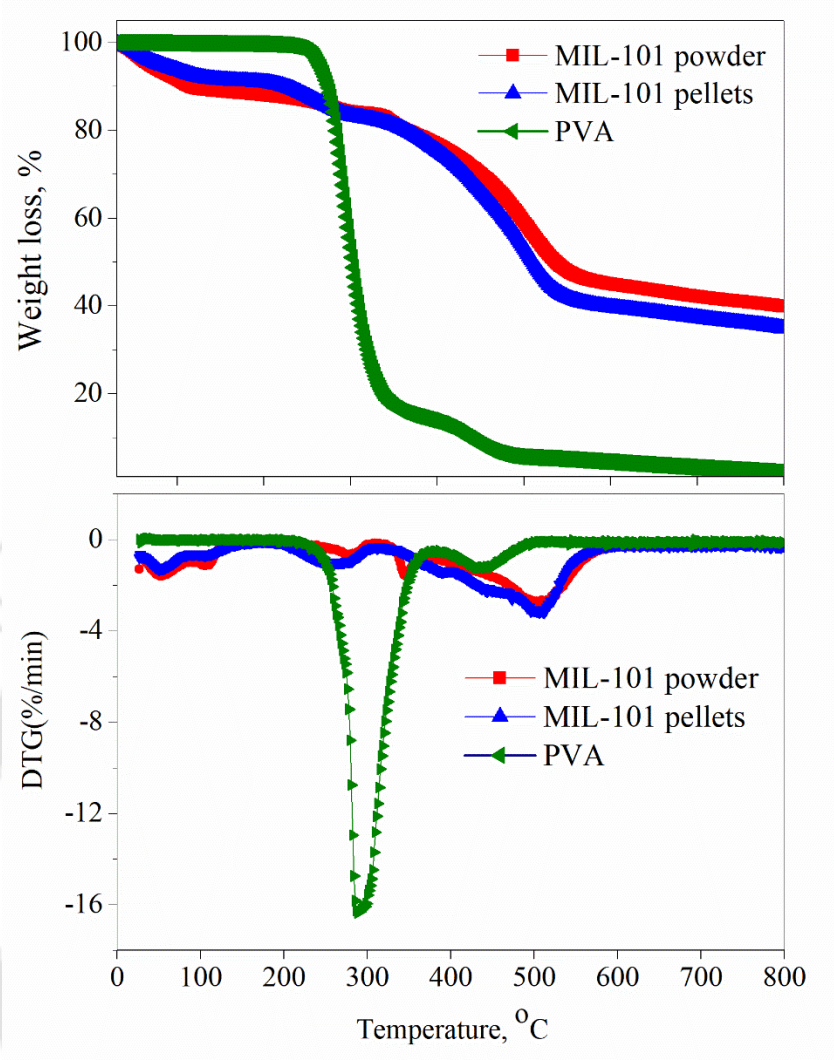

Figure 7.4: Thermogravimetry (TG) and differential thermogravimetry (DTG) curves of MIL-101 powder, 41PVA@MIL-101 pellets and pure PVA samples.

7.3.4 FTIR Analysis

The FT-IR spectra of PVA, MOF powder and pellets are given in **Figure. 7. 5**. The broad bond centered at 3400 cm^{-1} can be assigned to hydrogen bonded adsorbed water [130]. The two peaks appeared in PVA at 2940 and 2850 cm^{-1} are the characteristic bonds of asymmetric and symmetric C-H stretching respectively [131]. The peaks appeared in the spectra of MOF powder and MOF pellet samples at 1570 cm^{-1} and 1350 cm^{-1} correspond to stretching vibrational bonds of C=O and C=C

respectively. The vibration at 750 cm^{-1} is attributed to the Cr-O stretching because of the coordination of an oxygen atom with Cr.

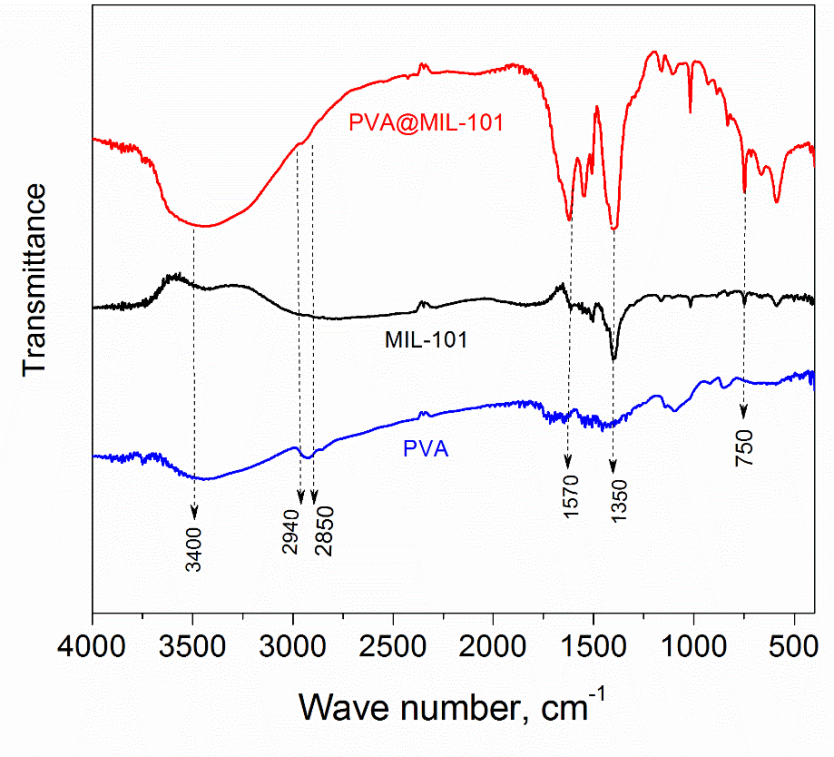

Figure 7.5: FTIR spectra of PVA, MIL-101 powder and 41PVA@MIL-101 pellets.

7.3.5 XRD Analysis

The X-ray diffraction patterns of synthesized MIL-101 powder is in good agreement with the published literature data [146]. The XRD patterns of powder and pellet samples are shown in in Figure 7.6. The observed identical patterns, indicating the crystal structure of the MIL-101 remained intact after pelletization.

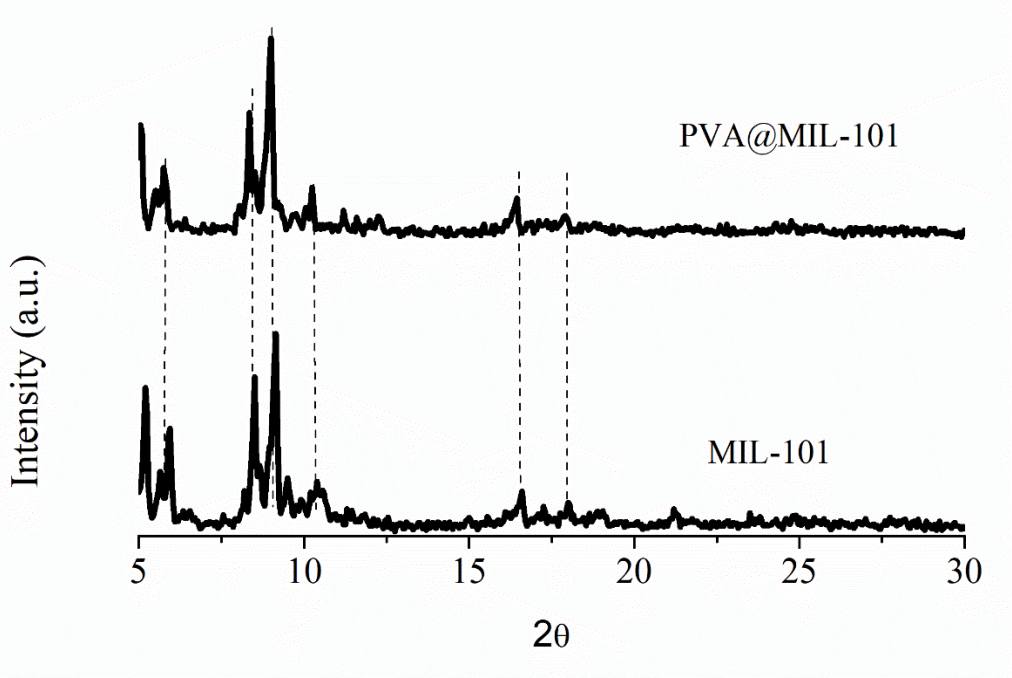

Figure 7.6: XRD patterns of MIL-101 powder and 41PVA@MIL-101 pellets.

7.4 Single Component equilibrium adsorption isotherms

Pure component adsorption equilibrium isotherms of CO_2, N_2 on MIL-101 were measured using iSorb-HP high pressure gas adsorption analyzer at three different temperatures 298 K, 318 K and 348 K. The adsorption isotherms are shown in the Figures 7.7 (a-b). The CO_2, N_2 adsorption isotherms were well described by the virial isotherm model (the Langmuir isotherm model is not sufficient to account the heterogeneity in MIL-101 adsorbent). The model fit parameters are given in Table 7.3. The loading for CO_2 at 298 K and 1 bar on MIL-101 powder, measured in this work is 1.5 mmol/g, which is higher than that on MOFs like MOF-2, MOF-177, MOF-5, IRMOF-6 and IRMOF-3. However, this CO_2 loading is lower when compared to Mg/DOBDC, Cu-BTC, Zeolite 13X, MIL-53(Al) and Zn/DABCO [Table 2.1 in chapter 2].

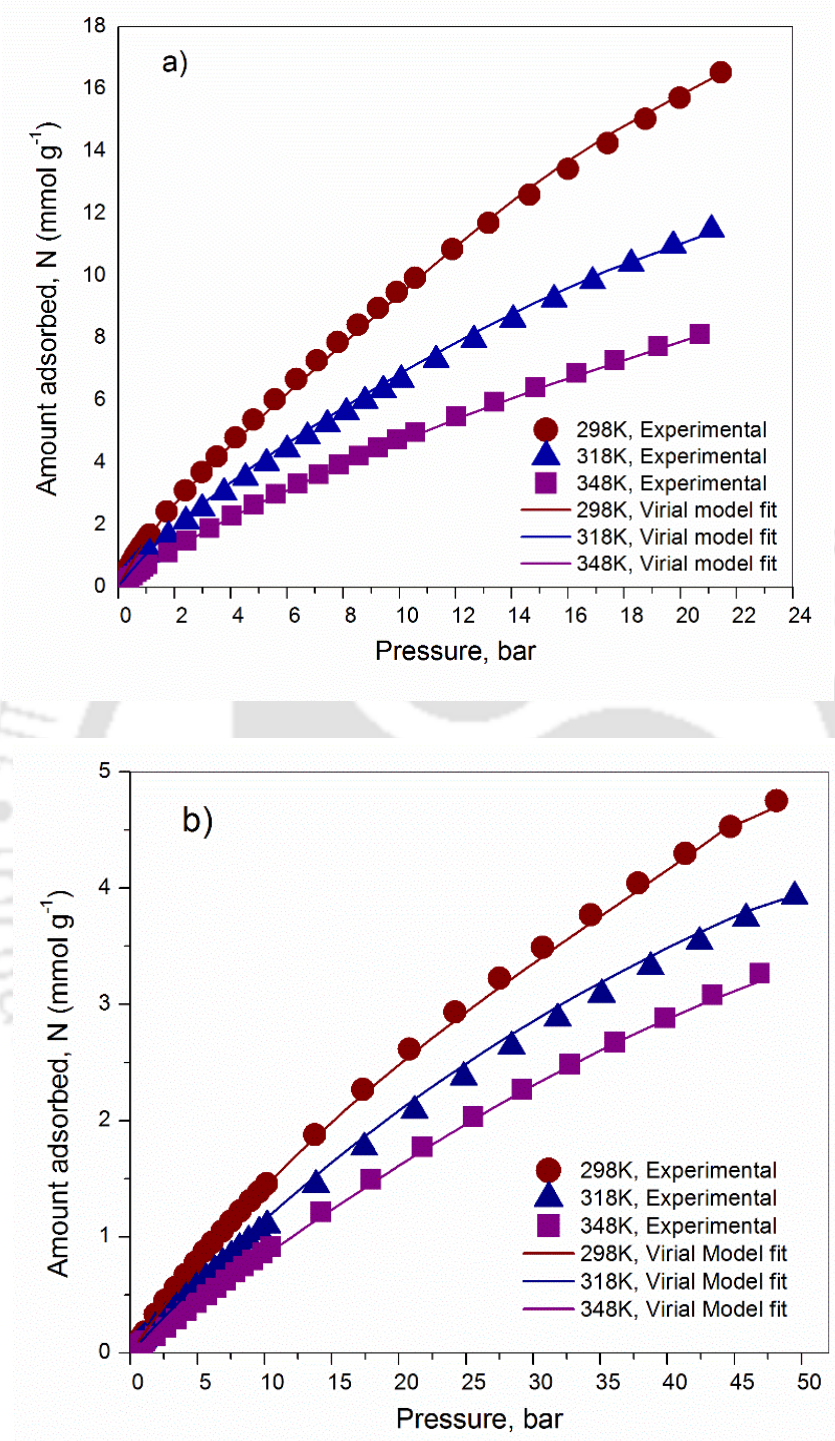

Figure 7.7: Isotherms on MIL-101 powder **(a)** CO_2 and **(b)** N_2. Lines are fits using model

Table 7.3: Virial model parameters for CO_2 and N_2 on MIL-101 powder

Parameters	Adsorbates	
	CO_2	N_2
β_0, mol kg^{-1} bar^{-1}	5.97	6.22
β_1, K	1965	1318
b_0, mol^{-1} kg	0.091	0.081
b_1, mol^{-1} kg K	21.35	-0.413
c_0, mol^{-2} kg^2	-0.037	-0.379
c_1, mol^{-2} kg^2 K	7.048	119.59
d_0, mol^{-2} kg^2	0.004	0.094
d_1, mol^{-2} kg^2 K	-1.10	-29.398

The enthalpy of adsorption for CO_2 and N_2 is calculated using model fit parameters**.** The calculated enthalpy of adsorption at zero coverage on MIL-101 is -31 kJ/mol. This value is lower than that on MOFs like MIL-100 (-62 kJ/mol) [139], Ni/DOBDC (-36 kJ/mol) [140], Cu-BTC (-23 kJ/mol) [135] and zeolites like 13X (-49 kJ/mol) [136]. The value of enthalpy of adsorption of N_2 on MIL-101 at zero loading is - 10 kJ/mol which is comparable to the IRMOF-1(-8.3 kJ/mol) [141], IRMOF-3(-9 kJ/mol) [133], Zn/DABCO (-11 kJ/mol) [138] and MOF-177(-10 kJ/mol) [142] and lower than that on Mg/DOBDC (-18 kJ/mol) [96], MIL-53(Al) (-15.9 kJ/mol) [137], and on silicalite (-16.7 kJ/mol) [143].

Figures 7.8 (a-b) shows the effect of pellatization on adsorption properties of MIL-101. Figure 7.8a compares the CO_2 adsorption isotherms at 298K for powder and pellet in terms of amount adsorbed per gram of adsorbent. About 13% reduction in CO_2 loadings were observed for pellets compared to powder sample. The volume of the adsorbent needed to pack inside an adsorber is

also an important factor while designing any adsorption based process. So, the packing densities of powder and pellets were measured and the values are 0.251, 0.313 g cc^{-1} respectively. Figure 7.8b shows the adsorption isotherms in terms of volume of adsorbent. In this case, higher loadings were observed for pellets due to the higher packing density of pellets.

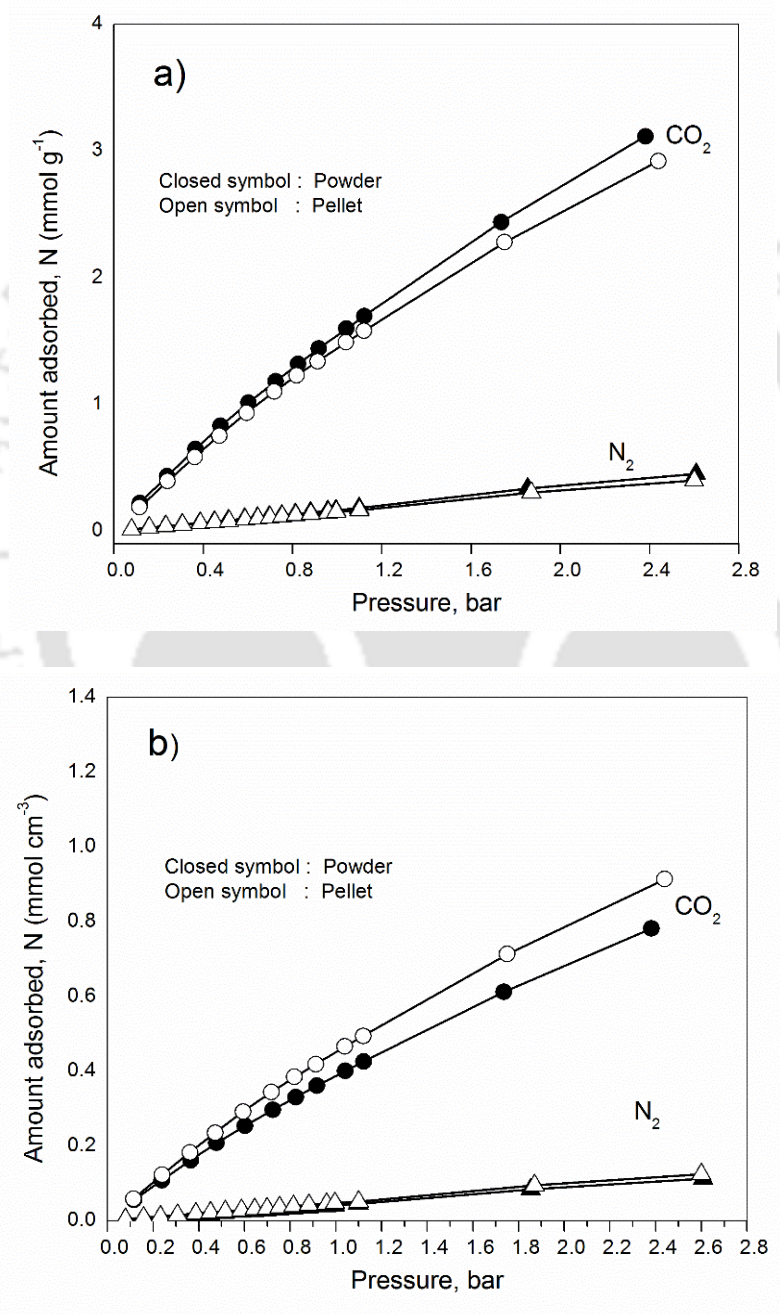

Figure 7.8: Adsorption isotherms at 298 K on powder and pellets a) amount adsorbed per gram

b) amount adsorbed per cm^3

7.5 CO_2/N_2 separation: Binary breakthrough experiments

The experimental set up used in UiO-66 process experiments was used without any further modifications. The adsorbent column was filled with 8 g of activated 41PVA@MIL-101 pellets. Properties of the column and breakthrough experimental conditions were given in Table 7.4. The adsorbent bed was pretreated under N_2 purge of 60 SCCM at 423 K for 6 h. After the initial activation, fixed bed column was allowed to reach the experimental temperature (i.e. 300 K). Prior to each breakthrough experiment, the adsorbent bed was activated and equilibrated with helium gas for 10 min at 1.3 bar. In the present work, during the breakthrough experiments, the column outlet gas composition was measured using a CO_2 gas analyzer.

Table 7.4: Properties of the fixed bed column and experimental conditions for breakthrough studies

Mass of adsorbent pellets (activated), g	8.0
Feed concentration, mol%	~15 % CO_2 balance N_2
Temperature, K	300
Feed flow rate, SCCM	75 – 200
Feed gas pressure, bar	1.3
Column length, mm	300
Column internal diameter, mm	10
Column Initial Condition	Filled with 1 bar He

Figure 7.9a shows the breakthrough curves of CO_2 in feed at different feed flow rates. As can be seen, the breakthrough times are decrease with increase in feed flow rate. Figure 7.9b is generated using the cumulative gas as abscissa (instead of time). The overlap of the curves at different flow rates suggests that negligible gas phase mass transfer resistance.

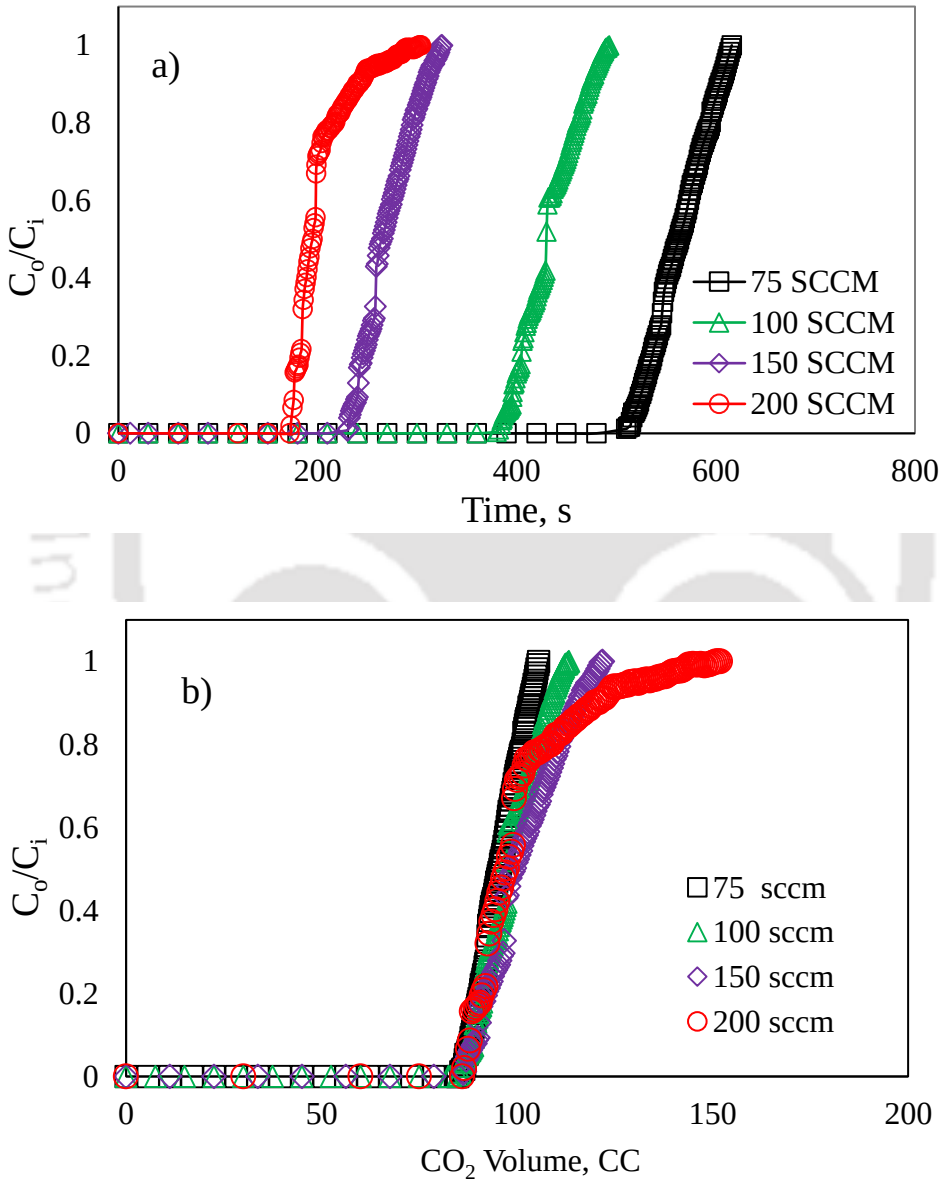

Figure 7.9: CO_2 breakthrough curves from binary mixture (CO_2/N_2:15/85) at different flow rates on 41PVA@ MIL-101 pellets at 300 K and 1.3 bar.

The measured breakthrough curves at different column pressures are given in Figure 7.10. As expected, the breakthrough time increases with increase in column pressure, since the adsorbent capacity is higher.

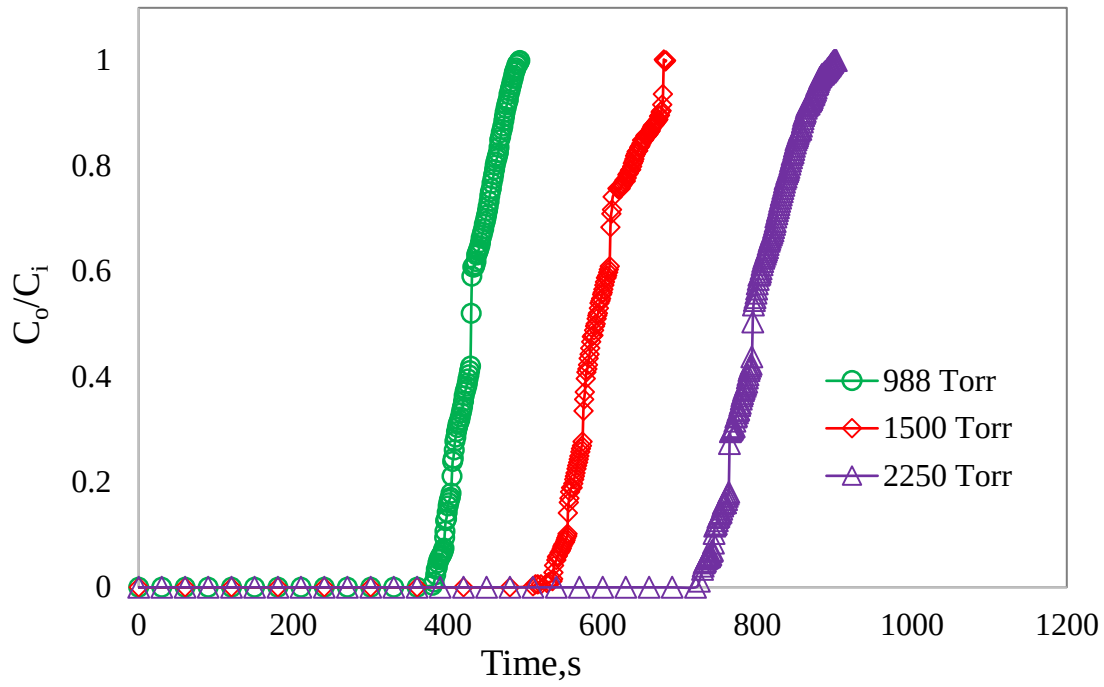

Figure 7.10: CO_2 breakthrough curves from binary mixture (CO_2/N_2:15/85) at different column pressures on 41PVA@ MIL-101 pellets at 300 K and 100 SCCM feed flow rate.

7.6 Single column PVSA experiments

A three step PVSA cycle consist of feed pressurization to 1.3 bar, adsorption at 1.3 bar and counter current blowdown to 0.1 bar was evaluated. Thereafter, N_2 purge step and heavy reflux steps (CO_2 rinse step) are also employed to see their effect on the process parameters. The cycle experiments have been carried out on 41PVA@MIL-101 pellets with feed mixture of about 15% CO_2 in nitrogen at a fixed flow rate of 200 SCCM and 1.3 bar pressure. From the breakthrough experiments, the observed

CO_2 breakthrough time at these experimental condition is 172 seconds. The cycle step times were chosen based on the breakthrough time except for the feed pressurization time fixed at 35 seconds (pressurization time taken to reach the column pressure of 1.3 bar at 200 SCCM). The configuration of cycle step times was shown in Table 7.5. In a typical experiment, the cyclic steady state (CSS) was achieved in about 20 no of cycles at which the difference between the CO_2 purity/recovery obtained in consecutive cycles is less than 0.5%.

Table 7.5: Configuration of PVSA cycle step times

Step	Duration
Pressurization	35 seconds
Adsorption	40%, 60%, 80% of breakthrough time
Co-current rinse with heavy (CO_2) component	7%, 15%, 30% of breakthrough time
Blow down	10 seconds
Evacuation + purge with light (N_2) component	17%, 35%, 70% of breakthrough time

Feed composition: 15% CO_2, 85% N_2, Adsorption pressure: 1.3 bar, CO_2 BT: 172 seconds, Desorption pressure: 0.15 bar, Temperature: 300 K, Pressurization flow rate: 200 SCCM, Feed flow rate: 200 SCCM, N_2 purge flow rate: 100 SCCM, Rinse flow rate: 50 SCCM.

Figure 7.11 shows the effect of adsorption time on PVSA performance of PVA@MIL-101 pellets. With increase in adsorption time, the CO_2 product purity increased from 27.9% to 34.4% while the CO_2 recovery and productivity were decreased from 61.9% to 53.6% and 0.293 $kgCO_2/(kg_{ads}\cdot h)$ to 0.243 $kgCO_2/(kg_{ads}\cdot h)$ respectively. The results indicate that with increase in adsorption time, the CO_2

purity was increases due to the progress of CO_2 mass transfer front into the adsorbent bed, and there replaces N_2, however, the recovery decreases due to the stronger adsorption of CO_2.

The best performance of the studied 3-step (viz. pressurization, feed and blowdown) PVSA process was: CO_2 purity: 33.3%, CO_2 recovery: 56.7%, productivity 0.265 $kgCO_2/(kg_{ads}\cdot h)$. These values are achieved at 60% adsorption time as breakthrough time for MIL-101 material. Thus, 60% adsorption time as breakthrough time was chosen for all further cyclic experiments.

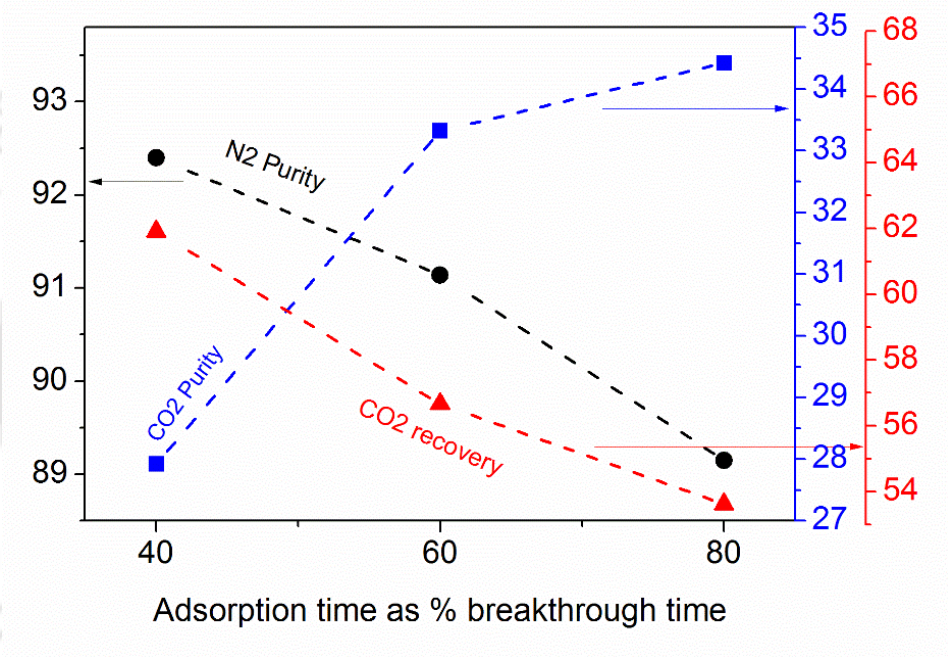

Figure 7.11: Effect of adsorption time on PVSA performance of PVA@MIL-101 pellets at 300 K. (CO_2 BT: 172 s; F_{PRES}= F_{FEED}=200 SCCM). Lines are drawn as guide to eye.

In the next set of experiments, the effect of N_2 purge along with evacuation studied. N_2 purge flow rate was fixed at 100 SCCM and purge time was varied as a fraction of CO_2 breakthrough time. The results obtained can be seen in Figure 7.12. N_2 product purity was increased from 89.1 % to 99.9% with the inclusion of purge step.

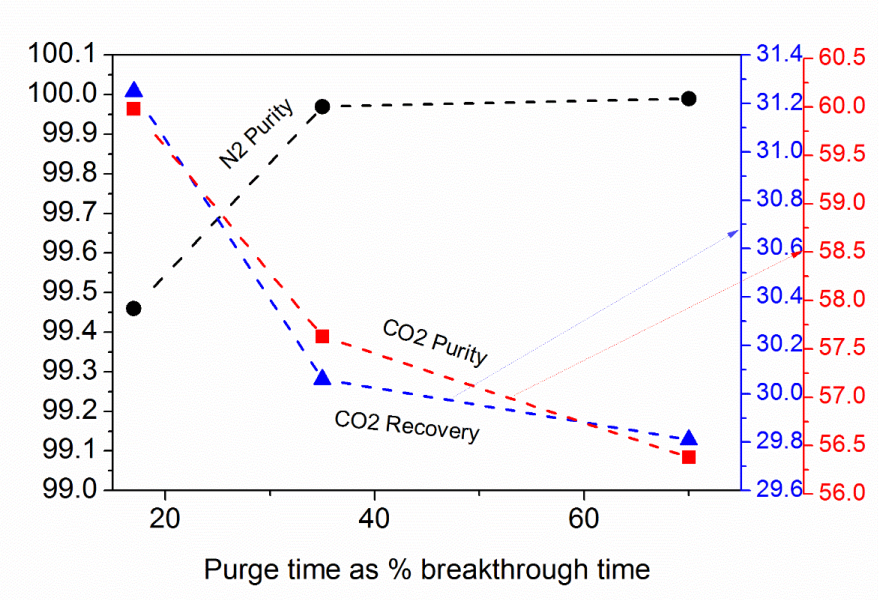

Figure 7.12: Effect of purge time on PVSA performance of PVA@MIL-101 pellets at 300 K. (CO_2 BT: 172 s; t_{FEED} = 103 s, F_{PRES} = F_{FEED} = 200 SCCM, F_{PUR} =100 SCCM). Lines are drawn as guide to eye.

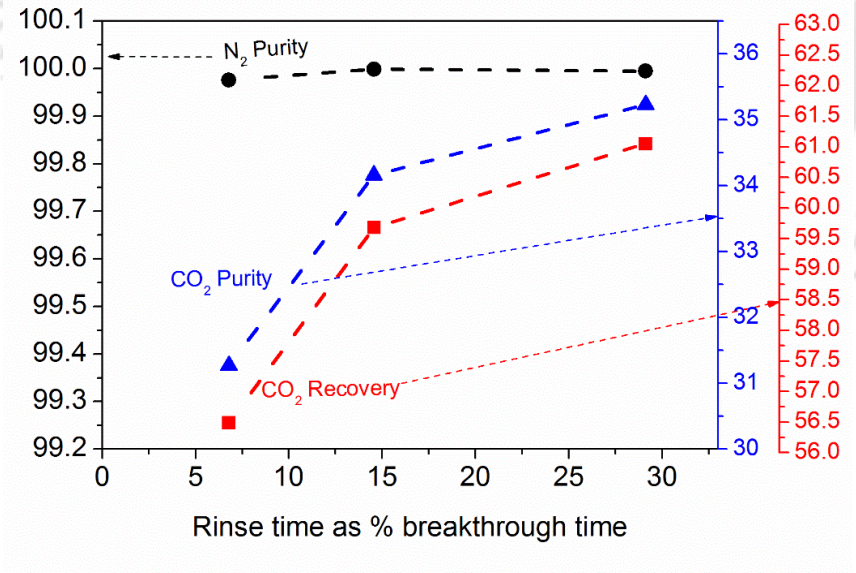

Figure 7.13: Effect of CO_2 rinse time on PVSA performance of PVA@MIL-101 pellets at 300 K. (CO_2 BT: 172 s; t_{FEED} = 103 s, t_{PUR}= 60 s, F_{PRES} = F_{FEED} = 200 SCCM, F_{PUR} =100 SCCM, F_{RIN} = 50 SCCM). Lines are drawn as guide to eye.

Figure 7.13 shows the effect of the addition of CO_2 rinse step. The inclusion of rinse step resulted in a slight increase in CO_2 product purity from 30.0% to 35.2%. The evaluated overall process performance of 5-step (pressurization, feed, rinse, blowdown and purge) PVSA cycle at 300 K and 1.3 bar was: CO_2 purity: 35.2%, CO_2 recovery: 61.1%, productivity: 0.269 $kgCO_2/(kg_{ads} \cdot h)$. The achieved CO_2 purity value was much lower compared to that on PVA@UiO-66 pellets (54.2%), whereas the CO_2 recovery and productivity are slightly higher compared to that on PVA@UiO-66 pellets (54.1% & 0.075 $kgCO_2/(kg_{ads} \cdot h)$).

CHAPTER 8

CO_2/N_2 SEPARATION PERFORMANCE ANALYSIS OF OPEN METAL SITE MOF Cu-BTC

In this chapter, the open metal site MOF Cu-BTC was evaluated for CO_2/N_2 separation. The synthesis procedure was scaled up to yield ca. 20 g Cu-BTC. Pellets with different binder content were made subsequently using polyvinyl alcohol. The effect of binder on the MOF structure and equilibrium adsorption capacity of the material are discussed. The results of the binary breakthrough experiments and process cycle performed on the pellets are presented

8.1 Scale up synthesis

Cu-BTC was synthesized according to the procedure suggested by Liu et al. [120] in 20 g level as described in section 4.1.2. The obtained product showed a BET surface area of 1476 $m^2 g^{-1}$ which was matches well with the reported value of 1482 $m^2 g^{-1}$ by Liu et al [120].

8.2 Pellet preparation

PVA@Cu-BTC pellets were prepared following the procedure suggested by Fisny et al. [108] using PVA as binder. Cu-BTC powder, 15 wt% PVA/H_2O and a few drops of water were mixed and manually shaped into 2-3 mm diameter of PVA@MOF beads. The obtained pellets were heated at 0.5 ^oC/min to reach 180 ^oC and kept at this temperature for 6 hours. The ratio of MOF

powder to binder was varied to optimize the pellet preparation. Table 8.1 shows the experimental conditions used for the pellet preparation. The final pellets are denoted as 25PVA@Cu-BTC, 33PVA@Cu-BTC and 43PVA@Cu-BTC corresponding to the initial weight percent of PVA/H_2O (see Table 8.1). The photographs of the synthesized Cu-BTC MOF powder and formulated PVA@Cu-BTC beads are shown in Figure 8.1. The beads are made into fractions manually for column studies.

Table 8.1: Experimental conditions and properties of the formulated Cu-BTC pellets

Sample	Mass of MOF (g)	Mass of 15wt% PVA/water (g)	Mass of water (g)	BET Surface area (m^2g^{-1})	Pore volume (cc/g)	Bulk density (g/cc)
Cu-BTC powder	--	--	--	1476	0.75	0.27
25PVA@Cu-BTC	0.300	0.100	0.5-1.0	1336	0.71	-
33PVA@ Cu-BTC	0.300	0.150	0.5-1.0	1257	0.65	0.34
43PVA@ Cu-BTC	0.300	0.225	0.5-1.0	1016	0.53	-

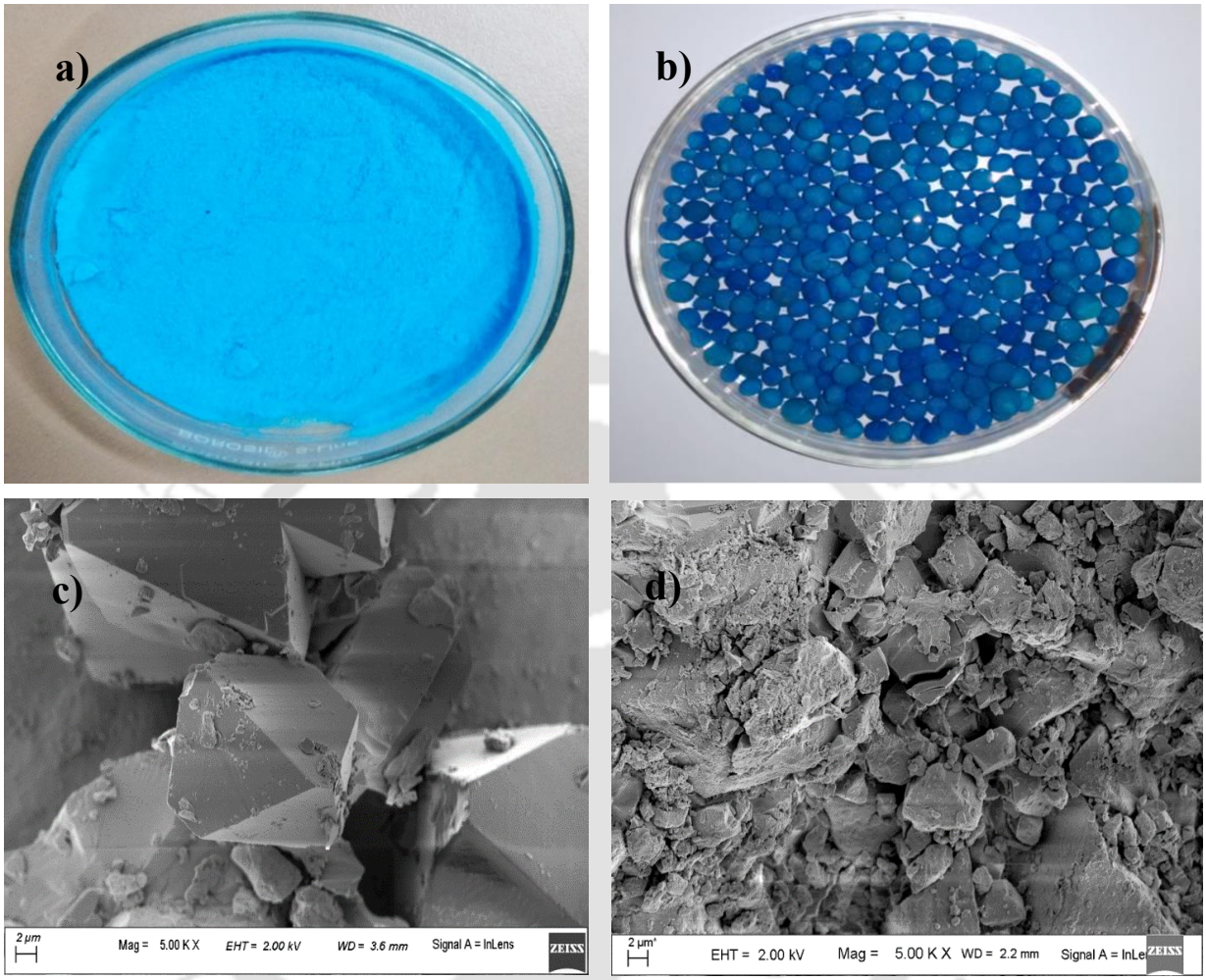

Figure 8.1: Images (a) Cu-BTC powder, (b) 33PVA@ Cu-BTC beads

FESEM images (c) Cu-BTC powder, (d) 33PVA@ Cu-BTC beads.

8.3 Characterization

8.3.1 Surface Area and Pore Volume Analysis

The textural properties of synthesized Cu-BTC powder and formulated PVA@Cu-BTC MOF beads were analyzed by N_2 physisorption isotherms measured at 77 K and results are shown in Figure 8.2. The Cu-BTC powder showed a BET surface area of 1476 $m^2 g^{-1}$ which was comparable to the literature reported values of 1482 $m^2 g^{-1}$ by Liu et al [120], 1507 $m^2 g^{-1}$ by Al-Janabi et al [147] and 1482 $m^2 g^{-1}$ by Pradip et al. [43]. The surface area and pore volume were decrease with the increase in the binder content. About 10 - 31 % decrease in surface area and pore volume was observed for the formulated beads compared to the powder sample.

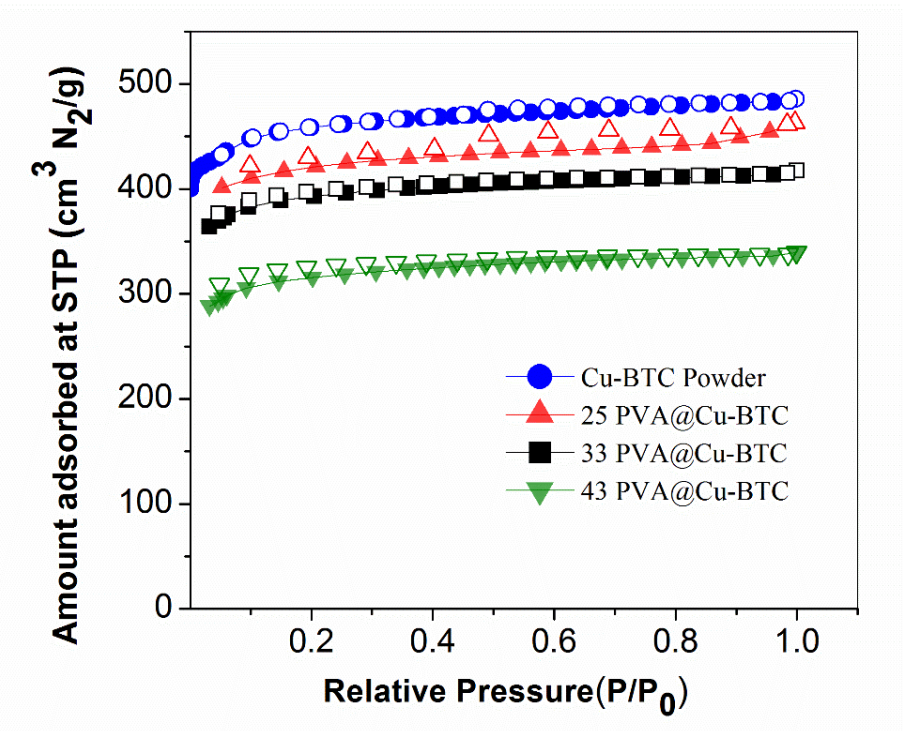

Figure 8.2: N_2 physisorption isotherms of Cu-BTC powder and PVA@Cu-BTC pellets at 77 K: Adsorption (filled symbols), Desorption (Open symbols).

8.3.2 Thermogravimetric Analysis

Figure 8.3 shows the obtained TG and DTG curves of powder, pellet and pure PVA samples. The initial weight loss at below 150 ^{o}C is due to moisture removal from the materials. Pure PVA sample was degraded around 200 ^{o}C and at temperatures higher than 300 ^{o}C, powder and pellet samples degraded due to the decomposition of organic linker. From the TG curves, the calculated binder content in pellet was about 7 %.

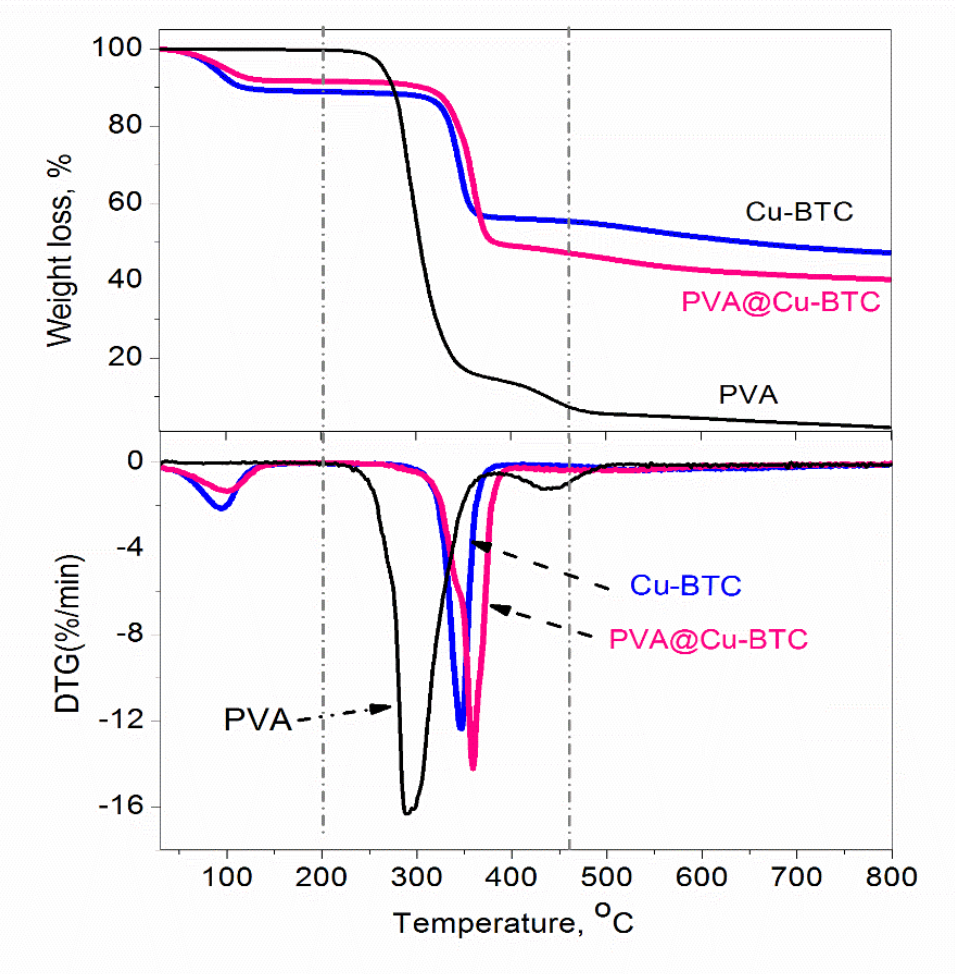

Figure 8.3: Thermogravimetry (TG) and differential thermogravimetry (DTG) curves of Cu-BTC, 33PVA@Cu-BTC pellets and pure PVA samples.

8.3.3 FTIR Analysis

Figure 8.4 shows the FT-IR spectra of Cu-BTC and 33PVA@Cu-BTC pellets. The FT-IR pattern of Cu-BTC is in agreement with those reported by Al-Janabi et al. [147]. The spectra of pellet sample were similar to the MOF powder. The symmetric and asymmetric vibrations of the carboxylate appear at 1645/1590 cm^{-1} and 1450/1370 cm^{-1}, respectively. The broad bond centered at 3400 cm^{-1} can be assigned to hydrogen bonded adsorbed water [130]. The two peaks at 2940 cm^{-1} and 2850 cm^{-1} are the characteristic bonds of asymmetric and symmetric C-H stretching in PVA, respectively [131].

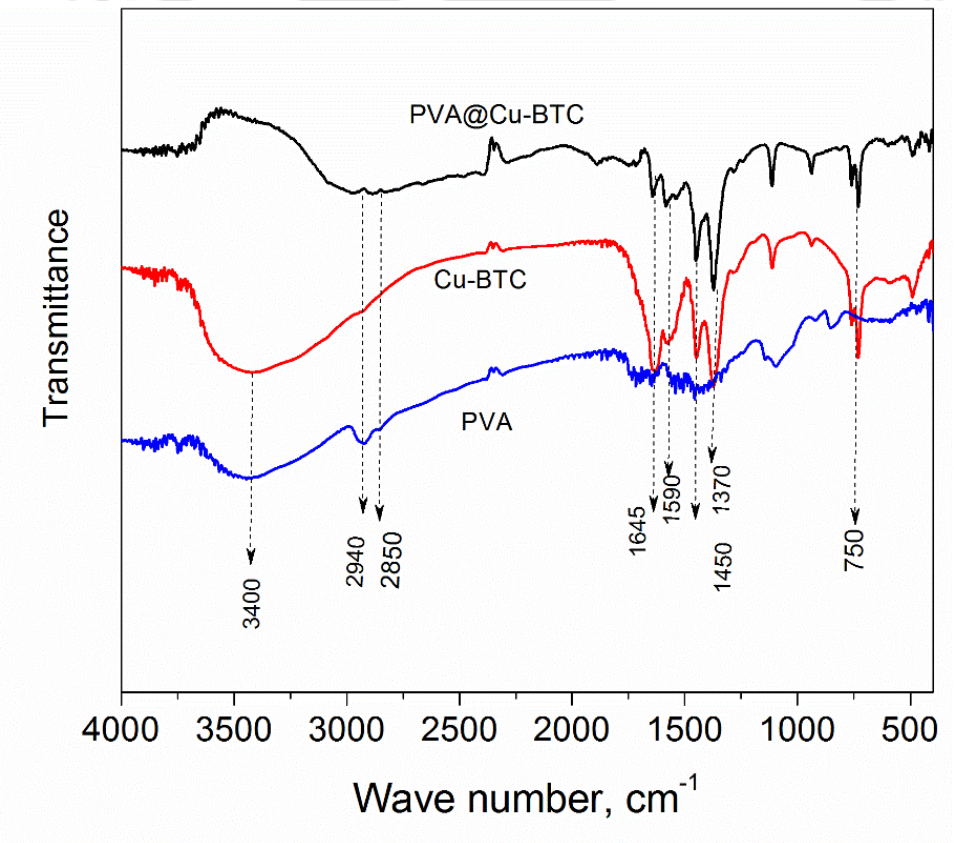

Figure 8.4: FTIR spectra of PVA, Cu-BTC powder and 33PVA@Cu-BTC pellet.

8.3.4 XRD Analysis

Figure 8.5 shows the powder XRD patterns of Cu-BTC and PVA@Cu-BTC pellets. The XRD patterns of Cu-BTC is in good agreement with that reported in literature [148], suggesting that Cu-BTC was successfully synthesized. The observed major diffraction patterns of the 33PVA@Cu-BTC pellets was same as that of Cu-BTC powder, indicating that the crystal structure of the Cu-BTC remained intact after pellatization.

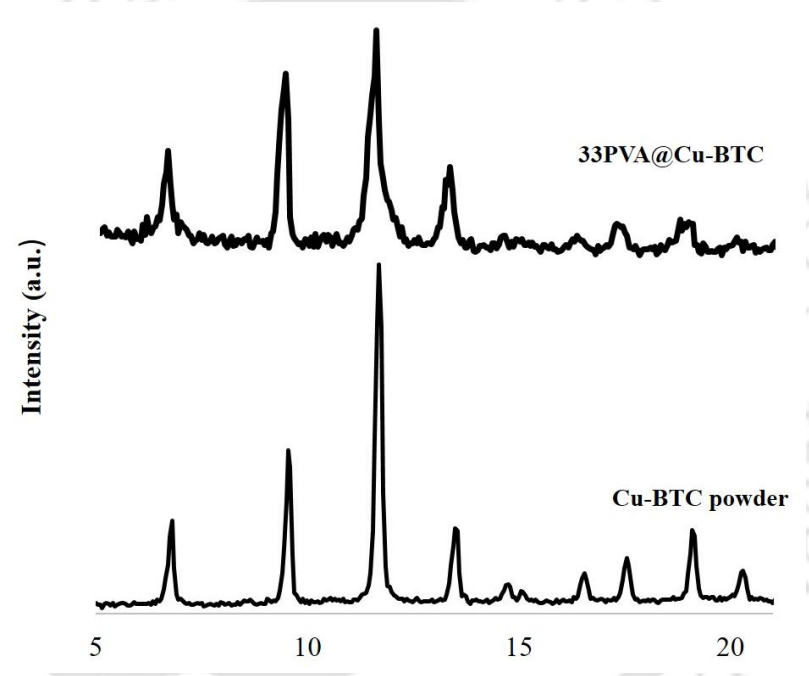

Figure 8.5: XRD patterns of Cu-BTC powder and 33PVA@Cu-BTC pellets.

8.4 Single Component equilibrium adsorption isotherms

Pure component adsorption equilibrium isotherms of CO_2 and N_2 on Cu-BTC powder were measured gravimetrically using Rubotherm magnetic suspension balance at three different temperatures 300 K, 318 K and 338 K up to 20 bar pressure. The adsorption isotherms were shown in the Figures 8.6 (a-b).

The measured isotherms were in good agreement with the isotherms reported by Pradip et al. [43]. Different adsorption models were proposed and found that Langmuir model solely sufficient to fit the experimental data. The fit parameters are given in Table 8.2.

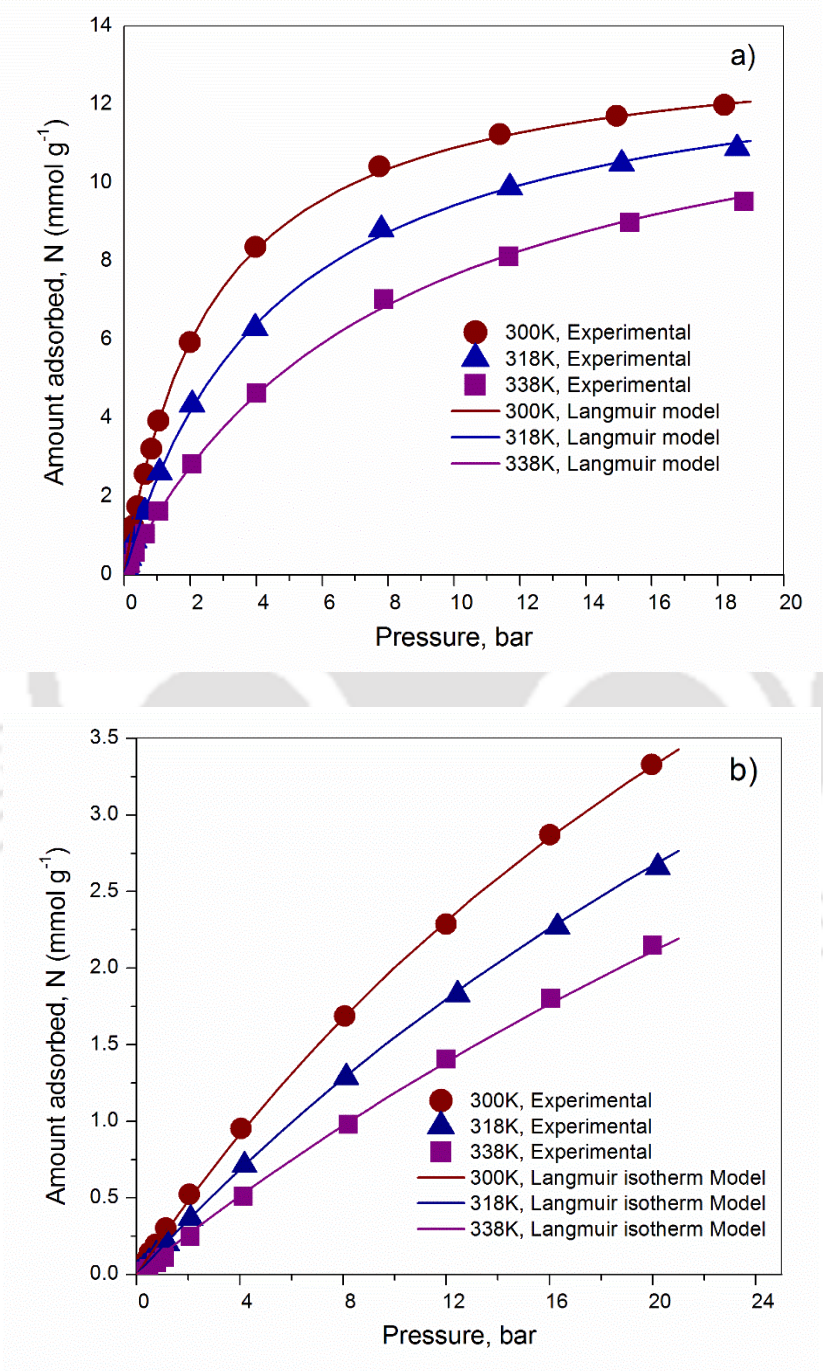

Figure 8.6: Isotherms on Cu-BTC powder **(a)** CO_2 and **(b)** N_2. Lines are fits using model

Table 8.2: Langmuir Model parameters for CO_2 and N_2 on Cu-BTC powder

	CO_2	N_2
N_{max}, mmol g^{-1}	13.74	9.69
b0, bar^{-1}	$1.91*10^{-05}$	$9.91*10^{-05}$
b1, K	2970.60	1671.91

The enthlpy of adsorption was calculated using the model fit parameters. The enthaphy of adsorpion at zero loading ($\Delta h_{ads,0}$) for CO_2 is -24.69 kJ/mol. This value is lower than that on MOFs like MIL-100 (-62 kJ/mol) [139], Ni/DOBDC (-36 kJ/mol) [140], MIL-101 (-32 kJ/mol) [139] and zeolites like 13X (-49 kJ/mol) [136]. The value of enthalpy of adsorption of N_2 on MIL-101 at zero loading is –13.9 kJ/mol which is comparable to the IRMOF-1(-8.3 kJ/mol) [141], IRMOF-3(-9 kJ/mol) [133], Zn/DABCO (-11 kJ/mol) [138] and MOF-177(-10 kJ/mol) [142] and lower than that on Mg/DOBDC (-18 kJ/mol) [96], MIL-53(Al) (-15.9 kJ/mol) [137], and on Silicalite (-16.7 kJ/mol) [143].

In order to investigate the effect of pellatization on adsorption characteristics, CO_2 and N_2 equilibrium isotherms were measured gravimetrically using Rubotherm magnetic suspension balance at 300. Figure 8.7a compares the CO_2 adsorption isotherms at 298K for powder and beads in terms of amount adsorbed per gram of adsorbent. Lower loadings were observed for beads compared to powder sample. However, when compared the isotherms in terms of amount adsorbed per volume of adsorbent (Figure 8.7b), the minimum change in adsorption isotherms was observed due to the higher bulk density of the pellets (Table 8.1).

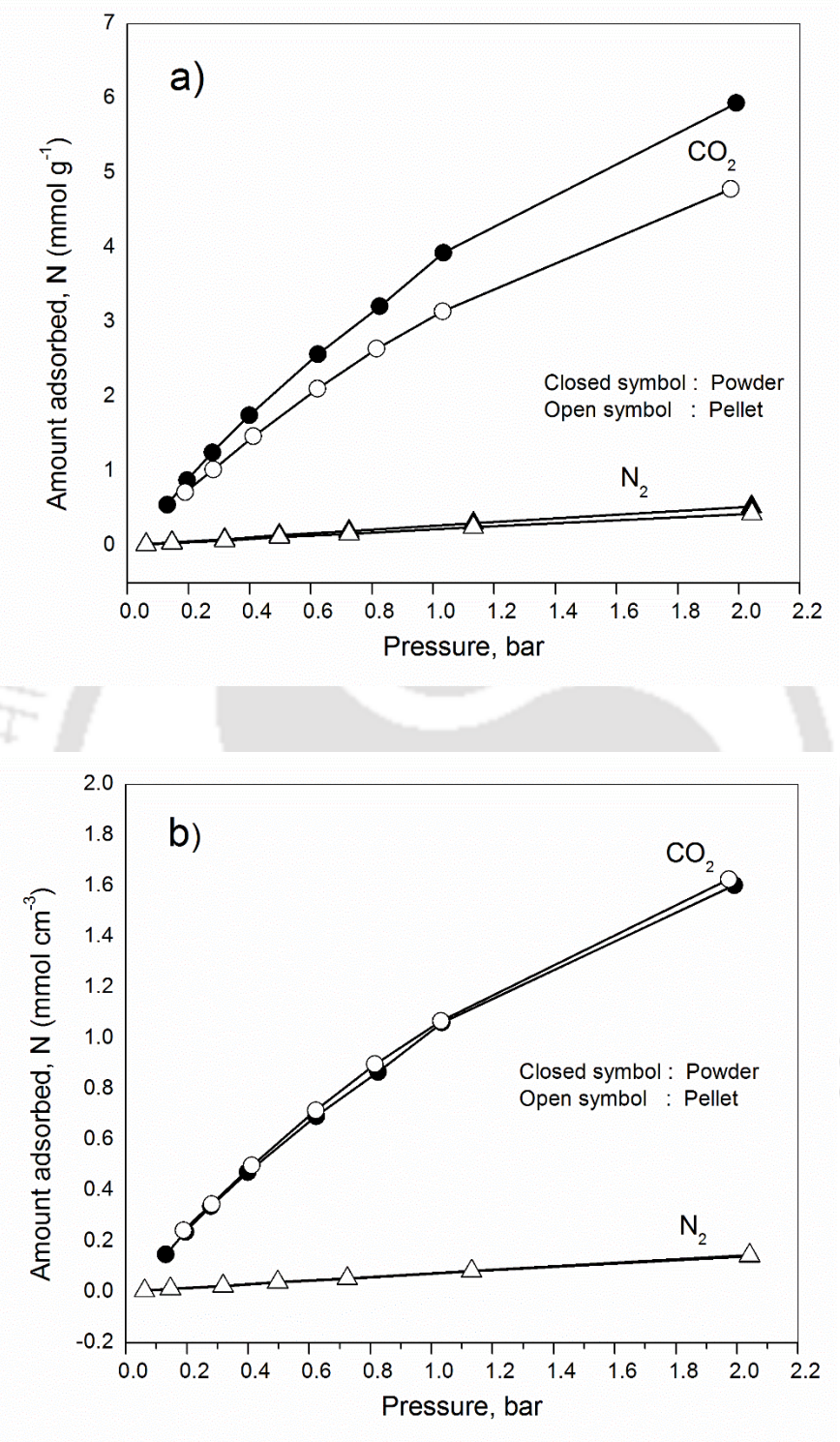

Figure 8.7: Adsorption isotherms at 300 K on Cu-BTC powder and 33PVA@Cu-BTC pellets a) amount adsorbed per gram b) amount adsorbed per cm^3. Lines are drawn as guide to eye.

8.5 CO_2/N_2 separation: Binary breakthrough experiments

The adsorbent column was filled with 12 g of 33PVA@Cu-BTC pellets. An initial activation of adsorbent bed was carried at 423 K for 6 h under N_2 purge flow of 60 SCCM. After the initial activation, fixed bed column was allowed to reach the experimental temperature (i.e. 300 K). Prior to each breakthrough experiment, the adsorbent bed was activated and equilibrated with a flow of helium for 10 minutes at 1.3 bar. During the breakthrough experiments, the column outlet gas composition was analyzed using the gas chromatograph (GC). Properties of the column and breakthrough experimental conditions were given in Table 8.3.

Table 8.3: Properties of fixed bed column and experimental conditions for breakthrough studies on Cu-BTC pellets

Mass of PVA@Cu-BTC pellets (un activated), g	12.00
Mass of PVA@Cu-BTC pellets (activated), g	11.76
Feed Concentration, vol %	~15 % CO_2 balance N_2
Temperature, K	300
Feed flow rate, SCCM	100 – 260
Adsorption/Desorption Pressure, bar	1.3/0.1
Column length, mm	300
Column internal diameter, mm	10
Initial Conditions	Filled with 1 bar He

Figure 8.8a shows the breakthrough curves of CO_2 in feed at different feed flow rates. Figure 8.8b is generated using the cumulative gas as abscissa (instead of time). The overlap of the curves at different flow rates suggests that negligible gas phase mass transfer resistance. As expected, the breakthrough times were decreased with increase in flow rate.

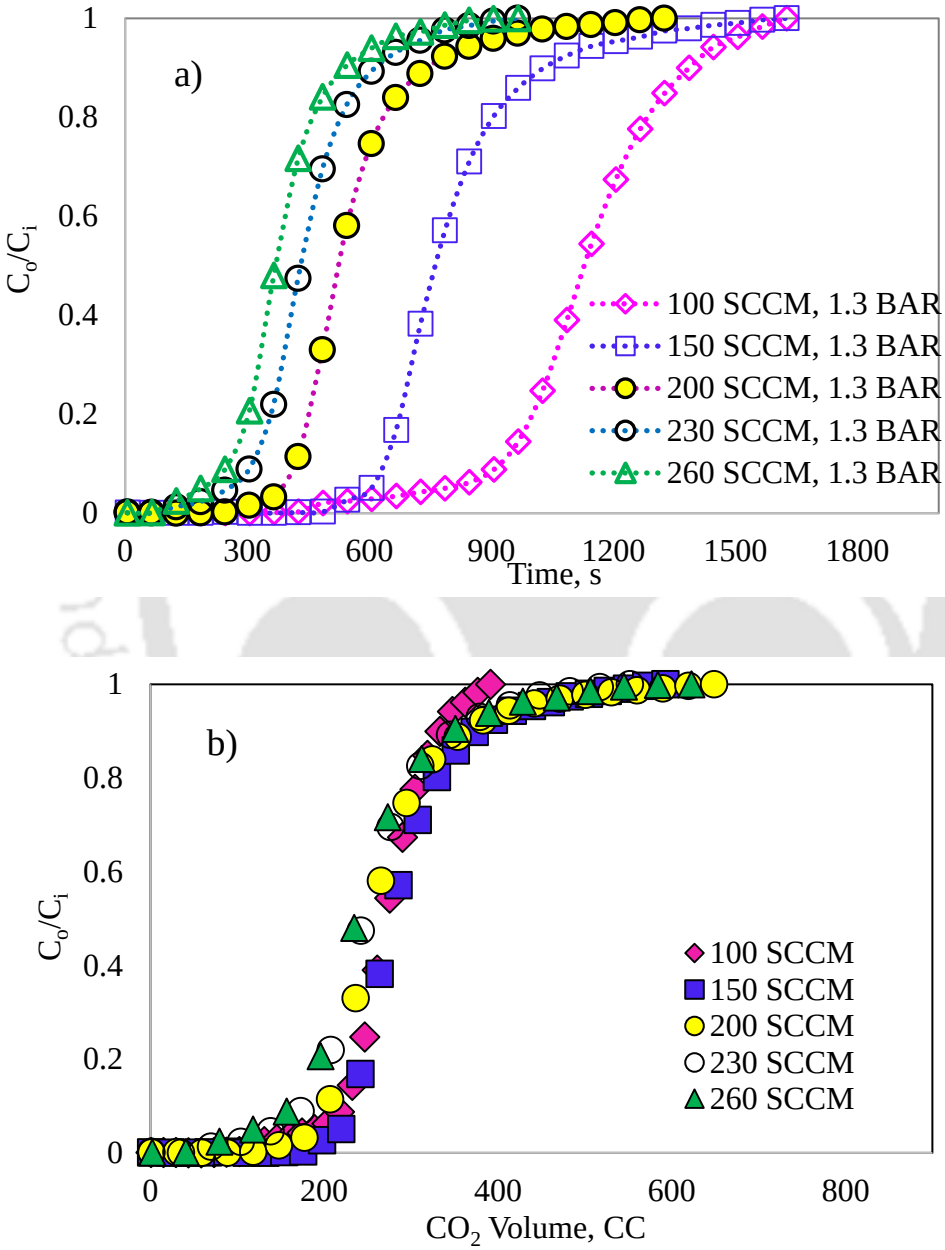

Figure 8.8: CO_2 breakthrough curves from binary mixture (CO_2/N_2:15/85) at different flow rates on 33PVA@Cu-BTC pellets at 300 K and 1.3 bar. Lines are drawn as guide to eye.

8.6 Single column PVSA experiments

The process cyclic experiments have been carried out on 33PVA@Cu-BTC pellets with feed mixture of about 15% CO_2 in nitrogen at a fixed flow rate of 200 SCCM and 1.3 bar pressure. Various cycle configurations (3-step, 4-step and 5-step) were employed. From the breakthrough experiments, the observed CO_2 breakthrough time at these conditions was 365 seconds. The cycle step times were chosen based on the breakthrough time except for the feed pressurization time and blow down times which were fixed at 50 seconds and 10 seconds respectively.

Table 8.4: Step times used in the PVSA cycle

Step	Range of step timings
Pressurization	50 seconds
Adsorption	20%, 40%, 60%, 80% of Breakthrough time
Co-current rinse	7%, 14%, 21% of Breakthrough time
Blow down	10 seconds
Evacuation + N_2 purge	8%, 16%, 32% of Breakthrough time

Feed composition: ~ 15% CO_2, 85% N_2, Adsorption pressure: 1.3 bar, CO_2 BT: 365 seconds, Desorption pressure: 0.15 bar, Temperature: 300 K, Pressurization flow rate: 200 SCCM, Feed flow rate: 200 SCCM, CO_2 rinse flow rate: 80 SCCM, N_2 purge flow rate: 100 SCCM.

Figure 8.9 shows the effect of adsorption time on process performance of a three step PVSA cycle consists of feed pressurization to 1.3 bar, adsorption at 1.3 bar and blowdown to 0.1 bar. The feed flow rate was fixed at 200 SCCM and only the adsorption time was varied. With increase in adsorption

time, the CO_2 product purity was increases from 28.6% to 43.1% while the CO_2 recovery and productivity decreases from 77.9% to 59.9% and 0.221 $kgCO_2/(kg_{ads}\cdot h)$ to 0.168 $kgCO_2/(kg_{ads}\cdot h)$ respectively.

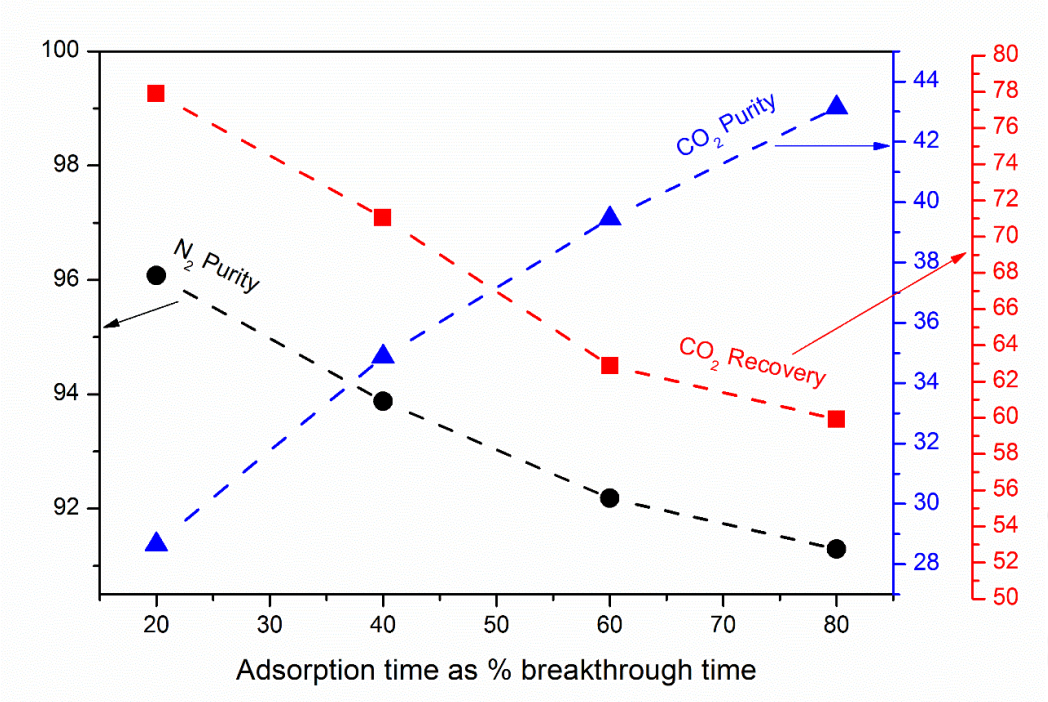

Figure 8.9: Effect of adsorption time on PVSA performance of PVA@Cu-BTC pellets at 300 K. (CO_2 BT: 365 s; $F_{PRES} = F_{FEED}$ = 200 SCCM). Lines are drawn as guide to eye.

For the studied 3-step PVSA cycle, the CO_2 purity/ CO_2 recovery obtained at 40 % of breakthrough time as adsorption time are 34.8/71.1. These values are slightly higher than the process performance of other studied MOFs UiO-66 (28.6/66.4) and MIL-101 (27.9/61.9).

The best achieved 3-step PVSA process performance on PVA@Cu-BTC pellets was: CO_2 purity: 43.1%, CO_2 recovery: 59.9%, productivity: 0.168 $kgCO_2/(kg_{ads}\cdot h)$. To enhance the PVSA process performance, all further process cycle experiments were carried out on adsorption step duration equal to 80 % of the break through time.

The effect of N_2 purge along with evacuation studied. N_2 purge flow rate was fixed at 100 SCCM and purge time was varied as a fraction of CO_2 breakthrough time. The results obtained can be seen in Figure 8.10. N_2 product purity was increased from 91.3 % to 99.9% with inclusion of purge step.

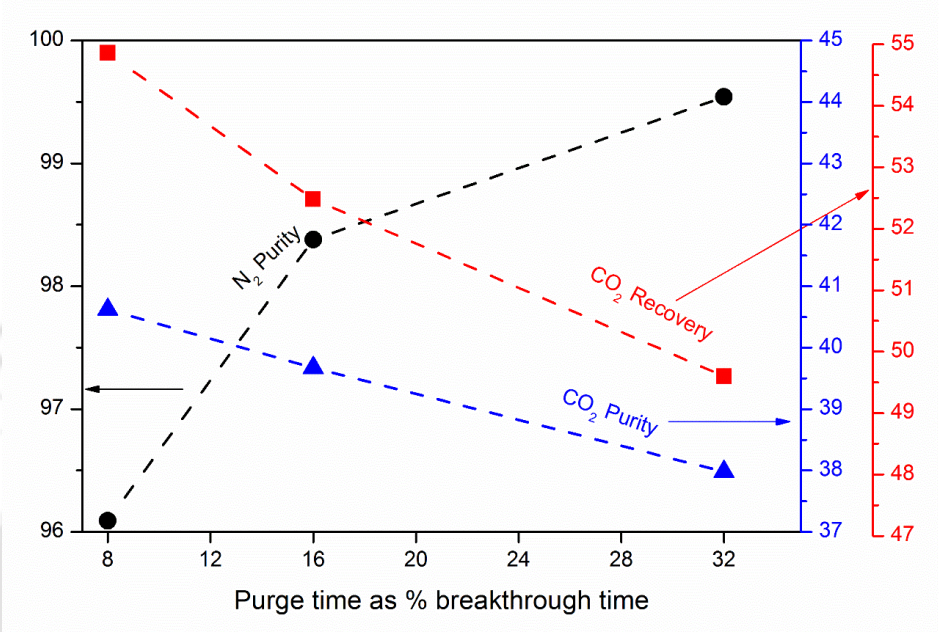

Figure 8.10: Effect of purge time on PVSA performance of PVA@Cu-BTC pellets at 300 K. (CO_2 BT: 365 s; t_{FEED} = 292 s, F_{PRES} = F_{FEED} = 200 SCCM, F_{PUR} =100 SCCM). Lines are drawn as guide to eye

Figure 8.11: shows the effect of the addition of CO_2 rinse step, due to the displacement of void fluid by pure CO_2 during the rinse step, a significant increase in CO_2 product purity from 43.1% to 57.5% was achieved.

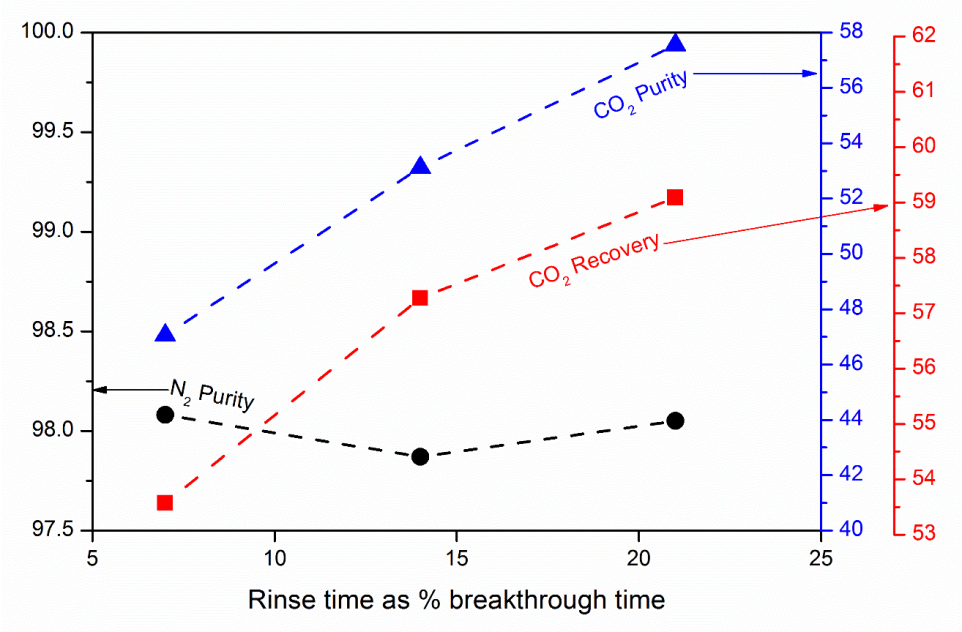

Figure 8.11: Effect of CO_2 rinse on PVSA performance of PVA@Cu-BTC pellets at 300 K. (CO_2 BT: 365 s; t_{FEED} = 292 s, t_{PUR} = 60 s, F_{PRES} = F_{FEED} = 200 SCCM, F_{PUR} =100 SCCM, F_{RIN} = 50 SCCM). Lines are drawn as guide to eye.

The evaluated overall process performance of 5-step (pressurization, feed, rinse, blowdown and purge) PVSA cycle at 300 K and 1.3 bar was: CO_2 purity: 57.6%, CO_2 recovery: 59.1%, productivity: 0.197 $kgCO_2/(kg_{ads}\cdot h)$. The obtained CO_2 purity value was much higher than on the MIL-101 (35.2%) and slightly higher than on UiO-66 (54.2%), whereas the CO_2 recovery, productivity values are slightly lower than that on MIL-101 (61.1% & 0.269 $kgCO_2/(kg_{ads}\cdot h)$) and slightly higher compared to that on PVA@UiO-66 pellets (54.1% & 0.075 $kgCO_2/(kg_{ads}\cdot h)$).

CHAPTER 9

CO_2/N_2 SEPARATION PERFORMANCE ANALYSIS OF FLEXIBLE METAL ORGANIC FRAMEWORK MIL-53(Al)

*In this chapter, the flexible MOF MIL-53(Al) was investigated for CO_2/N_2 separation. About 40 g of MOF powder was synthesized and shaped into beads using polyvinyl alcohol as the binder. Upon CO_2 adsorption at room temperature, the MIL-53(Al) shows two distinct phases called large pore(**lp**) and narrow pore (**np**). Here, we have successfully demonstrated a method and able to maintain these two distinct phases of MIL-53(Al). CO_2 and N_2 equilibrium adsorption isotherms were measured on **lp** and **np** phased MIL-53(Al) powder and beads. Then the binary breakthrough experiments and process cycle studies were performed on the **lp** and **np** beads.*

9.1 Background

The flexible metal organic framework MIL-53(Al) was first synthesized by Ferry and co-workers [29]. This material has attracted the attention of researchers due to its structural flexibility or breathing or shrinking of pores during adsorption between two distinct phases called the large-pore phase (**lp**) and the narrow pore phase (**np**), which have a remarkable difference in cell volume of up to ~ 35%. At higher temperature and in the absence of guest molecules, the **lp** phase of channel dimensions about 8.5×8.5 $Å^2$ is the most stable form. However, in the course of gas adsorption (such as CO_2), the **lp** phase transforms into the **np** phase (of channel dimensions about

2.6×13.6 Å^2) at low pressures, and the reverse transformation occurs at higher pressures. More structural details of both phases of this material are provided in Figure 9.1 and Table 9.1.

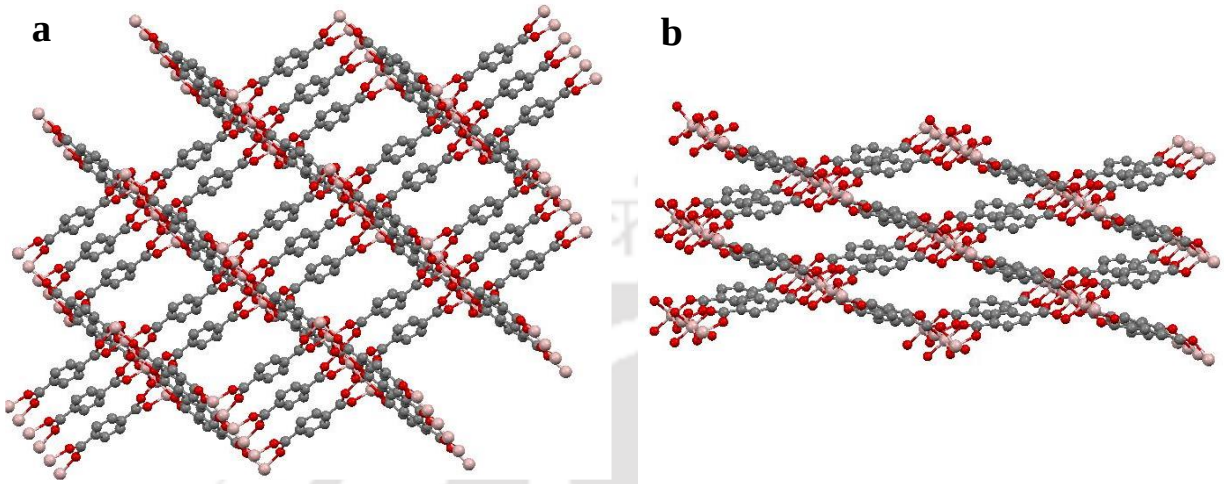

Figure 9.1: Crystal structure of MIL-53(Al) (**a**) in **lp** domain and (**b**) in **np** domain (O, red; C, grey; Al, pink) [29].

Table 9.1: Structural details of MIL-53(Al) MOF [29].

Chemical formula of unit cell	Formula weight of unit cell (**g**)	Unit cell parameters		Cell volume (**Å^3**)	Crystal density (**g cm^{-3}**)	Conversion factor for mol kg^{-1} to molecule unit cell^{-1} conversion
		Cell lengths (**Å**)	Cell angles			
$Al_4O_{20}C_{32}H_{20}$ (**lp** phase)	832.44	a = 6.6085 b = 16.675 c = 12.813	α = 90 β = 90 γ = 90	1411.9	0.979	0.832
$Al_4O_{20}C_{32}H_{20}$ (**np** phase)	832.44	a = 19.513 b = 7.612 c = 6.576	α = 90 β = 104 γ = 90	946.8	1.460	0.832

In literature, several attempts were made to explain this fascinating breathing characteristic of MIL-53(Al) material and found that apart from the guest molecules presence [CO_2, H_2O etc.], the structural transition was also observed by change in temperature [69] or by applying mechanical pressure [70, 149, 150].

Considerable amount of work has been reported in literature towards CO_2 adsorption on MIL-53(Al). The results and the data originating from different laboratories seem to be reproducible and comparable. The **lp** phase form of MIL-53(Al) was found to be highly stable towards moisture, but it had shown low CO_2 adsorption capacity and selectivity [151-153]. The modification of MIL-53(Al) by hydration [154] and functionalization [155] resulted in **np** phased MIL-53(Al) and these modified materials showed higher CO_2 selectivity over CH_4. The CO_2 adsorption capacity of hydrated form was lower than the parent MIL-53(Al). On the other hand, the amine functionalized form [156], at sub-atmospheric pressures has slightly higher CO_2 uptake compared to parent MIL-53(Al), however, at higher pressures the CO_2 uptake was actually lower than that of parent material due to the presence of additional functional groups.

In our earlier work [61, 96, 156], we have successfully presented a technique to tune the MIL-53(Al) material into np form. The tuning was achieved by simply changing the history of the sample (unlike the modification by hydration and amine functionalization). The necessary steps involved to tune MIL-53(Al) into the desired structural form were summarized in Figure 9.2. In brief,

(a) the activation at higher temperature (493 K) yields the material in its **lp** structure and that is retained even after cooled to experimental temperature (293K).

(b) adsorption of CO_2 followed by its complete desorption (by vacuum) at 293 K yields **np** phase. All these phases of MIL-53(Al) are confirmed by the XRD analysis.

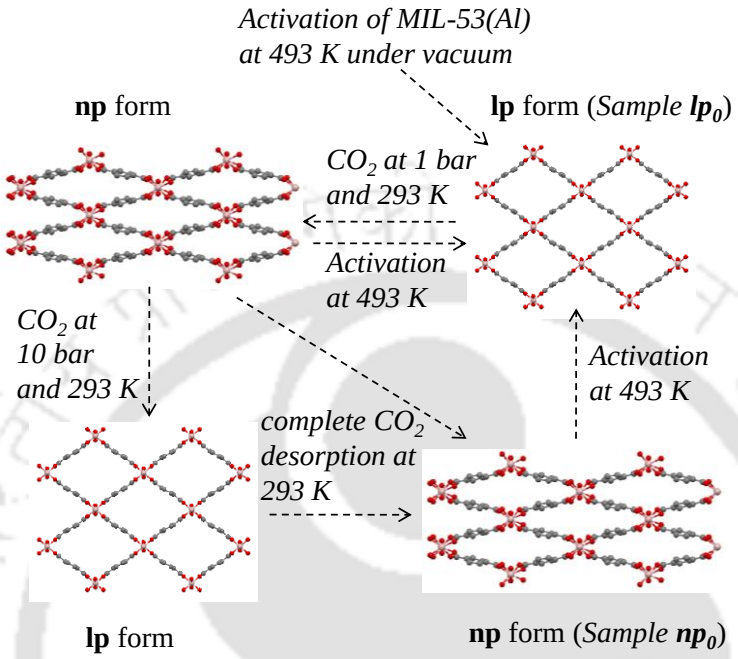

Figure 9.2: Structural transformations in MIL-53(Al) [61]

Using this technique, MIL-53(Al) was tuned into desired structure (i.e. lp or np). Figure 9.3 shows the measured CO_2 adsorption and desorption isotherms at 293 K on both **lp** and **np** phased MIL-53(Al). The measured CO_2 adsorption isotherms on both phases were different. For 0 to 0.8 bar (Figure 9.3b), CO_2 uptake on **np** phase was significantly higher than the **lp** phased form. Hence, this np phase form may be useful in CO_2/N_2 separation (in flue gases, partial pressure of CO_2 is typically between 0.12 – 0.20 bar). After 0.8 bar pressure both isotherms behaved similarly because after this pressure, pore size transformation will be same for both the cases. Desorption isotherms measured on both phases followed each other because structural transformation will be similar for both desorption cases.

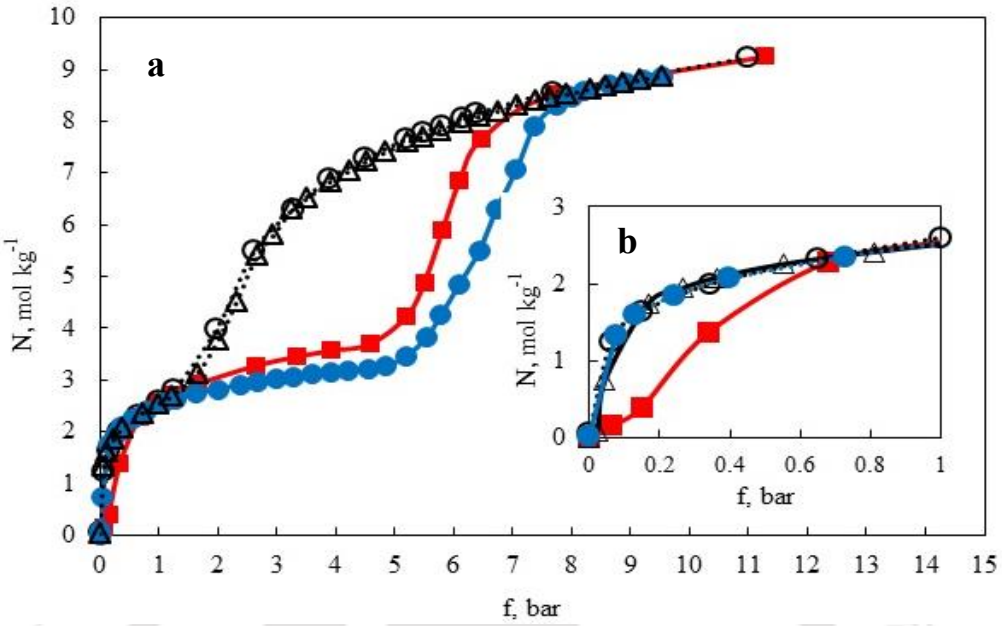

Figure 9.3: (a) CO_2 isotherms at 293 K on different structures of MIL-53(Al). (**b**) enlarged portion of the isotherms in the low pressure region. On **lp** phase: adsorption (■) desorption (Δ); on **np** phase: adsorption (●) desorption (○); Lines are drawn as a guide to the eye [156].

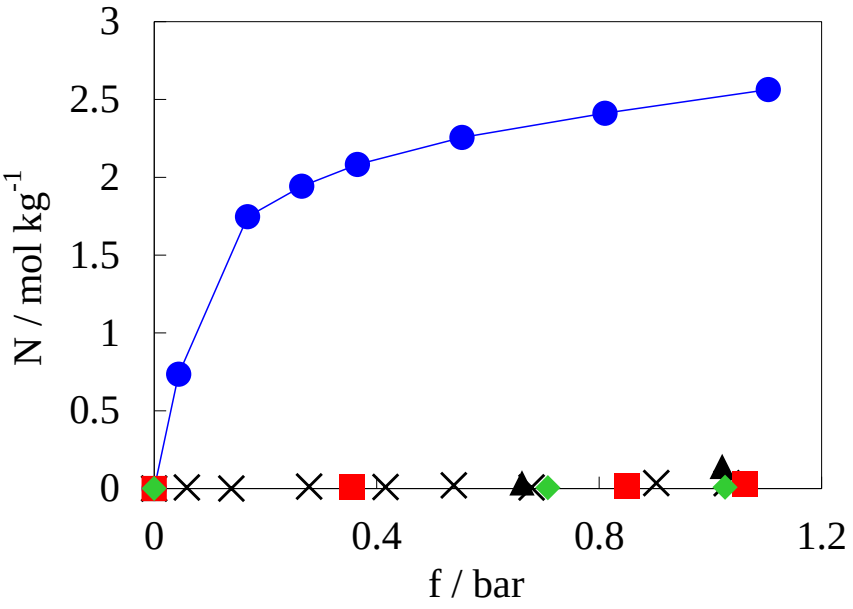

Figure 9.4: Adsorption capacities of CO_2 (●), N_2 (×), CH_4 (▲), CO (■) and O_2 (♦) on **np** structured MIL-53(Al), sample **np**$_0$ at 293 K. Lines are drawn as a guide to the eye. [61]

The other industrially important gases such as N_2, CH_4, CO and O_2 are also measured at 293 K on both **lp** phase and **np** phase of MIL-53(Al). As reported in literature [90, 157], structural transformation does not occur in case of sample **lp** and isotherm does not exhibit hysteresis. In constrast, the isotherms on **np** phase shown hysteresis and has neglible adsorption upto a certain pressure (~ca. 1 bar). Figure 9.4 shows the adsorpton isotherms of CO_2, N_2, CH_4, CO and O_2 on **np** phase MIL-53(Al) upto 1 bar pressure and highlights the usefulness of **np** form for separations. The **np** form has shown near zero uptake for CH_4, N_2, CO and O_2 at pressures below 1 bar. Thus very high CO_2 selectivity is achieved.

In this chapter, to invistigate the separation performance of CO_2/N_2 on both phases of MIL-53(Al), MIL-53(Al) MOF is synthesized in large scale. The material is shaped into pellets by use of PVA/H_2O as binder. The thorough characterization of MIL-53(Al) powder and pellets is carried out. The optimized PVA@MIL-53(Al) pellets are tuned into desired form (i.e. **lp** or **np**) following the above discussed technique and evaluated for CO_2/N_2 separation through breakthrough and process cycle experiements.

9.2 Scale up synthesis

The MIL-53(Al) was synthesized in 1g level following the procedure reported by Loiseau et al. [29] as described in Section 4.1.4. The obtained product showed a surface area of 1242 $m^2 g^{-1}$ which was comparable to the value of 1140 $m^2 g^{-1}$ by Loiseau et al. [29] Then the material synthesis was scaled up to 10g level. After synthesis, sample was subjected to DMF treatment followed by calcination at 553 K to remove the unreacted BDC molecules. 11g of final product was obtained and subjected to surface area analysis. After activation, the product showed a BET surface area of 910 $m^2 g^{-1}$, which is far below the value of 1242 $m^2 g^{-1}$ obtained in the small scale synthesis. From this analysis it is clear that an excess amount of unreacted BDC is still present in the product. For removal of this excess BDC, DMF treat was again performed for 15 h at 423 K. After calcination, 10.6g of product was obtained which showed a BET surface area of 1200 $m^2 g^{-1}$. The scale up synthesis of MIL-53(Al) was performed in another two batches (see Table 9.2) and in all three batches an additional DMF treat was needed to obtain MIL-53(Al) sample with surface area close to the small scale synthesized material. As the final products obtained in three batches were having similar surface area, they have mixed and the resulted final MIL-53(Al) sample (which showed a BET surface area of 1144 $m^2 g^{-1}$) was used for MIL-53(Al) pellets preparation.

Table 9.2: BET Surface areas of scale up synthesized MIL-53(Al)

Adsorbent	**Surface Area ($m^2 g^{-1}$)**	**Surface Area ($m^2 g^{-1}$)**
MIL-53(Al)	**After 1st DMF treat**	**After 2nd DMF treat**
Batch 1	910	1200
Batch 2	952	1165
Batch 3	919	1140

9.3 Pellet preparation

PVA@MIL-53(Al) beads were prepared following the procedure suggested by Fisny et al. [108] using PVA as binder. MOF powder, 15 wt% PVA/H_2O and a few drops of water were mixed and shaped into 2-4 mm diameter beads manually. The obtained beads were heated at 0.5 ^oC/min to reach 180 ^oC and kept at this temperature for 6 hours. Then the obtained beads were made into fractions manually and stored in vacuum desiccator. The ratio of MOF powder to binder was varied to optimize the pellets preparation. Table 9.3 shows the experimental conditions used for the pellets preparation. The final pellets are denoted as 17PVA@MIL-53(Al), 24PVA@MIL-53(Al) and 33PVA@MIL-53(Al) corresponding to the initial weight percent of PVA/H_2O (see Table 9.3). The photographs and scanning electron microscopy images of the synthesized MIL-53(Al) powder and 24PVA@MIL-53(Al) pellets are shown in Figure 9.5. The beads were made into fractions for use in column studies.

Table 9.3: Experimental conditions and properties of the formulated MIL-53(Al) pellets

Sample	Mass of MOF (g)	Mass of 15wt% PVA/water (g)	water (g)	BET Surface area (m^2g^{-1})	Pore volume (cc/g)	Bulk density (g/cc)
MIL-53(Al)	--	--	--	1144	0.63	0.36
17PVA@MIL-53(Al)	1.0	0.20	0.5-1.0	936	0.53	---
24PVA@MIL-53(Al)	1.0	0.32	0.5-1.0	792	0.46	0.41
33PVA@MIL-53(Al)	1.0	0.50	0.5-1.0	680	0.41	---

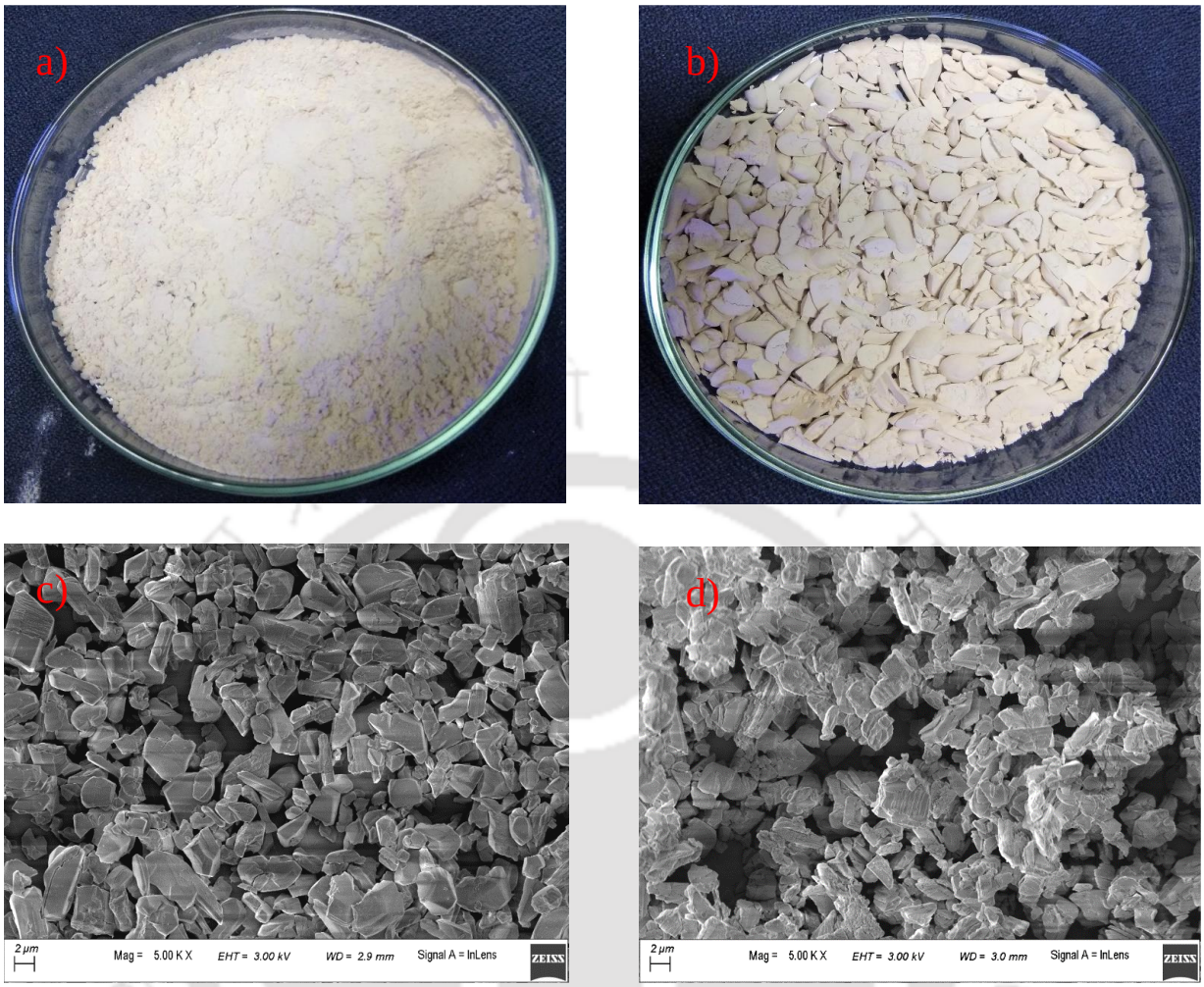

Figure. 9.5: Images (a) MIL-53(Al) powder, (b) 24PVA@MIL-53(Al) pellets

FESEM images (c) MIL-53(Al) powder, (d) 24PVA@MIL-53(Al) pellets.

9.4 Characterization

9.4.1 Surface Area and Pore Volume Analysis

Figure 9.6 shows the N_2 physisorption isotherms of MIL-53(Al) powder and shaped PVA@MIL-53(Al) pellets at 77 K. The calculated BET specific surface area of MIL-53(Al) powder is 1144 m^2/g and is comparable to the reported value of 1140 $m^2\ g^{-1}$ by Loiseau et al. [29]. Similar to the other studied MOFs, the surface area of prepared pellets was decreased with increase in binder content. About 18 to 40% decrease was observed for the prepared pellets compared to the powder.

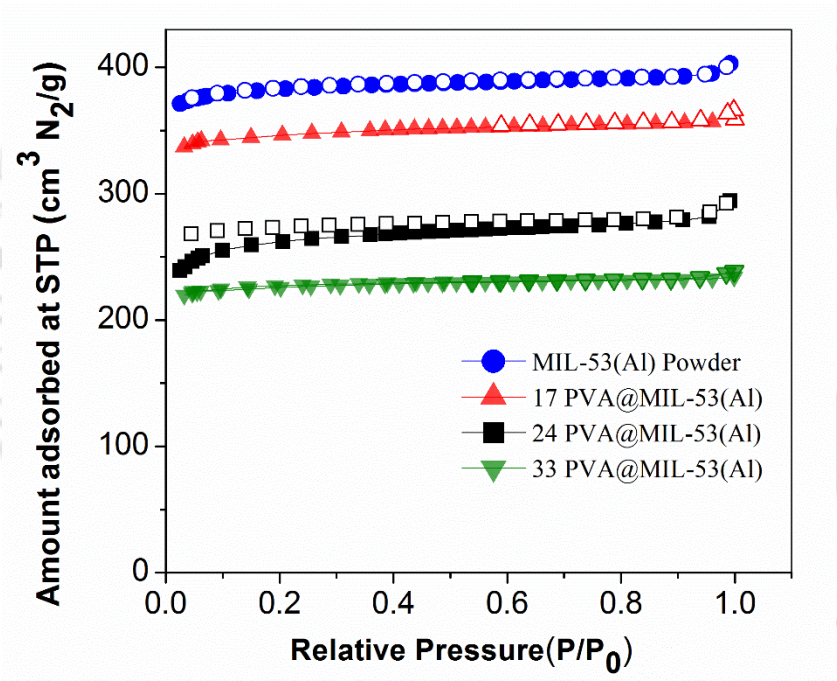

Figure 9.6: N_2 physisorption isotherms of MIL-53(Al) powder and PVA@MIL-53(Al) pellets at 77 K: Adsorption (filled symbols), Desorption (Open symbols).

The textual characterization results suggest that 24PVA@MIL-53(Al) pellets are having optimum properties in terms of less loss in surface characteristics. Hence, further material characterization and experiments are being performed on these optimum pellets, and from here onwards, the term pellet refers to 24PVA@MIL-53(Al) sample.

9.4.2 Thermogravimetric Analysis

Figure 9.7 shows the obtained TG and DTG curves of MOF powder, MOF pellets and pure PVA samples. The initial weight loss at around 100 ^{o}C is due to moisture removal from the materials. Thereafter, the MOF material continues to show stable weight up to 450 ^{o}C. The sharp increase in weight loss above 450 ^{o}C is due to the collapse of MIL-53(Al) structure *i.e.* removal of structural BDC linkers from the framework.

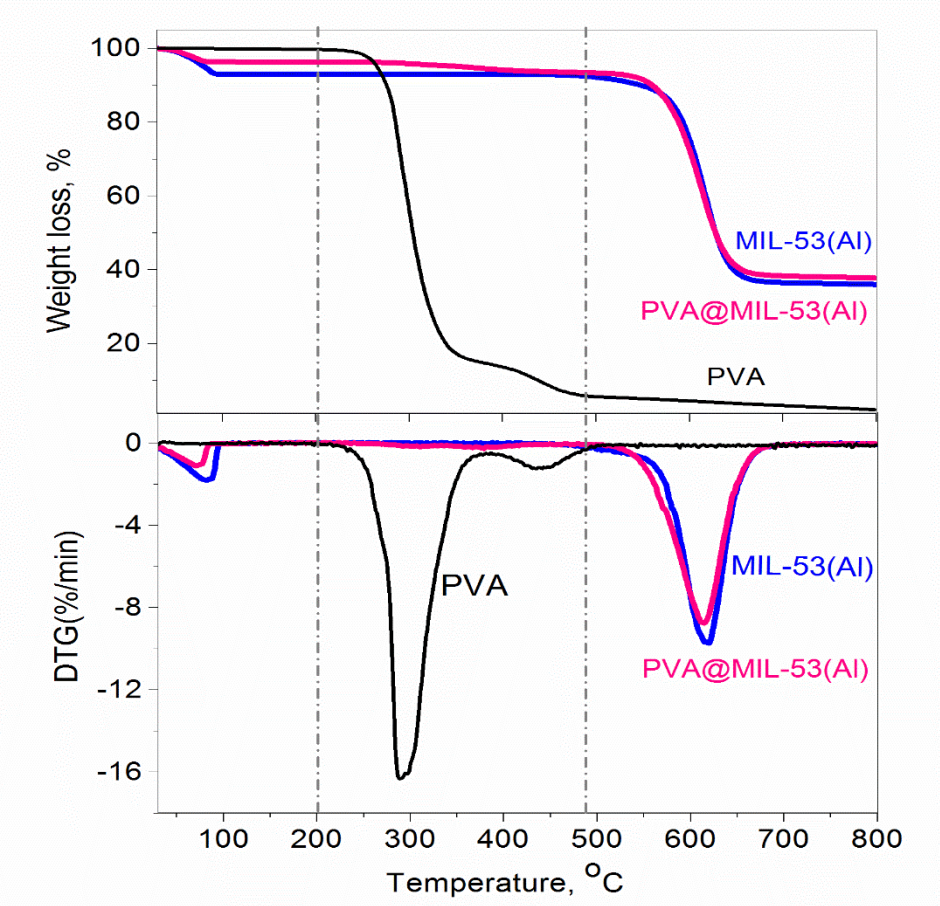

Figure 9.7: Thermogravimetry (TG) and differential thermogravimetry (DTG) curves of MIL-53(Al), 24PVA@MIL-53(Al) and pure PVA samples.

9.4.3 FTIR Analysis

The FT-IR spectra of PVA, MIL-53(Al) powder and pellets are given in **Figure. 9.8**. The vibration bonds in the region 1,400–1,700 cm^{-1} are attributed to the carboxylate (COO–) asymmetric and symmetric stretching vibrations of terephthalate (BDC). The broad bond centered at 3400 cm^{-1} can be assigned to hydrogen bonded adsorbed water [130]. The two peaks appeared in PVA at 2940 and 2850 cm^{-1} are the characteristic bonds of asymmetric ad symmetric C-H stretching respectively [131].

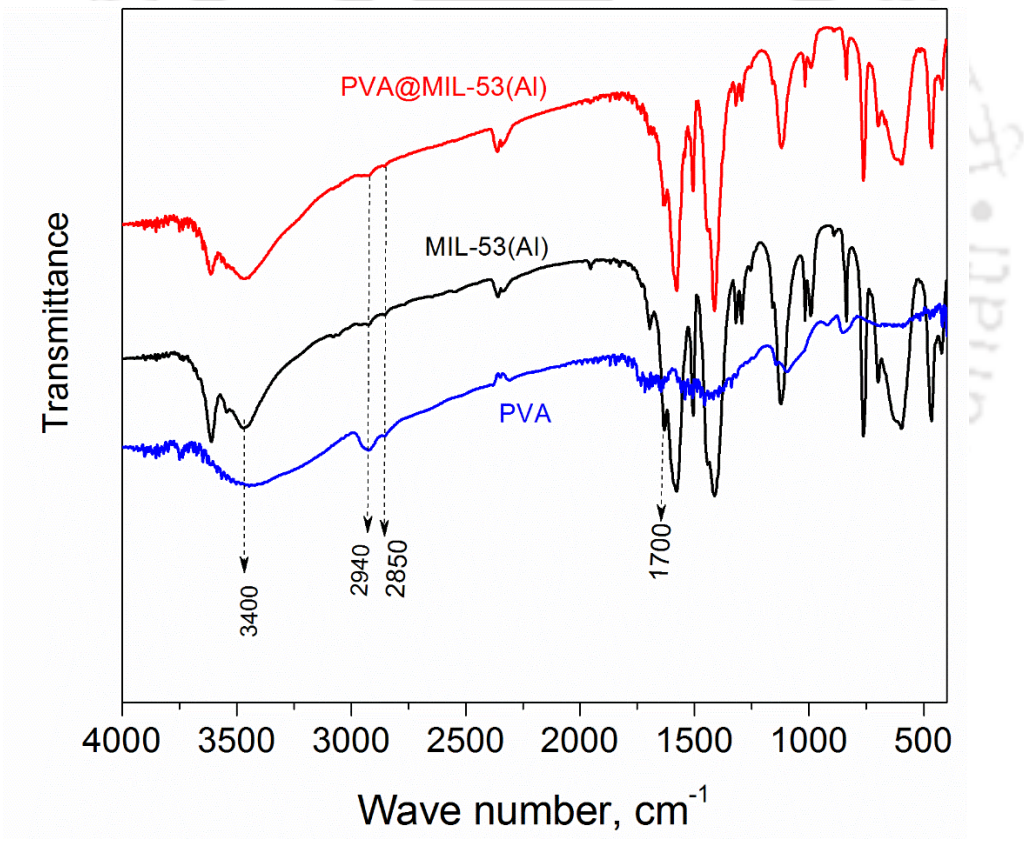

Figure 9.8: FTIR spectra of PVA, MIL-53(Al) powder and 24PVA@MIL-53(Al) pellets.

9.4.4 XRD Analysis

The diffraction patterns of the synthesized MIL-53(Al) powder and formulated pellet samples (Figure 9.9) showed high crystallinity with reflections in the range 5–30°. These patterns are similar to the XRD pattern reported by Loiseau et al. [29] for large pore (**lp**) domain of MIL-53(Al). The XRD patterns illustrated in Figure 9.9 show that characteristic features of MIL-53(Al) were preserved during the pellatization of MOF material.

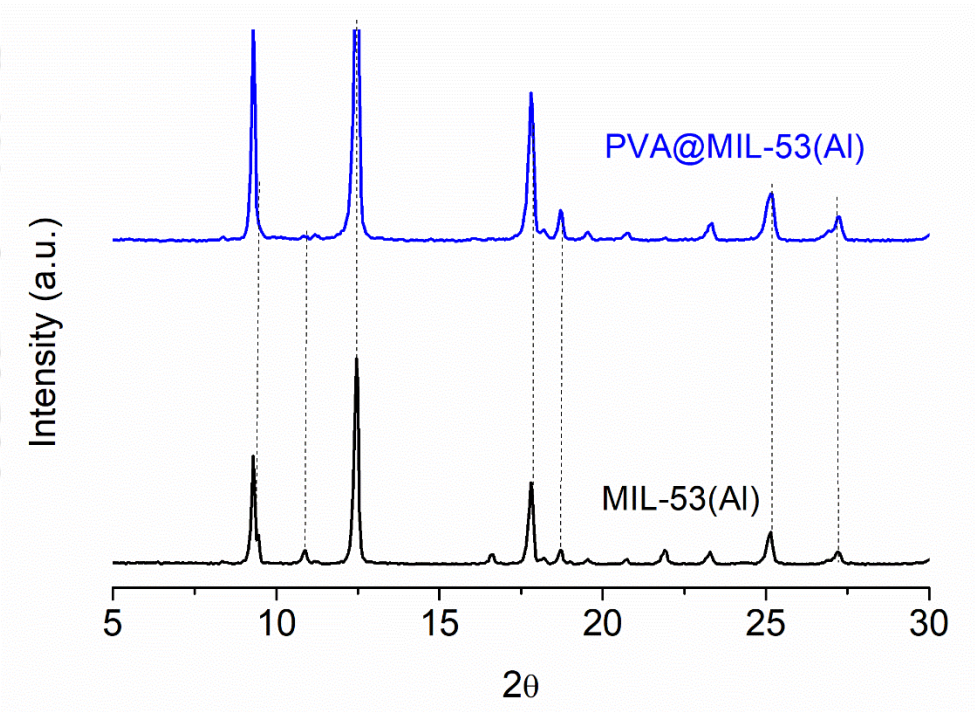

Figure. 9.9: XRD patterns of MIL-53(Al) powder and 24PVA@MIL-53(Al) pellets

9.5 Single component equilibrium adsorption isotherms

The synthesized MIL-53(Al) powder and formulated 24PVA@MIL-53(Al) pellets are tuned into desired structure as described in the Section 9.1. Briefly, activation at higher temperature (~ 493 K) yielded the materials into **lp** phase. The pure component isotherms are measured on this **lp** phase. Then the materials are equilibrated with CO_2 at 10 bar followed by complete desorption yielded the materials into **np** phase. Figure 9.10 shows the pure component equilibrium adsorption isotherms of CO_2 on both phases (i.e. **lp** and **np**) of MIL-53(Al) powder measured gravimetrically using Rubotherm magnetic suspension balance at 300 K. CO_2 isotherm on **lp** sample is different than that on sample **np**. At about 0.15 bar, CO_2 loading capacity on sample **np** (1.41 mol kg^{-1}) is significantly higher than that on sample **lp** (0.30 mol kg^{-1}). The CO_2 isotherms obtained in this work are similar to our earlier work presented in Figure 9.3.

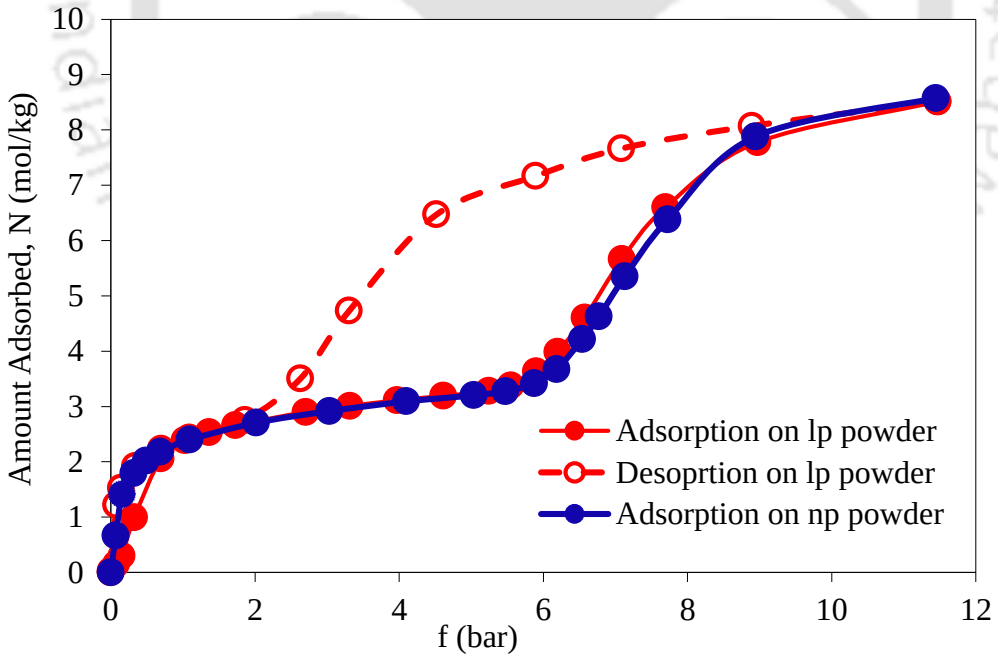

Figure 9.10: CO_2 isotherms on MIL-53(Al) powder at 300 K. Lines are drawn as a guide to the eye.

Figure 9.11 shows the CO_2 isotherms measured on formulated MIL-53(Al) pellets and are compared with CO_2 isotherms on MIL-53(Al) powder sample. The CO_2 isotherms on **lp** and **np** phases of MIL-53(Al) pellets have similar steps (which are known to be attributed to the structural transformation of MIL-53(Al)), which are seen in the isotherms on MIL-53(Al) powder. These results illustrate that the characteristics of breathing phenomena are not affected by the pellatization process. However, lower CO_2 loadings are observed on pellet samples due to the presence of binder.

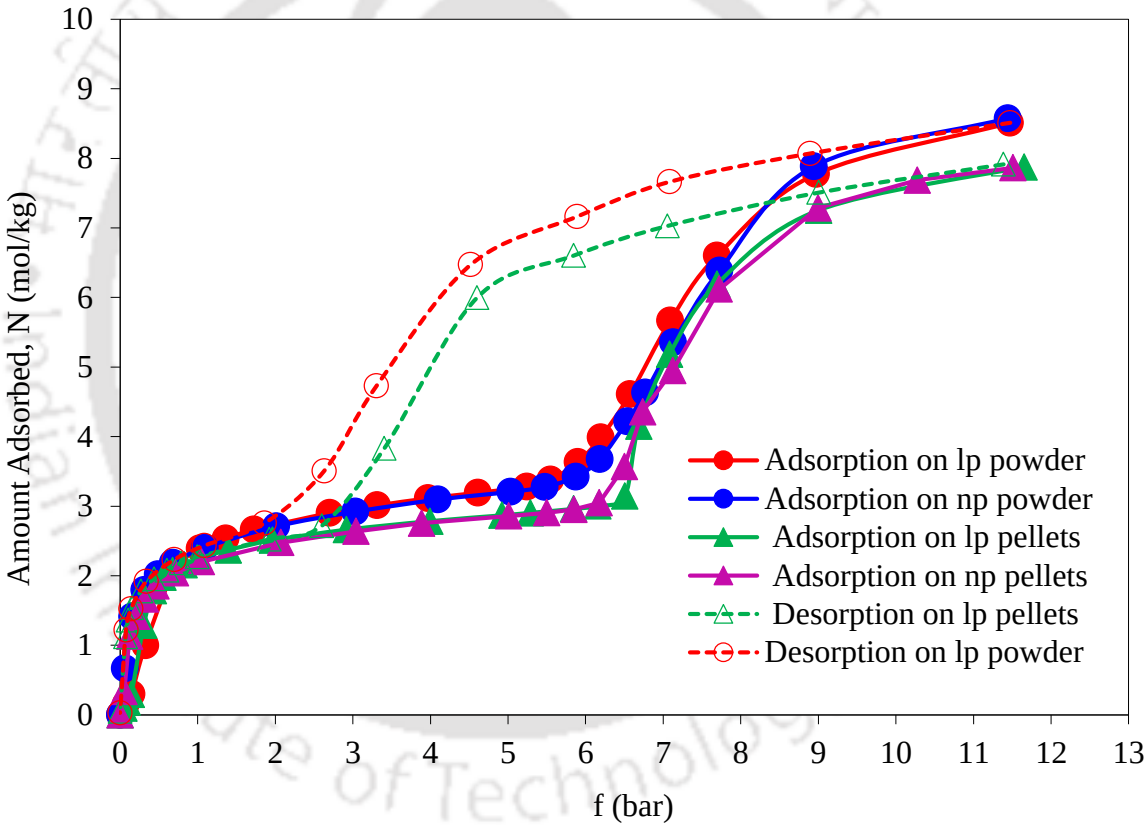

Figure 9.11: CO_2 isotherms on different phases of MIL-53(Al) powder and pellets at 300 K. Lines are drawn as a guide to the eye.

Figure 9.12 shows the measured N_2 adsorption isotherms on **lp** and **np** phases of MIL-53(Al) powder and pellet samples. The isotherms on **lp** and **np** phases have significant difference. N_2 adsorption was negligible upto to a certain pressure (~*ca.* 1 bar), as the **np** form of the sample excludes N_2 molecules with larger kinetic diameter and low adsorption energies [158]. This is the lowest uptake reported for N_2 on non-hydrated and non-functionalized form of MIL-53(Al) at 300 K, which corroborate the higher CO_2/N_2 selecyivity on **np** form. At higher pressures, increase in adsorption may be readily attributed to the **np**→**lp** transformation of the sample.

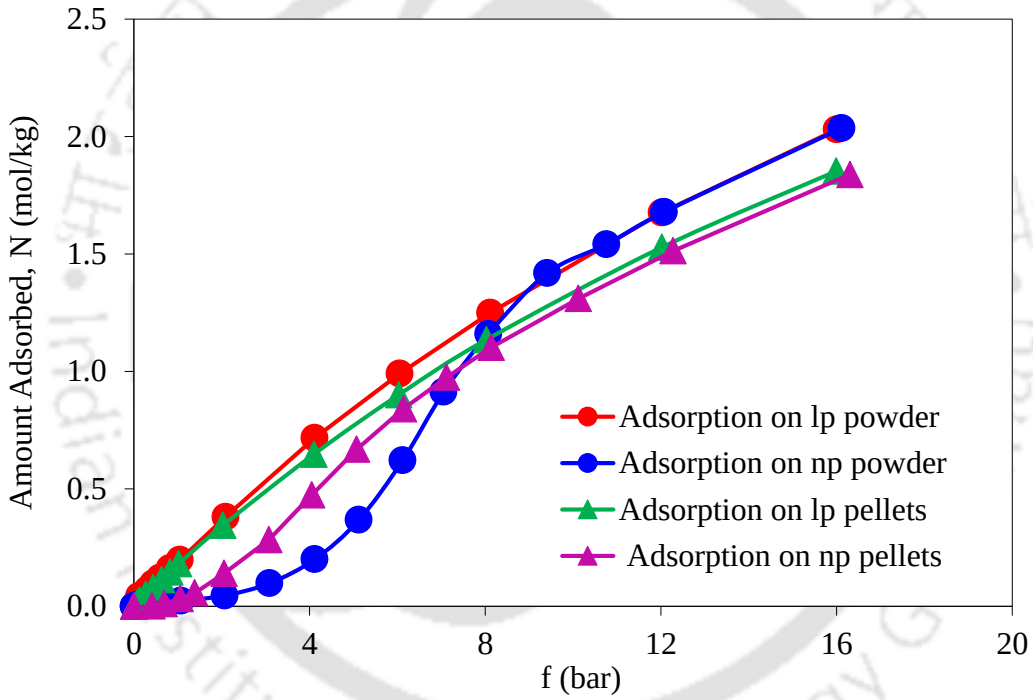

Figure 9.12: N_2 isotherms on MIL-53(Al) powder and pellets at 300 K. Lines are drawn as a guide to the eye.

The performed equilibrium experiments revealed that the tuned **np** phase of MIL-53(Al) material has higher CO_2 adsorption capacity and CO_2/N_2 selectivity. To investigate this materials CO_2/N_2 separation performance, further experiments will be carried on both phases of MIL-53(Al) samples in the form of pellets through breakthrough and process cycle experiments.

9.6 CO_2/N_2 separation: Binary breakthrough experiments

The designed and validated experimental set up shown in Figure 5.1 is used without any further modifications. The adsorbent column is packed with 13 g of un activated 24PVA@MIL-53(Al) pellets. Properties of the fixed bed column used and experimental conditions for breakthrough experiments are given in Table 9.4. An initial activation of adsorbent pellets to remove adsorbed moisture/other gas species, is performed at 423 K for 6 h under N_2 purge flow of 60 SCCM. Then the material is tuned into the desired structure (i.e. **lp** or **np**). After making the material into the desired structure, initially column is filled with helium gas at 1 bar and then started to fed with feed gas mixture to measure the breakthrough curves. The column outlet composition is analysed periodically using the gas chromatograph.

Table 9.4: Properties of the fixed bed column and experimental conditions for breakthrough studies

Mass of adsorbent pellets (activated), g	11.2
Feed Concentration, mol%	~15 % CO_2 balance N_2
Feeding Temperature, K	300
Feed flow rate, SCCM	100 – 235
Feed gas pressure, bar	1.3
Column length, mm	300
Column internal diameter, mm	10
Column initial condition	Filled with 1 bar He

Figure 9.13 (a-b) shows the obtained CO_2 breakthrough curves in feed (CO_2/N_2: 15/85) at different flow rates on **lp** and **np** phases of MIL-53(Al). As expected with increase in flowrate, the CO_2 breakthrough times are decreased. The measured dynamic breakthrough curves on **np** and **lp** phases of MIL-53(Al) are different. For comparison, the CO_2 breakthrough time on both phases of MIL-53(Al) at 235 SCCM feed flowrate, 300 K temperature and 1.3 bar column pressure is given in Table 9.5. At these conditions, the obtained CO_2 breakthrough time on **np** phased material is nearly three-fold as that of **lp** phased material. This higher CO_2 breakthrough time on **np** material is due to the higher CO_2 loading of np phase material, which is already evidenced by the measured CO_2 equilibrium isotherms. Hence, these results clearly indicate that using the same amount of material in **np** phase, a large amount of flue gas stream can be separated. The sharp nature of breakthrough curves on **lp** phase sample suggests the faster kinetics and good mass transfer rate. On the other hand, for **np** phase sample, small amount of CO_2 is continuously observed at the column outlet from the start of breakthrough experiment can be attributed due to the slower CO_2 adsorption/desorption kinetics on **np** sample.

Table 9.5: CO_2 breakthrough time at 235 SCCM feed flowrate on different phases of MIL-53(Al)

Sample	Feed flow rate (SCCM)	Feed composition (CO_2:N_2)	Temperature (K)	Column pressure (bar)	CO_2 Breakthrough time (s)
lp-MIL-53(Al)	235	15:85	300	1.3	186
np-MIL-53(Al)	235	15:85	300	1.3	510

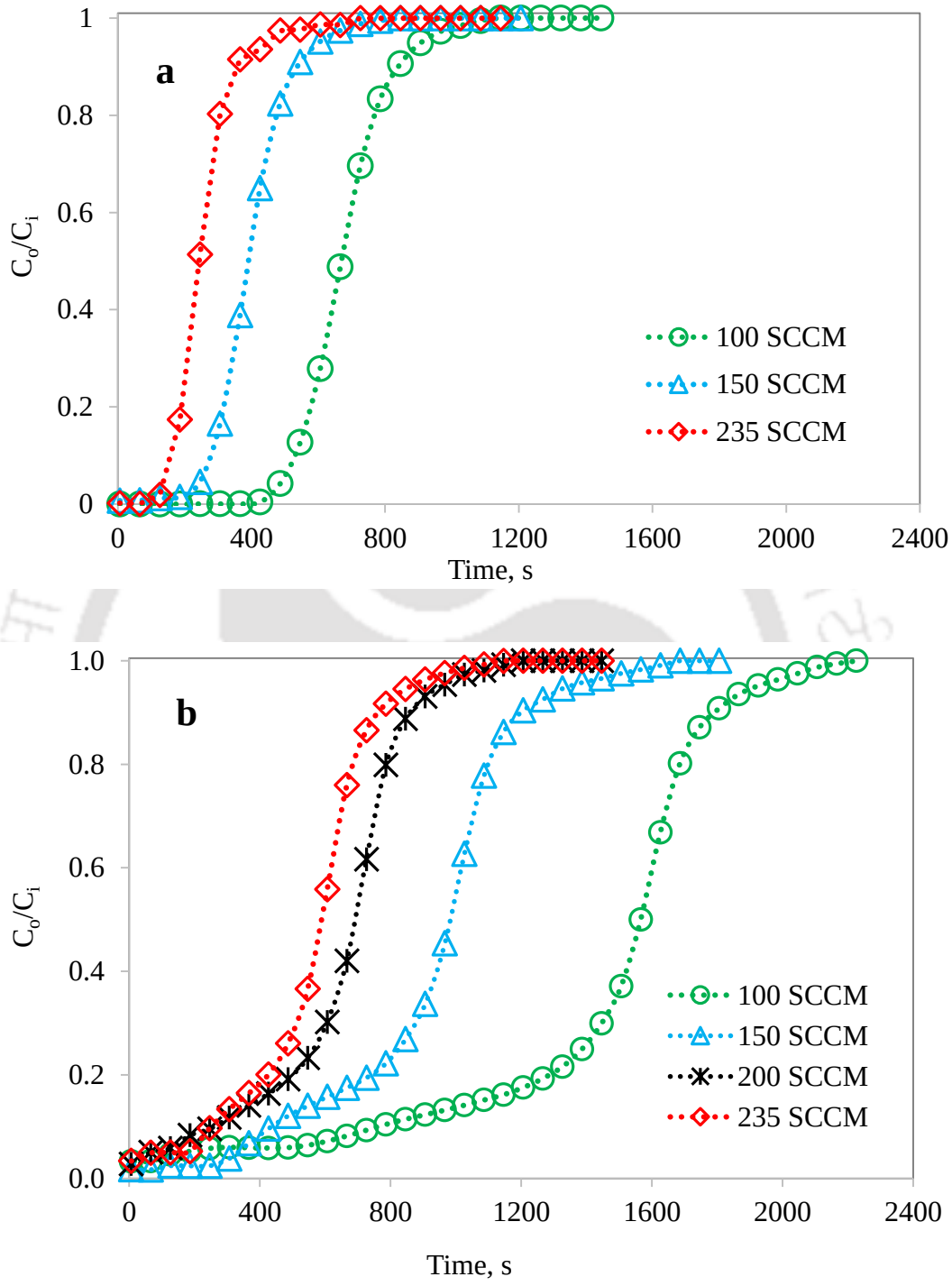

Figure 9.13: CO_2 breakthrough curves from a binary mixture (CO_2/N_2:15/85) at different flow rates on MIL-53(Al) pellets at 300 K and 1.3 bar: (a) on **lp** phase (b) on **np** phase. Lines are drawn as a guide to the eye.

9.7 Single column PVSA experiments

The PVSA process cycle experiments are carried out on both phases of MIL-53(Al) material with feed mixture of about 15% CO_2 in nitrogen at a fixed flowrate of 235 SCCM and 1.3 bar of adsorption pressure. The cycle step times are chosen based on the breakthrough time except for the feed pressurization step time fixed at 32 s (i.e. pressurization time taken to reach the column pressure of 1.3 bar at 235 SCCM) and blow down step time fixed at 10 s. Thus adsorption step time has been chosen to vary from 20% to 80% of the breakthrough time and likewise for the other step timings as shown in Table 9.6. In a typical experiment, the cyclic steady state (CSS) was achieved in about 20 no of cycles, ensured by a difference of < 0.5% between the CO_2 purity/recovery obtained in consecutive cycles.

Table 9.6: Configuration of PVSA cycle step times

Step	Duration
Pressurization	32 seconds
Adsorption	20%, 40%, 60%, 80% of breakthrough time
Co-current rinse with heavy (CO_2) component	7%, 15%, 30% of breakthrough time
Blow down	10 seconds
Evacuation + purge with light (N_2) component	16%, 24%, 36% of breakthrough time

*Feed composition: 15% CO_2, 85% N_2, Adsorption pressure: 1.3 bar, CO_2 BT on **lp** sample: 180 s, CO_2 BT on **np** sample: 510 s, Desorption pressure: 0.15 bar, Temperature: 300 K, Pressurization flow rate: 235 SCCM, Feed flow rate: 235 SCCM, N_2 purge flow rate: 100 SCCM. CO_2 rinse flow rate: 80 SCCM.*

The MIL-53(Al) pellets are tuned into the desired structure (i.e. **lp** and **np**) and their CO_2/N_2 separation performance was evaluated through various process cycle configurations. Initially, a three step process consists of feed pressurization, adsorption and blowdown was studied. Figure 9.14 and Figure 9.15 shows the effect of adsorption time on PVSA performance of **lp** phase and **np** phases of MIL-53(Al) pellets respectively.

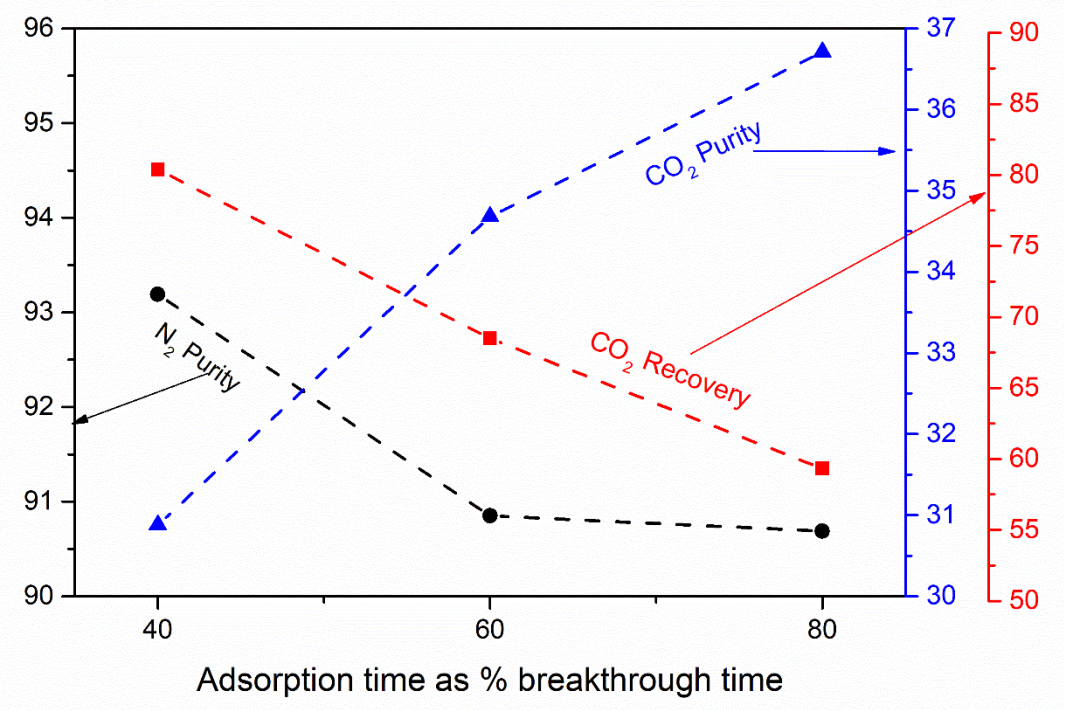

Figure 9.14: Effect of adsorption time on PVSA performance of **lp** phased PVA@MIL-53(Al) pellets at 300 K (CO_2 BT: 180 s; $F_{PRES} = F_{FEED} = 235$ SCCM), lines are drawn as guide to eye.

The CO_2 product purity is increases with increase in adsorption time for both phases of material. The CO_2 product purity increased from 30.9% to 36.7% for **lp** phase MIL-53(Al) and for **np** phase MIL-53(Al), it was from 43.1% to 45.9%. On the other hand, CO_2 product recovery and productivity were decreased with increase in adsorption time on both phases of the material. The evaluated three-step (pressurization, adsorption and blowdown) PVSA process performance was: on **lp**-MIL-53(Al), CO_2

purity: 30.9%, CO_2 recovery: 80.4%, productivity: 0.271 $kgCO_2/(kg_{ads} \cdot h)$ and on **np**-MIL-53(Al), it was, CO_2 purity: 43.0%, CO_2 recovery: 55.8%, productivity: 0.184 $kgCO_2/(kg_{ads} \cdot h)$.

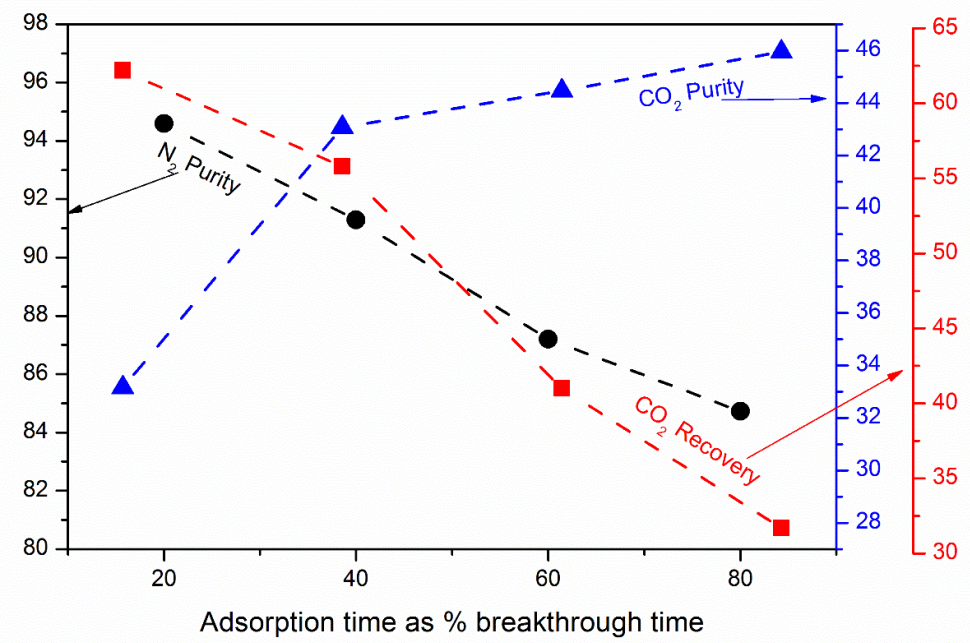

Figure 9.15: Effect of adsorption time on PVSA performance of **np** phased PVA@MIL-53(Al) pellets at 300 K (CO_2 BT: 510 s; $F_{PRES} = F_{FEED}$ = 235 SCCM), lines are drawn as guide to eye.

Further process cycle configurations were employed on np phased sample at adsorption step time equal to 40% of the breakthrough time. The effect of N_2 purge step time is shown in Figure 9.16. The inclusion of N_2 purge step significantly enhanced the N_2 product purity from 91.3% to 97.4%. On the other hand, the other process performance parameters CO_2 purity and CO_2 recovery were decreased marginally from 43.1% to 35.8% and from 55.8% to 40.9% respectively. To enhance the CO_2 purity and CO_2 recovery, a CO_2 rinse step was included between the adsorption step and blow down steps. The inclusion of CO_2 rinse step after the end of adsorption step, the void fluid inside the column is replaced by the pure CO_2 and hence the purity of CO_2 obtained in the following evacuation step is improved. The results of the studied five step PVSA process cycle are shown in Figure 9.17.

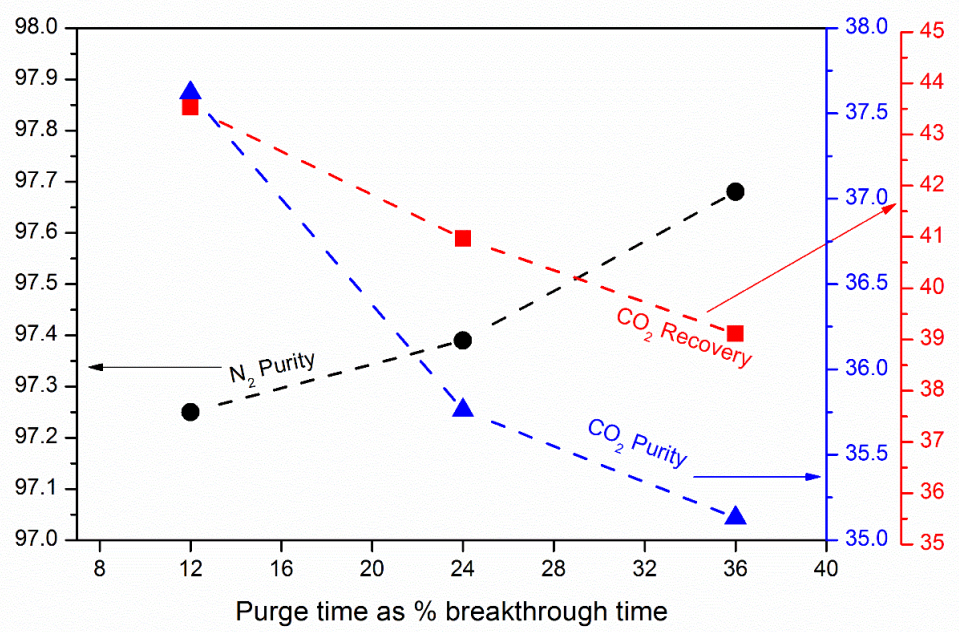

Figure 9.16: Effect of purge time on PVSA performance of **np** phased PVA@MIL-53(Al) pellets at 300 K (CO_2 BT: 510 s; t_{FEED} = 204 s, F_{PRES} = F_{FEED} = 235 SCCM, F_{PUR} = 100 SCCM).

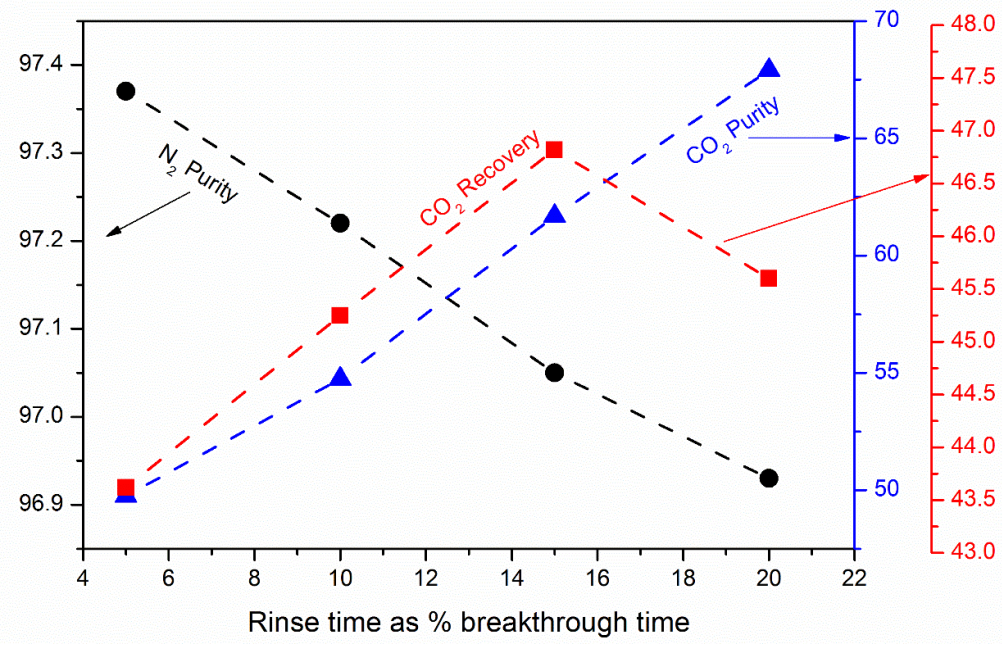

Figure 9.17: Effect of CO_2 rinse time on PVSA performance of **np** phased PVA@MIL-53(Al) pellets at 300 K (CO_2 BT: 510 s; t_{FEED} = 204 s, t_{PUR} = 120 s, F_{PRES} = F_{FEED} = 235 SCCM, F_{PUR} = 100 SCCM, F_{RIN} = 80 SCCM), lines are drawn as guide to eye.

The evaluated overall process performance of five-step (pressurization, feed, rinse, blowdown and purge) PVSA cycle at 300 K and 1.3 bar on **np** phased MIL-53(Al) was: CO_2 purity: 67.9%, CO_2 recovery: 45.6%, productivity: 0.187 $kgCO_2/(kg_{ads}\cdot h)$. The obtained CO_2 purity value on **np** phase MIL-53(Al) was higher than on the MIL-101 (35.2%), UiO-66 (54.2%) and Cu-BTC (57.6%). On the other hand, the achieved CO_2 recovery on **np** phased MIL-53(Al) was lower than on the MIL-101 (61.1%), Cu-BTC (59.1%) and UiO-66 (54.1%). The productivity of the studied **np** sample 5-step PVSA process was higher than that on UiO-66 (0.075 $kgCO_2/(kg_{ads}\cdot h)$), but lower, when compared to the MIL-101 (0.269 $kgCO_2/(kg_{ads}\cdot h)$) and Cu-BTC (0.197 $kgCO_2/(kg_{ads}\cdot h)$.

CHAPTER 10

CONCLUSIONS AND FUTURE SCOPE

This chapter summarizes the main conclusions of this thesis, and presents some recommendations for future research.

10.1 Conclusions

Many studies have shown that metal organic frameworks are promising materials for a range of adsorption and separation processes. However, majority of these studies are limited to equilibrium measurements due to the complexity associated in dynamic measurements such as the column break through studies and development of process cycles. In order to move forward from the conceptual stage towards the application stage, MOFs performance should be evaluated under practical conditions. The present study was undertaken to evaluate the CO_2/N_2 separation performance of four well-known metal organic frameworks (UiO-66, MIL-101(Cr), Cu-BTC and MIL-53(Al)) through an adsorption based process (PVSA). This involved the scale up synthesis of MOFs, shaping of MOF powders, measurement and modelling of adsorption equilibrium, dynamic breakthrough measurements and process cycle configurations.

The following are the main conclusions of the present research work:

- *Scale up synthesis*

  The MOF powders were synthesized in 10 g level using the 500 ml capacity autoclave reactor. The BET surface areas of the scale up synthesized materials: UiO-66 (1378 m^2 g^{-1}), MIL-101(Cr) (2690 m^2 g^{-1}), Cu-BTC (1476 m^2 g^{-1}) and MIL-53(Al) (1144 m^2 g^{-1}) were slightly lower than their small scale (~1 g) synthesis values of 1486 m^2 g^{-1}, 3100 m^2 g^{-1}, 1563 m^2 g^{-1} and 1242 m^2 g^{-1} respectively.

- *Pelletization of MOF powders*

  Various pelletization methods were attempted to make the MOF pellets. The use of clay binders proved to be an unsatisfactory method as it needs calcination at higher temperatures (studied four MOFs have thermal stability below 450 ^oC). The direct application of pressure on MOF powders yielded a drastic decrease in surface area. The use of quicklime, cement and white portland cement as binder also yielded a drastic decrease in surface area (for example: surface area of MIL-53 (Al) material was decreased from 1200 m^2 g^{-1} to 90 m^2 g^{-1} for MIL53-cement pellets and to 48 m^2 g^{-1} for MIL53-quiklime pellets).

  The use of polymer binder PVA also resulted in decrease of surface area of MOF materials. However, the decrease was small compared to the above discussed methods. PVA@MOF pellets were thermally stable up to 180 ^oC (beyond this temperature, PVA degradation observed in TGA curves).

- *Characterization of MOF powders and PVA@MOF pellets*

  The formulated PVA@MOF pellets have shown about 14% to 30% decrease in BET surface areas compared to the MOF powders. On the other hand, an increase in the bulk density of adsorbent samples was observed upon pelletization. In effect, the volumetric

adsorption capacity i.e. amount adsorbed per unit bed volume almost remained unchanged even after addition of the PVA binder for pelletization. TGA, FESEM, FTIR and XRD studies reveal that the original MOF structure is relatively unchanged.

- *Experimental validation of the designed PVSA apparatus*

  The developed 1-bed PVSA unit was experimentally validated using benchmark zeolite-13X adsorbent. A four step PVSA cycle consists of pressurization, adsorption, blowdown and purge along with evacuation was employed on Zeolite-13X for separation of 16% CO_2 balance N_2 mixture. The obtained purity and recovery values (CO_2 purity: 51.4%, CO_2 recovery: 63.5%) were comparable to the experimentally studied Zeolite-13X performance by Dantas et. al: CO_2 purity: 36.8%, CO_2 recovery: 90.0% and Zeolite-13X performance (P_{ads} = 2 bar, T_{ads}=35 ^oC) by Dasgupta et al: CO_2 purity: 60%, CO_2 recovery 60 %.

- *Equilibrium adsorption isotherms*

  The CO_2 adsorption uptake measured at ~0.15 bar and 298 K on MOF powders is in the order of **np**-MIL53 (1.41 mol kg^{-1}) > Cu-BTC (0.55 mol kg^{-1}) > **lp**-MIL53(0.30 mol kg^{-1}) > MIL-101 (0.22 mol kg^{-1}) > UiO-66 (0.21 mol kg^{-1}).

  The enthalpy of adsorption at zero coverage ($-\Delta h_{ads,0}$) is in the order of **np**-MIL53 (~ 41 kJ mol^{-1}) > MIL-101 (~ 31 kJ mol^{-1}) > **lp**-MIL53 (~ 26.3 kJ mol^{-1}) > Cu-BTC (~ 24.7 kJ mol^{-1}) > UiO-66 (~ 18.6 kJ mol^{-1}).

  A clear difference in the gravimetric CO_2 adsorption isotherms of MOF powder and pellets was observed. In the case of UiO-66, about 14 % lower loadings (in terms of amount adsorbed per gram of adsorbent) were observed on pellets compared to that on powder. However, when compared the loadings in terms of amount adsorbed per unit volume of adsorbent, pellets have slightly higher loadings due to the higher bulk density. This implies

that the increase in densification that occurs during the pelletization process is able to compensate for the slight loss in uptake due to the inclusion of binder. Similar results were obtained on the other three studied MOFs.

- *Binary breakthrough experiments*

  About 8 to 12 g of MOF pellets were loaded into the adsorbent column. The binary breakthrough experiments were performed using a synthetic dry flue gas containing 15% CO_2 and 85% N_2. The weakly adsorbed component N_2 was first detected at the column outlet and the strongly adsorbed component CO_2 was detected later. The observed clear difference in CO_2, N_2 breakthrough times indicate the ability of each studied MOF pellets to separate CO_2/N_2 mixtures. The overlap of CO_2 breakthrough curves at different flow rates (when plotted between cumulative flow of gas and concentration at the column outlet) suggests that there are no significant mass transfer resistances with in the flow rate ranges under consideration.

- *PVSA process experiments*

  Various cycle configurations were employed to evaluate the process performance of the chosen MOF materials for CO_2/N_2 separation. Initially, a 3-step PVSA cycle consists of pressurization with feed to 1.3 bar, adsorption at 1.3 bar and counter current blow down to 0.1 bar was studied. The effect of adsorption time on CO_2 purity, recovery and productivity were studied.

  The best performance achieved for the considered 3-step PVSA cycle was

  UiO-66(Zr): CO_2 purity: 31.7%, CO_2 recovery: 59.4%, productivity: 0.117 $kgCO_2/(kg_{ads}\cdot h)$

  MIL-101(Cr): CO_2 purity: 33.3%, CO_2 recovery: 56.7%, productivity 0.265 $kgCO_2/(kg_{ads}\cdot h)$

  Cu-BTC: CO_2 purity: 43.1%, CO_2 recovery: 59.9%, productivity: 0.168 $kgCO_2/(kg_{ads}\cdot h)$

lp-MIL-53: CO_2 purity: 30.9%, CO_2 recovery: 80.4%, productivity: 0.271 $kgCO_2/(kg_{ads} \cdot h)$

np-MIL-53: CO_2 purity: 43.0%, CO_2 recovery: 55.8%, productivity: 0.184 $kgCO_2/(kg_{ads} \cdot h)$

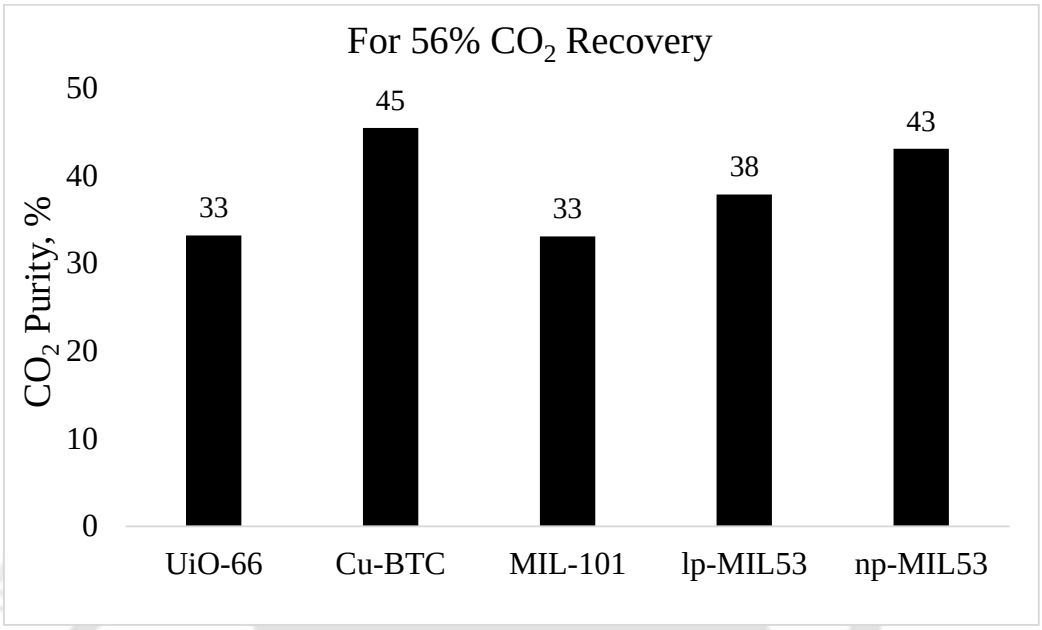

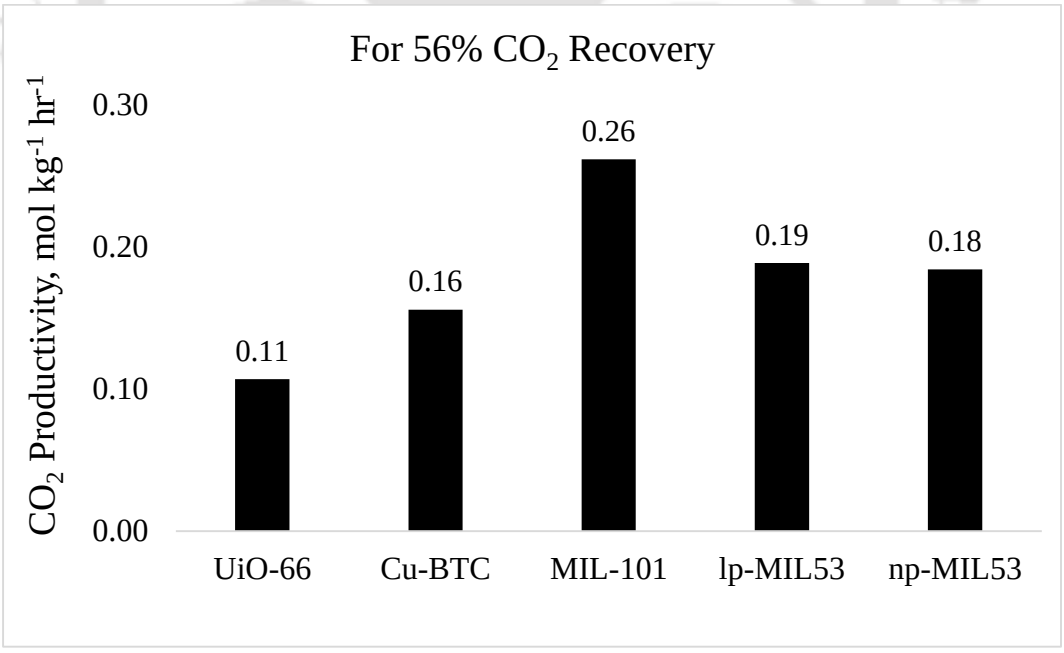

Figure 10.1 (a-b): Process performance comparison in a 3-step PVSA process for the materials studied (CO_2 recovery is fixed at 56%).

Figure 10.1(a-b) summarize typical process performance comparison in a 3-step PVSA process for the materials studied. For the sake of comparison, the CO_2 recovery is fixed at 56% and the other process parameters are compared. The highest productivity was achieved on MIL-101 MOF with a low CO_2 purity. Cu-BTC and np-MIL-53(Al) MOFs have shown highest CO_2 product purity. However, the productivity obtained on Cu-BTC was lower than the np-MIL-53(Al). On the other hand, the np-phased MIL-53(Al) is more stable towards moisture compared to the Cu-BTC MOF. Hence, among the studied materials, np-MIL-53(Al) could be a better adsorbent for CO_2/N_2 separation through PVSA process. However, a multi-bed PVSA process needs to be studied and optimized to achieve the desired CO_2 purity (>95%).

With the inclusion of N_2 purge step, N_2 product purity close to 99.9% was achieved. To this 4-step cycle, a CO_2 rinse step was included to enhance the CO_2 purity. The best performance achieved for this 5-step PVSA cycle (pressurization, adsorption, CO_2 rinse, blowdown and N_2 purge along with evacuation) was

UiO-66(Zr): CO_2 purity: 54.2%, CO_2 recovery: 54.1%, productivity: 0.075 $kgCO_2/(kg_{ads}\cdot h)$

MIL-101(Cr): CO_2 purity: 35.2%, CO_2 recovery: 61.1%, productivity 0.269 $kgCO_2/(kg_{ads}\cdot h)$

Cu-BTC: CO_2 purity: 57.6%, CO_2 recovery: 59.1%, productivity: 0.197 $kgCO_2/(kg_{ads}\cdot h)$

np-MIL-53: CO_2 purity: 67.9%, CO_2 recovery: 45.6%, productivity: 0.187 $kgCO_2/(kg_{ads}\cdot h)$

10.2 Future scope of present work

The following recommendations can be considered for future studies on evaluation of MOF materials for CO_2 capture from flue gas by vacuum swing adsorption:

- In our present study, the chosen metal organic framework materials were successfully synthesized in 10 g level. Further scale up synthesis can be attempted to yield ~100 to 500 g MOF powders.
- The shaping of MOF powders is still the challenging task. The shaped MOFs should maintain the intrinsic features of the original MOF powders. Their crystallinity, porosity and functionality should remain intact, and at the same time the shaped MOFs should possess sufficient mechanical and chemical stability. The shaping method used in the present work resulted in MOF pellets with good mechanical and chemical stability. However, about 14 to 30% decrease in BET surface area was observed for pellets compared to powder samples due to the presence of binder. So, a more efficient shaping method can be developed to overcome this challenge.
- The CO_2/N_2 separation performance of MOF materials was experimentally demonstrated using a synthetic dry flue gas. It is also worthwhile to experimentally demonstrate the CO_2 capture from a wet flue gas using the proposed 1-bed, 5-step PVSA process.
- In our study, the preliminarily process performance parameters obtained with single column PVSA look promising, however, a multi-bed PVSA process needs to be studied and optimized to achieve the desired CO_2 purities and recovery.
- Detailed cost analysis may be carried out to study the cost of CO_2 capture by vacuum swing adsorption process by taking into account all the components of capital and operating costs and comparing it with other capture technologies like absorption and membranes could be another interesting future work.

REFERENCES CITED

[1] Watts, R. G. Global Warming and the Future of the Earth, Morgan& Claypool Publishers, Denver, 2007.

[2] Intergovernmental Panel on Climate Change (IPCC) report 2009.

[3] Yang, R. T. Gas Separation by Adsorption Processes, Chapter-1; *Imperial College Press, London,* 1997.

[4] Davini, P. Flue gas treatment by activated carbon obtained from oil-fired fly ash. *Carbon,* 2002, 40, 1973-1979.

[5] Rodriguez, F.; Molina, M. Activated carbons from lignocellulosic materials by chemical and/or physical activation: an overview. *Carbon,* 1992, 30, 1111-1118.

[6] Sayari, A.; Belmabkhout, Y.; Serna, R. Flue gas treatment via CO_2 adsorption. *Chemical Engineering Journal*, 2011, 171, 760-774.

[7] Do, DD.; Wang, K. A new model for the description of adsorption kinetics in heterogeneous activated carbon. *Carbon* 1998, 36, 1539-1554.

[8] Ruthven, D. M.; and Sun, M. S. Principle of Adsorption and Adsorption Processes, Chapter-1; *Wiley-Interscience, New York,* 1984.

[9] Yang, R.T. 2003. Adsorbents-Fundamentals and applications. Wiley Interscience.

[10] Choi, S.; Drese, J.; Jones, C. Adsorbent materials for carbon dioxide capture from large anthropogenic point sources. *ChemSusChem* 2009, 2, 796-854.

[11] Wang, Y.; and LeVan, M. D. Adsorption Equilibrium of Carbon Dioxide and Water Vapor on Zeolites 5A and 13X and Silica Gel: Pure Components. *J. Chem. Eng. Data.*, 2009, *54*, 2839–2844.

[12] Robson, R. A net-based approach to coordination polymers, *J. Chem. Soc., Dalton Trans*, 2000, 21, 3735-3744.

[13] Robson, R. Design and its limitations in the construction of bi- and poly-nuclear coordination complexes and coordination polymers (aka MOFs): a personal view, *Dalton Trans*, 2008, 5113-5131.

[14] Hoskins, B. F.; Robson, R. Infinite polymeric frameworks consisting of three dimensionally linked rod-like segments. *J. Am. Chem. Soc.* 1989, 111(15), 5962-5964.

[15] Hoskins, B. F.; Robson, R. Design and construction of a new class of scaffolding-like materials comprising infinite polymeric frameworks of 3D-linked molecular rods. *J. Am. Chem. Soc.* 1990, 112(4), 1546-1554.

[16] Batten, S. R.; Hoskins, B. F.; Robson, R. 3D Knitting patterns. Two independent, interpenetrating rutile-related infinite frameworks in the structure of $Zn[C(CN)_3]_2$. *J. Chem. Soc., Chem. Commun.*, 1991, 0, 445-447.

[17] Batten, S. R.; Hoskins, B. F.; Moubarki, B.; Murray, K. S. Crystal structures and magnetic properties of the interpenetrating rutile-related compounds $M(tcm)_2$ [M = octahedral, divalent

metal; tcm– = tricyanomethanide, $C(CN)_3$–] and the sheet structures of $[M(tcm)_2(EtOH)_2]$ (M = Co or Ni), *J. Chem. Soc., Dalton Trans.*, 1999,0, 2977-2986.

[18] Abrahams, B. F.; Hoskins, B. F.; Michail, D. M.; Robson, R. Assembly of porphyrin building blocks into network structures with large channels, *Nature*, 1994, 369, 727–729.

[19] Gable, R. W.; Hoskins, B. F.; Robson, R. Synthesis and structure of $[NMe_4][CuPt(CN)_4]$: an infinite three-dimensional framework related to PtS which generates intersecting hexagonal channels of large cross section, *J. Chem. Soc., Chem. Commun.*, 1990,0, 762-763.

[20] Kondo, M.; Yosithomi, T.; Seki, K.; Matsuzaka, H.; Kitagawa, S. Three-Dimensional Framework with Channeling Cavities for Small Molecules: $\{[M_2(4, 4'\text{-bpy})_3(NO_3)_4]\cdot xH_2O\}_n$ (M = Co, Ni, Zn), *Angew. Chem., Int. Ed.* 1997, 36, 1725-1727.

[21] Li, H.; Eddaoudi, M.; O'Keeffe; Yaghi, O. M. Design and synthesis of an exceptionally stable and highly porous metal-organic framework, *Nature*, 1999, 402, 276–279.

[22] Li, J. R.; Ma, Y.; McCarthy, M.C.; Sculley, J.; Yu, J.; Jeong, H. K.; Balbuena, P. B.; Zhou, H. C. *Coordination Chemistry Reviews.*, 2011, 255, 1791–1823.

[23] Li, H.; Eddaoudi, M.; O'Keeffe, M.; Yaghi, O. M. Design and synthesis of an exceptionally stable and highly porous metal-organic framework. *Nature*, 1999, 402(6759), 276-279.

[24] Eddaoudi, M.; Kim, J.; Rosi, N.; Vodak, D.; Wachter, J.; O'Keeffe, M.; Yaghi, O. M. Systematic design of pore size and functionality in isoreticular MOFs and their application in methane storage. *Science*, 2002, 295,469-472.

[25] Yazaydin, A. O.; Snurr, R. Q.; Park, T. –H.; Koh, K.; Liu, J.; LeVan, M. D.; Benin, A. I.; Jakubczak, P.; Lanuza, M.; Galloway, D. B.; Low, J. J.; Willis, R. R. Screening of Metal Organic Frameworks for Carbon Dioxide Capture from Flue Gas Using a Combined Experimental and Modeling Approach. *J. Am. Chem. Soc*. 2009, 131, 18198–18199.

[26] Furukawa, H.; Ko, N.; Go, Y. B.; Aratani, N.; Choi, S. B.; Choi, E.; Yazaydin, A. O.; Snurr, R. Q.; O'Keeffe, M.; Kim, J.; Yaghi, O. M. Ultra high Porosity in Metal–Organic Frameworks. *Science* 2010, 329, 424–428.

[27] Serre, C.; Millange, F.; Thouvenot, C.; Noguès, M.; Marsolier, G.; Louër, D.; Férey, G. Very Large Breathing Effect in the First Nanoporous Chromium(III)-Based Solids: MIL-53 or CrIII(OH)•{$O_2C-C_6H_4-CO_2$}•{$HO_2C-C_6H_4-CO_2H$}x•H_2Oy. *J. Am. Chem. Soc*. 2002, 124, 13519–13526.

[28] Yaghi, O. M.; O'Keeffe, M.; Ockwig, N. W.; Chae, H. K.; Eddaoudi, M.; Kim, J. synthesis and the design of new materials. *Nature* 2003, 423, 705–714.

[29] Loiseau, T.; Serre, C.; Hugueanrd, C.; Fink, G.; Taulelle, F.; Henry, M.; Bataille, T.; Férey, G. A rationale for the large breathing of the porous Aluminum Terephthalate [MIL-53] upon hydration. *Chem.–Eur. J.* 2004, 10, 1373–1382.

[30] Bourrelly, S.; Llewellyn, P. L.; Serre, C.; Millange, F.; Loiseau, T. Férey, G. Different adsorption behaviors of methane and carbon dioxide in the isotypic nanoporous Metal Terephthalates MIL-53 and MIL-47. *J. Am. Chem. Soc*. 2005, 127, 13519–13521.

[31] Sumida, K.; Rogow, D. L.; Mason, J. A.; McDonald, T. M.; Bloch, E. D.; Herm, Z. R.; Bae, T. -H.; Long, J. R. Carbon dioxide capture in Metal-Organic Frameworks. *Chem. Rev*. 2012, 112, 724–781.

[32] Klinowski, J.; Almeida, F.; Silva, P.; Rocha, J. Microwave-Assisted Synthesis of Metal-Organic Frameworks. *Dalton Transaction*, 2011, 40(2), 321-330.

[33] Jung, D.; Yang, D.; Kim, J.; Kim, J.; Ahn, W. Facile synthesis of MOF-177 by a sonochemical method using 1-methyl-2-pyrrolidinone as a solvent. *Dalton Transaction*, 2010, 39(11), 2883-7.

[34] Pichon, A.; James, S. An array-based study of reactivity under solvent-free mechanochemical conditions-insights and trends. *CrystEngCommunity*, 2008, 10, 1839-1847.

[35]. Gaab, M.; Trukhan, N.; Maurer, S.; Gummaraju, R.; Müller, U. The progression of Al-based metal-organic frameworks – From academic research to industrial production and applications. *Microporous and Mesoporous Materials*, 2012. 157, 131-136.

[36] Schaate, A.; Roy, P.; Godt, A.; Lippke, J.; Waltz, F.; Wiebcke, M.; Behrens, P. Modulated synthesis of Zr-based metal-organic frameworks: from nano to single crystals. *Chemistry* (Weinheim an der Bergstrasse, Germany), 2011. 17, 6643-51.

[37] Forster, P. M.; Burbank, A. R.; Livage, C.; Férey, G.; Cheetham, A. K. The role of temperature in the synthesis of hybrid inorganic–organic materials: the example of cobalt succinates. *Chem. Commun.*, 2004, 0, 368-369.

[38] Cao, Y.; Zhao, Y.; Lv, Z.; Song, F.; Zhong, Q. Preparation and enhanced CO_2 adsorption capacity of UiO-66/graphene oxide composites, *Journal of Industrial and Engineering Chemistry*, 2015, 27, 102–107.

[39] Loiseau, T.; Serre, C.; Hugueanrd, C.; Fink, G.; Taulelle, F.; Henry, M.; Bataille, T.; Férey, G. A rationale for the large breathing of the porous Aluminum Terephthalate [MIL-53] upon hydration. *Chem.–Eur. J.* 2004, *10***,** 1373–1382.

[40] Chowdhury, P.; Bikkina, C.; Gumma, S. Gas adsorption properties of the Chromium-Based Metal Organic Framework MIL-101. *J. Phys. Chem.C.* 2009, *113*, 6616–6621.

[41] Arstad, B.; Fjellvåg, H.; Kongshaug, K.; Swang, O.; Blom, R. Amine functionalised metal organic frameworks (MOFs) as adsorbents for carbon dioxide. *Adsorption.* 2008, *14,* 755–762.

[42] Millward, A. R.; Yaghi, O. M. Metal Organic Frameworks with Exceptionally High Capacity for Storage of Carbon Dioxide at Room Temperature. *J. Am. Chem. Soc.* 2005, *127,* 17998–17999.

[43] Chowdhury, P.; Bikkina, C; Meister, D; Dreisbach, F.; Gumma, S. Comparison of adsorption isotherms on Cu-BTC metal organic frameworks synthesized from different routes. *Microporous and Mesoporous Materials* 2009, *117*, 406–413.

[44] Sumida, K.; Her, J.-H.; Dinc_a, M.; Murray, L. J.; Schloss, J. M.; Pierce, C. J.; Thompson, B. A.; FitzGerald, S. A.; Brown, C. M.; Long, J. R. A Metal-Organic Framework with Exposed Cr^{2+} Sites. *J. Phys. Chem. C* 2011, *115*, 8414–8421.

[45] Herm, Z. R.; Swisher, J. A.; Smit, B.; Krishna, R.; Long, J. R. Metal–Organic Frameworks as Adsorbents for Hydrogen Purification and Precombustion Carbon Dioxide Capture. *J. Am. Chem. Soc.* 2011, *133*, 5664–5667.

[46] Wu, H.; Zhou, W.; Yildirim, T. High-Capacity Methane Storage in Metal–Organic Frameworks M_2(dhtp): The Important Role of Open Metal Sites. *J. Am. Chem. Soc.* 2009, *131*, 4995–5000.

[47] Liang, Z.; Marshall, M.; Chaffee, A. L. CO_2 adsorption, selectivity and water tolerance of pillared-layer metal organic frameworks. *Microporous and Mesoporous Materials* 2010, *132*, 305–310.

[48] Achmann, S.; Hagen, G.; Hämmerle, M.; Malkowsky, I.; Kiener, C.; Moos, R. Sulfur Removal from Low-Sulfur Gasoline and Diesel Fuel by Metal-Organic Frameworks. *Chem. Eng. Technol.* 2010, *33*, 275–280.

[49] Horike, S.; Shimomura, S.; Kitagawa, S. Soft porous crystals. *Nat Chem*. 2009, 9, 695-704.

[50] Zhao, D.; Yuan, D. Q.; Zhou, H. C. The current status of hydrogen storage in metal–organic frameworks. *Energy Environ. Sci.* 2008, *1*, 222–235.

[51] Hu, Y. H.; Zhang, L. Hydrogen Storage in Metal–Organic Frameworks. *Adv. Mater.* 2010, *22*, E117–E130.

[52] Murray, L. J.; Dinca, M.; Long, J. R. Hydrogen storage in metal–organic frameworks. *Chem. Soc. Rev.* 2009, *38*, 1294–1314.

[53] Dinca, M.; Long, J. R. Hydrogen Storage in Microporous Metal–Organic Frameworks with Exposed Metal Sites. *Angew. Chem., Int. Ed.* 2008, *47*, 6766–6779.

[54] Férey, G.; Serre, C.; Devic, T.; Maurin, G.; Jobic, H.; Llewellyn, P. L.; DeWeireld, G.; Vimont, A.; Daturi, M.; Chang, J. -S. Why hybrid porous solids capture greenhouse gases? *Chem. Soc. Rev.* 2011**,** *40*, 550–562.

[55] D'Alessandro, D. M.; Smit, B.; Long, J. R. Carbon Dioxide Capture: Prospects for New Materials. *Angew. Chem., Int. Ed.* 2010, *49*, 6058–6082.

[56] Li, J. R.; Ma, Y.; McCarthy, M. C.; Sculley, J.; Yu, J.; Jeong, H. K.; Balbuena, P. B.; Zhou, H. C. Carbon dioxide capture-related gas adsorption and separation in metal-organic frameworks. *Coord. Chem. Rev.* 2011, *255*, 1791–1823.

[57] Wang, Z.; Chen, G.; Ding, K. L. Self-Supported Catalysts. *Chem. Rev.* 2009, *109*, 322–359.

[58] Corma, A.; Garcia, H.; Xamena, F. X. L. Engineering Metal Organic Frameworks for Heterogeneous Catalysis. *Chem. Rev.* 2010, *110,* 4606–4655.

[59] Horcajada, P.; Serre, C.; Vallet-Regi, M.; Sebban, M.; Taulelle, F.; Férey, G. Metal–Organic Frameworks as Efficient Materials for Drug Delivery. *Angew. Chem., Int. Ed.* 2006, *45,* 5974–5978.

[60] Huxford, R. C.; Della Rocca, J.; Lin, W. B. Metal-organic frameworks as potential drug carriers. *Curr. Opin. Chem. Biol.* 2010, *14,* 262–268.

[61] Mishra, P.; Edubilli, P.; Uppara, H. P.; Mandal, B.; Gumma, S. Effect of Adsorbent History on Adsorption Characteristics of MIL-53(Al) Metal Organic Framework. *Langmuir,* 2013, 29 (39), 12162–12167.

[62] Chui, S. S. Y.; Lo, S. M. F.; Charmant, J. P. H.; Orpen, A. G.; Williams, I. D. A Chemically Functionalizable Nanoporous material $[Cu_3(TMA)_2(H_2O)_3]_n$. *Science,* 1999, 283, 1148-1150.

[63] http://www.chemtube3d.com/solidstate/MOF-HKUST-1.html

[64] Férey, G.; Mellot-Draznieks, C.; Serre, C.; Millange, F.; Dutour, J.; Surblé S.; Margiolaki, I. A Chromium Terephthalate-Based Solid with Unusually Large Pore Volumes and Surface Area, *Science,* 2005, 309, 2040-2042.

[65] http://www.metal-organic-frameworks.eu/adsorbentien_engl.shtml

[66] Cavka, J. H.; Jakobsen, S.; Olsbye, U.; Guillou, N.; Lamberti, C.; Bordiga, S.; Lillerud, K. P. A New Zirconium Inorganic Building Brick Forming Metal Organic Frameworks with Exceptional Stability, *J. Am. Chem. Soc.* 2008, 130, 13850–13851.

[67] http://www.chemtube3d.com/solidstate/MOF-UiO66.html

[68] Loiseau, T.; Serre, C.; Haguenard, C.; Fink, G.; Taulelle, F.; Henry, M.; Bataille, T.; Ferey, G. A Rationale for the Large Breathing of the Porous Aluminum Terephthalate (MIL-53) Upon Hydration. *Chem. Eur. J,* 2004, 10, 1373-1382.

[69] Liu, Y.; Her, J. -H.; Dailly, A.; Ramirez-Cuesta, A. J.; Neumann, D. A.; Brown, C. M. Reversible structural transition in MIL-53 with large temperature hysteresis. *J. Am. Chem. Soc.* 2008, *130,* 11813–11818.

[70] Beurroies, I.; Boulhout, M.; Llewellyn, P. L.; Kuchta, B.; Férey, G.; Serre, C.; Denoyel, R. Using Pressure to Provoke the Structural Transition of Metal–Organic Frameworks. *Angew. Chem., Int. Ed.* 2010, *49,* 7526–7529.

[71] Chowdhury, P.; Mekala, S.; Dreisbach, F.; Gumma, S. Adsorption of CO, CO_2 and CH_4 on Cu-BTC and MIL-101 metal organic frameworks: Effect of open metal sites and adsorbate polarity. *Microporous and Mesoporous Materials* 2012, *152,* 246–252.

[72] Arstad, B.; Fjellvåg, H.; Kongshaug, K.; Swang, O.; Blom, R. Amine functionalised metal organic frameworks (MOFs) as adsorbents for carbon dioxide. *Adsorption* 2008, 14, 755-62.

[73] Millward, A. R.; Yaghi, O. M. Metal Organic Frameworks with Exceptionally High Capacity for Storage of Carbon Dioxide at Room Temperature. *J. Am. Chem. Soc.* 2005, *127,* 17998–17999.

[74] Herm, Z. R.; Swisher, J. A.; Smit, B.; Krishna, R.; Long, J. R. Metal–Organic Frameworks as Adsorbents for Hydrogen Purification and Precombustion Carbon Dioxide Capture. *J. Am. Chem. Soc.* 2011, *133,* 5664–5667.

[75] Dietzel, P. D. C.; Besikiotis, V.; Blom, R. Application of metal–organic frameworks with coordinatively unsaturated metal sites in storage and separation of methane and carbon dioxide. *J. Mater. Chem.*, 2009, *19*, 7362–7370.

[76] Caskey, S. R.; Wong-Foy, A. G.; Matzger, A. J. Dramatic Tuning of Carbon Dioxide Uptake via Metal Substitution in a Coordination Polymer with Cylindrical Pores. *J. Am. Chem. Soc.* 2008, *130*, 10870–10871.

[77] Liang, Z.; Marshall, M.; Chaffee, A. L. CO_2 adsorption, selectivity and water tolerance of pillared-layer metal organic frameworks. *Microporous and Mesoporous Materials* 2010**,** *132*, 305–310.

[78] Yazaydin, A. O.; Benin, A.; Faheem S. A.; Jakubczak, P.; Low, J.; Willis R. R.; Snurr R. Q. Enhanced CO_2 adsorption in metal-organic frameworks via occupation of open-metal sites by coordinated water molecules. *Chemistry of Materials*, 2009, 21, 1425-30.

[79] Herm, Z. R.; Swisher, J. A.; Smit, B.; Krishna, R.; Long, J. R. Metal–Organic Frameworks as Adsorbents for Hydrogen Purification and Precombustion Carbon Dioxide Capture. *J. Am. Chem. Soc.* 2011, *133*, 5664–5667.

[80] Kim, J.; Yang, S.; Choi, S.; Sim, J.; Kim, J.; Ahn, W. Control of catenation in CuTATB-n metal-organic frameworks by sonochemical synthesis and its effect on CO_2 adsorption. Journal of Materials Chemistry 2011, 21, 3070.

[81] An, J.; Geib, S.; Rosi, N. High and selective CO_2 uptake in a cobalt adeninate metalorganic framework exhibiting pyrimidine- and amino-decorated pores. *J. Am. Chem. Soc.* 2010, 132,38-9.

[82] Chen, S.; Chen, M.; Takamizawa, S.; Wang, P.; Lv, G.; Sun, W. Porous cobalt(ii)-imidazolate supramolecular isomeric frameworks with selective gas sorption property. *Chemical Communications*, 2011, 47, 4902-4.

[83] Morris, W.; Leung, B.; Furukawa, H.; Yaghi, O. M.; He, N.; Hayashi, H. A combined experimental-computational investigation of carbon dioxide capture in a series of isoreticular zeolitic imidazolate frameworks. *J. Am. Chem. Soc.* 2010, 132, 11006-8.

[84] Liang, Z.; Marshall, M.; Chaffee, A. L. CO_2 Adsorption-Based Separation by Metal Organic Framework [Cu-BTC] versus Zeolite 13X. *Energy & Fuels* 2009, *23*, 2785–2789.

[85] Pakseresht, S.; Kazemeini, M.; Akbarnejad, M. M. Equilibrium isotherms for CO, CO_2, CH_4 and C_2H_4 on the 5A molecular sieve by a simple volumetric apparatus, *Sep. Purf. Tech.*, 2002, 28, 53-60.

[86] Himeno, S; Komatsu, T.; Fujita, S. High-Pressure Adsorption Equilibria of Methane and Carbon Dioxide on Several Activated Carbons. *J. Chem. Eng. Data* 2005, *50*, 369–376.

[87] Golden, T. C., and Sircar, S., Gas Adsorption on Silicalite" *J. Coll. Inter. Sci.*, 1994, 162, 182-188.

[88] Aprea, P.; Caputo, D.; Gargiulo, N.; Iucolano, F.; Pepe, F. J. Modeling Carbon Dioxide Adsorption on Microporous Substrates: Comparison between Cu-BTC Metal−Organic Framework and 13X Zeolitic Molecular Sieve. *Chem. Eng. Data*. 2010, 55, 3655-61.

[89] Weiland, R. H.; Dingman, J. C.; Cronin, D. B. Heat Capacity of Aqueous Monoethanolamine, Diethanolamine, N-Methyldiethanolamine, and N-Methyldiethanolamine-Based Blends with Carbon Dioxide. *J. Chem. Eng. Data*, 1997, 42, 1004-6.

[90] Mason, J. A.; Sumida, K.; Herm, Z. R.; Krishna, R.; Long, J. R. Evaluating metal–organic frameworks for post-combustion carbon dioxide capture via temperature swing adsorption, *Energy Environ. Sci.*, 2011, 4, 3030-3040.

[91] Prasad, T. K.; Hong, D. H.; Suh, M. P. High Gas Sorption and Metal-Ion Exchange of Microporous Metal–Organic Frameworks with Incorporated Imide Groups, *Chem. Eur. J.* 2010, 16, 14043.

[92] Demessence, A.; D'Alessandro, D. M.; Foo, M. L.; Long, J. R. Strong CO_2 Binding in a Water-Stable, Triazolate-Bridged Metal−Organic Framework Functionalized with Ethylenediamine *J. Am. Chem. Soc.* 2009, 131, 8784-86.

[93] Phan, A.; Doonan, C. J.; Uribe-Romo, F. J.; Knobler, C. B.; O'Keefe, M.; Yaghi, O. M. Synthesis, Structure, and Carbon Dioxide Capture Properties of Zeolitic Imidazolate Frameworks, *Acc. Chem. Res*. 2010, 43, 58-67.

[94] Wang, B.; Cote, A. P.; Furukawa, H.; O'Keefe, M.; Yaghi,O. M. Colossal cages in zeolitic imidazolate frameworks as selective carbon dioxide reservoirs, *Nature*, 2008, 453, 207-211.

[95] Rallapalli, P.; Prasanth, K. P.; Patil, D.; Somani, R. S.; Jasra, R. V.; Bajaj, H. C. Sorption studies of CO_2, CH_4, N_2, CO, O_2 and Ar on nanoporous aluminum terephthalate [MIL-53(Al)]. *J. Porous Mater.* 2011, *18*, 205–210.

[96] Prsanth Mishra, Ph. D Thesis (2014), Indian Institute of Technology, IIT Guwahati.

[97] Bloch, E. D.; Britt, D.; Lee, C.; Doonan, C. J.; Uribe-Romo, F. J.; Furukawa, H.; Long, J. R.; Yaghi, O. M. Metal Insertion in a Microporous Metal−Organic Framework Lined with 2,2′-Bipyridine. *J. Am. Chem. Soc.* 2010, 132, 14382-84.

[98] Dreisbach, F.; Staudt, R.; Keller, J. U. High Pressure Adsorption Data of Methane, Nitrogen, Carbon Dioxide and their Binary and Ternary Mixtures on Activated carbon. *Adsorption* 1999, *5*, 215–227.

[99] Golden, T. C.; Sircar, S. Gas Adsorption on Silicalite. *J. Coll. Inter. Sci.* 1994, *162*, 182–188.

[100] Bastin, L.; Patrick S. Ba´rcia, P. S.; Hurtado, E. J.; Silva J. A. C.; Rodrigues, A. E.; Chen. B. A Microporous Metal-Organic Framework for Separation of CO_2/N_2 and CO_2/CH_4 by Fixed-Bed Adsorption. *J. Phys. Chem. C.* 2008, 112, 1575-1581.

[101] Liu, J.; Tian, J.; Thallapally, P. K.; McGrail, B. P. Selective CO_2 Capture from flue gas Metal Organic Frameworks- A Fixed Bed Study, *J. Phys. Chem. C.* 2012, 116, 9575-9581.

[102] Asadi, T.; Ehsani, M. R. An Experimental Study of Adsorption Breakthrough Curves for CO_2/CH_4 Separation in a Fixed Bed of Nanoporous Shaped Copper Trimesate Metal Organic Framework, *Iranian Journal of Oil & Gas Science and Technology*, 2013, 2, 54-66.

[103] Peter, S. A.; Baron, G. V.; Gascon, J.; Kapteijn, F.; Denayer, J. F. M. Dynamic desorption of CO_2 and CH_4 from amino-MIL-53(Al) adsorbent, *Adsorption*, 2013, 19, 1235–1244.

[104] Remy, T.; Peter, S. A.; Perre, S. V. P.; Valvekens, P.; Vos, D. E.; Baron, G. V.; Denayer, J. F. M. Selective Dynamic CO_2 Separations on Mg-MOF-74 at Low Pressures: A Detailed Comparison with 13X, *J. Phys. Chem. C.*2013, 117, 9301-9310.

[105] Kizzie, A. C.; Wong-foy, A. G.; Matzger, A. J. Effect of Humidity on the Performance of Microporous Coordination Polymers as Adsorbents for CO_2 Capture, *Langmuir*, 2011, 27, 6368–6373.

[106] Kim, S. N.; Lee, Y. R.; Hong, S. H.; Jang, M. S.; Ahn, W. S. Pilot scale synthesis of a Zirconium-benzenedicarboxylate UiO-66 for adsorption and catalysis, *Catal. Today*, 2015, 245, 54–60.

[107] Dasgupta, S.; Divekar, S; Aarti.; Spjelkavik, A. I.; Didriksen, T.; Nanoti, A.; Blom, R. Adsorption properties and performance of CPO-27-Ni/alginate spheres during multicycle pressure-vacuum-swing adsorption (PVSA) CO_2 capture in the presence of moisture, *Chemical Engineering Science*, 2015, 137, 525–531.

[108] Finsy, V.; Ma, L.; Alaerts, L.; Vos, D. E.; Baron, G. V.; Denayer, J. F. M. Separation of CO_2/CH_4 mixtures with the MIL-53(Al) metal–organic framework, *Microporous and Mesoporous Materials*, 2009, 120, 221–227.

[109] Dasgupta, S.; Biswas, N.; Aarti, Gode, N. G.; Divekar; Nanoti, A.; Goswami, A. N. CO_2 recovery from mixtures with nitrogen in a vacuum swing absorber using metal organic framework adsorbent: a comparative study, *Int. J. Greenhouse Gas Control.* 2012, 7, 225–229.

[110] Andersen, A.; Divekar, S.; Dasgupta, S.; Cavka, J. H; Aarti, Nanoti, A.; Spjelkavik, A.; Goswami, A. N.; Garg M. O; Blom, R. On the development of Vacuum Swing adsorption (VSA) technology for post-combustion CO_2 capture, *Energy Procedia*, 2013, 37, 33 – 39.

[111] Dantas, T. L. P.; Luna, F. M. T.; Silva Jr, I. J.; Torres, A. E. B.; Azevedo, D. C. S. de.; Rodrigues, A. E.; Moreira, R. F.P.M. Carbon dioxide–nitrogen separation through pressure swing adsorption, *Chem. Eng. J.* 2011,172, 698– 704.

[112] Dantas, T. L. P.; Rodrigues, A. E.; Moreira, R. F.P.M. Separation of Carbon Dioxide from Flue Gas Using Adsorption on Porous Solids, book chapter in 'Greenhouse Gases – Capturing, Utilization and Reduction', DOI: 10.5772/2521.

[113] Liu. Z.; Grande, C. A.; Li, P.; Yu, J.; Rodrigues, A. E. Multi-bed Vacuum Pressure Swing Adsorption for carbon dioxide capture from flue gas, *Separation and Purification Technology*, 2011,81, 307–317.

[114] Nanoti, A.; Dasgupta, S.; Aarti, Biswas, N.; Goswami, A. N.; Garg, M. O.; Divekar, S.; Pendem, C. Reappraisal of the Skarstrom Cycle for CO_2 Recovery from Flue Gas Streams: New Results with Potassium-Exchanged Zeolite Adsorbent, *Ind. Eng. Chem. Res.* 2012, 51, 13765−13772.

[115] Yang, R. T., Gas Separation by Adsorption Processes, Imperial College Press, London (1997), Chapter-1.

[116] Barton, T. J.; Bull, L. M.; Klemperer, W. G.; Loy, D. A.; McEnaney, B.; Misono, M.; Monson, P. A.; Pez, G.; Scherer, G. W.; Vartuli, J. C.; Yaghi, O. M. Tailored Porous Materials. *Chem. Mater*. 1999**,** *11,* 2633–2656.

[117] Siperstein, F. R.; Myers, A.L. Mixed-Gas Adsorption. *AIChE J*. 2001**,** *47*, 1141–1159.

[118] Myers, A.L. and J.M. Prausnitz, Thermodynamics of Mixed-Gas Adsorption. *Aiche Journal*, 1965. 11(1): 121.

[119] Katz, M. J.; Brown, Z. J.; Colon, Y. J.; Siu, P. W.; Scheidt, K. A.; Snurr, R. Q.; Hupp, J. T.; Farha, O. K. A facile synthesis of UiO-66, UiO-67 and their derivatives, *Chem. Commun*.,2013, 49, 9449-9451.

[120] Liu, J.; Culp, J. T.; Natesakhawat, S.; Bockrath, B. C.; Zande, B.; Sankar, S. G.; Garberoglio, G.; Johnson, K. J. Experimental and Theoretical Studies of Gas Adsorption in Cu3(BTC)2: An Effective Activation Procedure, *J. Phys. Chem. C*. 2007, 111, 9305.

[121] Zhao. T.; Jeremias. F.; Boldog. Ishtvan.; Nguyen. B.; Henninger. H. K.; Janiak. C.; High-yield, fluoride-free and large-scale synthesis of MIL-101(Cr), *Dalton Trans.*, 2015, 44, 16791-16801.

[122] Spjelkavik; aarti. A.; Divekar, S.; Didriksen, T.; Blom, R. Forming MOFs into Spheres by Use of Molecular Gastronomy Methods, *Chem. Eur. J.*, 2014, 20, 8973 –8978.

[123] Bragg, W.L; *The Crystalline State: Volume I.* New York: The Macmillan Company, 1934.

[124] Kawatra, S.K.; Ripke. S. J., *Int. J. Min Process*, 2002, 65, 141-149.

[125] Ren, J.; Musyoka, N. M.; Langmi, H. W.; Swartbooi, A.; North, B. C.; Mathe, M. A more efficient way to shape metal-organic framework (MOF) powder materials for hydrogen storage applications, *Int J Hydrogen Energy*, 2015,40, 4617-4622.

[126] Cmarik, G. E.; Kim, M.; Cohen, S. M.; Walton, K. S.; Tuning the Adsorption Properties of UiO-66 via Ligand Functionalization, *Langmuir*, 2012, 28,15606−15613.

[127] Cao, Y.; Zhao, Y.; Lv, Z.; Song, F.; Zhong, Q. Preparation and enhanced CO_2 adsorption capacity of UiO-66/graphene oxide composites, *J. Ind. Eng. Chem.*, 2015,27,102–107.

[128] Xian, S.; Wu, Y.; Wu, J.; Wang.; Xiao, J. Enhanced Dynamic CO_2 Adsorption Capacity and CO_2/CH_4 Selectivity on Polyethylenimine-Impregnated UiO-66, *Ind. Eng. Chem. Res.*, 2015, 54,11151−11158.

[129] Asadi, T.; Ehsani, M. R.; Ribeiro, A. M.; Loureiro, J. M.; Rodrigues, A. E. CO_2/CH_4 separation by adsorption using nanoporous metal organic framework copper-benzene-1,3,5-tricarboxylate tablet, *Chem. Eng. Technol.*, 2013, 36, 1231-1239.

[130] Morrison, R. T.; Boyd, R. N. Organic Chemistry, Vol 36. 6th ed., Prentice hall, New Jersey, 1992, p. 3089.

[131] Ali, Z. I.; Ali, F. A.; Hosam, A. M. Effect of electron beam irradiation on the structural properties of PVA/V_2O_5 xerogel, *Spectrochim. Acta A,* 2009,72,868-875.

[132] Chavan, S.; Vitillo, J. G.; Gianolio, D.; Zavorotynska, O.; Civalleri, B.; Jakobsen, S.; Nilsen, M. H.; Valenzano, L.; Lamberti, C.; Lillerud, K. P.; and Bordiga, S. H_2 storage in isostructural UiO-67 and UiO-66 MOFs, *Phys. Chem. Chem. Phys*., 2012, 14, 1614–1626.

[133] Millward, A. R.; Yaghi, O. M. Metal Organic Frameworks with Exceptionally High Capacity for Storage of Carbon Dioxide at Room Temperature. *J. Am. Chem. Soc.*, 2005, 127, 17998–17999.

[134] Herm, Z. R.; Swisher, J. A.; Smit, B.; Krishna; R.; Long, J. R. Metal–Organic Frameworks as Adsorbents for Hydrogen Purification and Precombustion Carbon Dioxide Capture. *J. Am. Chem. Soc.* 2011,133, 5664–5667.

[135] Chowdhury, P.; Mekala, S.; Dreisbach, F.; Gumma, S. Adsorption of CO, CO_2 and CH_4 on Cu-BTC and MIL-101 metal organic frameworks: Effect of open metal sites and adsorbate polarity. *Microporous and Mesoporous Materials*, 2012, 152, 246–252.

[136] Liang, Z.; Marshall, M.; Chaffee, A. L. CO_2 Adsorption-Based Separation by Metal Organic Framework [Cu-BTC] versus Zeolite [13X]. *Energy & Fuels*, 2009, 23, 2785–2789.

[137] Bourrelly, S.; Llewellyn, P. L.; Serre, C.; Millange, F.; Loiseau, T.; Férey, G.; Different adsorption behaviors of methane and carbon dioxide in the isotypic nanoporous Metal Terephthalates MIL-53 and MIL-47, *J. Am. Chem. Soc.*, 2005, 27, 13519–13521.

[138] Liang, Z.; Marshall, M.; Chaffee, A. L. CO_2 adsorption, selectivity and water tolerance of pillared-layer metal organic frameworks. *Microporous and Mesoporous Materials*, 2010, 132, 305–310.

[139] Llewellyn, P. L.; Bourrelly, S.; Serre, C.; Vimont, A.; Daturi, M.; Hamon, L.; Weireld, G. D.; Chang, J. S.; Hong, D. Y.; Hwang, K.; Jhung, S. H.; Fe´rey, G.; High Uptakes of CO_2 and CH_4 in Mesoporous Metals Organic Frameworks MIL-100 and MIL-101. *Langmuir*, 2008, 24, 7245–7250.

[140] Dietzel, P. D. C.; Besikiotis, V.; Blom, R. Application of metal–organic frameworks with coordinatively unsaturated metal sites in storage and separation of methane and carbon dioxide. *J. Mater. Chem.*, 2009, 19, 7362–7370.

[141] Farrusseng, D.; Daniel, C.; Gaudillere, C.; Ravon, U.; Schuurman, Y.; Mirodatos, C.; Dubbeldam, D.; Frost, H.; Snurr, R. Q.; Heats of Adsorption for Seven Gases in Three Metal-Organic Frameworks: Systematic Comparison of Experiment and Simulation. *Langmuir*, 2009, 25, 7383–7388.

[142] Mason, J. A.; Sumida, K.; Herm, Z. R.; Krishna, R.; Long, J. R.; Evaluating metal–organic frameworks for post-combustion carbon dioxide capture via temperature swing adsorption. *Energy Environ. Sci.*, 2011, 4, 3030-3040.

[143] Sun, M. S.; Shah, D. B.; Xu, H. H; Talu, O. Adsorption equilibria of C1 to C4 alkanes, CO_2, and SF_6 on silicalite. *J. Phys. Chem. B*, 1998, 102, 1466-1473.

[144] Liu, Z.; Grande, C. A; Li, P.; Yu, J.; Rodrigues, A.E. Adsorption and desorption of carbon dioxide and nitrogen on zeolite 5A, Sep. Sci. Technol., 2011, 46, 434-451.

[145] Ye. S.; Jiang. X.; Ruan. Li. W.; Liu. B.; Wang. Yi. M.; Zhu. J. F.; Qiu. L. G.; Microporous and Mesoporous Materials, 2013, 179, 191–197.

[146] Munusamy. K.; Sethia. G.; Patil. D. V.; Rallapalli. P. B. S.; Somani. R. S.; Bajaj. H. C. Chemical Engineering Journal, 2012, 195–196, 359–368.

[147] Janabi, N. Al.; Deng, H.; Borges, J.; Liu, X.; Garforth, A.; Siperstein, F. R.; Fan, X. A Facile Post-Synthetic Modification Method to Improve Hydrothermal Stability and CO_2 Selectivity of CuBTC Metal Organic Framework, *Ind. Eng. Chem. Res.* 2016, 55, 7941−7949.

[148] Pradip Chowdhury, Ph. D Thesis (2010), Indian Institute of Technology, IIT Guwahati.

[149] Neimark, A.V.; Coudert, F. -X.; Triguero, C.; Boutin, A.; Fuchs, A. H.; Beurroies, I.; Denoyel, R. Structural Transitions in MIL-53(Cr): View from Outside and Inside. *Langmuir* 2011, *27***,** 4734–4741.

[150] Ortiz. A. U.; Boutin, A.; Fuchs, A. H.; Coudert, F. -X. Anisotropic Elastic Properties of Flexible Metal-Organic Frameworks: How Soft are Soft Porous Crystals? *Phys. Rev. Lett.* 2012, *109***,** 195502 (1–5).

[151] Bourrelly, S.; Llewellyn, P. L.; Serre, C.; Millange, F.; Loiseau, T. Férey, G. Different adsorption behaviors of methane and carbon dioxide in the isotypic nanoporous Metal Terephthalates MIL-53 and MIL-47. *J. Am. Chem. Soc*. 2005, *127*, 13519–13521.

[152] Rallapalli, P.; Prasanth, K. P.; Patil, D.; Somani, R. S.; Jasra, R. V.; Bajaj, H. C. Sorption studies of CO_2, CH_4, N_2, CO, O_2 and Ar on nanoporous aluminum terephthalate [MIL-53(Al)]. *J. Porous Mater.* 2011, *18***,** 205–210.

[153] Hamon, L.; Llewellyn, P. L.; Devic, T.; Ghoufi, A.; Clet, G.; Guillerm, V.; Pirngruber, G.D.; Maurin, G.; Serre, C.; Driver, G.; Beek, W.; Jolimaître, E.; Vimont, A.; Daturi, M.; Férey, G. Co-

adsorption and Separation of CO_2−CH_4 Mixtures in the Highly Flexible MIL-53(Cr) MOF. *J. Am. Chem. Soc.* 2009, *131***,** 17490–17499.

[154] Llewellyn, P. L.; Bourrelly, S.; Serre, C.; Filinchuk, Y.; Férey, G. How hydration drastically improves adsorption selectivity for CO_2 over CH_4 in the flexible chromium terephthalate MIL-53. *Angew. Chem. Int. Ed.* 2006, *45*, 7751–7754.

[155] Couck, S.; Denayer, J. F. M.; Baron, G. V.; Rémy, T.; Gascon, J.; Kapteijn, F. An amine-functionalized MIL-53 Metal-Organic Framework with large separation power for CO_2 and CH_4. *J. Am. Chem. Soc.* 2009, *131*, 6326–6327.

[156] S. Edubilli. Effect of adsorption history on flexibility of MIL-53(Al) metal organic frame work, M. Tech thesis, IIT Guwahati (2012).

[157] Boutin, A.; Coudert, F. -X.; Springuel-Huet, M. -A.; Neimark, A. V.; Férey, G.; Fuchs, A. H. The behavior of flexible MIL-53(Al) upon CH_4 and CO_2 adsorption. *J. Phys. Chem. C.* 2010, *114***,** 22237–22244.

[158] Stavitski, E.; Pidko, E. A.; Couck, S.; Rémy, T.; Hensen, E. J. M.; Weckhuysen, B. M.; Denayer, J.; Gascon, J.; Kapteijn, F. Complexity behind CO_2 capture on NH_2-MIL-53(Al). *Langmuir* 2011, *27***,** 3970–3976.

Research Output

Journal Publications

1. Satyannarayana Edubilli and Sasidhar Gumma, A systematic evaluation of UiO-66 MOF for CO_2/N_2 separation. Separation and Purification Technology 224 (2019) 85-94.
2. Prashant Mishra, Satyannarayana Edubilli, Bishnupada Mandal, and Sasidhar Gumma, Adsorption Characteristics of Metal Organic Frameworks Containing Coordinatively Unsaturated Metal Sites: Effect of Metal Cations and Adsorbate Properties, J. Phys. Chem. C 118 (2014) 6847–6855.
3. Sravanthi Loganathan, Mayur Tikmani, Satyannarayana Edubilli, Aakanksha Mishra, and Aloke Kumar Ghoshal, CO_2 adsorption kinetics on mesoporous silica under wide range of pressure and temperature, Chemical Engineering Journal 256(2014) 1-8.
4. Prashant Mishra, Satyannarayana Edubilli, Hari Prasad Uppara, Bishnupada Mandal, and Sasidhar Gumma, Effect of Adsorbent History on Adsorption Characteristics of MIL-53(Al) Metal Organic Framework, Langmuir 29 (2013).
5. Prashant Mishra, Satyannarayana Edubilli, Bishnupada Mandal, and Sasidhar Gumma, Adsorption of CO2, CO, CH4 and N2 on DABCO based Metal Organic Frameworks, Microporous Mesoporous Mater. 169 (2013) 75–80.
6. Debjyoti Sahu, Prashant Mishra, Satyannarayana Edubilli, Anil Verma, and Sasidhar Gumma, Hydrogen Adsorption on Zn-BDC, Cr-BDC, Ni-DABCO and Mg-DOBDC Metal Organic Frameworks, J. Chem. Eng. Data 58 (2013).

Conferences Proceedings

1. Satyannarayana Edubilli and Sasidhar Gumma, Evaluation of MOFs for CO_2 capture: From synthesis to process development, AMEEA-2018, NIT Rourkela, India (2018).
2. Rushik G Bandodkar, Dustin Bowden, Satyannarayana Edubilli, Orhan Talu and Sasidhar Gumma, “Chemical Potential Difference between the Large and Narrow Pore Forms of MIL-53 (Al)”, AIChE Annual Meeting 2018, Pittsburgh, PA, USA (2018).

3. Satyannarayana Edubilli and Sasidhar Gumma, "Separation of CO_2/N_2 mixture Using MIL-101(Cr)/PVA Pellets by PSA Process", AIChE Annual Meeting 2017, Minneapolis, MN, USA (2017).
4. Satyannarayana Edubilli and Sasidhar Gumma, "Scale Up Synthesis and Experimental Investigation of Porous Metal Organic Frameworks in Gas Adsorption", ICETNMST_2017, NIT Nagaland, India (2017).
5. Satyannarayana Edubilli and Sasidhar Gumma, "Preparation and Characterization of Metal Organic / Polymer Binder Composites to Use in Gas Separation" ICSIMR2017, CIF, IIT Guwahati, India (2017).
6. Satyannarayana Edubilli and Sasidhar Gumma, "Synthesis, Pelletization and Systematic Evaluation of Chosen Metal Organic Frameworks in Gas Adsorption by Vacuum Pressure Swing Adsorption Process", Research Conclave 2017, IIT Guwahati, India (2017).
7. Satyannarayana Edubilli and Sasidhar Gumma, "Synthesis, Characterization and gas adsorption properties of UIO-66 MOF", ChEmference'16, IIT Gandhinagar, India (2016).
8. Satyannarayana Edubilli, Pradip Das and Sasidhar Gumma, "CO_2/N_2 Separation Using Cu-BTC, UIO-66 and MIL-53(Al) Metal Organic Frameworks", AIChE Annual Meeting 2016, San Francisco, CA, USA (2016).
9. Satyannarayana Edubilli and Sasidhar Gumma, Flue gas separation by flexible porous framework MIL-53(Al), 3rd Indo-German Workshop on "Advances in Materials, Reaction & Separation Processes", IIT Guwahati, India (2016).
10. Satyannarayana Edubilli and Sasidhar Gumma, Adsorption Process Performance Analysis of Metal Organic Frameworks, Invited Talk in 3rd Indo-German Workshop on "Advances in Materials, Reaction & Separation Processes", IIT Guwahati, India (2016).
11. Satyannarayana Edubilli and Sasidhar Gumma, Fixed bed separation of CO_2-N_2 mixture by Zeolite 13X Adsorbent, CHEMCON-2015, IIT Guwahati, India (2015).
12. Satyannarayana Edubilli and Sasidhar Gumma, Equilibrium and Dynamic Adsorption Measurements of CO_2 and N_2 on Zeolite 13X, REFLUX-2015, IIT Guwahati, India (2015).
13. Satyannarayana Edubilli and Sasidhar Gumma, Comparison of Cu-BTC and Zeolite 13X adsorbents for flue gas separation, NCOSDOES, IIT Guwahati, Guwahati, India (2014).
14. Prashant Mishra, Satyannarayana Edubilli, Bishnupada Mandal, and Sasidhar Gumma, "Capitalization of Breathing Phenomena of Flexible MIL-53 (Al) Solid to Enhance Its Carbon

Dioxide Capacity and Selectivity", AIChE Annual Meeting 2013, San Francisco, CA, USA (2013).

15. Prashant Mishra, Satyannarayana Edubilli, Bishnupada Mandal, and Sasidhar Gumma, "Adsorption Characteristics of Coordinatively Unsaturated Metal Sites Containing Dhtp Series of Metal Organic Frameworks" Adsorbent Materials: MOFs, AIChE Annual Meeting 2013, San Francisco, CA USA (2013).

Workshops Attended

1. **State of the art in refinery operations**

   A one-day workshop titled "State of the art in refinery operations" organized by Department of chemical engineering IIT Guwahati and Guwahati Refinery on 4th April 2018.

2. **Australia-India Joint Symposium**

   Australia-India Joint Symposium on "Nano porous Materials for Clean Energy Applications", CSIR-IIP, Dehradun, India on 8 March, 2016 (jointly organized by CSIRO, Australia and CSIR-IIP Dehradun, India).

3. **Indo-German Workshop**

   Indo-German Workshop on "Advances in Materials, Reaction & Separation Processes", IIT Guwahati, February 23-26, 2016(jointly organized IIT Guwahati, India and the Max Planck Institute for Dynamics of Complex Technical Systems, Magdeburg, Germany).

4. **Workshop on Hydrogen Storage Materials**

   An Industry-Academia Workshop on "Hydrogen storage materials", December 7, 2018 at Indian Oil R&D Centre, Faridabad.